



DELTA Annual Report 2022

**Dortmund
30. November 2022**

Edited by C. Sternemann, R. Wagner,
D. Lützenkirchen-Hecht (2022)

Preface

Dear readers, dear colleagues,

this DELTA annual report is now the third without having a regular user's meeting. As many cooperation meetings as well as synchrotron beamtimes took place at the end of this year, it was impossible for the organizers to find a date suited for a majority of the active DELTA users. We therefore decided to postpone the meeting to Spring 2023, and we hope that many of you will find their way to Dortmund and participate to a lively discussion of the science undertaken at DELTA. We will communicate the date as soon as possible, so please regularly visit the websites of the facility and watch out for updates.

This year, an impressive number of contributions to the annual report have been submitted by the users, and we appreciate with great pleasure 14 reports dedicated to instrumentation and 38 reports on X-ray scattering and X-ray spectroscopy, respectively. Obviously, DELTA users got back to work and were extremely productive at the different instruments. In parallel, the operation of the superconducting wiggler installed in 2020 smoothly worked over the entire year, allowing the delivery of intense (hard) X-ray beams for beamline 8, 9 and 10. Similar to previous years, many users mailed-in their samples, and the DELTA staff and the beamline scientists did their best to get the external users satisfied.

The reports included in this annual report reflect a broad spectrum of scientific activities, ranging from machine-related research, studies on fundamental research questions as well as of applied character from various disciplines such as physics, chemistry, geology, biology and engineering. We take the opportunity to thank the involved scientists and researchers, as well as the technicians and engineers, for their individual advocacy and commitments, which made this success possible. We gratefully acknowledge the financial support by the funding agencies and the local government, as well as we like to thank the universities and research institutions, in particular the TU Dortmund for their manifold efforts, that allowed the successful operation of the DELTA synchrotron in 2022.

Christian Sternemann, Ralph Wagner & Dirk Lützenkirchen-Hecht

Contents:

<u>Instrumentation</u>	1
Recent status of machine learning-based applications at DELTA D. Schirmer, A. Althaus, S. Hüser, S. Khan, T. Schüngel	3
Improvement of the electron beam lifetime at DELTA G. Schmidt, B. Büsing, G. Dahlmann, B. Sawadski	7
Reconfiguration of the Undulator U250 for EEHG B. Büsing, A. Althaus, T. Dybiona, A. Held, S. Khan, A. Leinweber, C. Mai, A. Radha Krishnan, H.-P. Ruhl, B. Sawadski, D. Schirmer, G. Schmidt, T. Schulte-Eickhoff	11
DELTA Radiofrequency Systems P. Hartmann, V. Kniss, A. Leinweber and the DELTA team	13
Study of Seed Laser Properties from CHG Radiation Spectra A. Radha Krishnan, B. Büsing, S. Khan, C. Mai, Z. Usfoor, V. Vijayan	15
SPEED: Worldwide first EEHG Signal at a Storage Ring S. Khan, B. Büsing, A. Held, C. Mai, A. Radha Krishnan, W. Salah, Z. Usfoor, V. Vijayan	17
FEL Microbunching in Drift Sections S. Khan, G. Perosa, F. Sottocorona, E. Allaria, A. Brynes, G. Penco, P. R. Ribič, S. Spampinati, C. Spezzani, M. Trovò, L. Giannessi, G. De Ninno, E. Ferrari, E. Schneidmiller	21
Measurement and Simulation of Radiation Doses S. Khan, C. Mai	25
Ultrafast X-ray sources and angle-resolved electron spectroscopy L. Funke, A. Held, D. Reinke, S. Savio, N. Wieland, L. Wülfing, W. Helml	27
Studies of Instabilities and Energy Spread at the Canadian Light Source P. Hartmann, D. Bertwistle, M. Boland, S. Martens, H. Shaker	31
Testing the von Hamos spectrometer setup with white beam excitation N. Thiering, C. Albers, R. Sakrowski, E. Schneider, M. Paulus, C. Sternemann	35
A new high-pressure cell for wide-angle X-ray scattering K. Lehninger, E. Schneider, J. Savelkouls, M. Paulus, C. Sternemann, M. Tolan	37
A New Spectrometer for the Characterization of VUV/XUV Radiation at DELTA Z. Usfoor, B. Büsing, A. Held, S. Khan, A. Radha Krishnan, C. Mai, V. Vijayan	39
Preparation and measurement of millisecond X-ray pulses at DELTA beamline 10 C. Grundmann, D. Lützenkirchen-Hecht	41

<u>Soft X-ray spectroscopy</u>	43
Comparison of two different sub-monolayer Sn $\sqrt{3}$ -phases on Au(111) J. A. Hochhaus, L. Kesper, U. Berges, C. Westphal	45
<u>X-ray scattering</u>	49
Pressure-dependent protein-protein interactions in aqueous protein solutions M. Dargasz, M. Paulus, J. Savelkouls	51
Kinetics of aggregation of egg yolk low-density lipoproteins revealed by X-ray scattering N. Das A, S. Timmermann, M. Kowalski, S. Dogan-Surmeier, M. Paulus, C. Gutt	53
Temperature-induced structural rearrangements in high-density lipoproteins S. Dogan-Surmeier, M. Paulus, N. Das A, C. Gutt	55
The effect of pressure and additives on the lamellar-to-cubic transition dynamics of monoolein at excess water conditions J. Savelkouls, M. Dargasz, M. Paulus	57
Temperature dependent behavior of micelle structure formation in NIPA Ö. Öztürk, G. Evingür, C. Gutt	59
Apoferritin adsorption on solid-supported DMPC bilayers J. Savelkouls, S. Dogan, M. Moron, C. Sternemann, M. Paulus	61
Adsorption of supercritical fluids on hydrophobic interfaces near the critical point M. Moron, S. Dogan, M. Moron, N. Thiering, M. Paulus, J. Nase	63
A small- and wide-angle x-ray scattering study on morphology changes in a polyurethane shape memory polymer Y. Shen, K. Neuking, G. Eggeler, M. Paulus, C. Sternemann	65
Investigation of temperature dependent aggregation dynamics of thermoresponsive polymers Ö. Öztürk, M. Meier, K. Heckhäuser, C.J.B. Kunzler, U. Jonas, C. Gutt	67
Probing chain alignment in polymer electrolytes upon ion transport in electric fields using operando 2D wide angle X-ray scattering A. Kuhlmann, M. Huck, H.-G. Steinrück, C. Mönich, A. Hockmann, M. Schönhoff, C. Sternemann	69
Effect of TEACl treatment on the surface structure of perovskite X. Zhang, W. Qiu, C. Sternemann	71
Real-time investigation of phase transformations of MOF nanoparticles in responsive porous liquids A. Koutsianos, S. Henke	75
Photoswitching vesicles containing phospholipids and photo-sensitive azobenzene-glycolipids S. Hövelmann, R. Giri, E. Dieball, M. Paulus, B. Murphy	79
Insights into high-pressure and temperature induced phase transitions of fatty core packing in low-density lipoproteins S. Dogan-Surmeier, M. Paulus, N. Das A, C. Gutt	81

X-ray emission spectroscopy study of the spin transition upon CO ₂ adsorption in an amine-functionalized porous coordination polymer V. Rubio-Giménez, C. Bartual-Murgui, M. Romero-Ángel, S. Tatay, C. Martí-Gastaldo, M. Paulus, C. Sternemann, J. A. Real	83
Optimized Charge Transport in Molecular Semiconductors by Control of Fluid Dynamics and Crystallization Process O. Yildiz, H- Makowska, S. Wang, Z. Ling, W. Waliszewski, W. Pisula, T. Marszalek	85
Apoferitin under high hydrostatic pressure G. Scholz, M. Paulus, C. Gutt, S. Dogan	87
Oxidation Resistance of PECVD Ti-Si-C-N Nanocomposite Coatings A. Thewes, C. Kipp, P.M. Reinders, T. Brückner, C. Sternemann, M. Paulus	89
Surface passivation of perovskite nanocrystals B. Pradhan, C. Sternemann	93
Influence of bias voltage on the structural properties of TiAlN coatings deposited by hybrid DC/HiPIMS technology D. Stangier, N.F. Lopes Dias ¹ , C. Sternemann, M. Paulus, W. Tillmann	95
Influence of increased temperature on the compound layer of nitrided steels C. Kipp, P. Reinders, T. Brückner, H. Paschke, A. Thewes, C. Sternemann, M. Paulus	99
Synthesis of sulfur-containing nanoparticles based on Cu and Mo W. Tillmann, D. Kokalj, F. Ontrup, J. Urbanczyk, C. Sternemann, M. Paulus	103
Advanced Arc-Enhanced Glow Discharge Etching High-Speed Tool Steel Substrates for PVD Deposition of TiAlN D. Stangier, N. F. Lopes Dias, C. Sternemann, M. Paulus, W. Tillmann	107
An X-ray diffraction study on AlCrVYN thin films E. Schneider, F. Ontrup, N. Thiering, S. Dogan, J. Savelkouls, K. Lehninger, C. Sternemann, M. Paulus, N. F. Lopes Dias, W. Tillmann, M. Tolan	111
A study on the phase evolution in ID-HVOF sprayed coatings using WC-CoCr feedstocks with different WC particle sizes L. Hagen, M.D. Kensity, M. Paulus, W. Tillmann	113
Oberflächenanalyse von lichtbogengespritzten amorphen und In-Situ-legierten Schichten K. Porscha, H. Steinhoff, M. Abdulgader	117
In situ XRD investigation of crystallization in FeCoSiB metallic glass N. Hayen, B. M. Murphy, P. Jordt, L. Petersdorf, M. Paulus, C. Sternemann	123
Characterization of ZTO/Ag/ITO thin films using X-ray reflectivity S. Bieder, P. Schlenz, S. Dogan-Surmeier, C. Albers, M. Paulus, E. Schneider, N.Thiering, C. Sternemann, S. Cornelius	125
Low-temperature plasma nitriding to enhance tribocorrosive resistance of corrosion-resistant steel T. Brückner, H.Paschke, A. Thewes, P. Reinders, C. Kipp, C. Sternemann, M. Paulus	127
Solid solutions Ln _x U _{1-x} C ₂ with Ln = Sm, Er C. Tobeck, U. Ruschewitz	131
Uncovering the thermal behaviour of pristine and linker-exchanged ZIF-8 with variable temperature X-ray powder diffraction W. Xue, C. Das, R. Pallach, S. Henke	133

<u>Hard X-ray spectroscopy</u>	137
X-ray absorption studies of the EBDC fungicide Maneb in solid state L. Kubens, J. Bornhorst, F. Mohr, D. Lützenkirchen-Hecht	139
Time-resolved, quick X-ray absorption spectroscopy at DELTA beamline 10 D. Lützenkirchen-Hecht, F. Eckelt, S. Paripsa, L. Voss, F. Braun, P. Rothweiler, R. Wagner	141
EXAFS investigations of Nb interlayer on Nb ₃ Sn coatings on Cu F. Braun, L. Voss, N. Schäfer, M. Major, L. Alff, D. Lützenkirchen-Hecht	143
XANES Investigation of the Solid solution Er _x U _{1-x} C ₂ C. Tobeck, S. Kirchhoff, D. Lützenkirchen-Hecht, U. Ruschewitz	145
An X-ray absorption near-edge structure study on AlCrVYN thin films E. Schneider, F. Ontrup, N. Thiering, S. Dogan, S. Bieder, C. Sternemann, M. Paulus, D. Kokalj, D. Stangier, N.F. Lopes Dias, R. Wagner, D. Lützenkirchen-Hecht, W. Tillmann, M. Tolan	147
EXAFS investigations of PtCu Nanoalloys on Nitrogen-Doped Carbon for Applications in Fuel Cells B. Wu, J. Xiao, L. Li, Y. Wu, X. Tang, T. Hu, M. Qiu, F. Braun, F. Eckelt, L. Voss, D. Lützenkirchen-Hecht, K. Yuan, Y. Chen	149
<u>Notes</u>	151

Instrumentation

Recent status of machine learning-based applications at DELTA

D. Schirmer, A. Althaus, S. Hüser, S. Khan, T. Schüngel

Zentrum für Synchrotronstrahlung (DELTA), Technische Universität Dortmund

At many accelerator facilities, applications based on machine learning (ML) are used as standard tools for accelerator optimization, automated control tasks, and beam diagnostics. Since last year, further progress in this field has also been made at the DELTA storage ring [1]. For example, the simulated ML-based pre-studies for chromaticity control [2] were successfully transferred to real machine operation [3, 4] and the ML-based electron transfer optimization (injection optimization) from the booster synchrotron to the storage ring was also improved [4, 5].

Automated injection efficiency optimization

Within the framework of a diploma thesis [5], preliminary work on ML-driven automated injection optimization was performed. For this purpose, 13 parameters of the transfer line T2 between booster and storage ring were randomly as well as systematically varied and the corresponding impact on the injection efficiency was measured. These data served as input for supervised training of two types of injection models based on Neural Networks (NN) and Extremely Randomized Trees (Extra Trees [6], a special case of Decision Trees [7]), respectively. First benchmark comparisons showed that NNs are better suited as an injection prediction model (so-called surrogate model) than Extra Trees (see Fig. 1).

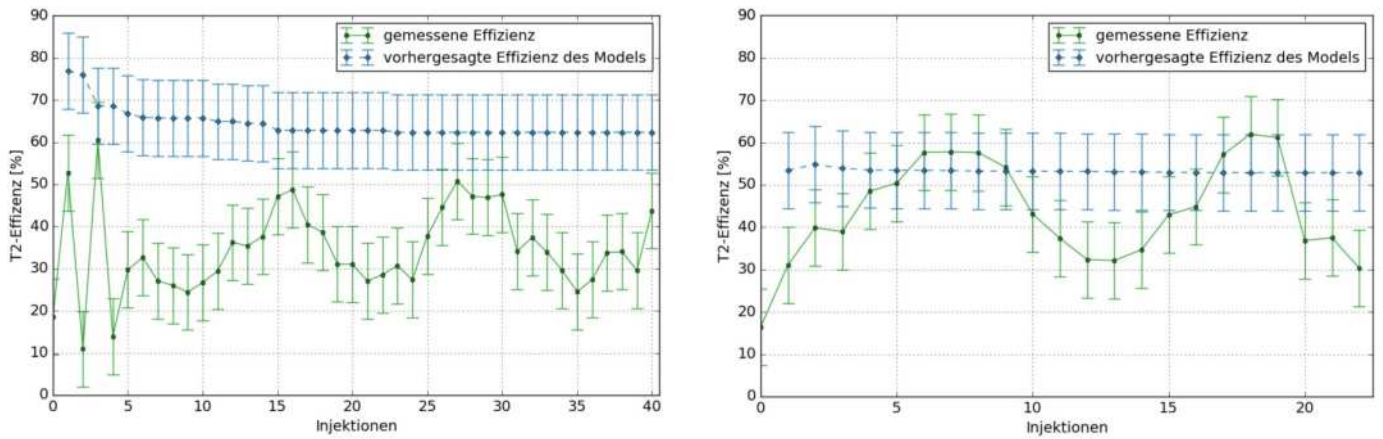


Figure 1: Left: Measured T2 injection efficiencies (green) obtained by injection parameter settings which were proposed by an Extra Trees-trained model. The efficiencies achieved the model predictions (blue) only poorly. **Right:** Measured T2 injection efficiencies (green) optimized by an NN-driven surrogate model. After a few injections, the measured efficiency approaches the NN-model prediction (blue) quite well. In both cases, the efficiency fluctuations were probably caused by a malfunctioning T2 dipole magnet. Data were taken from [5].

These preliminary studies were continued in the scope of a subsequent master's thesis [4]. In this work the injection parameter space was extended to 17 dimensions and the database for ML-based training was enlarged. In addition to the strength settings of the T2 transfer line magnets, the injection elements of the storage ring (e. g., kicker magnets, magnets of a static injection bump) as well as some trigger timings of the pulsed T2 transfer line and kicker magnets were now taken into account, too. Furthermore, Gaussian Process Regressions methods (GPR) were applied for the optimization process [8]. Since GPRs get by with less training data and are more efficient for lower dimensional problems, the parameter space has been divided into 4 subgroups of similar magnet types (e.g., quadrupole-, corrector- and kicker magnets). See Fig. 2 right as an example. Figure 2 (left) shows the associated comparison of injection optimization runs based on GPR- and NN-driven surrogate models, respectively. Both methods improve the injection efficiency, with GPRs performing significantly better.

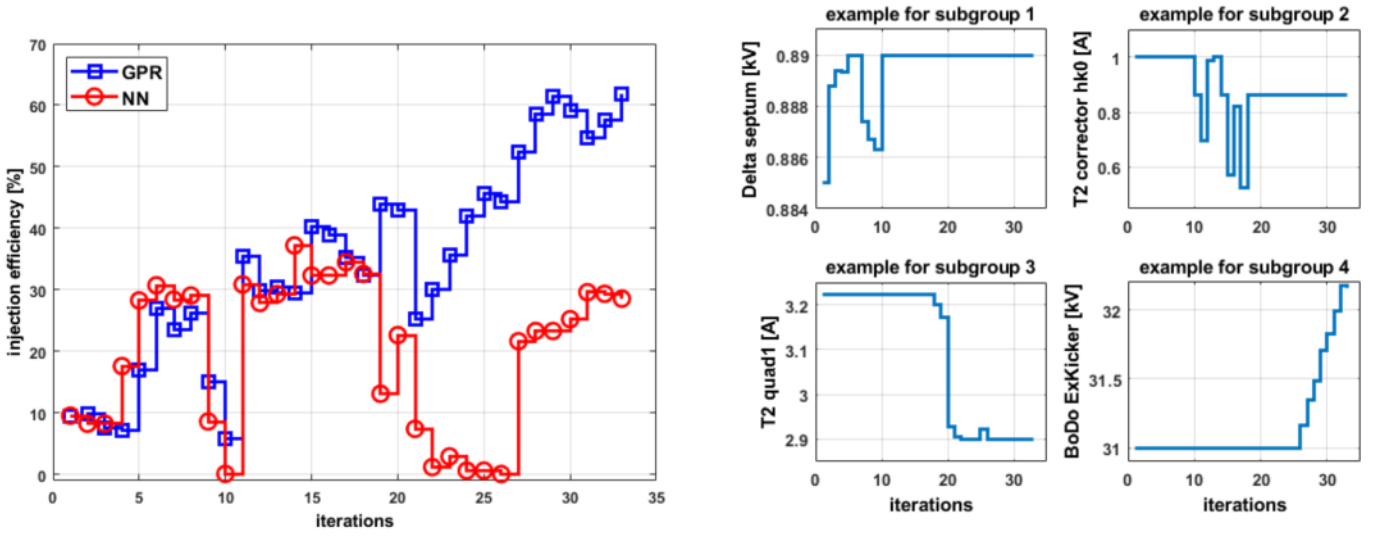


Figure 2: Left: Injection efficiencies optimized by a Gaussian Process Regression (GPR) model (blue) in comparison to an NN-driven model (red). Right: Variation of set values during injection optimization (iterations) for one example from each of four injection parameter subgroups. Data were taken from [4].

Chromaticity control

To increase the degree of freedom for automated chromaticity control, we repeated the pre-studies in [1, 2], but now utilizing all 15 sextupole power supply (PS) circuits individually (see Fig. 3). A detailed lattice model of the DELTA storage ring served as the basis for x,y -coupled optics and chromaticity (ξ_x, ξ_y) computation. A similar approach was adapted to real machine operation. Here too, all seven sextupole families were split into 15 individual PS circuits (see Fig. 4). For more details see [3] and [4].

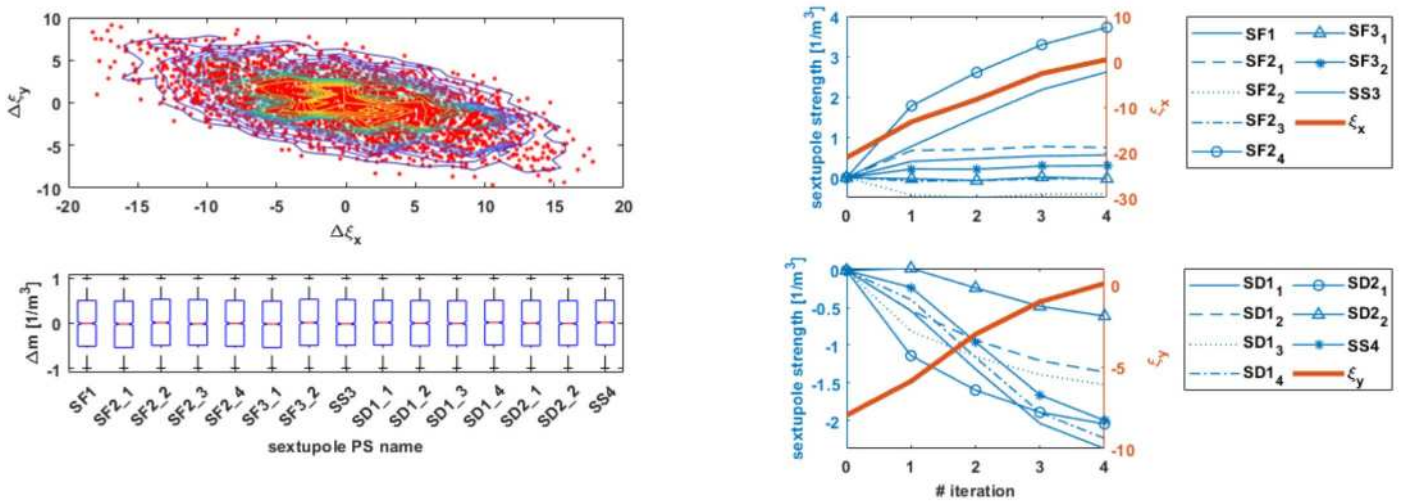


Figure 3: Left: Distribution of 3000 simulated chromaticity shifts $\Delta\xi_{x,y}$ (top) invoked by uniformly randomized strength variations Δm of 15 independent sextupole power supplies (PS) circuits (bottom). The data are obtained by optics simulations based on a DELTA storage ring lattice model. Right: Example for verification of NNs trained by simulated data and applied to the DELTA storage ring model. The desired target values for compensated chromaticity (goal: $\xi_x = \xi_y = 0$) were reached in 4 iterative steps (red curves) starting at the setting for natural chromaticity ($\xi_x = -21, \xi_y = -8$, all sextupoles switched off). The corresponding sextupole strength adaptations are shown as blue lines. In total, 15 individual power supplies (PS) are available to operate 7 sextupole magnet families. They are grouped in four horizontally (top: SF1, SF2, SF3, SS3) and three vertically (bottom: SD1, SD2, SS4) focusing families. The indices label the individual PS circuits.

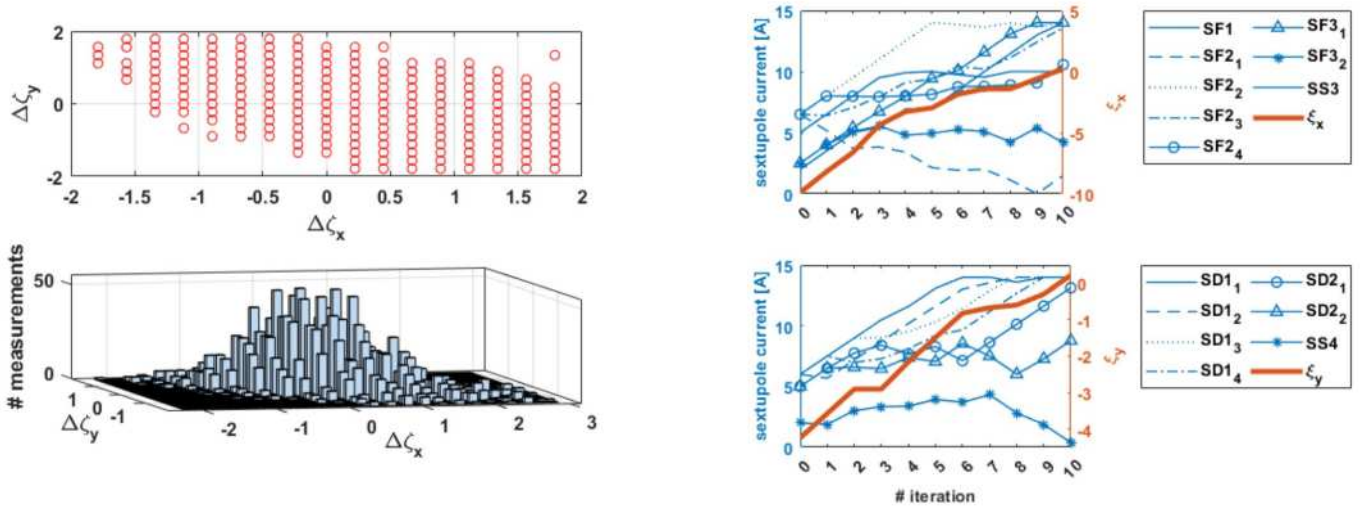


Figure 4: **Left:** Distribution of 2749 measured chromaticity shifts (cleaned data) invoked by uniformly and Gaussian randomized strength variations of 15 independent sextupole power supply circuits (bottom). Due to granularity constrictions of the chromaticity measurements $\Delta\xi_{x,y}$, all values are distributed on a resolution-limited grid (top). **Right:** Example application to test NNs trained by experimental data and applied to the real storage ring. The desired target values for compensated chromaticity (target: $\xi_x = \xi_y = 0$) were reached in 10 iterative steps starting with chromaticity values of $\xi_x = -10$ and $\xi_y = -4.4$.

The studies have demonstrated that classical machine learning methods like conventional feed-forward neural networks are appropriate for chromaticity control in simulation as well as in real storage ring operation. Furthermore, it could be shown that splitting the sextupole PS families into individual PS circuits has increased the flexibility to approach desired chromaticity settings in real storage ring operation.

References:

- [1] D. Schirmer, A. Althaus, S. Hüser, S. Khan, T. Schüngel, *New machine learning projects at DELTA*, in 17th DELTA Annual Report 2021, pp. 3–4, Dortmund, Germany, November 2021.
https://www.delta.tu-dortmund.de/cms/Medienpool/User_Reports/DELTA_User_Report_2021.pdf.
- [2] D. Schirmer, A. Althaus, S. Hüser, S. Khan, T. Schüngel, *Machine Learning Projects at the 1.5 GeV Synchrotron Light Source DELTA*, Proc. of ICALEPCS’21, Shanghai, China, pp. 631-635 (2021),
doi:10.18429/JACoW-ICALEPCS2021-WEPV007
- [3] D. Schirmer, A. Althaus, T. Schüngel, *Machine learning methods for chromaticity control at the 1,5 GeV synchrotron light source DELTA*, Proc. of IPAC’22, Bangkok, Thailand, pp. 1141-1144 (2022),
doi:10.18429/JACoW-IPAC2022-TUPOPT059.
- [4] T. Schüngel, *Development of a Container-Based Work Environment for an automated Optimization of the Sextupole Settings and Injection Efficiency using Machine-Learning at the Storage Ring DELTA*, Master’s Thesis, TU Dortmund, August 2022.
- [5] S. Hüser, *Implementierung neuartiger Optimierungsalgorithmen an der Speicherringanlage DELTA*, Diploma Thesis, TU Dortmund, May 2022.
- [6] P. Geurts, E. Damien and L. Wehenkel, *Extremely randomized trees*, Machine Learning, 63, Nr. 1 (2006): 3–42.
- [7] L. Breiman, J. H. Friedman, R. A. Olshen, and C. J. Stone, *Classification and Regression Trees*, Chapman & Hall, Boca Raton, FL (1984).
- [8] C. E. Rasmussen and C. Williams, *Gaussian processes for machine learning*, MIT Press, Cambridge, MA, ISBN 9780262182539, (2005).

Improvement of the electron beam lifetime at DELTA

G. Schmidt, B. Büsing, G. Dahlmann, B. Sawadski

Zentrum für Synchrotronstrahlung (DELTA), Technische Universität Dortmund

Overview: The electron beam lifetime is an important parameter for a storage ring operated with a few injection periods per day. Synchrotron light users benefit from a larger electron beam lifetime due to the higher average electron beam current and the smaller change of the heat load on the probe system.

At DELTA the electron beam lifetime has improved significantly during the last year. We show that the main improvement was achieved by reactivating the integrated non-evaporable getter (NEG) pumps.

Electron beam lifetime: Apart from electron-electron scattering (Touschek effect), the beam lifetime depends on the stored beam current because the emitted synchrotron photons cause gas desorption when striking the vacuum chamber surface. This effect increases the vacuum pressure and therefore the scattering of the stored electrons on residual gas molecules in the vacuum chamber, thus reducing the beam lifetime with increasing beam current.

All values of the beam lifetime and vacuum pressure given here are measured at beam currents between 99 mA and 101 mA, representing the typical beam current during measurements using synchrotron light at DELTA, and are shown from the beginning of 2019 until mid-November 2022.

Activation of NEG and ion getter pumps: The surface of the NEG and ion getter pumps can be reactivated following a certain heating procedure. A system of several pumps needs a clear procedure and strict order of steps in heating and pumping [1,2]. New power supplies and cabling of the NEG pumps had to be installed for this purpose. Also, first test with titanium sublimation pumps were performed [2].

As a result, the vacuum pressure around beam currents of 100 mA and 101 mA is significantly reduced in several sectors of the storage ring, directly leading to an improved gas scattering lifetime after a short recovery time (few days) after each intervention (see Figs. 1 to 3). The vacuum pressure further evolves over several months. It is clearly visible that reactivation of the NEG pumps greatly increases their pumping speed.

Measures improving the beam lifetime at DELTA: The following work on the DELTA vacuum system was performed during the last years:

- 1) Installation of a EU-type radiofrequency (RF) resonator (April 2019) [3].
- 2) Dual-cavity operation after installation of a second RF amplifier and a digital low-level RF system (DLLRF) (September 2019) [3].
- 3) Installation and alignment of a new superconducting wiggler (September/October 2020).
- 4) Exchange of a bellow and valve at beamline BL 5a, activation of NEG and ion getter pumps in the north-west quadrant 2 (November 2021).
- 5) Activation of NEG and ion getter pumps in the north-east quadrant 1 (March 2022).
- 6) Activation of NEG and ion getter pumps in the south-west quadrant 4 (March 2022).
- 7) Activation of NEG and ion getter pumps in the south-east quadrant 3 (April 2022).
- 8) Activation of NEG and ion getter pumps at the wiggler outlet chamber (May 2022).
- 9) Activation of NEG and ion getter pumps in the undulator U250 region (June 2022).
- 10) Adjustment of the beamline BL 6 vacuum chamber (September 2022).
- 11) Reduction of RF power to save energy (since mid-October 2022).

Outlook: After reactivation of most pumps in the storage ring, a significant improvement of the beam lifetime was achieved. By improving the bake-out procedure at the storage ring and beamline vacuum chambers up to the first valve, further progress in reducing the vacuum pressure and increasing the beam lifetime is anticipated.

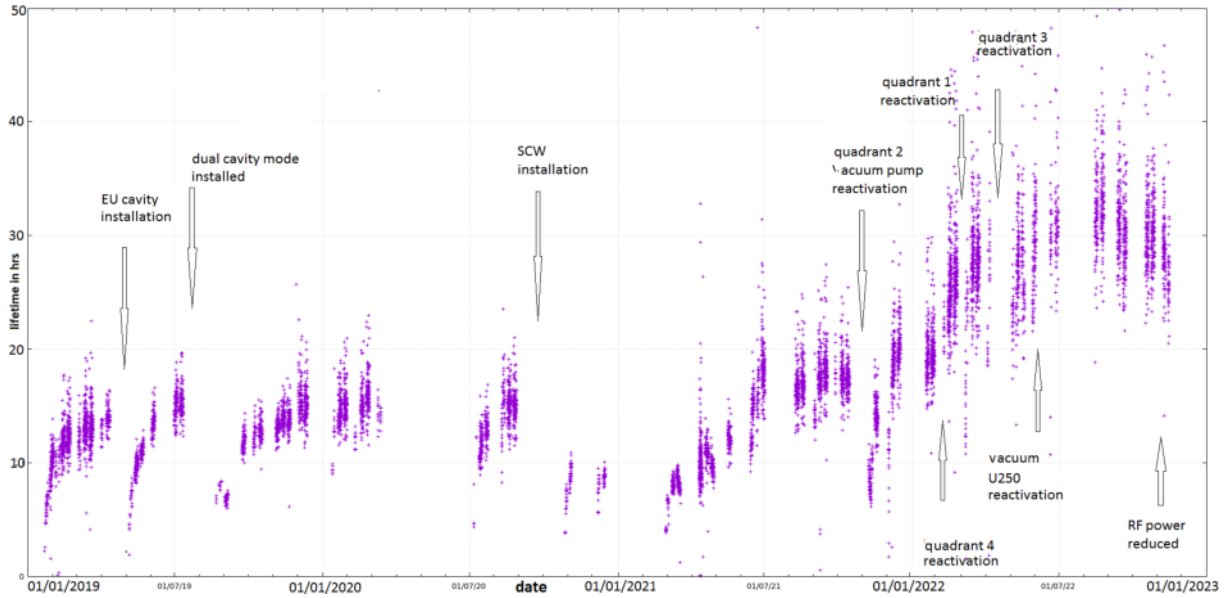


Figure 1: Development of the beam lifetime in the DELTA storage ring at an electron beam current around 100 mA from January 2019 to mid-November 2022.

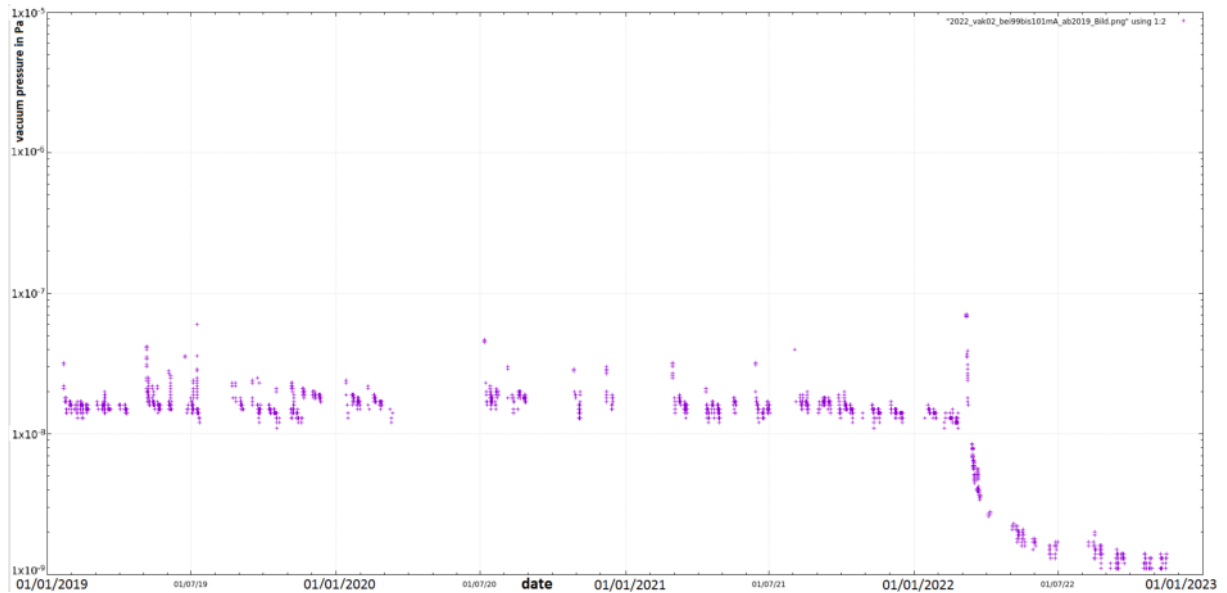


Figure 2: Development of the vacuum pressure (in Pa) in the north-east quadrant 1 of the DELTA storage ring at a beam current around 100 mA. Clearly visible is the reduction of the pressure after the activation of NEG pumps in March 2022.

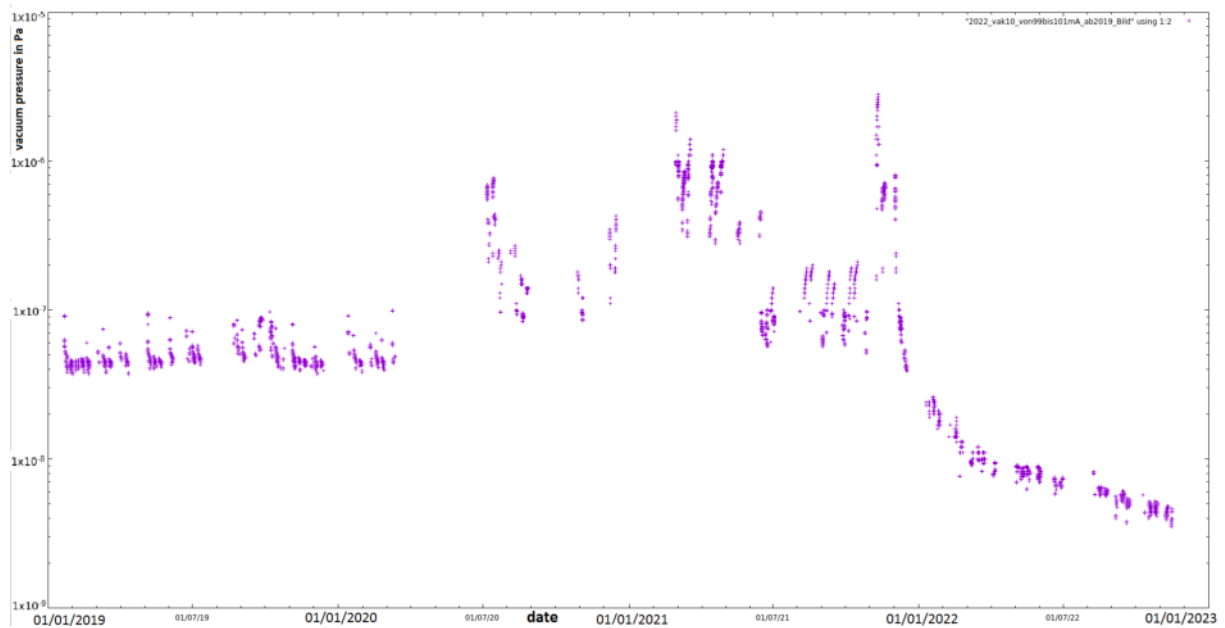


Figure 3: Development of the vacuum pressure (in Pa) in the north-west quadrant 2 of the DELTA storage ring at a beam current around 100 mA. Clearly visible is the effect of a persisting vacuum leak at a bellow of the THz beamline BL 5a. After replacing the bellow and activation of ion getter as well as internal NEG pumps in the nearby quadrant 2 in November 2021, the vacuum pressure dropped significantly and is presently more than a factor 10 better than in 2019.

References

- [1] SAES, Italy (producer of the NEG material used at DELTA), private communication.
- [2] G. Schmidt et al., *Activation procedure of the NEG pumps, ion getter pumps and titanium sublimation pumps in DELTA*, Internal Report, to be published.
- [3] P. Hartmann, V. Kniss, private communication.

Reconfiguration of the Undulator U250 for EEHG

B. Büsing, A. Althaus, T. Dybiona, A. Held, S. Khan, A. Leinweber, C. Mai, A. Radha Krishnan, H-P. Ruhl, B. Sawadski, D. Schirmer, G. Schmidt, T. Schulte-Eickhoff
Zentrum für Synchrotronstrahlung (DELTA), Technische Universität Dortmund

Overview: Since 2011, the DELTA short-pulse source is operated at the storage ring [1]. To enable the Coherent Harmonic Generation scheme (CHG) [2], the electromagnetic undulator U250 was wired in a way that three sections (modulator, chicane and radiator) were achieved and a switchboard with copper bars was used to switch between the CHG- and the normal BL 5 mode. The more complex scheme Echo-enabled Harmonic Generation (EEHG) [3] requires two modulators, two chicanes and one radiator, and promises to achieve shorter wavelengths compared to CHG.

In April 2022, the SPEED project (Short-Pulse Emission via Echo at DELTA) was born, a setup for the worldwide first demonstration of EEHG at a storage ring with moderate hardware modification. For this purpose, the U250 had to be rewired to achieve the five necessary sections with only a few periods each (see Tab. 1). In the following two months, this idea was vigorously pursued and the rewiring was executed in the summer shutdown.

Rewiring of the U250: To obtain one more period, the usual undulator design of two additional poles at either end ($1/4$ and $-3/4$ of the full field) was dropped and single endpoles with $1/2$ field were chosen. Figure 1 shows a schematic of the U250 in BL 5 and SPEED mode. A detailed wiring diagram was developed accordingly. In addition, three new switchboards, based on the existing board for switching between CHG and BL5 mode, were designed to enable alternation between the SPEED and BL 5 configuration with moderate effort.

Based on the coil properties and the required magnetic fields for the experiment, it was decided to use 14 power supplies. The requirements and the chosen power supplies are listed Tab. 2. All these power supplies were already in house, either for the CHG setup, the previously used superconducting wiggler SAW or the new undulators U200.

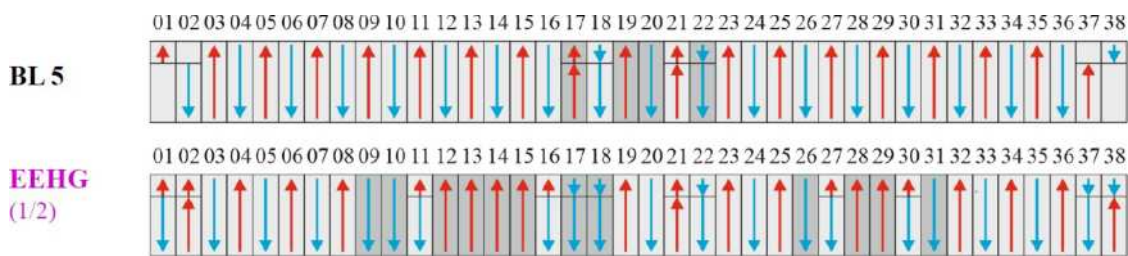


Figure 1: Polarity (magnetic field up or down) of the undulator U250 in two configurations. The length of the arrows indicates the strength of the field and dark grey color shows the chicane coils.

Table 1: U250 in CHG and EEHG Configuration

CHG	modulator	14 poles
	chicane (R_{56})	6 poles ($170 \mu\text{m}$)
	radiator	14 poles
EEHG	1. modulator	8 poles
	1. chicane (R_{56})	8 poles ($550 \mu\text{m}$)
	2. modulator	8 poles
	2. chicane (R_{56})	6 poles ($105 \mu\text{m}$)
	radiator	6 poles

Table 2: Requirements for and Choice of the Power Supplies

	Voltage (V)	Current (A)	Power Supplies
Modulator 1	48,2	400	2x Topcon 200 A
Pole 11	3,0	200	Delta Elektronika 200 A
Chicane 1	96,4	800	3x Topcon 308 A
Pole 16	2,1	140	Delta Elektronika 200 A
Modulator 2	54,2	400	2x Topcon 200 A
Pole 27	2,1	140	Delta Elektronika 200 A
Chicane 2	48,2	800	Danfysik 800 A
Pole 30	1,5	100	Delta Elektronika 200 A
Radiator	42,2	400	2x Topcon 308 A

The rewiring and construction of the switch boards started beginning of July. First, the cables of the old setup were removed and all racks for the power supplies were set up. Since two racks are located outside of the radiation protection wall, the wall was opened to install a cable channel on the floor. In parallel, the copper bars and boards were prepared. After that, all cables were cut and connected to the coils or the switchboards. Overall, 190 cables were prepared, and 12 meters of copper bars were processed.

In addition to the main coils, 16 of the correction coils were rewired. A new water distributor was installed, and the water distribution was changed to provide adequate cooling for the high-current chicane coils. The interlock system to shut down the power supplies in case of water failure or excessive coil temperature was extended to all power supplies. All work was completed within the five weeks of the summer shutdown.

During the first week after rewiring, the control of the power supplies was tested and optimized. The polarity of the coils was checked with a Hall probe in both, SPEED and BL5 mode, and no fault was found. The coil temperature at maximum currents was checked with a thermographic camera to ensure that the new water distribution worked as expected.



Figure 2: Rewired undulator U250 with three new switchboards in front of it.

References

- [1] S. Khan et al., *Generation of Ultrashort and Coherent Synchrotron Radiation Pulses at DELTA*, Sync. Rad. News 26:3, 25 (2013).
- [2] R. Coisson and F. De Martini, *Free-electron coherent relativistic scatterer for UV-generation*, Quantum Electronics, vol.9, p. 939, 1982.
- [3] G. Stupakov, *Using the Beam-Echo Effect for Generation of Short-Wavelength Radiation*, Phys. Rev. Lett. 102, 074801 (2009).

DELTA Radiofrequency Systems

P. Hartmann, V. Kniss, A. Leinweber and the DELTA team

Zentrum für Synchrotronstrahlung (DELTA), Technische Universität Dortmund

Linac RF System

The LINAC RF system performed well within the last year. An old klystron tube was refurbished by the manufacturer.

Booster RF System

A power supply unit and the driver module of the booster solid-state amplifier had to be replaced. The defective parts were repaired by the manufacturer or replaced by new components. Other than that, the booster RF system performed well.

Saving Energy:

The parking power of the booster RF was reduced from 5.7 kW to 2.8 kW. The new parking power is selected such that the booster cavity just does not cool down when the injection is switched off. A thermal load on the cavities is thus avoided. With 3000 operating hours per year and a power amplifier efficiency of 40%, the annual savings in primary electrical energy amount to about 20 MWh.

Storage Ring RF System

The storage ring RF system performed well within the last year.

Saving Energy:

To save energy, the power in the two cavities is reduced to such an extent that the lifetime of the stored beam is approximately 25 hours. This means that standard operation with two injections within 24 hours can be maintained and the beam current does not drop below 80 mA. Although investigations are still ongoing, a primary electrical energy saving of 20 MWh for cavity 2, which is operated with a solid-state amplifier, can be anticipated. For cavity 1, which is still operated with a klystron tube, the reduction of the cavity voltage alone does not result in saving primary electrical energy. Here we plan to reduce the high voltage of the klystron tube from 24 kV to 23 kV. Provided that the focusing of the electron beam in the klystron is not too strongly impaired, this would result in additional savings of about 10 MWh per year.

Study of Seed Laser Properties from CHG Radiation Spectra

A. Radha Krishnan, B. Büsing, S. Khan, C. Mai, Z. Usfoor, V. Vijayan

Zentrum für Synchrotronstrahlung (DELTA), Technische Universität Dortmund

At DELTA, Coherent Harmonic Generation (CHG) is employed to produce ultrashort coherent radiation pulses in the vacuum ultraviolet (VUV) spectral range. This is achieved via a laser-induced modulation of the electron energy which is then converted to density modulation by a dispersive chicane. Since the electric field profile of the seed laser pulse is imprinted onto the induced energy modulation, the properties of the resulting CHG radiation can be manipulated by controlling the properties of the seed. The spectral phase of the seed pulse and the strength of the dispersive chicane (transport matrix element R_{56}) are two effective parameters to control the CHG pulse properties [1].

CHG spectra up to the 6th harmonic of the 800 nm seed were recorded using an iCCD camera and an XUV spectrometer [2] under variation of the chicane strength and laser spectral phase controlled by adjusting the distance between the gratings in the compressor of the laser amplifier [3]. The spectral map (CHG intensity versus wavelength and R_{56}) shows an asymmetry in the spectral features which suggests a strong third-order dispersion in the seed pulse.

Using a convolutional neural network (CNN), the group-delay dispersion (GDD) and third-order dispersion (TOD) of the seed pulse was predicted from the observed spectral map of the CHG radiation. The CNN was trained on a set of simulated spectral maps for different combinations of GDD and TOD [4]. Figure 1 shows the observed and predicted distributions for different spectral phases of the seed laser.

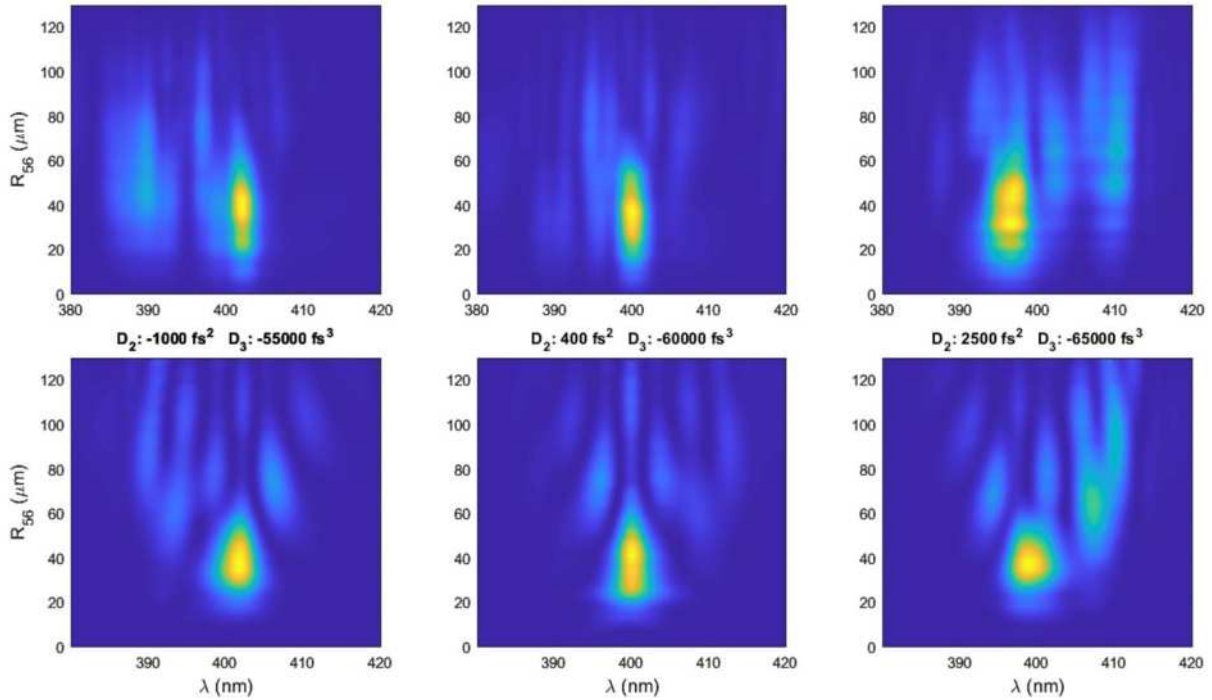


Figure 1: Observed (top) and predicted (bottom) CHG spectral maps for 3 different compressor grating separations. The predicted values of GDD and TOD (D_2 and D_3) are shown for each instance.

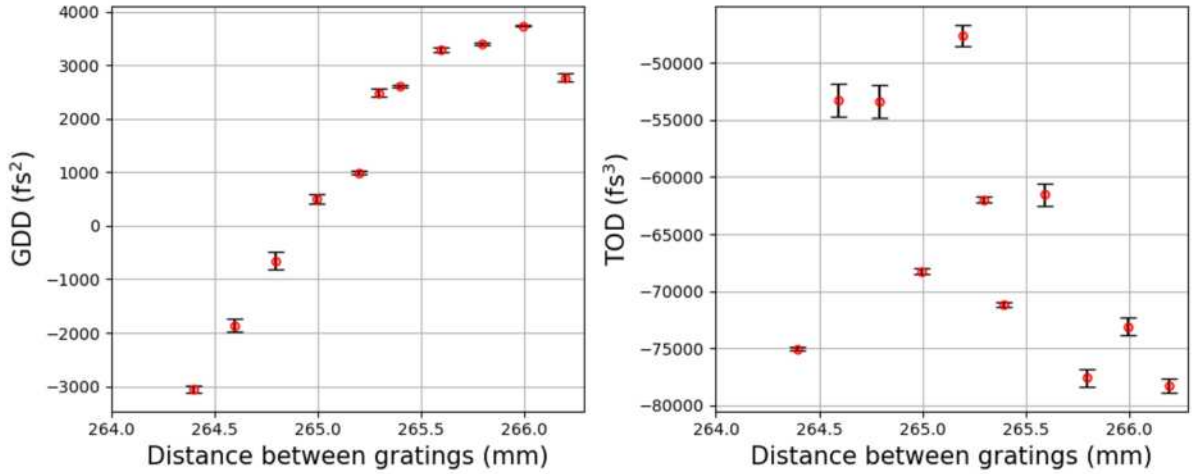


Figure 2: Predicted values of GDD (left) and TOD (right) for different grating distances. Red dots with error bars indicate the mean values and standard deviation of the prediction from 10 independently trained models.

The spectra were recorded at different compressor grating separations and the GDD and TOD for each setting was predicted using the CNN as shown in Fig. 2. The red dots represent the mean value of predictions from 10 independently trained models and the error bars indicate the standard deviation. The predictions reveal the presence of a large negative third-order dispersion in the seed pulses. The source of this TOD is thought to be an under-compensation of the TOD introduced by the pulse stretcher in the chirped-pulse amplification scheme. In addition, a linear relationship between the GDD and the grating distance was also observed, which shows good agreement with the theory.

References

- [1] S. Khan et. al., *Spectral Studies of Ultrashort and Coherent Radiation Pulses at the DELTA Storage Ring*, Proc. of IPAC'16, Busan, Korea, p. 2851 (2016).
- [2] Z. Usfoor et. al., *A New Spectrometer for the Characterization of Vacuum-UV radiation at DELTA*, DELTA Annual Report 2022.
- [3] P. Ungelenk et. al., *Continuously tunable narrowband pulses in the THz gap from laser-modulated electron bunches in a storage ring*, Phys. Rev. ST Accel. Beams 20, 020706 (2017).
- [4] A Radha Krishnan et al., *Investigation of Spectro-Temporal Properties of CHG Radiation at DELTA*, Proc. of IPAC'22, Bangkok, Thailand, p. 1423 (2022).

SPEED: Worldwide first EEHG Signal at a Storage Ring

S. Khan¹, B. Büsing¹, A. Held¹, C. Mai¹, A. Radha Krishnan¹, W. Salah^{1,2},
Z. Usfoor¹, V. Vijayan¹

¹Zentrum für Synchrotronstrahlung (DELTA), Technische Universität Dortmund

²The Hashemite University, Zarqa, Jordan

Introduction: Until recently, the short-pulse source operated at DELTA [1] was based on coherent harmonic generation (CHG) [2]. In this scheme, the interaction between ultrashort laser pulses and electrons in an undulator (modulator) results in a sinusoidal modulation of the electron energy. A dispersive section (chicane) leads to a density modulation (microbunching) and coherent emission of ultrashort radiation pulses in a second undulator (radiator) tuned to a harmonic of the laser pulses. At DELTA, a Ti:sapphire laser system at 800 nm was employed for CHG, and the shortest observed wavelength was 80 nm.

Echo-enabled harmonic generation (EEHG) [3] was proposed in 2009 as a seeding scheme for free-electron lasers and was demonstrated at linac-based facilities [4-7]. However, it can also be adopted for storage rings to generate ultrashort radiation pulses at shorter wavelengths than CHG. The scheme is based on a twofold laser-electron interaction. After the first modulation, strong overbunching by a chicane creates stripes of small energy spread in longitudinal phase space. Following a second energy modulation, a weaker chicane leads to a complex density pattern which gives rise to coherent emission at high harmonics of the laser wavelength.

EEHG was proposed for existing and future synchrotron light sources [8-12], but was never demonstrated at any storage ring because it would either require two straight sections or a particularly long one. In summer 2022, however, the electromagnetic undulator U250 at DELTA was rewired for the SPEED project (Short-Pulse Emission via Echo at DELTA) to demonstrate EEHG at a storage ring for the first time [13]. A single device now provides two modulator sections, two chicanes and a radiator section, each with only a few undulator periods.

U250 layout: Figure 1 shows the characteristics of the undulator U250 before (left, CHG) and after (right, EEHG) the modification as described in the figure caption and in [13]. Technical details on the reconfiguration of the magnetic coils are given in [14]. The undulator comprises 19 periods with a length of 250 mm, i.e., 38 coil pairs including endpoles, which were reduced from 4 to 2 in the new design.

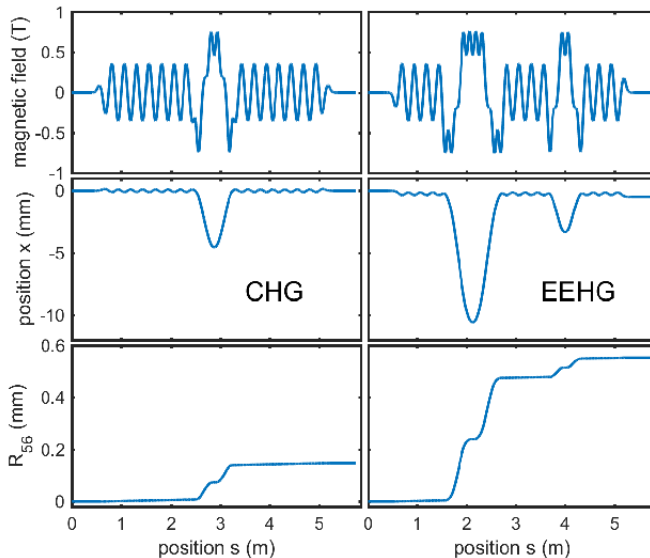


Figure 1: Magnetic field (top), electron path (center), and calculated cumulative R_{56} matrix element (bottom) as function of position along the undulator U250 before (left) and after (right) the modification.

Chicane Strength: The transport matrix element R_{56} describes the dependence of pass length difference on the momentum deviation of a particle and thus measures the strength of a magnetic chicane. This parameter was calculated from magnetic field simulations using the program CST [15]. Experimentally, it can be obtained from spectral interference of two undulators before and after the chicane tuned to the same wavelength (“optical klystron”) [16]. Figure 2 shows the calculated and measured R_{56} values of the first (left) and the second (right) EEHG chicane as function of current through the coils. For the second chicane, the simulated values match the measured data well, while for the first chicane. The interference pattern above 450 A cannot be resolved and a discrepancy is observed at higher chicane current.

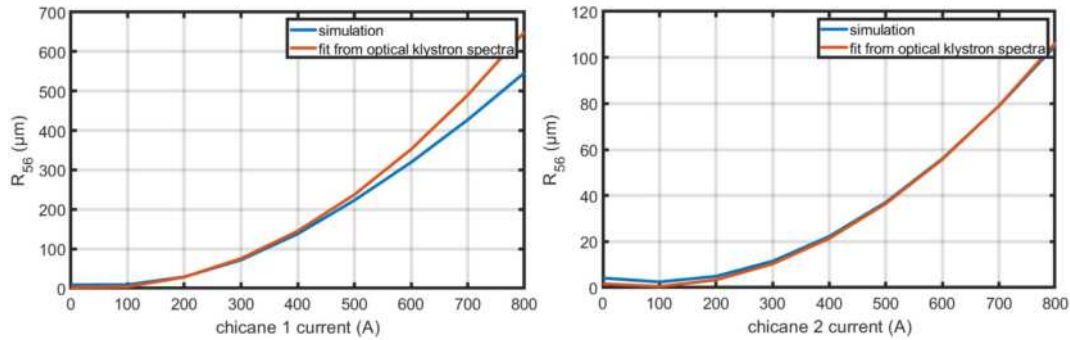


Figure 2: Comparison of simulated (blue) and measured (red) chicane strength as function of the chicane currents for the first (left) and the second (right) chicane.

First EEHG-Signal: On the evening of Friday 2022-09-16, a first indication of EEHG was observed which is, to our knowledge, the worldwide first EEHG demonstration at a storage ring. Pulses from the Ti:sapphire laser system were frequency-doubled by SHG (second-harmonic generation) resulting in residual 800 nm pulses for the first and 400 nm pulses for the second energy modulation. While the first chicane was set to 460 A which strongly overbunches the first modulation, the second chicane was powered with 500 A which optimized the microbunching. A coherent signal was observed at 267 nm when scanning the delay between the two pulses with mirrors on a linear stage (see Fig. 2). This signal is a clear indication of the EEHG process, since strong overbunching prevents CHG from the 800 nm pulse and 267 nm is not a harmonic of the 400 nm pulse. The dependence on the delay shows that both pulses are required to produce the signal.

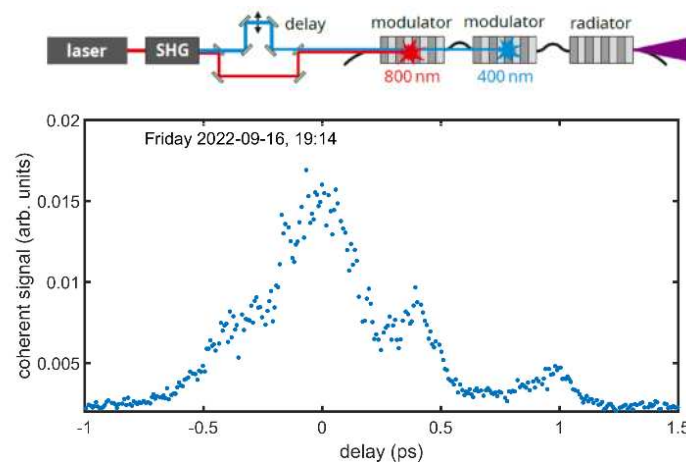


Figure 3: Setup (top) and recorded signal at 267 nm as function of the relative delay between the 800 nm and 400 nm pulses. The multiple peaks are caused by the pulse shape being influenced by higher-order dispersion. Note that the distribution is not symmetric (as, e.g., in autocorrelation) because the two pulses play a different role in the EEHG process.

Outlook: The SPEED setup demonstrates that the EEHG scheme is capable of generating coherently emitted ultrashort radiation pulses at a storage ring. It also shows that EEHG can be performed within a single straight section, even though the U250 period length is rather large. With an optimized setup comprising undulators with shorter periods together with chicanes mounted on a common girder, a compact EEHG insertion device could be used at existing storage rings to generate ultrashort pulses for experiments in the extreme ultraviolet regime.

In the near future, the new setup at DELTA will be used to study the properties of EEHG under different conditions. A new in-vacuum spectrometer currently being commissioned [17] will allow to detect higher harmonics of the seed wavelength.

References

- [1] S. Khan et al., *Generation of Ultrashort and Coherent Synchrotron Radiation Pulses at DELTA*, Sync. Rad. News 26:3, p. 25 (2013).
- [2] R. Coisson and F. De Martini, *Free-electron coherent relativistic scatterer for UV-generation*, Quantum Electronics, vol.9, p. 939, 1982.
- [3] G. Stupakov, *Using the Beam-Echo Effect for Generation of Short-Wavelength Radiation*, Phys. Rev. Lett. 102, 074801 (2009).
- [4] D. Xiang et al., *Demonstration of Echo-Enabled Harmonic Generation Technique for Short-Wavelength Seeded Free-Electron Laser*, Phys. Rev. Lett. 105, p. 114801 (2010).
- [5] Z.T. Zhao et al., *First lasing of an echo-enabled harmonic generation free-electron laser*, Nat. Photonics 6, p. 360 (2012).
- [6] E. Hemsing et al., *Echo-enabled harmonics up to the 75th order from precisely tailored electron beams*, Nat. Photonics 10, p. 515 (2016).
- [7] P. Rebernik Ribič et al., *Coherent soft X-ray pulses from an echo-enabled harmonic generation free-electron laser*, Nat. Photonics 13, p. 555 (2019).
- [8] R. Molo et al., *Echo-enabled harmonic generation at DELTA*, Proc. of IPAC'11, San Sebastián, Spain, p. 3074 (2011).
- [9] C. Evain et al., *Soft x-ray femtosecond coherent undulator radiation in a storage ring*, New J. Phys. 14, p. 023003 (2012).
- [10] H. Li et al., *Echo-Enabled Harmonic Generation Based on Hefei Storage Ring*, Proc. of IPAC'13, Shanghai, China, p. 1208 (2013).
- [11] A. Streun et al., *SLS-2 – the upgrade of the Swiss Light Source*, J. Synchrotron Radiat. 25, p. 631 (2018).
- [12] J.-G. Hwang et al., *Generation of intense and coherent sub-femtosecond X-ray pulses in electron storage rings*, Scient. Reports 10, p. 10093 (2020).
- [13] B. Büsing et al., *Preparatory Experimental Investigations in View of EEHG at the DELTA Storage Ring*, Proc. of FEL'22, Trieste, Italy, paper TUP70 (2022).
- [14] B. Büsing et al., *Reconfiguration of the U250 for EEHG*, DELTA Annual Report 2022.
- [15] CST STUDIO SUITE®, <https://www.cst.com/products/csts2>
- [16] P. Elleaume, *Optical Klystrons*, Journal de Physique Colloques 44, p.C1-333 (1983).
- [17] Z. Usfoor et al., *A New Spectrometer for the Characterization of VUV/XUV Radiation at DELTA*, DELTA Annual Report 2022.

FEL Microbunching in Drift Sections*

S. Khan, Zentrum für Synchrotronstrahlung (DELTA), Technische Universität Dortmund
 G. Perosa¹, F. Sottocorona¹, E. Allaria, A. Brynes, G. Penco, P. R. Ribič, S. Spampinati,
 C. Spezzani, M. Trovò, L. Giannessi², G. De Ninno³
 Elettra Sincrotrone Trieste SCpA, Basovizza, Italy
 E. Ferrari, E. Schneidmiller, DESY, Hamburg, Germany

¹ also at Università degli Studi di Trieste, Trieste, Italy

² also at Laboratori Nazionali di Frascati, INFN, Frascati, Italy

³ also at University of Nova Gorica, Nova Gorica, Slovenia

The FERMI user facility [1] at Elettra Sincrotrone Trieste in Italy provides powerful radiation in the spectral range from 100 to 4 nm with two externally seeded free-electron laser (FEL) lines – see Fig. 1. Until recently, FEL-1 [2] was based on high-gain harmonic generation (HG) [3] with a single undulator (modulator) for seeding, a dispersive section to convert the laser-induced energy modulation into microbunching, and six undulators (radiators) for the FEL process. FEL-1 is presently being upgraded to implement the echo-enabled harmonic generation (EEHG) [4,5] scheme employing two modulators, while FEL-2 [6] is based on two successive HG stages.

The formation of microbunches with high charge density gives rise to longitudinal space charge (LSC) effects. In drift sections, which may occur in complex seeding schemes such as EEHG, LSC increases the energy spread within the microbunches causing a longitudinal elongation (debunching). On the other hand, the correlated energy spread between the microbunches can be reduced which may improve the HG output [7].

In order to investigate these LSC-induced effects, measurements were performed at FEL-1 under variation of peak current and drift length after the dispersive section. Figure 2 shows scans of the longitudinal dispersion R_{56} with a single undulator as radiator. The pulse energy at the 10th seed laser harmonic was recorded using a photo-ionization monitor [8] and background radiation was subtracted. The debunching effect generally reduces the pulse energy with increasing drift length. Except for high peak current (1400 A), however, the red curves (drift 5.2 m) seem to be comparable to the blue ones (drift 1.5 m), which may indicate FEL amplification enhanced by reduced energy spread between the microbunches as suggested in [7]. Definite conclusions, however, are subject to further analysis.

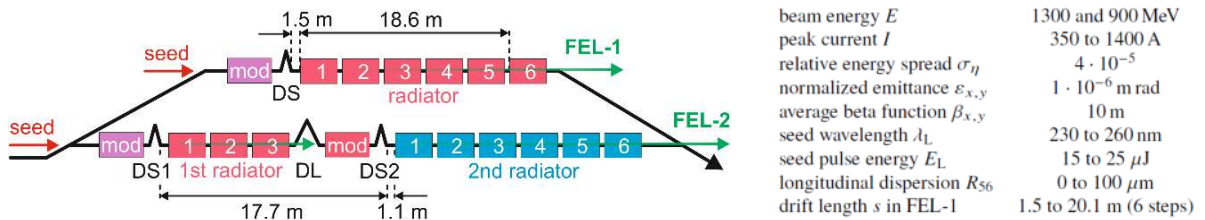


Figure 1: FEL lines of FERMI with modulators (mod), radiators, and dispersive sections (DS). The table summarizes the experimental parameters in the investigation of longitudinal space charge effects.

* Work supported by Heinrich-Hertz-Stiftung during a sabbatical granted by the TU Dortmund. The kind hospitality of the FERMI team and the support during the measurements and data analysis is gratefully acknowledged.

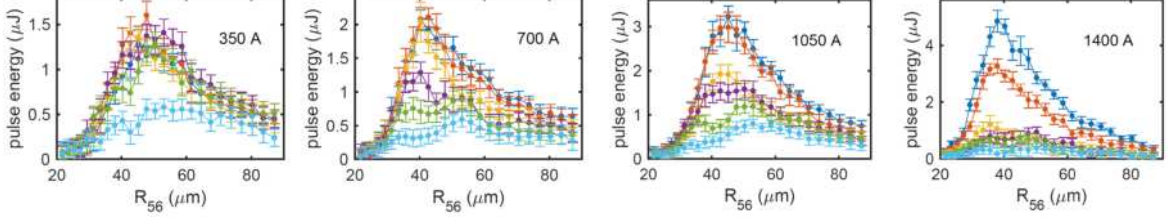


Figure 2: Measured pulse energy as function of R_{56} for drift lengths from 1.5 to 20.1 m (sequence: blue, red, orange, purple, green, cyan) and estimated peak currents ranging from 350 to 1400 A.

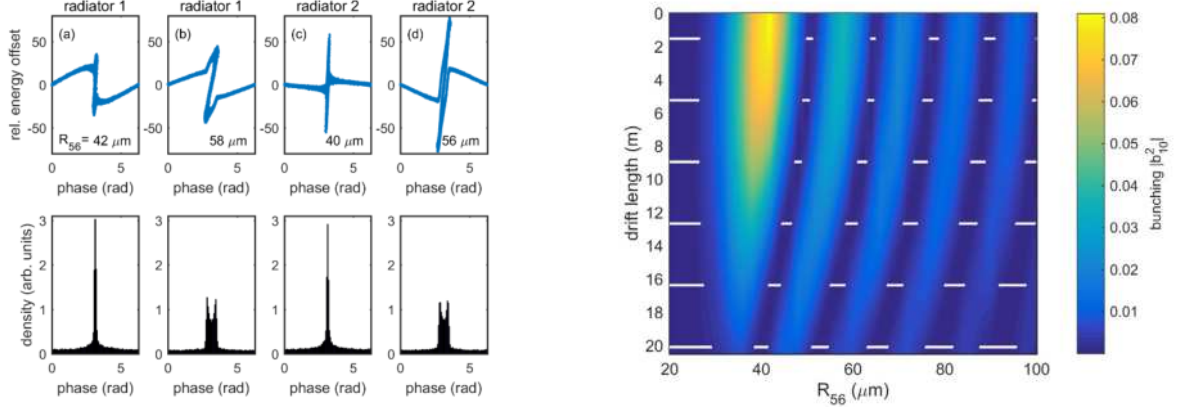


Figure 3: Left: Simulated phase space evolution (top) and projected electron density (bottom) after a drift length of 1.5 and 5.2 m for the R_{56} value with the largest bunching factor (a,c) at the 10th seed harmonic and at larger R_{56} with a second maximum of the bunching factor (b,d) with two density maxima with $\pi/5$ phase difference. Right: Squared bunching factor as function of R_{56} and drift length (peak current 700 A). The white lines indicate the drift lengths in the experiment.

Assuming a laser-induced modulation of the electron energy followed by a dispersive section with given R_{56} , the effect of repulsive LSC forces was simulated. As shown in Fig. 3 (left), the energy spread within the microbunches increases, while the energy offset of electrons between them is reduced. In a one-dimensional model [7], the coupled equations for the normalized energy offset $p_i = \eta_i / \sigma_\eta$ with $\eta_i = \Delta\gamma_i / \gamma$ and phase $\theta_i = k_L z_i$ of macroparticle i

$$\frac{dp_i}{d\tau} = \frac{2}{\alpha} \sum_{h=1}^{\infty} b_h \frac{\sin h\theta_i}{h} \quad \text{and} \quad \frac{d\theta_i}{d\tau} = \alpha p_i \quad \text{with} \quad \alpha \equiv \frac{k_L \sigma_\eta}{k_p \gamma^2}, \quad k_L \equiv \frac{2\pi}{\lambda_L}, \quad k_p \equiv \sqrt{\frac{e^2 n_0}{m_e c^2 \epsilon_0 \gamma^3}}$$

are iterated in small steps of plasma phase advance $\tau = k_p s$ along the longitudinal position s .

Here, $-e$ and m_e are the electron charge and mass, n_0 is the electron density, ϵ_0 the dielectric constant, γ the Lorentz factor, and for other symbols see Fig. 1. The bunching

factor $b_h = \sum_{i=1}^n \exp(ih\theta_i) / n$ at laser harmonic h is updated at every iteration. The right part of Fig. 3 shows a maximum of the squared bunching factor along the R_{56} scale for optimum microbunching, followed by maxima for microbunches with two peaks of phase difference $2\pi j / h$ ($j = 1, 2, \dots$). With increasing drift length, the LSC-induced evolution shifts these maxima to lower R_{56} and reduces the first maximum faster than the second, which explains why the centroid of the smeared-out experimental distribution (Fig. 2) shifts towards higher R_{56} . A more detailed description with further experimental results is given in [9].

References

- [1] E. Allaria et al., *The FERMI free-electron lasers*, J. Synchrotron Radiation 22, pp. 485-491 (2015).
- [2] E. Allaria et al., *Highly coherent and stable pulses from the FERMI seeded free-electron laser in the extreme ultraviolet*, Nat. Photonics 6, pp. 699-704 (2012).
- [3] L. H. Yu, *Generation of intense uv radiation by subharmonically seeded single-pass free-electron lasers*, Phys. Rev. A 44, pp. 5178-5193 (1991).
- [4] G. Stupakov, *Using the beam-echo effect for generation of short-wavelength radiation*, Phys. Rev. Lett. 102, p. 74801 (2009).
- [5] P. Rebernik Ribič et al., *Coherent soft X-ray pulses from an echo-enabled harmonic generation free-electron laser*, Nat. Photonics 13, pp. 555-561 (2019).
- [6] E. Allaria et al., *Two-stage seeded soft-X-ray free-electron laser*, Nat. Photonics 7, pp. 913-918 (2013).
- [7] E. Hemsing et al., *Correlated Energy-Spread Removal with Space Charge for High-Harmonic Generation*, Phys. Rev. Lett. 113, p. 134802 (2014).
- [8] M. Zangrando et al., *The photon analysis, delivery, and reduction system at the FERMI@Elettra free electron laser user facility*, Rev. Sc. Instrum. 80, p. 113110 (2009).
- [9] S. Khan et al., *Evolution of Microbunching in Drift Sections*, Proc. of the FEL'22 Conference, Trieste, Italy, paper MOP01 (2022).

Measurement and Simulation of Radiation Doses

S. Khan, C. Mai, Center for Synchrotron Radiation (DELTA), TU Dortmund

Given the plan of a new building west of DELTA, the question arises whether the radiation shielding wall surrounding the accelerator complex partly without roof is sufficient to keep the radiation in that building well below the legally required limit of 1 mSv/year. To this end, flat glass photoluminescence as well as thermoluminescence dosimeters (see, e.g., [1]) were placed on both sides of the west wall of the DELTA accelerator hall from April to July 2022.

As a first-order estimate of the relative radiation distribution, simulations were performed assuming an equal amount of emission from equally spaced points along the storage ring. Presuming that electromagnetic showers from lost electrons and ejectiles from direct nuclear reactions remain in the plane of the storage ring, only isotropic emission as from compound nucleus reactions is considered. The radiation shielding wall is modelled by upright rectangles surrounding the storage ring. Radiation is assumed to arrive at the observation point, if the line of sight from the source point does not intersect any of these rectangles. Figure 1 shows a top view of the simulation geometry with $(x,y,z) = (0,0,0)$ on floor level at the center of the storage ring. For the selected observation point (green dot), the contributing source points basically form two line sources in the northern and southern part of the ring (red).

The considered observation points form a grid in a y - z -plane, e.g., at $x = -36.5$ m (the west wall of the DELTA hall, where the dosimeters were placed) and at $x = -114.0$ m (the distance to the planned building). The resulting fraction of emitted radiation hitting 1 m^3 of these two planes is shown in Fig. 2. Scattering and absorption processes are ignored. Furthermore, no assumption is made on the absolute amount of radiation. The total energy of lost electrons is given by the number of injected electrons per year and the beam energy, usually 1.5 GeV, but its fraction escaping the vacuum vessel and the storage ring plane via electromagnetic or particle radiation is unknown. A Monte-Carlo calculation including all details of the whole facility is practically impossible and the result of such an attempt would be doubtful.

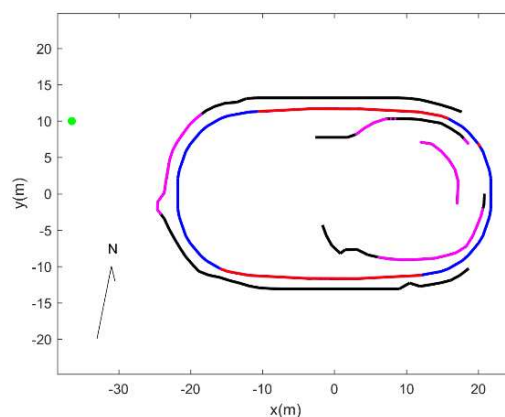


Figure 1: Example of the simulation geometry. The storage ring is shown in blue with source points of radiation hitting the observation point (green, $x = -36.5$ m, $y = 10.0$ m, $z = 8.0$ m) marked in red. The radiation shielding wall is shown in black with intersection points of lines between storage ring and observation point in magenta.

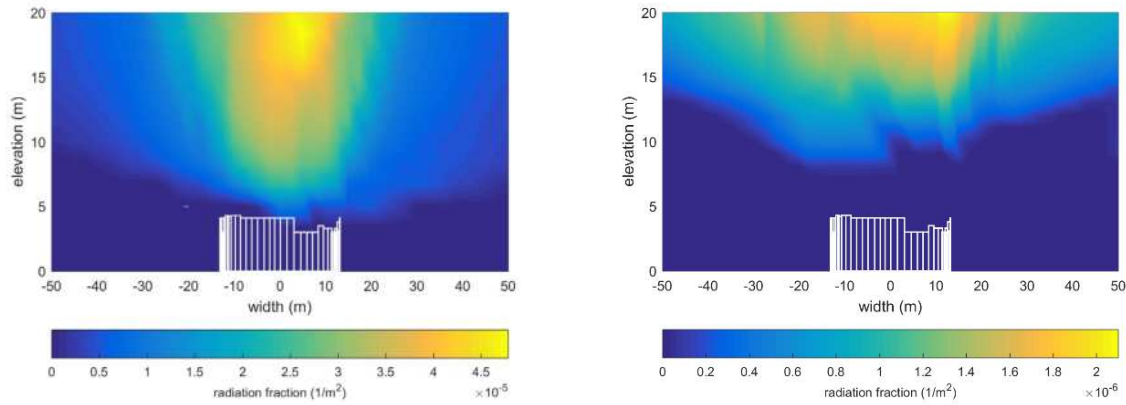


Figure 2: Color-coded distribution of radiation (fraction of total emission per m^2) on the west wall of the DELTA hall at $x = -36.5$ m (left) and in a plane at $x = -114.0$ m (right) as seen from the storage ring. Note the factor >20 between the color scales. The radiation shielding wall is shown in white.

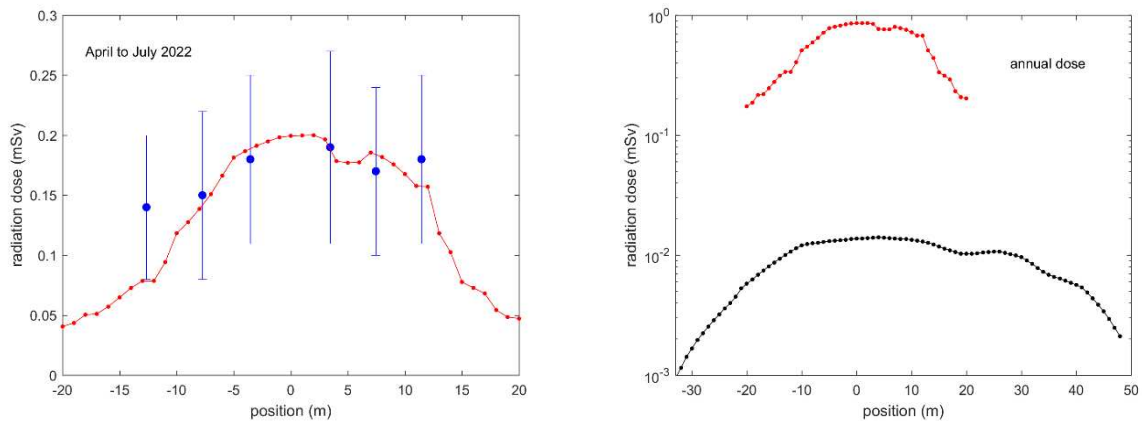


Figure 3: Left: Measured dose (blue dots) accumulated between April and July 2022 at elevation $z = 7.3$ m outside along the west wall of DELTA ($x = -36.5$ m). The simulated distribution (red curve) is scaled to the data. Right: Simulated distribution from the left figure scaled to one year of DELTA operation (red) and distribution at $x = -114.0$ m (black) with an elevation of $z = 14.3$ m.

While the dosimeters at low elevation outside the radiation shielding wall are dominantly exposed to so-called skyshine, i.e., radiation scattered from air or the roof of the hall, the dosimeters above the wall can be used to estimate the radiation distribution at the planned building by scaling the measured values to one year of DELTA operation and to the radiation fraction according to the simulation. Figure 3 (left) shows the measured dose at an elevation of 7.3 m and the scaled simulation result as function of position from south to north. A natural dose level of 0.11 mSv as deduced from four reference dosimeters was subtracted [2]. Despite the large error bars, the measured data follow the trend given by the simulation, i.e., higher radiation level in the northwest part due to a lower radiation shielding wall. The dose for a full year of DELTA operation is higher by a factor 4.3, as shown in Fig. 3 (right), while the maximum annual dose at the planned building (maximum considered elevation 14.3 m and 114.0 m from the storage ring) is $14 \mu\text{Sv}$ and even with large systematic errors far below the limit.

[1] H. Krieger, *Strahlungsmessung und Dosimetrie*, Springer (2021).

[2] Report 220916_UG1_20392, Materialprüfungsamt NRW (September 2022).

Ultrafast X-ray sources and angle-resolved electron spectroscopy

L. Funke, A. Held, D. Reinke, S. Savio, N. Wieland, L. Wülfing & W. Helml

Zentrum für Synchrotronstrahlung (*DELTA*), Technische Universität Dortmund
Intelligent Embedded Systems, University of Kassel, 34121 Kassel
Deutsches Elektronen-Synchrotron (*DESY*), Notkestr. 85, 22607 Hamburg

During the last year, our group in close cooperation with Dr. Markus Ilchen from DESY continued on implementing the angular streaking scheme for attosecond experiments at the European XFEL and FLASH with a new, dedicated detector setup. Once fully established, the experimental results will provide direct information about the full time–energy distribution of the stochastic SASE X-ray pulses with attosecond resolution on a single-shot basis, including X-ray pulse duration, intensity substructure and chirp. In the frame of the BMBF-Verbundprojekt 05K19PE1 ‘SpeAR XFEL’ (Spectrometer with Angular Resolution for ultrafast experiments at X-ray FELs), together with the group of Prof. Bernhard Sick from Universität Kassel, we started developing a new detector design and analysis methods for the resulting measurements [1].

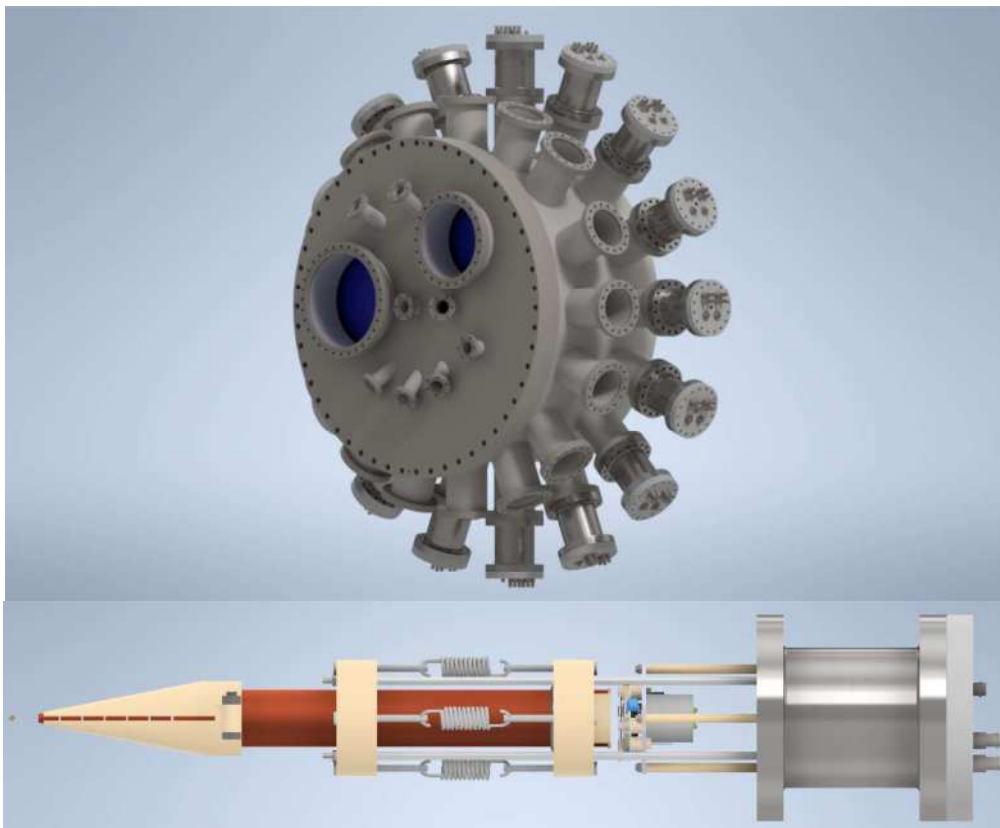


Figure 1: CAD models of the new detector chamber and spectrometer.

(Chamber): One of two interaction planes is equipped with 16 spectrometers. The second plane can be used for simultaneous experiments, e. g. measurements in the liquid phase. (Spectrometer): Side view on the new spring-loaded time-of-flight electron spectrometer holding mechanism. The setup also implements a new approach of isolating electron optics using a single injection-moulded PEEK part. Images generated in Autodesk Inventor.

Based on the previous work of the group, the design for this detector has been mostly finalized, with the building phase having begun this year. The improved detector concept incorporates a vacuum chamber with an inner mu-metal shield and two consecutive electron spectrometer planes for multiple angular streaking setups. The design makes use of gas targets and also allows for the future implementation of a water jet [2]. These liquid-phase experiments are planned to be a part of the newly begun ‘TRANSALP’ project (Time-Resolved ANgular Spectroscopy Applied to the Liquid Phase, BMBF 05K22PE3), continuing the development of the new detector.

In addition to the vacuum chamber, a new electron time-of-flight spectrometer design has been developed along with the detailed inner layout of the vacuum chamber. The supporting structure and the spring-loaded holding mechanism for the time-of-flight tubes provide a rigid solution focused on reducing the mechanical stress in the device resulting from the baking process of the vacuum chamber and granting a well aligned detector geometry, all while keeping the design comparably simple, very flexible and easy to maintain.

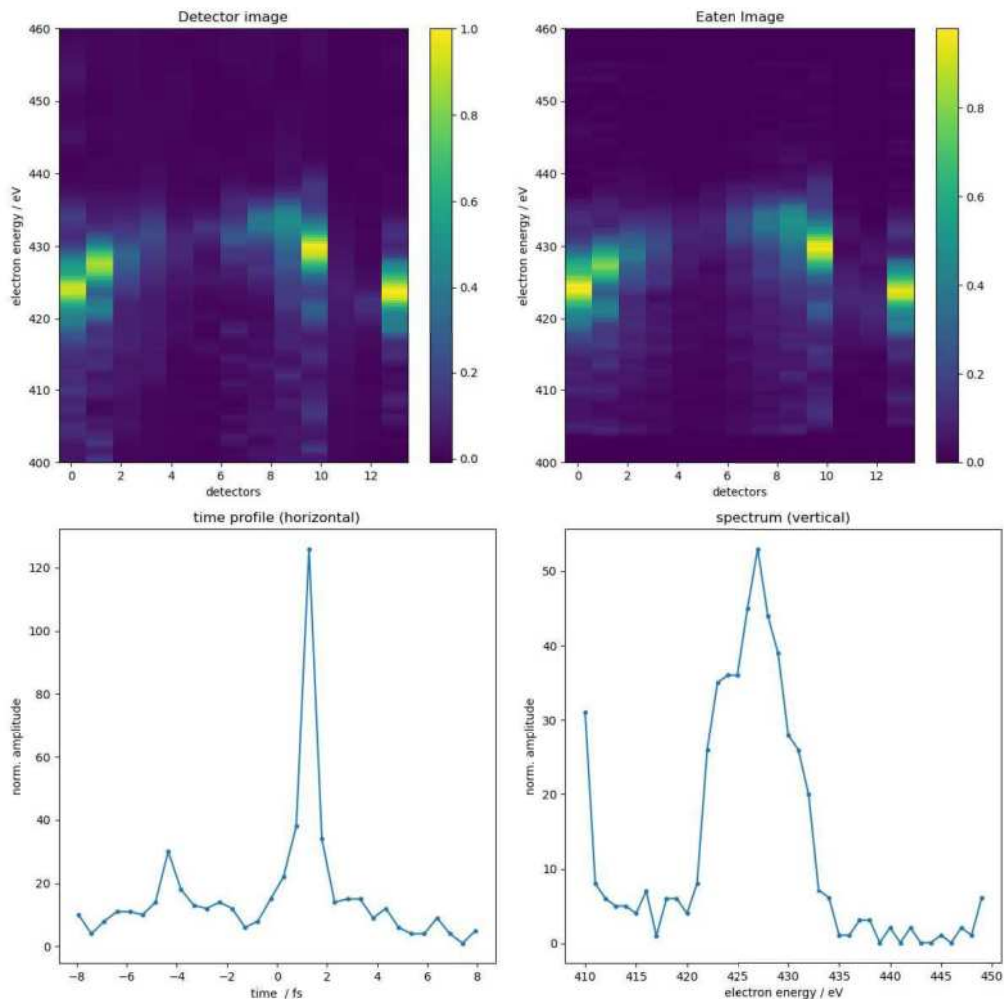


Figure 2: Exemplary attosecond shot at the European XFEL: Detector image (left) and reconstruction (right) of the 16 used electron spectrometers (upper plots: each column corresponds to one streaked spectrum measured with a specific spectrometer), the derived temporal shape of the X -ray pulse (lower left) and the spectrum of the pulse (lower right).

In the last year, extensive simulation studies on the electron dynamics in the upcoming detector chamber have been made and were used to derive the specific geometry and settings for the electrostatic retardation in the new spectrometers. In cooperation with Universität Kassel we tested a novel method of machine learning-based live pulse reconstruction during a dedicated angular streaking beam time at the SQS beamline at the European XFEL in June 2022. This proposal (#2828) utilized the ‘ballchamber’ for an angular streaking setup with 16 spectrometers and a neon gas target.

During this beam time, the live reconstruction of ultrashort SASE FEL pulses was done for the first time, showing ultrashort pulses in the regime of few femtoseconds with attosecond resolution. The same measurements were able to show the pulse shapes of multi-peak pulses along with the spectral composition as well as the nonlinear process of double-core hole ionization in neon in a single FEL shot. In the offline analysis following the experiment, the AI-based method was compared to the analytical approach of the ‘PACMAN’ algorithm. Currently specific effort is going into the time-domain analysis of the acquired data from this experiment for revealing the transient intensity-dependent electron dynamics of the generated doubly core-excited states [3, 4].

Finished Works:

Master Thesis

Lasse Wülfing – *Development of a variable detector design for angular streaking.*



Figure 3: Group photo of participating scientists after the experiment #2828 at European XFEL in Hamburg.

- [1] K. Dingel *et al.* Artificial intelligence for online characterization of ultra-short X-ray free-electron laser pulses, *Scientific Reports* **12** (2022).
- [2] M. Mittermair *et al.* Water jet space charge spectroscopy: route to direct measurement of electron dynamics for organic systems in their natural environment, *New Journal of Physics* **24**, 073040 (2022).
- [3] S. Li *et al.* Attosecond coherent electron motion in Auger-Meitner decay, *Science* **375**, 285–290 (2022).
- [4] M. Ilchen, W. Helml, M. Meyer, and R. Kienberger, Freie-Elektronen-Laser bringen Licht in den Auger-Prozess, *Physik in unserer Zeit* **53**, 220–228 (2022).

Studies of Instabilities and Energy Spread at the Canadian Light Source

P. Hartmann¹, D. Bertwistle², M. Boland², S. Martens², H. Shaker²

¹Zentrum für Synchrotronstrahlung (DELTA), TU Dortmund University

²Canadian Light Source, Saskatoon, Canada

Beam Instabilities at the Canadian Light Source Storage Ring

Coupled-bunch instabilities are oscillations of particle bunches in a storage ring around their equilibrium position. They are generated by wakefields that may be trapped in narrowband resonant structures in the vacuum chamber of the accelerator.

Previous observations at the Canadian Light Source (CLS) storage ring indicated vertical betatron oscillations whenever the gap of the in-vacuum so-called Brockhouse wiggler was closed to less than 6 mm. In order to investigate these oscillations in detail, we applied an excite-damp method using a bunch-by-bunch (bbb) feedback system.

Coupled-bunch oscillations are characterized by h oscillation modes, where h is the harmonic number of the storage ring. The bbb system excites these modes one by one and measures the relaxation after the excitation is switched off. The measured relaxation time is then converted to a growth rate. Higher growth rates indicate a higher sensitivity of the beam when excited with the given mode frequency. The use of the excite-damp method was necessary because the oscillations of interest are masked by oscillations caused by the resistive-wall instability, having an order of magnitude higher growth rates.

Figure 1 shows the growth rate of all 285 coupled bunch modes, where modes 0 to 142 are displayed in blue from left to right while modes 143 to 284 in red from right to left. Modes 0 to 9 and 275 to 284 are suppressed because their growth rates are dominated by the resistive-wall effect. The highest growth rates were measured around mode 180.

Detailed studies of modes 172 to 181 as a function of the wiggler gap width are shown in Fig. 2. With increasing gap size, the maximum growth rate moves from mode 180 towards lower mode numbers with higher mode frequencies.

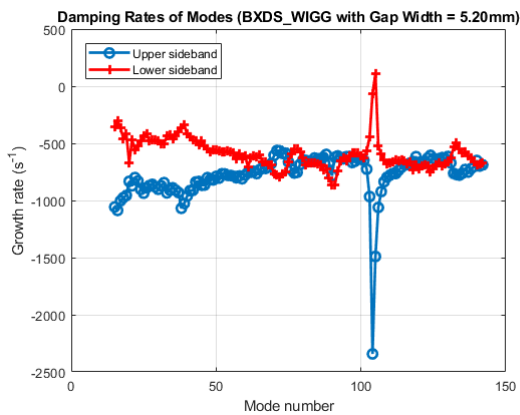


Figure 1: Growth rate of all 285 coupled bunch modes except the resistive-wall dominated ones as seen from an excite-damp measurement.

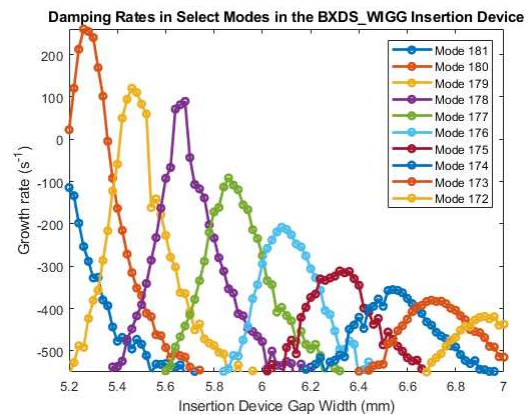


Figure 2: Growth rate of CBM 172 to 181 versus wiggler gap width.

A possible explanation is a beam excitation by trapped electromagnetic fields in the wiggler. These are excited by the beam's wakefields and act back on the beam in case the frequency of the trapped mode coincides with the frequency of a coupled-bunch mode. The resonance frequency increases with the gap width and excites lower mode numbers. Further simulations of eigenmodes of the wiggler are ongoing.

Energy Spread of the Canadian Light Source LINAC

Recent Linac upgrade plans at the CLS suggest the abandonment of the Energy Compression System (ECS). The ECS is part of the actual Linac-to-Booster beamline, located immediately behind the last accelerator section of the Linac. It consists of a magnet chicane followed by a cavity. Its purpose is to compress the energy spread of the electron beam emitted from the Linac from approximately 1% to less than 0.15% before injection into the booster. Simulations of the booster ring done by W. Wurtz result in an energy acceptance of the booster of slightly less than 1% [3].

Energy spread measurements were performed in order to support the decision on the future use of the ECS. The measurement of the beam energy spread was realized in the so-called switchyard using a dipole magnet and a movable slit in a region with high dispersion and a horizontal beam waist (see Fig. 3). The bunch charge transmitted through the slit was measured using a beam position monitor equipped with 'Libera' BPM electronics operated in single-shot mode.

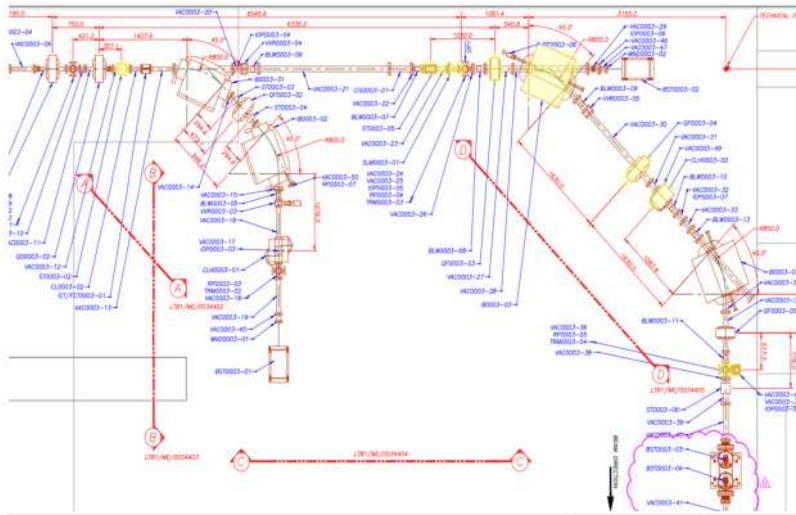


Figure 3: Floor plan of the switchyard following the ECS system. The beamline elements relevant to the measurement are marked in yellow.

Since a fine-grained setup of the beam energy for calibration is not available, the dispersion at the slit position was instead determined by varying the magnetic field of the dipole magnet (see Fig. 4). In good approximation

$$\frac{\Delta B}{B} \approx \frac{\Delta E}{E}.$$

The energy spread in the so-called 'Machine Study Mode' (MS-mode, 132 ns long bunch train) is compared with the energy spread in 'Normal Mode' (N-mode, 66 ns long bunch train), where the latter is the standard injection mode for user beam.

The FWHM beam energy spread with the ECS switched on at standard settings was measured to be slightly over 0.16 % for both modes while the energy spread with ECS off was measured to be roughly 0.7 % (see Fig. 5). Regarding the energy acceptance of the booster [3], only a small quantity of the charge coming from the Linac should be lost due to energy spread when the ECS is switched off.

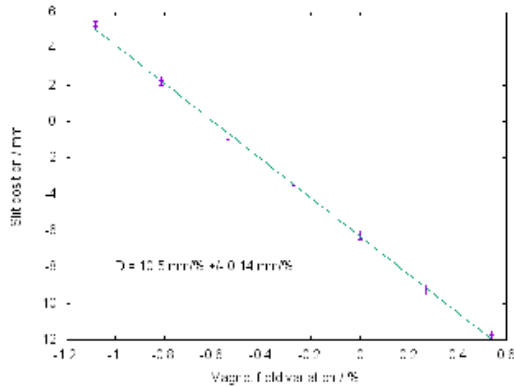


Figure 4: Slit position vs. magnet field variation. ECS on/off bunch charges are on a different scale. The data was collected by following the high-energy edge of the beam. A fit of a straight line to the data points yields the dispersion D .

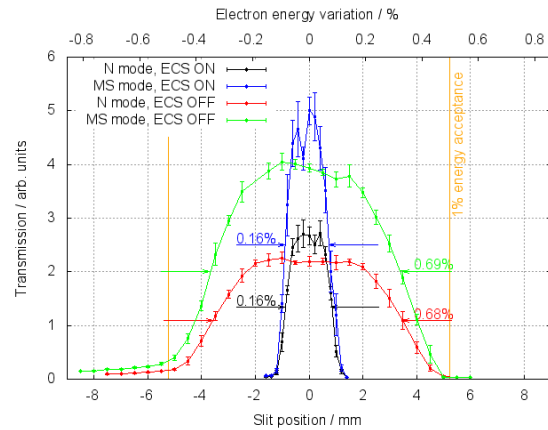


Figure 5: Measurement of the beam energy spread with ECS on and off for 132 ns bunch trains (MS-mode) and 66 ns long bunch trains (N-mode). ECS on/off bunch charges are on a different scale.

References

- [1] S. Martens, D. Bertwistle, M. J. Boland, P. Hartmann, *Studying Instabilities in the Canadian Light Source Storage Ring Using the Transverse Feedback System*, Proc. Int. Part. Accel. Conf. 2022, Bangkok, Thailand, pp. 230-232.
- [2] P. Hartmann, H. Shaker, *Energy Spread Measurements in the Canadian Light Source Injector*, to be published.
- [3] W. Wurtz, *Booster Capture Simulations with Unsynchronized and 3 GHz Linac Beams*, CLS internal report, 2021.

Testing the von Hamos spectrometer setup with white beam excitation

Nicola Thiering, Christian Albers, Robin Sakrowski, Eric Schneider, Michael Paulus, Christian Sternemann

Fakultät Physik/DELTA, Technische Universität Dortmund, 44227 Dortmund, Germany

Aim of this experiment is an evaluation of possible applications of the von Hamos spectrometer using white beam excitation to perform X-ray emission spectroscopy (XES) of the $K\beta$ and the valence-to-core (vtc) emission of transition metals compounds in order to study their electronic and structural

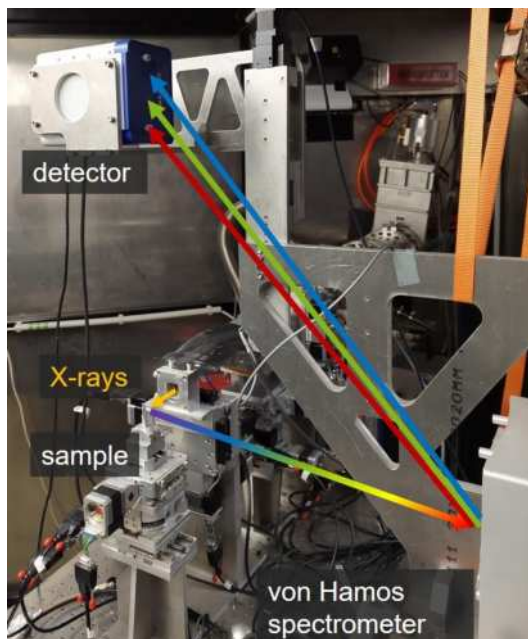


Fig. 1: Experimental X-ray emission setup using a von Hamos spectrometer at BL2. Missing in this photo is shielding and a helium flushed bag for reducing scattering and absorption in air.

to compare similar detection efficiencies due to the bending radius, analyzer distance and beam size. A one-hour measurement with white beam at BL2 provides an improved data quality compared to a seven-hour measurement at BL9 using monochromatic beam. To further emphasize the difference a one-hour measurement at BL9 is also shown in Fig. 2. The use of white beam offers about a factor of 10 more intensity and consequently lowers measuring time significantly.

The analyzers disperse the emission signal onto the detector. To assign the corresponding emission energies to the pixels of the detector, the established way of energy calibration makes use of the detection of quasi-elastic lines for different monochromatic excitation energies which is not possible when white beam radiation is used. We had to conclude another way for energy calibration using emission lines of known reference samples providing a geometric assignment of pixel to energy.

This setup up is currently installed at beamline BL9. However, due to the monochromatic beam, we have a limited flux there. Thus, we transferred the von Hamos spectrometer to BL2 and investigated the usability of polychromatic excitation without any use of a monochromator. The von Hamos setup includes four cylindrically bent Si(111) analyzer crystals with 500 mm bending radius as well as a Pilatus 100K area detector (Fig. 1). Extensive shielding on sample and detector as well as a helium flushed bag between von Hamos spectrometer, sample and detector were used to prevent air scattering and absorption, drastically improving the signal to background ratio. The beam size was approx. $0.5 \times 0.5 \text{ mm}^2$. A $60 \mu\text{m}$ thick aluminum absorber was used for beam hardening of the incident radiation.

At first, we measured a nickel foil to compare the results of the $K\beta_{1,3}$ X-ray and vtc emission of BL2 and BL9 as presented in Fig. 2. In both cases we used Si(111) analyzer crystals, but with different bending radii (250 mm at BL9) and beam sizes ($1 \times 0.2 \text{ mm}^2$ at BL9) in order

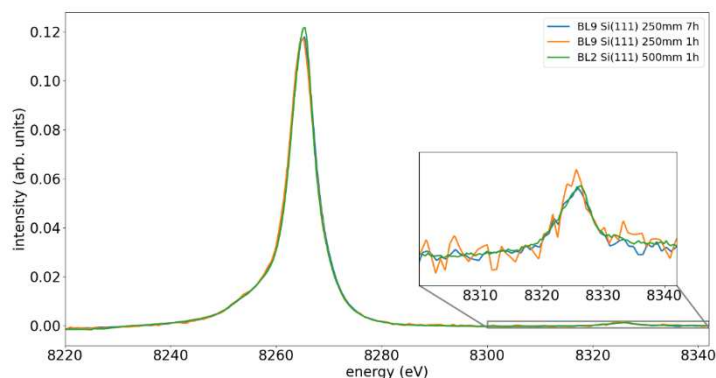


Fig 2: $K\beta_{1,3}$ spectra and valence-to-core emission (latter zoomed in the inset) of a nickel foil measured at BL2 and BL9. The emission lines have been normalized to their integrated intensity between 8220 eV and 8300 eV. BL2 offers significantly improved data quality using white beam excitation.

We tested the application possibilities to more complex systems, we used AlCrVYN coatings on Wc-Co substrate before and after heating up to 1000°C to determine changes in electronic and local properties of chromium, especially with regard to the vtc emission spectrum (Fig. 3). We characterized the oxidation state and chemical environment of the unheated samples by comparison with references from Eeckhout et al. [1] CrN, CrP, Cr₃C₂ and K₂Cr₂O₇ (see Fig. 3 left). For the combined spectrum of the satellite maximum Kβ'' around 5974 eV and the Kβ_{2,5} peak at about 5985 eV CrN provides the best agreement. The Kβ'' energy position is dependent on the 2s binding energy of the ligand and is therefore an indicator of the ligand [2] which favors CrN. Yet, we cannot exclude contributions of Cr₂N in the reference sample, which could explain the peak splitting observe in the vtc main line and slight shift in the satellite position. However, minor difference in energy positions may due to the deficiencies

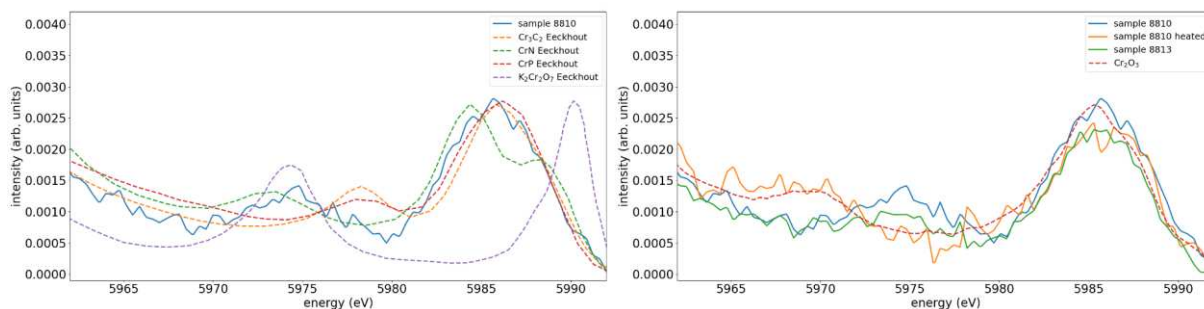


Fig. 3: Chromium valence-to core emission spectra of different coatings. – **left**: unheated samples compared to CrN, CrP, Cr₃C₂ and K₂Cr₂O₇ [1]. – **right**: sample 8810, sample 8810 heated and sample 8813 compared to a Cr₂O₃ reference.

of energy calibration method, which will be optimized in future experiments. These observations are in line with results of X-ray diffraction measurements where mainly CrN was found in the unheated samples. In Fig. 3 on the right hand side, the heated sample (orange) shows a clear similarity to Cr₂O₃ (red) which verifies the formation of chromium oxides during heating.

Generally, the vtc emission is sensitive to changes in the valence orbitals and provides information about the chemical bond between atom and ligand, but it displays also interaction with metal's 3d orbitals. Therefore, an in depth analysis needs calculations via density function theory [2], which are out of scope of this report.

Overall, this experiment clearly shows the potential and advantages using white beam excitation regarding measuring time and data quality. Not only Kβ_{1,3} emission measurements of transition metals can be performed but also vtc spectroscopy is feasible. Although the energy calibration is currently not as precise as it is using a monochromatic beam, we will improve the technique by optimization of sample alignment so that we can exploit the full potential of BL2 for XES.

[1] Eeckhout et al. "Cr local environment by valence-to-core X-ray emission spectroscopy", J. Anal. At. Spectrom. 24 (2009) 215-223 doi:10.1039/B808345M

[2] Erik Gallo, Pieter Glatzel „Valence to core X-ray emission spectroscopy“ Advanced Materials 26.46 (2014), S. 7730–7746. doi:10.1002/adma.201304994

A new high-pressure cell for wide-angle x-ray scattering

Kevin Lehninger¹, Eric Schneider¹, Jaqueline Savelkouls¹, Michael Paulus¹, Christian Sternemann¹, Metin Tolan¹

¹Fakultät Physik/DELTA, Technische Universität Dortmund, 44221 Dortmund, Germany

Hydrostatic high-pressure cells for wide-angle X-ray scattering (WAXS) at moderate pressures below 5 kbar are of increasing relevance for the investigation of pressure sensitive biological and functional materials e.g. proteins or metal-organic frameworks, respectively. Since the existing high-pressure cells at DELTA were optimised for small-angle scattering applications and thus did not allow large scattering angles, a new cell was developed that enables WAXS measurements. One of the experimental challenges was the precise pressure control in the pressure range up to 5 kbar with simultaneous separation of the sample volume from the pressure-transmitting medium. For this purpose, we developed a hydrostatic high pressure cell for use at beamlines BL2 and BL9 of the DELTA synchrotron radiation source, using water for pressure transmission. The new pressure cell is made of 718 alloy and has an opening angle of 60 degrees for the scattered radiation. The sample volume has a cross-sectional area of one square millimetre and is sealed by two diamond windows. The entrance window consists of a cylindrical diamond disk on a base mount. The exit window is a prismatic diamond for stability reasons. The sample is placed in a polyimide capillary tube (\varnothing 1mm) vertically into the WAXS cell and thus into the beam. Overall, the X-ray beam passes through 1.6 mm water, 1.0 mm sample volume, 2.5 mm diamond window (1 mm entrance window + 1.5 mm exit window) and the polyimide capillary. The cell is sealed with an NBR O-ring and a matching groove. Sliding systems were used to counteract corrosion damage and pressure forces. To estimate the material deformations at 5 kbar, a load analysis was carried out using the software Inventor [1].

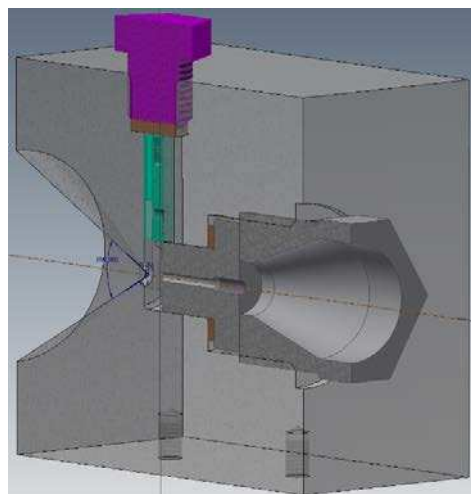


Figure 1: Schematic representation of the WAXS cell.

For the commissioning of the WAXS cell, potassium bromide (not shown) and gold were investigated by X-ray diffraction (XRD) at hydrostatic pressure up to 4 kbar using an incident photon energy of 27 keV and a beam size of $1.0 \times 0.9 \text{ mm}^2$ ($v \times h$) at beamline BL9 of DELTA. The distance between sample position and the Pilatus area detector was 1015 mm. As an example, the diffraction patterns of gold under different pressures are shown in Figure 2. One can see a shift of the Bragg reflections with increasing pressure to higher scattering angles, which can be interpreted as a compression of the unit cell. This observation is consistent with calibration data (dashed lines in figure 2).

pressure [bar]	lattice constant [\AA]	volume [\AA^3]
1	4.070400	67.439
1000	4.069665	67.402
2000	4.068890	67.364
3000	4.068137	67.326
4000	4.067382	67.289

Table 1: Pressure-dependent lattice constants and volume of the unit cell of gold.

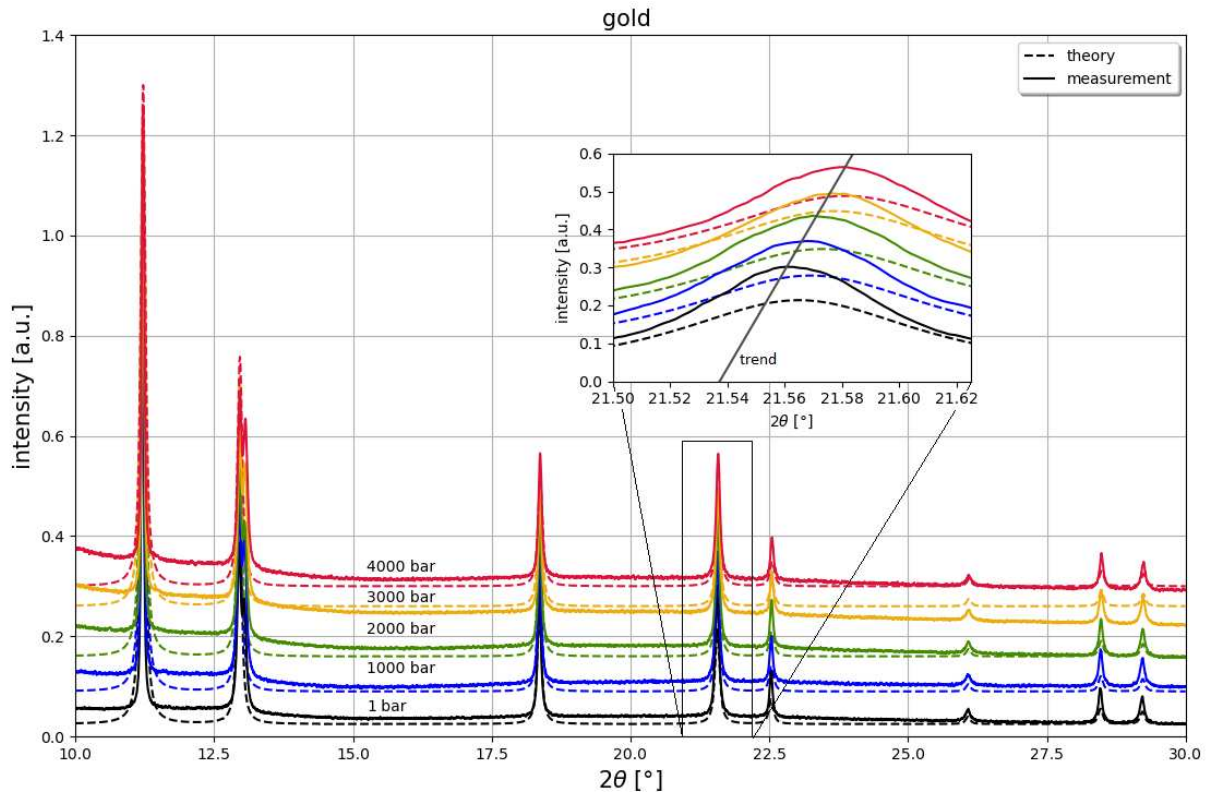


Figure 2: Diffraction patterns of gold at 27keV photon energy up to 4000bar hydrostatic pressure.

The theory curves were calculated for the applied pressures up to 4000 bar. From the material-specific compression modulus ($K_{\text{KBr}}=13.05$ GPa, $K_{\text{Au}}=180$ GPa) one obtains the volume change of the unit cell at applied pressure. With the pressure-dependent lattice constants [see table 1], the structure factor is determined analogously to [2].

The measurements show a successful agreement with the theory and thus a successful commissioning of the WAXS cell. With this cell, a q_{max} of 7.1 \AA^{-1} can be achieved at a maximum photon energy of 27 keV. With diagonal geometry, a larger q can be expected.

References

- [1] Autodesk® Inventor® 2019, 3D-CAD-Software, since 1999
- [2] Spieß, L., Genzel, C., Behnken, H., Teichert, G., Schwarzer, R. (2019). Moderne Röntgenbeugung: Röntgendiffraktometrie für Materialwissenschaftler, Physiker und Chemiker. Deutschland: Springer Fachmedien Wiesbaden. 72-84

Acknowledgments

We thank the DELTA team for providing synchrotron radiation.

A New Spectrometer for the Characterization of VUV/XUV Radiation at DELTA

Z. Usfoor, B. Büsing, A. Held, S. Khan, A. Radha Krishnan, C. Mai, V. Vijayan
Zentrum für Synchrotronstrahlung (DELTA), Technische Universität Dortmund

Previously, the spectra of radiation emitted through the coherent harmonic generation (CHG) process [1] were analysed using a Czerny-Turner-type spectrometer combined with an image-intensified charge-coupled device (iCCD) camera [2]. Using this method with radiation in air, wavelengths down to 200 nm could be measured, which enabled the measurement of the 2nd, 3rd and 4th harmonic of the 800-nm seed laser used in the CHG process.

A new spectrometer for the measurement of radiation spectra in the VUV (vacuum ultraviolet) and XUV (extreme ultraviolet) wavelength ranges was recently added to DELTA at the beamline BL 4 laboratory. It enables the in-vacuum detection of radiation of wavelengths from 210 nm down to 30 nm [3]. This opens up new possibilities for the characterization of radiation emitted through the CHG as well as the EEHG (echo-enabled harmonic generation) processes [4].

Through the use of only one optical element, which is a spherical grating, radiation can be detected with minimal losses. A gated MCP (microchannel plate) coupled with a phosphor screen enables the readout of the light spectrum from the grating as an image. This image is then recorded through a vacuum window using a charge-coupled device (CCD) camera (Fig.1) [5].

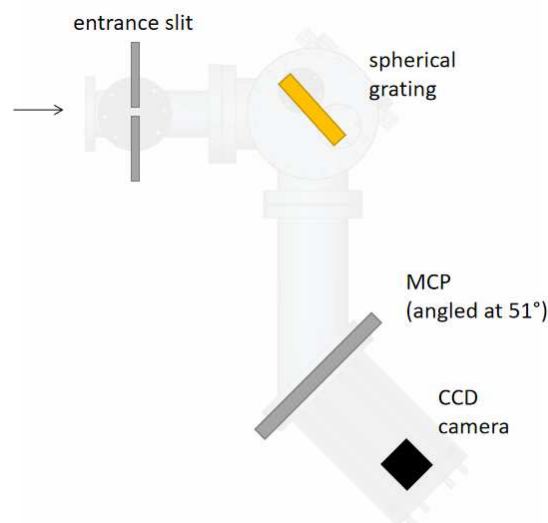


Figure 1: Overview of the main components of the VUV/XUV spectrometer [3].

So far, the 4th, 5th and 6th harmonics of the seed laser generated by the CHG scheme at 200 nm, 160 nm and 133 nm, respectively, could be analysed using the new spectrometer (Fig. 2) [4]. Higher harmonics will soon be detectable after the removal of a MgF window in the beam path to the spectrometer.

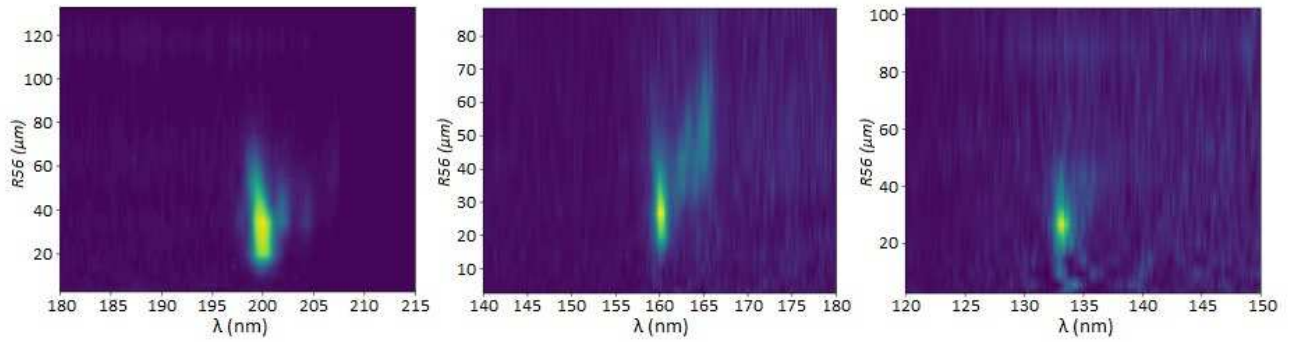


Figure 2: The 4th, 5th and 6th harmonics of the seed laser measured by the new VUV spectrometer as a function of the longitudinal dispersion parameter R_{56} , which measures the strength of a magnetic chicane involved in the CHG process [4].

References

- [1] S. Khan et al., *Generation of Ultrashort and Coherent Synchrotron Radiation Pulses at DELTA*, Sync. Rad. News 26:3, 25 (2013).
- [2] Andor iStar DH334T 18U-E3.
- [3] hp Spectroscopy easyLIGHT XUV.
- [4] B. Büsing et al., *SPEED: First EEHG Signal at a Storage Ring*, DELTA Annual Report 2022.
- [5] A. Radha Krishnan et al., *Investigation of Spectro-Temporal Properties of CHG Radiation at DELTA*, Proc. of IPAC'22, Bangkok, Thailand, p. 1423 (2022), doi:10.18429/JACoW-IPAC2022 TUPOMS012.

Preparation and measurement of millisecond X-ray pulses at DELTA beamline 10

C. Grundmann, D. Lützenkirchen-Hecht

Faculty of Mathematics and Natural Sciences-Physics Department, Bergische Universität Wuppertal, Gauss-Str. 20, D-42119 Wuppertal, Germany

Short X-ray pulses are important for pump-probe measurements as well as for time-resolved experiments, for example in time-resolved X-ray absorption spectroscopy. While usually high-brightness X-ray sources such as the ESRF or PETRA III are used for such purposes, we want to evaluate the preparation and measurement of millisecond X-ray pulses at DELTA. To do so, we have employed an X-ray chopper that utilizes a notched, rotating disk driven by a conventional hard-disk drive motor with 7200 rpm ($f = 120$ Hz) rotation speed [1]. The rotation of the disk with the cut-out segments periodically interrupts the incident X-ray beam. From the geometry of the disk (ca. 70 mm radius (R), two cut-out segments), and assuming a typical beam size at DELTA beamline 10 of about 1 mm, the rise time t_R of the chopper can be calculated to $t_R \approx 1 \text{ mm} / 2\pi f R = 20 \mu\text{s}$, while the pulse length t_P is simply given by the frequency and the number of segments of the chopper to $t_P = 1/4f \approx 2.1 \text{ ms}$ (eq. 1).

For the experiments, the incident beam was defined by a slit system to a size of typically 1-2 mm horizontally and vertically, and the intensity of the pulsed beam was measured with a gas-filled parallel-plate ionization chamber. We have used different filling gases (N_2 , Ar, Kr) at ambient pressure. The high voltage at the counter plate was varied between 500 V and 1000 V, and the current was measured with an analog Keithley 427 current amplifier applying a gain of 10^7 V/A or 10^8 V/A, and rise times of 40 μs and 60 μs , respectively. Due to the fast temporal changes of the X-ray intensities, voltage to frequency converters and counters cannot be used for the present measurements. Thus we have employed a fast analog to digital converter (PicoScope 3204) with a sampling rate of 8-12 MHz and the data were recorded on a PC [2]. Typical results obtained with nitrogen and argon as filling gases of the ionization chamber are presented in Fig. 1 and Fig. 2 respectively.

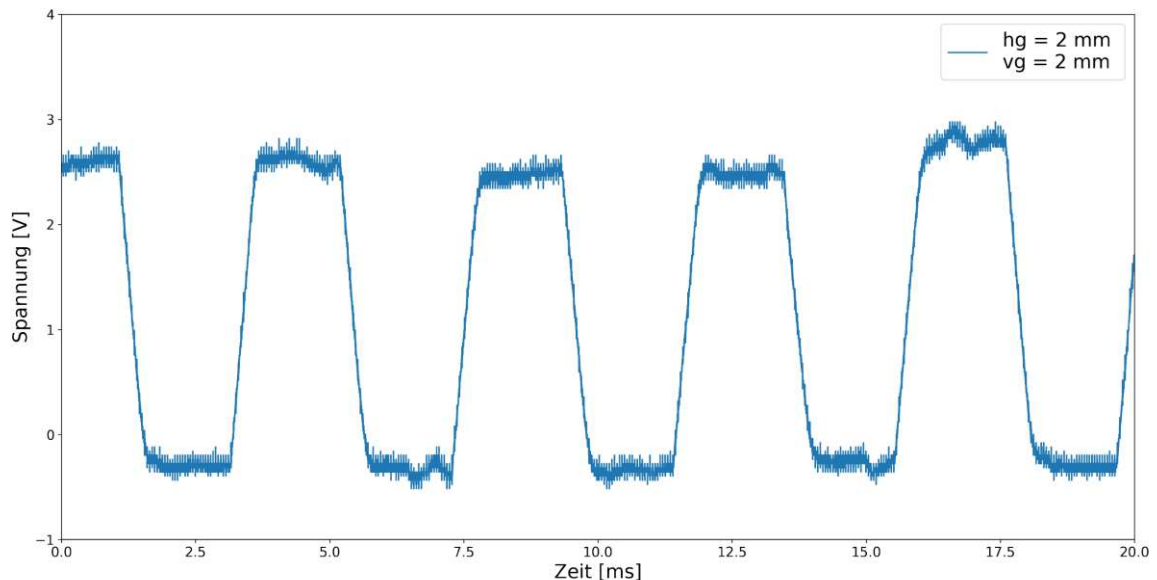


Fig. 1: Step response function of a parallel plate ionization chamber filled with nitrogen at ambient pressure. Approximately linear increases and decreases of the intensity are measured at the beginning and the end of the X-ray pulses, respectively. (Photon energy $E = 7800$ eV, beam size = $2 \times 2 \text{ mm}^2$ ($h \times v$)).

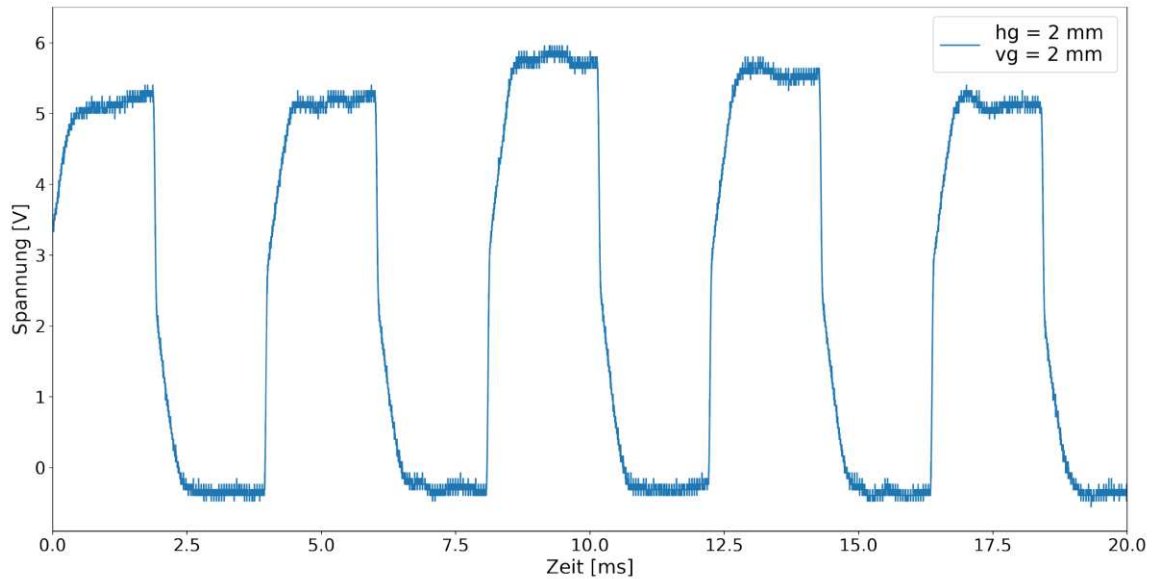


Fig. 2: Step response function of a parallel plate ionization chamber filled with argon at ambient pressure. Increasing and decreasing flanks of the X-ray pulses are deformed. (Photon energy $E = 7800$ eV, beam size = 2×2 mm² (h x v)).

As can be seen by comparison of Fig. 1 and Fig. 2, the flanks of the X-ray pulses are substantially broadened using Ar: Due to the lower drift velocity of the Ar-ions to the counter electrode, more time is needed to reach the full intensity of the X-ray pulse. In more detail, the fast response in the increasing edge originated from the fast and highly mobile electrons, and subsequent slower increase with smaller slope is caused by the ions. This behavior is even more pronounced in the case of Kr as filling gas. It is worth to note that the kink in the slope is always at 50% intensity, i.e. 50% of the measured current is related to the electrons, and 50% to the ions. In all cases, moreover, the measured pulse length of the X-ray pulses correspond well to the predicted duration according to eq. 1.

Thus, in conclusion, X-ray measurements of ms X-ray pulses are feasible at DELTA. Using a hard-disk drive with 5400 rpm or 15000 rpm, an easy variation of the pulse length is feasible. The results also have implications for time-resolved X-ray absorption spectroscopy at DELTA. The increase of the X-ray absorption at the edge is equivalent to the change of the intensity when the X-ray chopper releases or blocks the beam. Thus, the monochromator speed at the edge can practically be in the order of some few milliseconds, and from the detection sensitivity, a the measurement of a full X-ray absorption spectrum should be feasible at DELTA within less than a second. Thus the presented results are very promising for future, time-resolved EXAFS experiments at DELTA beamline 10.

Acknowledgement

We gratefully acknowledge the DELTA machine group for providing synchrotron radiation reliably.

References

- [1] O. Müller, D. Lützenkirchen-Hecht, R. Frahm, Rev. Sci. Instrum. 86 (2015) 035105.
- [2] C. Grundmann, BSc. Thesis, University of Wuppertal, 2022.

Soft X-ray Spectroscopy

Comparison of two different sub-monolayer Sn $\sqrt{3}$ -phases on Au(111)

J. A. Hochhaus^{1,2,*}, L. Kesper^{1,2}, U. Berges^{1,2}, and C. Westphal^{1,2}

¹ Experimentelle Physik I - Technische Universität Dortmund, Otto-Hahn-Str. 4a, D-44227 Dortmund

² DELTA - Technische Universität Dortmund, Maria-Goeppert-Mayer-Str. 2, D-44227 Dortmund

* corresponding author: julian.hochhaus@tu-dortmund.de

The discovery of graphene in 2004 with its remarkable mechanical and electronic properties paved the way for the investigation of other 2D materials from the carbon group, the so-called Xenes. In particular, Xenes of the heavier elements of the carbon group are of great interest, since these Xenes, in contrast to the atomically flat graphene, exhibit a band gap due to their buckled arrangement [1]. Moreover, some two-dimensional analogues of the heavier elements of the carbon group are even predicted to have topological properties [2]. The first synthesis of stanene, which consists of Sn-atoms and thus belongs to the heavier Xenes, was successful on Bi₂Te₃ in 2015 [3]. In the following years, the synthesis of stanene on further substrates such as Sb(111), InSb(111), PbTe(111), and Ag(111) was achieved [4–7]. It was found that the structural arrangement of stanene has a great influence on its electronic properties. In fact, extraordinary electronic properties were found, such as an exceptionally high Fermi velocity for Sn on Au(111) which is even an order of magnitude higher than predicted for free-standing stanene [8]. Additionally, in 2018 the preparation of ultraflat stanene on Cu(111) with a topological bandgap of $\Delta E = 0.3$ eV succeeded [9], which is considered as a milestone in the research of 2D topological devices.

As evident from the examples above, the surface and interface structure of low-dimensional materials often influences their electronic properties. Therefore, our analysis focuses on the structural and chemical investigation of sub-monolayer Sn-phases on Au(111) at room temperature by means of low-energy electron diffraction (LEED) and photoelectron spectroscopy (XPS).

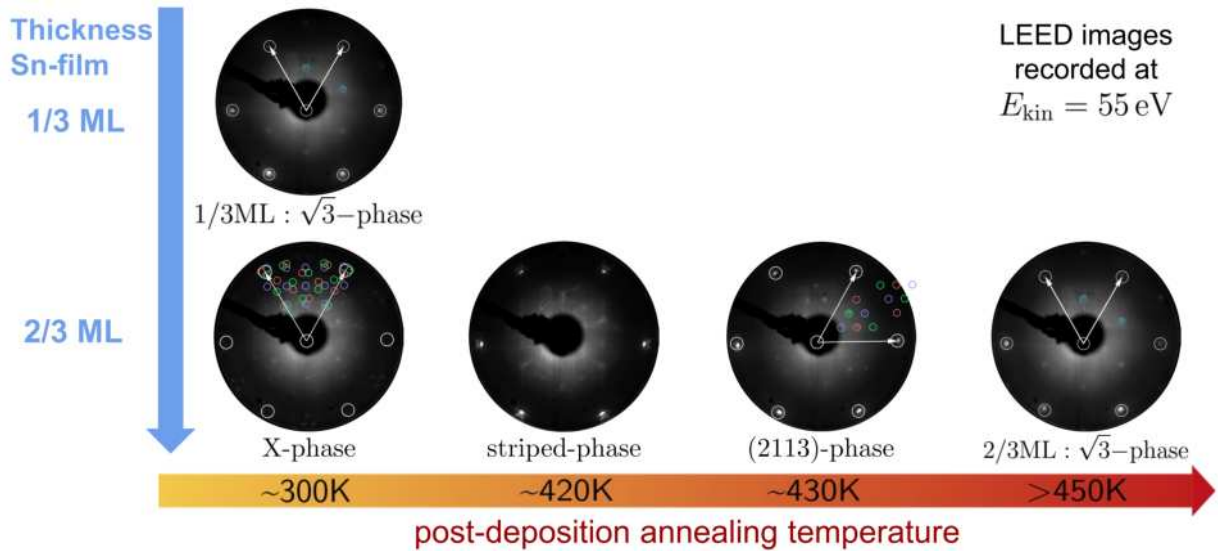


Fig. 1: Structural phase diagram of the Sn/Au(111) interface. Depending on the Sn coverage and post-deposition annealing temperature, several different superstructures of Sn on Au(111) are observed.

The preparation of the sample as well as all measurements are conducted at the UHV-endstation at beamline 11 at DELTA with a base pressure of $p \leq 5 \times 10^{-11}$ mbar.

As shown in Figure 1, the structural arrangement visible by LEED exhibits a film thickness dependence as well as a dependence on the post-deposition temperature. Evidently, $\sqrt{3}$ reconstruction results both for a film thickness of $\approx 1/3$ -ML and for $\approx 2/3$ -ML of Sn. To verify that these two phases are two different phases and that post annealing does not lead to unintended desorption of Sn, we will focus

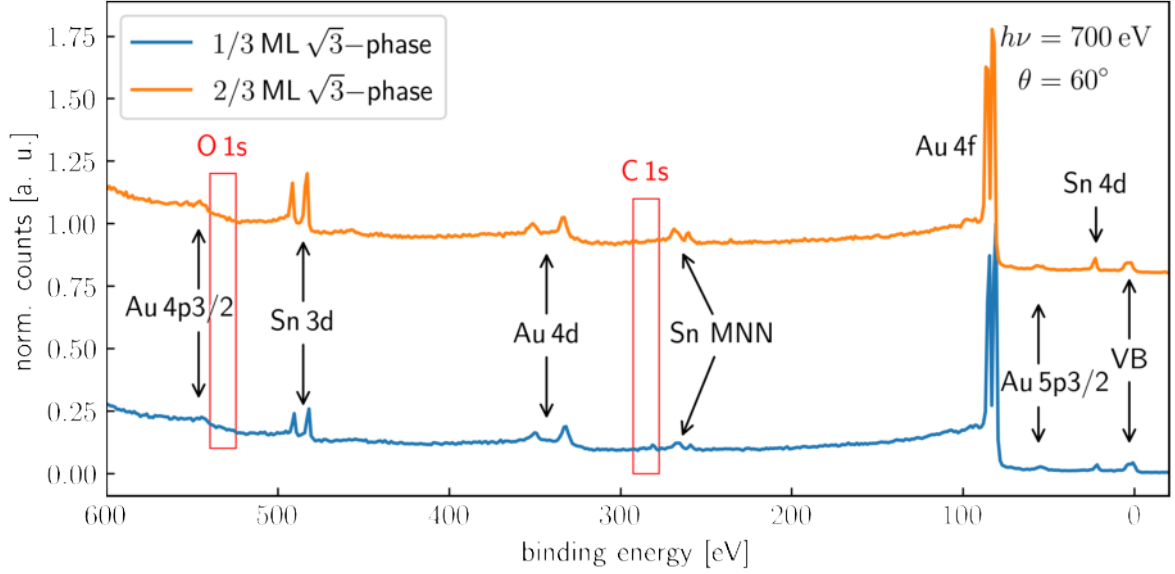


Fig. 2: XPS survey spectra of the two observed $\sqrt{3}$ -Sn/Au(111) interface reconstructions. The two spectra differ significantly in the amount of Sn adsorbed on the Au(111) sample and no evidence of unwanted residuals such as oxygen or carbon is observed.

on the comparison of the two $\sqrt{3}$ phases in the following. In Figure 2, survey spectra over a broad energy range of the two $\sqrt{3}$ -phases are shown. From the comparison of the spectra, it is evident that the two phases differ in the amount of Sn adsorbed on the Au(111) surface. Beyond that, no evidence of residues such as carbon or oxygen is visible.

In addition, as shown in the comparison of the high-resolution spectra of the two $\sqrt{3}$ -phases in Figure 3, the spectra of the two different layer thicknesses could not be fitted with the same number of components.

The Au 4f signal of the $\sqrt{3}$ -reconstruction at a layer thickness of $\frac{1}{3}$ -ML was fitted with two components. The dark green component at a binding energy of $E_{\text{bin}} = 83.99$ eV is assigned to the bulk. Subsequently, the light green component shifted by $\Delta E = 0.35$ eV to higher binding energy is assigned to the $\sqrt{3}$ -reconstruction which is known in the literature as an Au_2Sn -alloy [10]. Meanwhile, the Sn 4d signal is fitted with a single component at $E_{\text{bin}} = 24.00$ eV.

In contrast, for the fit of the high resolution spectra of $\sqrt{3}$ -reconstruction at a layer thickness of $\frac{2}{3}$ -ML to converge, an additional component was necessary. In comparison with the Au 4f bulk signal, this additional component is shifted by $\Delta E = 0.18$ eV to higher binding energies. For the Sn signal, the second component which we named *Alloy B*, is shifted by $\Delta E = 0.21$ eV to higher binding energies in relation to the *Alloy A* component at $E_{\text{bin}} = 24.00$ eV. In addition, a strong angular dependence for the *Alloy B* is observed, therefore we suggest that the additional Sn atoms of the $\frac{2}{3}$ -ML phase are arranged on top of the *Alloy A* reconstruction obtaining the same periodicity as evident from LEED.

For further insights, a large number of different sub-monolayer thicknesses have already been investigated by XPS. To date, the analysis was mainly focused on the reconstructions of $\frac{2}{3}$ -ML Sn on Au(111). In order to gain a detailed understanding of the structure formation of Sn on Au(111), further analysis of the already recorded data of reconstructions at Sn coverages below $\frac{1}{3}$ -ML will be carried out.

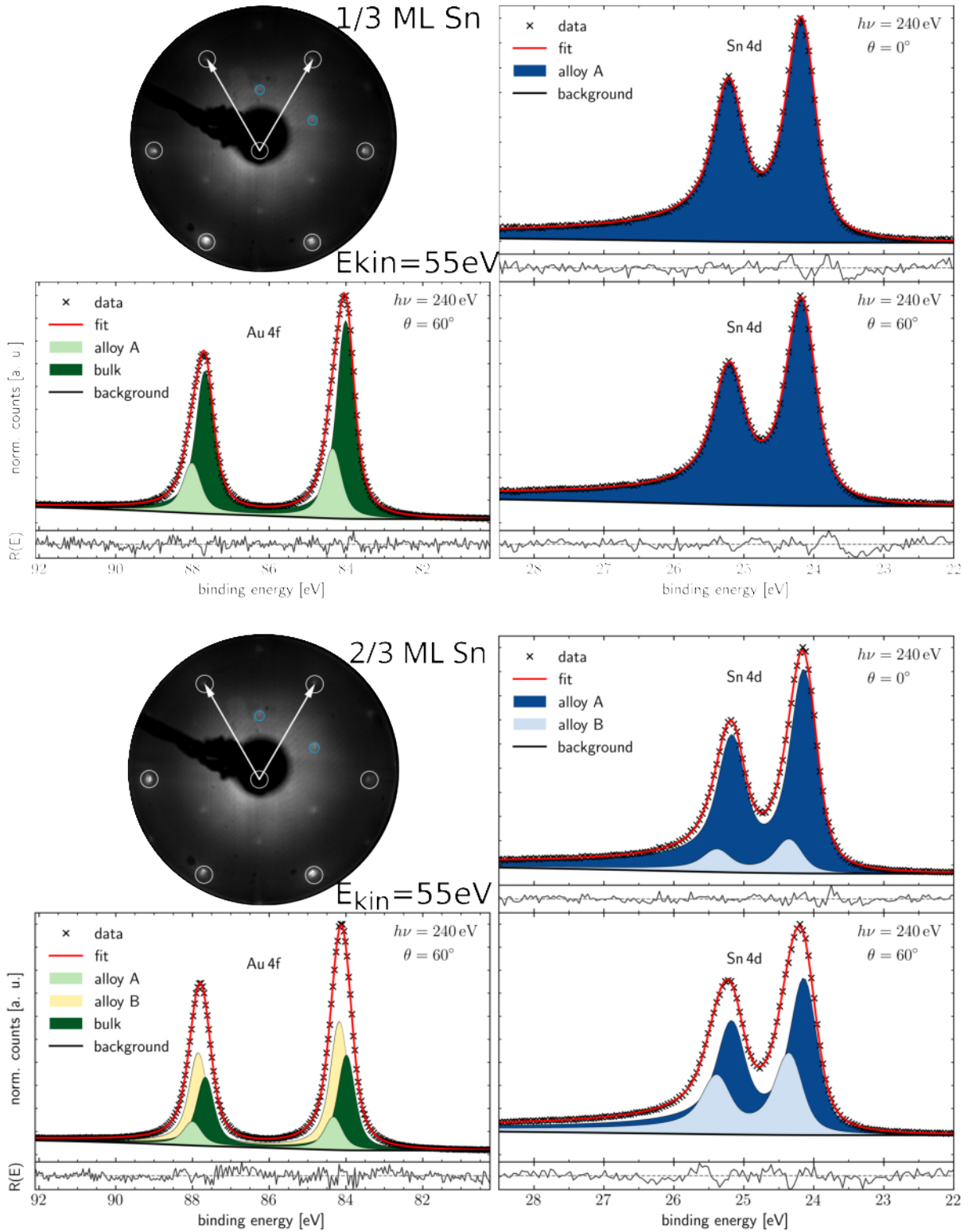


Fig. 3: The comparison between high-resolution spectra of the two $\sqrt{3}$ phases reveals that the $2/3$ -ML phase obtains an additional component in the Au 4f spectra. Moreover, the Sn 4d signal could no longer be fitted with a single component, a second component is necessary for the fit to converge.

References

- [1] A. Molle, J. Goldberger, M. Houssa, Y. Xu, S.-C. C. Zhang, and D. Akinwande, *Nat. Mater.* **16**, 163 (2017).
- [2] I. Gablech, J. Pekárek, J. Klempa, V. Svatoš, A. Sajedi-Moghaddam, P. Neuzil, and M. Pumera, *Trends Anal. Chem.* **105**, 251 (2018).
- [3] F. Zhu, W.-J. Chen, Y. Xu, C.-l. Gao, D.-D. Guan, C. Liu, D. Qian, S.-C. Zhang, and J.-F. Jia, *Nat. Mater.* **14**, 1020 (2015), arXiv:1506.01601 .
- [4] J. Gou, L. Kong, H. Li, Q. Zhong, W. Li, P. Cheng, L. Chen, and K. Wu, *Phys. Rev. Mater.* **1**, 054004 (2017).
- [5] C.-Z. Xu, Y.-H. Chan, P. Chen, X. Wang, D. Flötotto, J. A. Hlevyack, G. Bian, S.-K. Mo, M.-Y. Chou, and T.-C. Chiang, *Phys. Rev. B* **97**, 035122 (2017), arXiv:1711.08523 .
- [6] Y. Zang, T. Jiang, Y. Gong, Z. Guan, C. Liu, M. Liao, K. Zhu, Z. Li, L. Wang, W. Li, C. Song, D. Zhang, Y. Xu, K. He, X. Ma, S. Zhang, and Q. Xue, *Adv. Funct. Mater.* **28**, 1802723 (2018).
- [7] J. Yuhara, Y. Fujii, K. Nishino, N. Isobe, M. Nakatake, L. Xian, A. Rubio, and G. Le Lay, *2D Mater.* **5**, 025002 (2018).
- [8] M. Maniraj, B. Stadtmüller, D. Jungkenn, M. Düvel, S. Emmerich, W. Shi, J. Stöckl, L. Lyu, J. Kollamana, Z. Wei, A. Jurenkow, S. Jakobs, B. Yan, S. Steil, M. Cinchetti, S. Mathias, and M. Aeschlimann, *Commun. Phys.* **2**, 12 (2019).
- [9] J. Deng, B. Xia, X. Ma, H. Chen, H. Shan, X. Zhai, B. Li, A. Zhao, Y. Xu, W. Duan, S.-C. Zhang, B. Wang, and J. G. Hou, *Nat. Mater.* **17**, 1081 (2018).
- [10] P. Sadhukhan, D. Pandey, V. K. Singh, S. Sarkar, A. Rai, K. Bhattacharya, A. Chakrabarti, and S. Roy Barman, *Appl. Surf. Sci.* **506**, 144606 (2020).

X-ray Scattering

Pressure-dependent protein-protein interactions in aqueous protein solutions

Michelle Dargasz, Michael Paulus, Jaqueline Savelkouls

Fakultät Physik/DELTA, TU Dortmund, 44221 Dortmund, Germany

Studies of protein systems using high pressure are of particular interest since high pressure mainly affects the volume of the proteins without changing the chemical or thermal properties of the system [1]. This allows consideration of the influence of volume-related changes on the protein stability [2]. Protein conformation is closely related to functionality and since there are some areas in which high pressure is applied to proteins, an investigation in which proteins are subjected to pressures up to 4 kbar is worthwhile. In the food industry for example high pressure is used to inactivate pathogens or vegetative cells and thus to improve the digestibility and shelf life of groceries [4]. High pressure mainly effects the non-covalent bonds of a protein [3], which is why not only intramolecular but also intermolecular interactions are affected. In small angle X-ray scattering (SAXS) studies investigating the interaction mechanisms within concentrated lysozyme solutions, a nonlinear relationship between the interaction potential and the hydrostatic pressure exerted has been established [1]. This nonlinear relationship is represented in a shift of the correlation peak to higher q -values ($q = (4\pi/\lambda) \sin(\theta/2)$) with increasing pressure with a maximum at 2 kbar. So far, the cause of this effect has not been clarified. To determine whether this effect occurs also in other protein solutions pressure dependent SAXS experiments on concentrated BSA, HSA and β -lactoglobulin solutions were made. This enabled also an investigation of the pressure stability of the aforementioned proteins.

To investigate the nonlinear relationship of the interaction potential, a 7 wt% lysozyme solution with a 25 mM BisTris buffer at pH 7 was used. For the BSA and HSA solution, a 25 mM bicin buffer at pH 8.5 and a protein concentration of 10 wt% was set. The measurements of β -lactoglobulin were made with a 25 mM BisTris buffer at pH 7.5 and a protein concentration of 10 wt% and 15 wt%. For the SAXS experiments beamline BL2 of the DELTA synchrotron radiation source was used, which provides a photon energy of 12 keV. Using a high pressure cell, the pressure was increased in 250 bar steps from 0 to 4 kbar. The measured SAXS curves of the lysozyme solution can be seen in Figure 1. The pressure dependent shift of the correlation peak position with a maximum at 2 kbar is clearly visible.

The SAXS curves of the BSA, HSA and β -lactoglobulin solution are shown in Figure 2 on the left. It is visible that the shape of the SAXS curves changes depending on the pressure. At low q -values a shift to higher intensities indicates a more attractive part of the

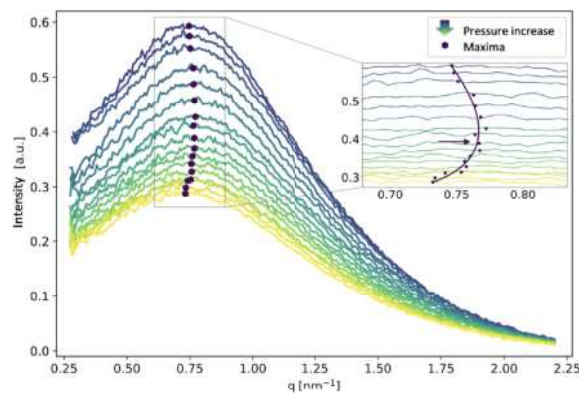


Figure 1: Pressure dependent SAXS curves of a 7 wt% lysozyme solution. The dark dots mark the correlation peak position, which is shifting nonlinear while pressure increases.

interaction potential. A Gaussian fit allows the correlation peak position to be determined as a function of pressure. Both plotted against each other can be seen in Figure 2 on the right. Initially, the correlation peak shifts to higher q -values. Above a certain pressure, this reverses. Following the analysis of the form factor measurements, it was possible to show an aggregation for the three proteins above this certain pressure. For HSA and β -lactoglobulin an unfolding process could also be detected.

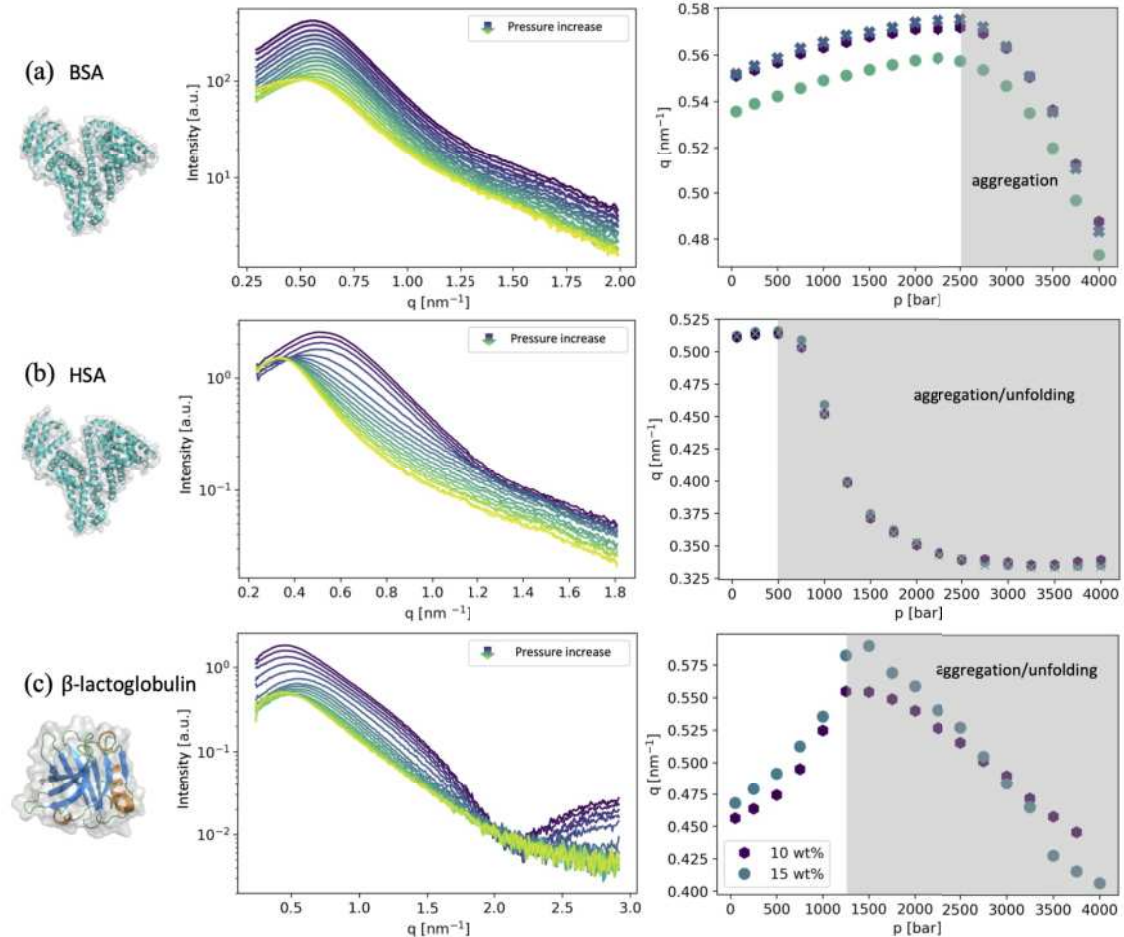


Figure 2: Pressure dependent SAXS curves of a (a) 10 wt% BSA, (b) 10 wt% HSA and (c) 15 wt% β -lactoglobulin solution on the left. On the right the correlation peak position is shown as a function of pressure. Above a certain pressure there's a shift of the correlation peak position back to lower q -values.

In summary, BSA, HSA and β -lactoglobulin are not pressure stable up to 4 kbar. Thus, only conclusions could be drawn in the low pressure regions. There, the shift of the correlation peak to higher q -values with increasing pressure observed in lysozyme solutions could also be reproduced in the other protein solutions.

References:

- [1] Martin A. Schroer et al. *Phys. Rev. Lett.* 106, 178102 (2011); [2] Karin Julius. *Diss. TU Dortmund* (2019); [3] B.B. Boonyaratanakornkit et al. *Biochimica et Biophysica Acta (BBA) - Protein Structure and Molecular Enzymology* 1595, 235-249 (2002); [4] L.A. Tedford et al. *Food Research International* 32, 1731-1739 (2017)

Kinetics of aggregation of egg yolk low-density lipoproteins revealed by X-ray scattering

Nimmi Das A^{1,2}, Sonja Timmermann², Marvin Kowalski², Susanne Dogan-Surmeier³, Michael Paulus³, and Christian Gutt²

¹Deutsches Elektronen-Synchrotron DESY, Notkestraße 85, Hamburg, 22607, Germany.

²Department Physik, Universität Siegen, Siegen, 57072, Germany.

³Fakultät Physik/DELTA, TU Dortmund University, Dortmund 44221, Germany.

Corresponding author; christian.gutt@uni-siegen.de

Hen egg yolk is widely utilized as a culinary component, owing not only to its taste, but also its excellent coagulating, emulsifying and gelling abilities. Aside from that it has a significant biological and therapeutic value due to the presence of proteins and other nutrients in micro and nano-assemblies [1-4]. About 68% of egg yolk's dry matter is made of low-density lipoproteins (LDL) which is primarily responsible for egg yolk's emulsifying characteristics [1]. The yolk-LDLs are spherical core-shell nanoparticles with average diameter of 30 nm with a lipid core of triglycerides and cholesterol esters in a liquid state surrounded by a monolayer of phospholipids and proteins [1], which is structurally very similar to human LDLs [5]. It is known that stability of LDLs depends on its structural features and any changes to its native structure can lead to loss of its functionality. Specifically, thermal denaturation leads to unfolding and aggregation [2]. The information on these out-of-equilibrium processes are not only crucial for understanding origin of its kinetic stability, but also valuable for other application fronts such as food industry and pharmaceuticals.

In this study we investigated the kinetics of aggregation of egg yolk LDLs at temperatures in the range 75-100 °C. The measurements were performed at the small-angle and wide-angle X-ray scattering (SAXS and WAXS) beamline BL2 of the DELTA synchrotron radiation source. We used an incident energy of 12 keV with a bandwidth of 1.5% and beam size of 0.6x0.6 mm². The SAXS data were collected by a MAR345 image plate detector with a constant exposure of 60 s. The egg yolk LDL rich fraction – egg yolk plasma was extracted from egg yolk by centrifugation as specified in the literature [1]. For temperature measurements, the samples were filled into borosilicate capillaries. In-situ heating measurements were performed by exploiting a Linkam temperature cell.

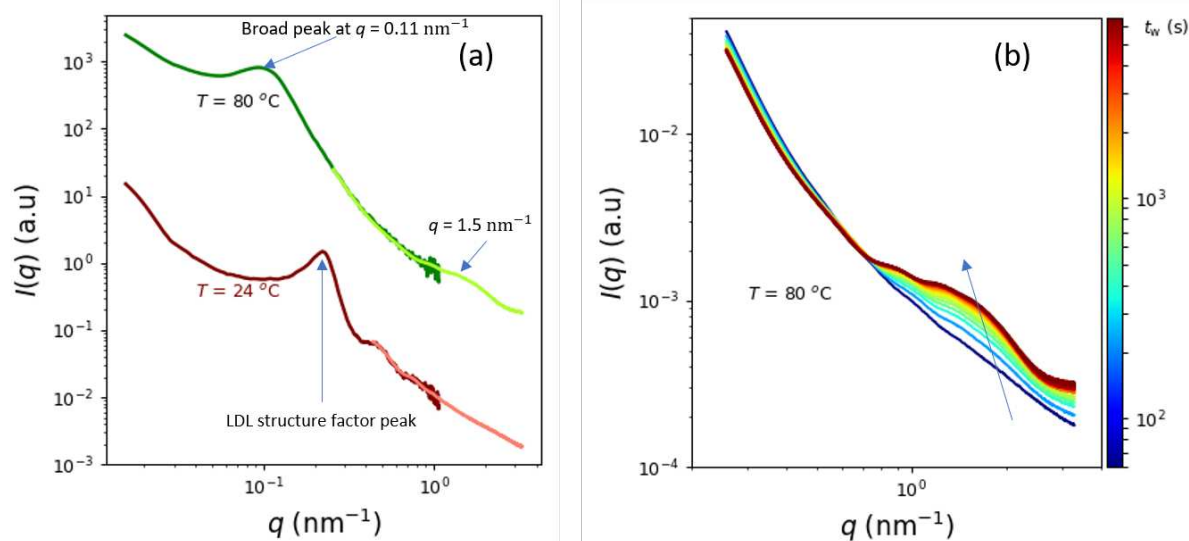


Figure 1: (a) Comparison of scattering profiles of egg yolk plasma at 24°C (bottom) and 80°C (top). The full profiles were generated by combining scattering data collected at BL2, DELTA (light red and light green) with that collected at P10, PETRA III (maroon and green). The plots are shifted for clarity. (b) Temporal evolution of scattering profiles of egg yolk plasma heated to 80°C as a function of waiting time as indicated by the scale bar. The arrow indicates the shift in the peak position along with increase in scattering intensity.

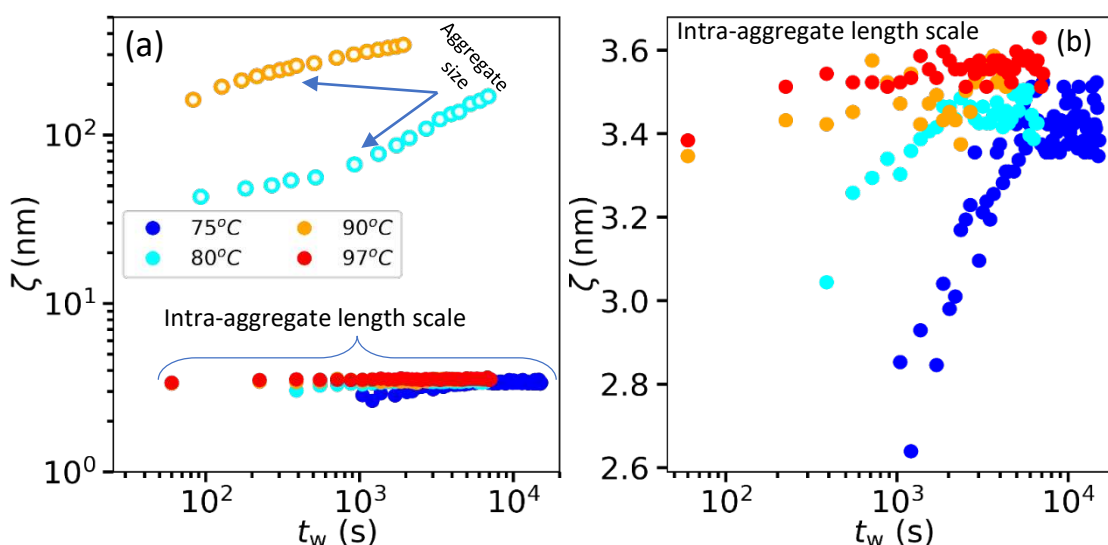


Figure 2: (a) The evolution of aggregate size and intra-aggregate length scale as a function of waiting time. (○) The aggregate size and (●) intra-aggregate length scale. For better clarity, evolution of intra-aggregate length scale is depicted in (b).

Fig. 1a depicts the comparison of representative scattering profiles of egg yolk plasma at room temperature and heated to 80 °C. The structure factor peak at $q = 0.22 \text{ nm}^{-1}$ and higher order oscillations in room temperature scattering data is indicative of LDL core-shell structure and presence of hard sphere type interaction potential. With heating, the structure factor peak and higher order oscillations disappear and a broad peak appears at low q ($= 0.11 \text{ nm}^{-1}$) which indicates the LDL denaturation and further aggregation. Interestingly, a second broad peak is also emerging at $q = 1.5 \text{ nm}^{-1}$, indicating the structural complexity of these aggregates. The temporal evolution of representative scattering profiles collected at a sample temperature of 80 °C is shown in Fig. 1b. A small shift in the second broad peak position to low- q and increase in scattering intensity reflects the growth of these intra-aggregate structures. Further quantification is done by extracting the correlation length scale, ζ using the relation $\zeta \sim \frac{2\pi}{q_{\text{peak}}}$, where q_{peak} is the position of peak. The extracted ζ values corresponding to low- q and high- q peak provide the mean aggregate size and intra-aggregate length scale respectively. The evolution of correlation lengths is shown in Fig. 2a. Clearly, the aggregation process is temperature dependent. Moreover, for a given temperature, the aggregate size increases as a function of waiting time, t_w . Concurrently, some interesting structures evolving inside these bigger aggregates, size of which increases as a function of time and saturates to a final value of 3.5 nm. Comparing the results from literature on human LDLs [5], we speculate that the broad peak emerged at $q = 1.5 \text{ nm}^{-1}$ is indicative of the formation of cholesterol layering.

References:

- [1] M. Anton, EPC Proceedings of 12th European Poultry Conference, Verona, Italy, pp. (2006): 10-14.
- [2] M. Anton, J Sci Food Agric, 93 (2013): 2871–2880.
- [3] M. Zhou et al. Food Hydrocolloids 57 (2016): 20-29
- [4] C. Zhu and Y. Xia, Chem. Soc. Rev., 46 (2017): 7668.
- [5] S. Maric et al. ACS Nano 11, no. 1 (2017): 1080-1090.

Acknowledgments: We thank the DELTA team for providing beamtime and support.

Temperature-induced structural rearrangements in high-density lipoproteins

Susanne Dogan-Surmeier^{*,a}, Michael Paulus^a, Nimmi Das^{A^{b,c}}, and Christian Gutt^c

^aFakultät Physik/DELTA, Technische Universität Dortmund, Dortmund, Germany

^bDeutsches Elektronen-Synchrotron DESY, Notkestraße 85, Hamburg, 22607, Germany

^cDepartment Physik, University of Siegen, Siegen, 57072, Germany

*corresponding author: susanne.dogan@tu-dortmund.de

Cholesterol is an essential hydrophobic molecule that plays a key role in the architecture and phase behaviour of mammalian cell membranes. Moreover, it is an important precursor for crucial metabolic pathways (for example vitamin D, steroids, bile acid)¹. Intercellular plasma lipoproteins such as high density lipoproteins (HDL) and low density lipoproteins (LDL), are responsible for cholesterol transport. The quasi-spherical molecules have different sizes and lipid compositions. They possess a core-shell structure, whereas the core is filled with triglycerides, cholesterol esters and triglycerides surrounded by a phospholipid shell permeated by apolipoproteins^{1,2}. The proteins are essential for the interaction with specific cell-membrane receptors and the structural integrity of the particles. HDL is responsible for the reverse cholesterol transport and contains in contrast to LDL which has only one apolipoprotein, several apolipoproteins. It is well known, that lipoproteins play a role in the development of arteriosclerosis in which the walls of the artery develops abnormalities, so-called lesions that can when severe, result in coronary artery disease, stroke, peripheral artery disease or kidney problems. Increased (decreased) plasma LDL (HDL) concentrations have been associated with an increase in coronary heart disease. The dimensions of HDL particles are between 7.3 – 13 nm^{2,3}, denser but smaller than LDL. A sketch of the cross-section of LDL and HDL with its apolipoproteins is shown in figure 1.

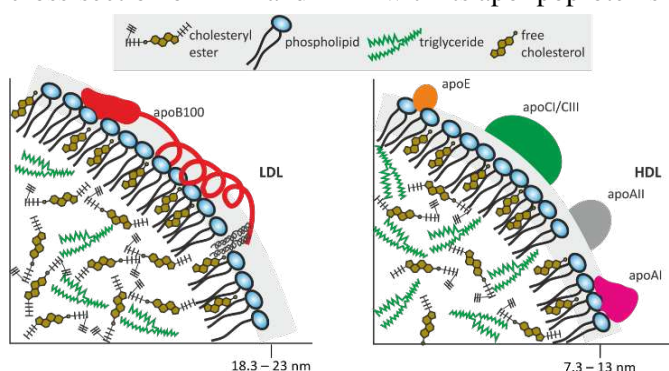


Figure 1: Sizes and composition of comparison of LDL (left) and HDL (right).

A systematic investigation of thermal denaturation and fusion of HDLs can reveal the kinetic origin of their thermal stability. Here we investigate the thermal stability of HDLs using the small-angle X-ray scattering setup at beamline 2 of DELTA⁴. The measurements were performed using a Linkam stage with borosilicate capillaries

and data were collected at constant temperatures which was controlled via a temperature control unit (20 – 90°C).

We studied HDL from Sigma Aldrich (Darmstadt, Germany; purity > 95%). The samples were used as they were delivered. We used an incident energy of 12 keV with a beam size of 0.7 x 0.7 mm² and a MAR345 image plate detector to collect the diffraction data.

Figure 2 shows a SAXS temperature series of HDL from room temperature up to 95°C. It becomes clear that the thermal decomposition of HDL proceeds via a two-step process as proposed for example in⁵ on the basis of LDL. At a temperature around 80°C, a strong reduction of the oscillation period is observed, which originates from the form factor of the HDL particles. This behaviour can be explained by a temperature induced fusion of the particles which increases the particle diameter. When reaching 95°C the system seems to change into a very disordered state where no spherical particle structure is present.

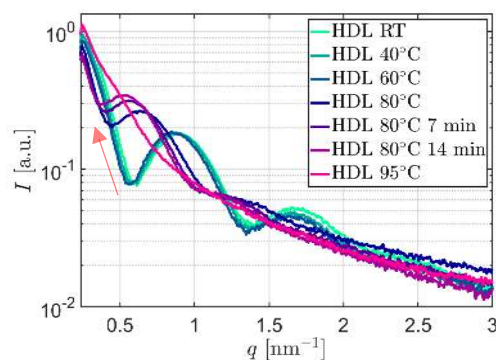


Figure 2: Experimental SAXS data for HDL at different temperatures. The red arrow follows the minima change.

References

1. Gursky, O. (2015), FEBS Letters 589, 2627–2639. 10.1016/j.febslet.2015.02.028.
2. Wojczynski, M.K. et al. (2011), Lipids in Health and Disease 10, 181. 10.1186/1476-511X-10-181.
3. Dobiášová et al. (2005), Physiol Res 54, 159–165.
4. Tolan, M. et al. (2003), DELTA: Synchrotron light in nordrhein-westfalen, 5. Lu, Mengxiao and Gursky, Olga. *BioMolecular Concepts*, vol. 4, no. 5, 2013, pp. 501-518

Acknowledgements

We thank the DELTA machine team for providing synchrotron radiation.

The effect of pressure and additives on the lamellar-to-cubic transition dynamics of monoolein at excess water conditions

Jaqueline Savelkouls*, Michelle Dargasz, Michael Paulus
 Fakultät Physik/DELTA, TU Dortmund, 44221 Dortmund, Germany
 *E-mail: jaqueline.savelkouls@tu-dortmund.de

One of the most important classes of molecules of every living organism are lipids. Due to their hydrophilic and hydrophobic structural parts, they have an amphiphilic character. As a result, lipids can spontaneously self-assemble into supramolecular structures in polar solvents [1]. These structures form the starting point for the morphological diversity of lipids and are essential for the execution of numerous functions in biological cells [2]. One class of morphological structures are the inverse bicontinuous cubic mesophases. They are useful in the biological field, in pharmacy and in various industrial branches [3, 4, 5, 6]. These inverse cubic phases include the highly ordered Pn3m structure, which is particularly well suited to the uptake, storage and controlled release of drugs in the human body [7].

To prepare this Pn3m structure, 20% by weight of the synthetic lipid monoolein is mixed in water with the desired drugs at room temperature. The monoolein samples are examined in pressure-dependent measurements. The measurements are performed at the beamline BL2 using the small angle X-ray scattering (SAXS) set-up at a constant temperature of 25°C and using a photon energy of 12 keV. While the pressure is varied between 100 bar and 4000 bar, a detector image with an exposure time of 150 s is recorded for each pressure step. Integrated SAXS data are shown in Figure 1 as an example for monoolein in excess water without added cosolvents. The morphological phases and the associated lattice parameters a can be deduced from the observed reflection patterns with $a = \frac{2\pi}{q_{hkl}\sqrt{h^2+k^2+l^2}}$. The lattice parameters resulting from Figure 1 are illustrated in Figure 2a.

At a pressure of 100 bar, the Pn3m structure is in equilibrium.

Figure 2b shows the corresponding equilibrium values of the Pn3m lattice constant of monoolein in the presence of different additives. It can be seen that additives affect the size of the lattice parameters. Salts decrease the Pn3m lattice constant due to dehydration of the lipid headgroups, while drugs and other cosolvents increase the Pn3m lattice constant through their respective binding to the lipid headgroups.

By increasing the pressure up to 3000 bar, the lipid chains are stretched and the Gaussian curvature and the occupied volume of the lipids decreases. As a result, there is a transition from the cubic Pn3m phase to the metastable lamellar phase.

After a pressure reduction to 1500 bar, the lipids rearrange into a stable lamellar phase. The corresponding lattice parameters d are illustrated in Figure 2c. It turns out that salts increase the lattice spacing. The reason for this is based on the accumulation of the ions in the aqueous interlayer. As a result, the water molecules of the respective hydration shell interact with the free water molecules, limiting the mobility of the interlayer water molecules and allowing less water to diffuse out of the interlayer. In comparison, the other substances, such as caffeine or human serum albumin, displace the water from the interlayer. This reduces the lattice spacing.

Finally, the pressure is reduced to 100 bar again and the system is observed for 8 hours. After the pressure reduction, coexisting inverse bicontinuous cubic structures with swollen water channels and increased lattice parameters form. Over time, the excess water is released from the channels as the lipid molecules relax back into their original geometry. The release of excess water is sped up in the presence of salts. Meanwhile, aspirin complex, caffeine and human serum albumin slow down the release (see Figure 2d).

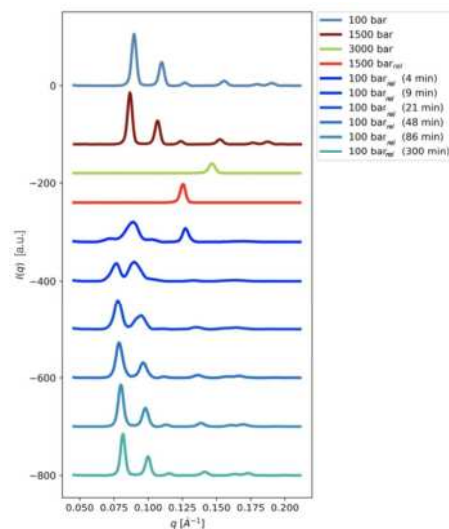


Figure 1: Integrated SAXS data of monoolein depending on the pressure. The index “rel” indicates the values at pressure reduction.

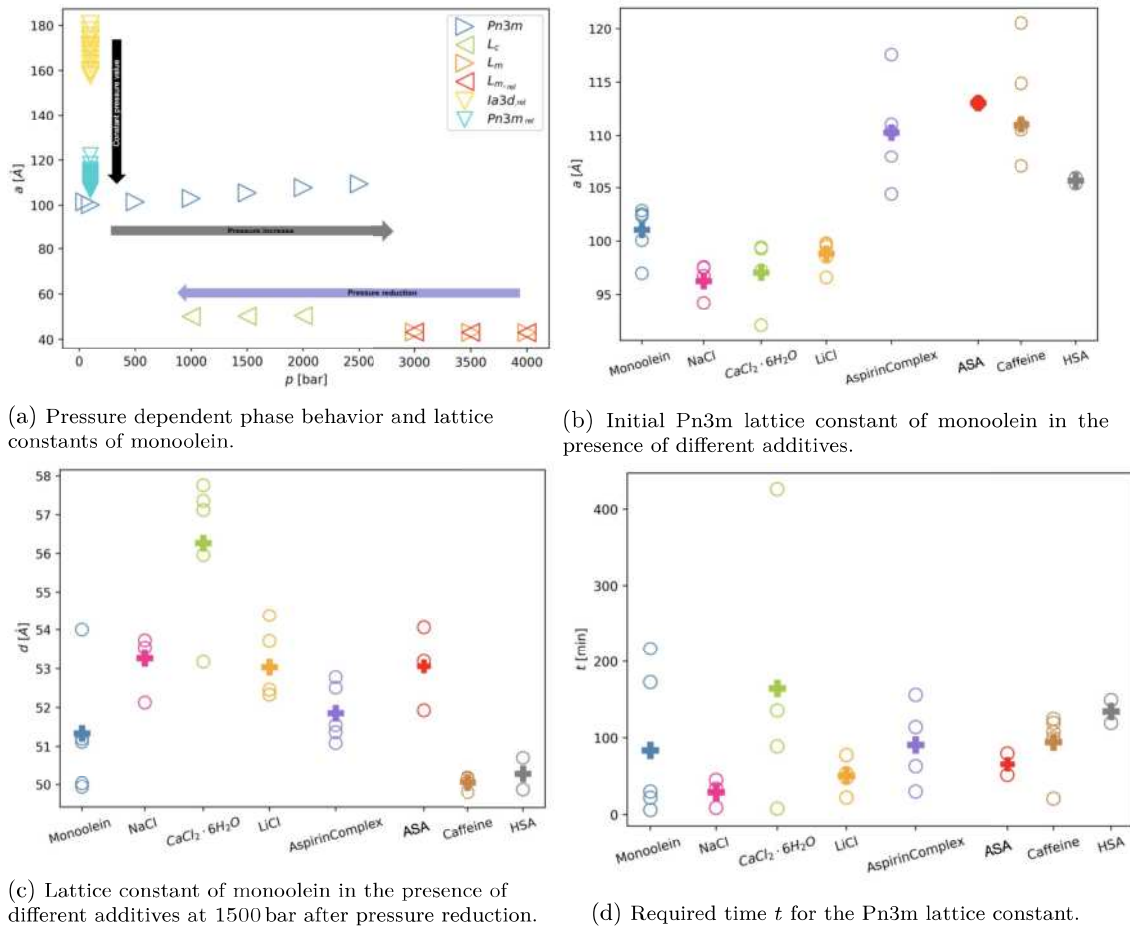


Figure 2: (a) Phase behavior and lattice constants of monoolein in excess water as a function of pressure. Each mesophase is labeled with its own color. (b) Equilibrium values of the $Pn3m$ lattice constant of monoolein at 100 bar in presence of different additives. The circles represent the values for different samples and the crosses mark the mean values. (c) Spacing d of the L_c phase of monoolein at 1500 bar after pressure reduction in presence of different additives. (d) Required time t for the lattice constant to fall below 110% of the equilibrium value after pressure jumps in presence of additives.

In summary, the pressure as well as the addition of additives influences the effective area of the lipids, the Gaussian curvature and the phase behaviour of the morphological structure. Furthermore, additives can speed up or slow down the release of the excess water from the water channels of the inverse cubic phases.

Reference:

[1.] Thomas Heimburg. „Membrane Structure“. In: Thermal Biophysics of Membranes (2007), p. 15–27. [2.] D. Uhríková. „Phospholipid bilayers in model membranes and drug delivery systems: From physics to pharmacy“. In: European Pharmaceutical Journal 68 (2021), p. 66–71. [3.] Chandrashekhara V. Kulkarni et al. „Monoolein: a magic lipid?“ In: Physical Chemistry Chemical Physics 13.8 (2011), p. 3004–3021. [4.] Vadim Cherezov et al. „Membrane Protein Crystallization In Meso: Lipid Type-Tailoring of the Cubic Phase“. In: Biophysical Journal 83 (2002), p. 3393–3407. [5.] Pieter R.Cullis; Michael J.Hope and Colin P.S Tilcock. „Lipid polymorphism and the roles of lipids in membranes“. In: Chemistry and Physics of Lipids 40.2 (1986), p. 127–144. [6.] Adriana Ganem-Quintanar; David Quintanar-Guerrero and Pierre Buri. „Monoolein: A Review of the Pharmaceutical Applications“. In: Drug Development and Industrial Pharmacy 26.8 (2000), p. 809–820. [7.] Chandrashekhara V. Kulkarni et al. „Self-Assembled Lipid Cubic Phase and Cubosomes for the Delivery of Aspirin as a Model Drug“. In: American Chemical Society (2017).

Acknowledgments:

We thank the DELTA machine group for providing synchrotron radiation.

Temperature dependent behavior of micelle structure formation in NIPA

Özgül Öztürk¹, Gülsen Evingür², Christian Gutt¹

¹Department of Physics, University of Siegen, Walter-Flex-Str. 3, 57072 Siegen, Germany

²Department of Industrial Engineering, Piri Reis University, 34940 Tuzla/İstanbul, Turkey

Due to its temperature responsive behavior, the Poly(*N*-isopropylacrylamide) (NIPA) hydrogel has attracted great interest for a wide variety of applications in tissue engineering and regenerative medicine. NIPA hydrogel undergoes an abrupt volume phase transition at a lower critical solution temperature (LCST) of 30-35 °C [1]. LCST can be easily manipulated by different parameters like cross linking agent, by copolymerization with suitable monomers [2]. This transition affects both the structural, optical and mechanical properties of the material.

The measurements of this study were done at BL2 in SAXS geometry with an energy of 12keV. NIPA samples prepared with different NIPA molarities were dissolved in pure water and inserted in glass capillaries. Different weight percentages of crosslink agent Bissulfosuccinimidyl suberate (BIS) were added and the reaction was accelerated by using TEMED as a catalyzer. The samples were measured in 2°C steps where the temperature was increased by 0.29°C/min and each step took 300s. Pure water sample using the same capillary was measured first to use for normalization.

Figure 1 shows the Porod plots ($I(q)$ vs q) of two samples prepared by 0.5 molar and 1 molar NIPA. The scattering intensities increase for all temperatures when the NIPA molarity is larger. At low q region a peak could be observed for all temperatures for both samples. This increase of intensity with temperature marks that there is a temperature-induced clustering enhancement resulting with more micelle like compact structures at large length scales. For 0.5M NIPA there is a pronounced rise at 34°C, then the scattering intensity decreases pointing out the loss of this temperature-induced clustering. For 1M NIPA, this is also observed at 34°C, but the decrease starts after 36°C and observed to be augmented.

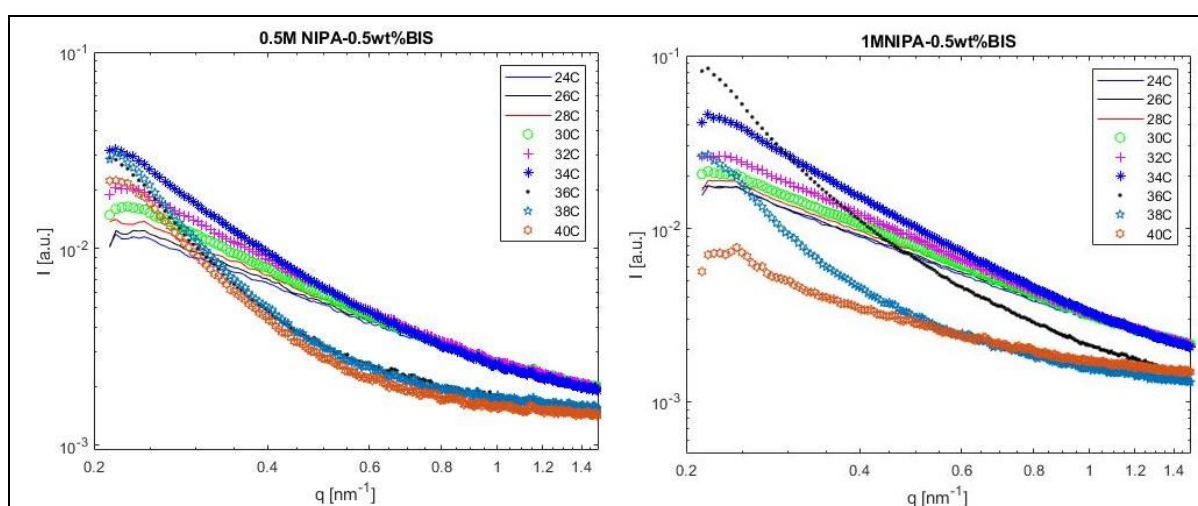


Figure 1 Porod plots of samples with 0.5 molar NIPA (right) and 1molar NIPA (left) with 0.5wt% BIS.

According to Porod, scattering measurements provide information on the mass fractal dimension by determining the exponent that describe the power law decay of the scattering

intensity at values of q , that are larger than $1/R$, where R is the physical average radius, but sufficiently small that the particle surface is not being probed. This means the intensity decays as [3]

$$I(q) \propto \frac{c}{q^b}$$

Where c is a constant and b is the mass fractal dimension. The value of b depends on whether the polymer is globule or swollen or has an ideal chain conformation [4]. The Porod plots of the samples shown in Figure 1 has different b values in low q region as a function of temperature. For the temperatures below 36°C , a power-law ($\sim q^{-2}$) is observed, which is attributed to an ideal chain conformation like partially folded proteins. For 36°C and the higher temperatures ($\sim q^{-4}$) dominates the scattering, which is a characteristic of collapsed structures with sharp interfaces.

By using the Kratky plot ($q^2 I(q)$ vs q), deviations from the high q (scattering vector) behavior of the scattering intensity could be used to identify disordered states and distinguish them from the globular structures [3]. In Figure 2, the Kratky plots of two 0.5 molar NIPA samples with two different amounts of BIS are seen. At high q regimes, the upward deviation of the curves indicates the swollen, less compact state. At low q regimes it could be clearly observed that formation of a globular conformation starts between $34\text{-}36^\circ\text{C}$ and continues for higher temperatures with a decreasing intensity. The general behavior of the measurements with different amount of BIS indicates that the BIS amount does not have a clear effect on either the critical temperature or the scattering intensity.

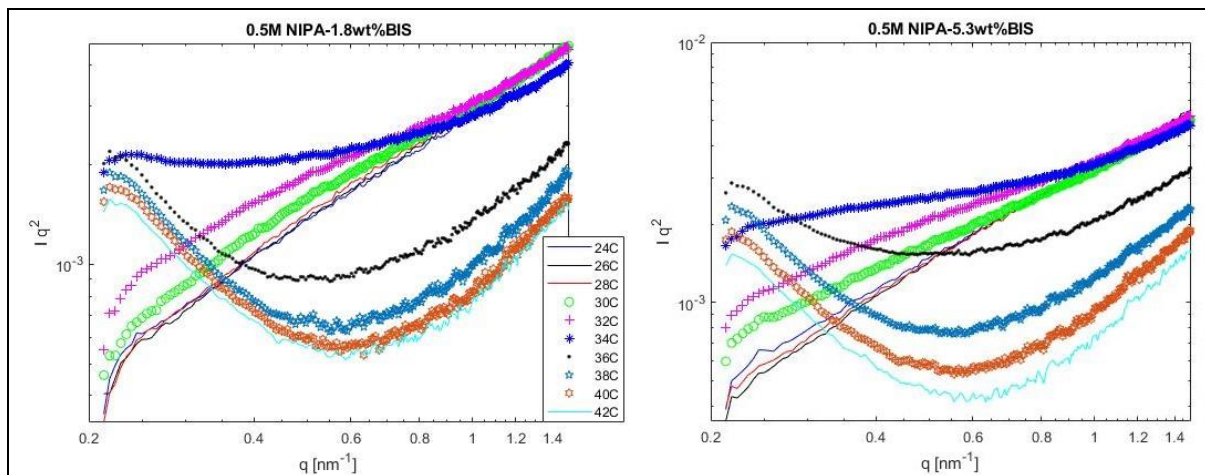


Figure 2 Kratky plots of 0.5molar NIPA samples with 1.8wt% BIS (right) and 5.3wt% BIS (left) concentrations.

The measurements done at DELTA, BL2 brought a perception about the temperature dependence of NIPA and how the molarity of NIPA and amount of crosslink agent affect this dependence.

References:

1. N. Zhang et.al. *Polymers*, 2018, 10(4):358.
2. M. Najafi et.al. *Soft Matter*, 2021, 17, 2132-2141.
3. G. Pizzorusso et.al., *Langmuir*, 28,3952-3961, 2012.
4. Y. Wie and M.J. A. Hore, *Journal of Appl. Phys.*, 129, 171101, 2021.

Apoferritin adsorption on solid-supported DMPC bilayers

Jaqueline Savelkouls*, Susanne Dogan, Mike Moron, Christian Sternemann, Michael Paulus

Fakultät Physik/DELTA, TU Dortmund University, 44221 Dortmund, Germany
*jaqueline.savelkouls@tu-dortmund.de

Biological membranes, consisting of lipid bilayers, are essential components in living organisms. Membranes form barriers that separate the interior of a cell from the extracellular space. In addition, they are involved in numerous biological processes, such as signal transduction and energy storage [1]. These biochemical processes can be influenced by the interaction of proteins with lipid interfaces [2]. Hence, the effects of protein adsorption are of interest for understanding the organisms' biochemistry and for current issues in the pharmaceutical industry. In addition, knowledge about the interactions between proteins and cell membranes are useful in bio- and nanotechnology [3]. One protein that lends itself to various nanomedical applications is apoferritin. Apoferritin belongs to the iron-free ferritins that are mainly found in the intestinal mucosa membrane. The oligomeric protein forms a cavity inside that serves to collect and store free iron. In nanomedicine, the cage structure is used as a nanotransporter for example in contrast agents [4,5].

For a deeper understanding of apoferritin's structural stability upon adsorption and its pH-dependent adsorption behavior to membranes, we studied apoferritin at solid-supported phospholipid bilayers using X-ray reflectometry (XRR) at BL9 of DELTA [6,7]. The XRR data were collected using a PILATUS 100k area detector at an incident photon energy of 27 keV. All measurements were performed at room temperature. As a suitable model system for lipid membranes, a stable phospholipid bilayer is applied to a silicon single-crystal wafer via spin-coating [8]. The phospholipid film consists of highly oriented bilayers of the lipid 1,2-dimyristoyl-sn-glycero-3-phosphocholine (DMPC) (CAS number: 18194-24-6). To investigate the adsorption processes, the lipid-coated wafers are applied in an aqueous environment at pH 7 in a Polytetrafluorethylen-XRR sample cell.

First, reference reflectivity curves from the liquid-solid-supported DMPC bilayer interface without apoferritin are recorded. Figure (1) illustrates the measured reflectivities and electron density profiles of the bilayer system in water. The results show no significant changes after the first hour. Therefore, the lipid bilayer is stable over this period. The resulting head-to-head layer thickness (d_{hh}) is $d_{hh} \approx (36.5 \pm 0.8) \text{ \AA}$.

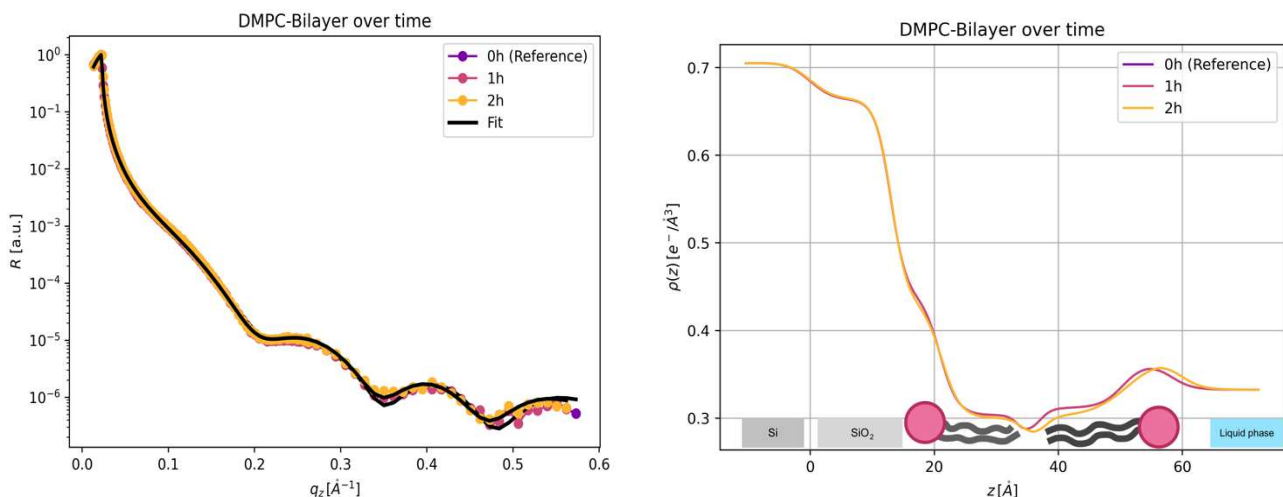


Figure 1: Left: X-ray reflectivities of solid-supported DMPC layer on Si/SiO₂. Right: Electron density profiles corresponding to the refinements with a sketch of the underlying model.

Figure (2) presents the DMPC layer without apoferritin as a function of the pH value. The results reveal no change in the layer thickness or electron density profile. Only the head groups at the Si/SiO₂ layer become rougher with decreasing pH.

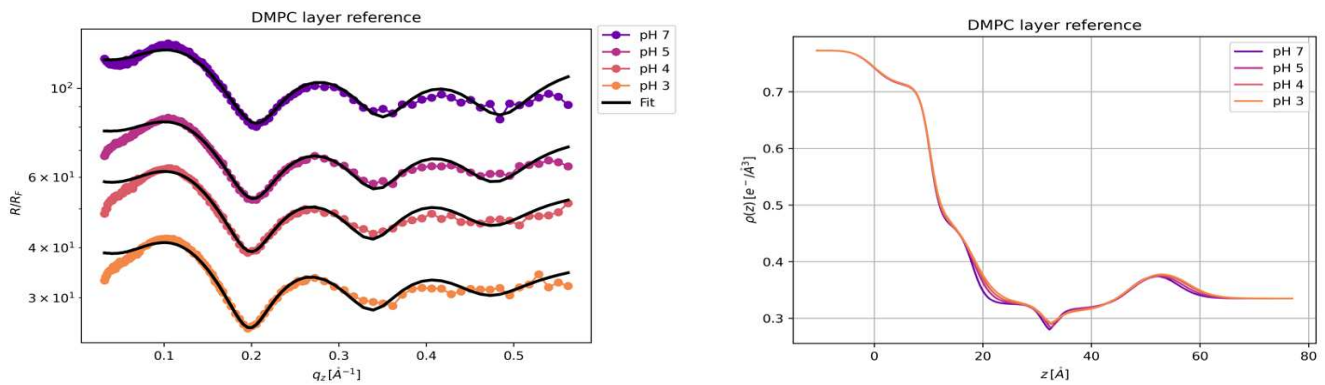


Figure 2: Left: Fresnel normalized XRR curves shifted vertically for better visibility. Right: Electron density profiles.

In the following, the effects of the apoferritin-DMPC interaction are analysed. For this purpose, apoferritin is added to the aqueous environment in which the coated silicon wafer is located. Figure (3) illustrates the resulting measurement data as a function of the pH value for addition of 100 μl (2,5 wt%) apoferritin und figure (4) shows the corresponding results as a function of protein concentration at pH 7. We observe that the pH-value hardly influences the system even if 100 μl apoferritin is added. The normalized reflectivities as well as the electron density profiles shift slightly. In contrast the change of protein concentration causes a major effect, i.e. increasing concentration increases the dispersion and roughness of the system. The exact analysis and final interpretation of the XRR data are in progress.

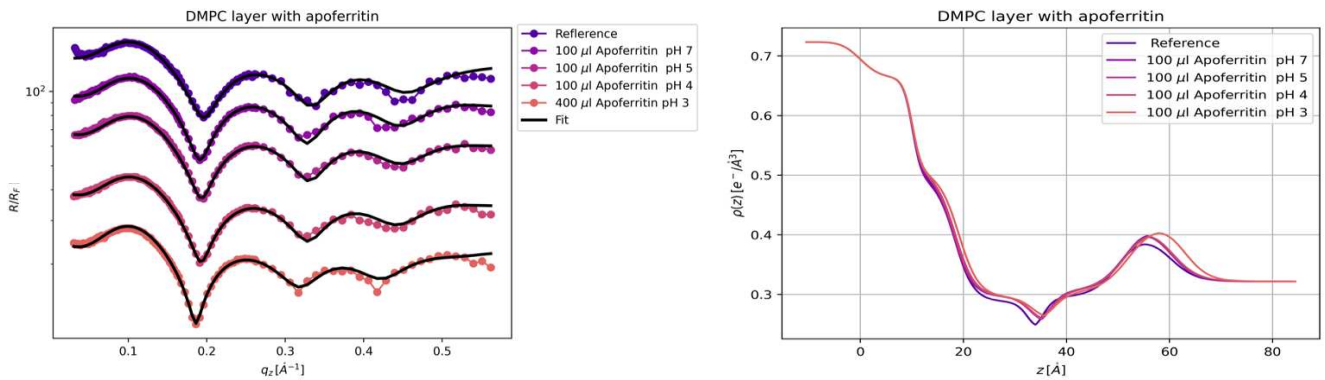


Figure 3: Left: Fresnel normalized XRR curves of the pH-dependent adsorption of apoferritin to DMPC bilayer. The curves are shifted vertically for better visibility. Right: Corresponding electron density profiles.

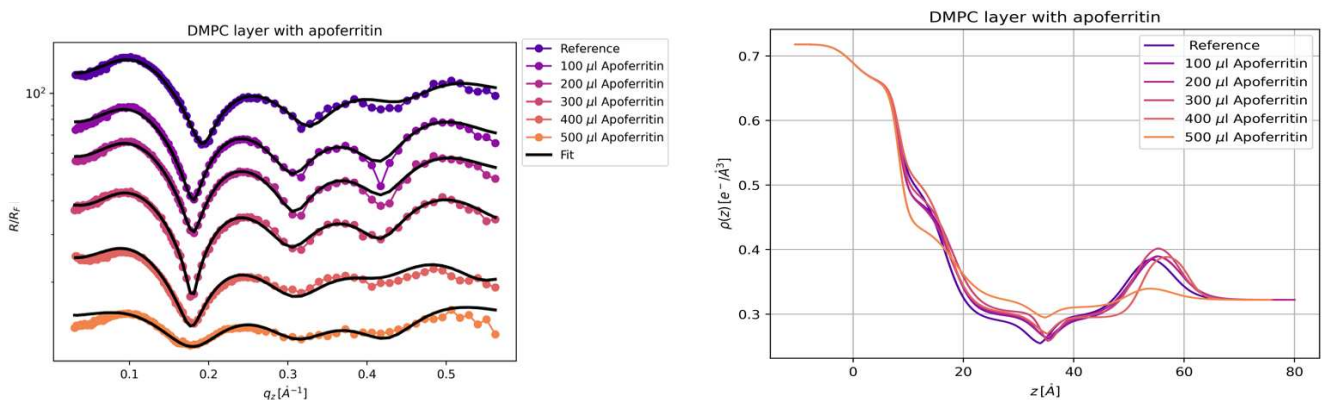


Figure 4: Left: Fresnel normalized XRR curves of concentration-dependent apoferritin (pH 7) measurements at DMPC bilayer. The curves are shifted vertically for better visibility. Right: Electron density profiles.

References

- [1] Werner Mäntele. „Biophysik“. Bd. 1. Ulmer (2012), pp. 56–97; [2] Niels Gregersen and Peter Bross, “Protein misfolding and cellular stress: an overview”, in: *Protein Misfolding and Cellular Stress in Disease and Aging*, Springer (2010), pp. 3–23; [3] Jeffrey J Gray, “The interaction of proteins with solid surfaces”, in: *Current opinion in structural biology* 14.1 (2004), pp. 110–115; [4] Radhakrishnan Narayanaswamy, “Apoferritin-based nanoparticles as imaging agents”, in: *Basics to different imaging techniques, different nanobiomaterials for image enhancement* (2016), pp.107; [5] Zbynek Heger, “Apoferritin applications in nanomedicine”, in: *Nanomedicine* Vol. 9, No.14, (2014), pp.2233-2245; [6] F.J. Wirkert et al., „X-ray reflectivity measurements of liquid/solid interfaces under high hydrostatic pressure“, in: *Journal of Synchrotron Radiation* 21, 76 (2014) [7] Michael Paulus et al., “An access to buried interfaces: the X-ray reflectivity set-up of BL9 at DELTA”, in: *Journal of Synchrotron Radiation*, (2007), pp.60-605 [8] U. Mennicke et al., “Preparation of Solid-Supported Lipid Bilayers by Spin-Coating”, in: *Langmuir*, (2002), pp. 8172–8177.

Acknowledgments We thank the DELTA machine group for providing synchrotron radiation.

Adsorption of supercritical fluids on hydrophobic interfaces near the critical point

*Mike Moron, Susanne Dogan, Marc Moron, Nicola Thiering, Michael Paulus, and Julia Nase
Fakultät Physik/DELTA, TU Dortmund, 44221 Dortmund, Germany*

We investigated the pressure- and temperature-dependent adsorption of supercritical carbon dioxide (CO₂) on hydrophobic surfaces. Silicon wafers were hydrophobized by coating with a self-assembled octadecyltrichlorsilane (OTS) monolayer following the procedure by Mezger et al.¹ When the OTS wafer is placed in the sample cell and CO₂ is introduced to the cell volume, a thin adsorption layer forms on the wafer surface. Since the thickness of the adsorbed layer is on the atomic scale, we performed X-ray reflectivity (XRR) experiments with a photon energy of 27 keV at the beamline BL9 of the DELTA synchrotron radiation source. With the XRR technique, we obtain direct insight into the vertical electron density profiles of the substrate and the adsorbed CO₂-layers.

CO₂ has its critical point at a pressure of $p_{\text{crit}} = 74$ bar and at a temperature of $T_{\text{crit}} = 31$ °C. The maximum gas pressure in the gas cylinder is approx. 57 bar, so that it is not possible to exceed the critical pressure without heating the gas in the sample cell under isochoric conditions. Hence, a new sample cell was developed that enables to reach temperatures of up to 500 °C at a maximum pressure of 1000 bar. The OTS wafer is placed inside the sample cell in a custom-built holder. The X-ray beam passes through a sapphire window with a thickness of $d = 7.5$ mm, is reflected by the sample and then passes the exit sapphire window of the same thickness. The reflected beam is detected by a Pilatus 100k detector. A thermocouple measures the temperature directly in the sample volume. It is connected to a temperature controller (Eurotherm 3508), which regulates the heating power of the heating cartridges. The pressure is monitored via a Keller LEO3 pressure sensor.

We recorded reflectivity curves for pressure/temperature series at pressures between 1 bar and 78 bar and temperatures between 24 °C and 200 °C for CO₂. One of the pressure/temperature series with CO₂ will be discussed exemplarily in this report. We first performed a reference measurement of the OTS wafer with air in the sample cell. Then, the sample cell is flushed with CO₂ and a reflectivity is recorded at 1 bar gas pressure. After that, the gas pressure in the sample cell is increased up to the maximum pressure of the gas bottle and a measurement is taken. The sample cell is shut off with a valve and reflectivities are recorded at higher temperatures. The recorded reflectivity curves for CO₂ at different pressures are presented in Figure 1 (left).

With increasing pressure, the reflectivities show a shift of the first minimum in the direction of smaller wave vector transfers q_z , which indicates an increased adsorption of CO₂ molecules on the surface. The minimum shifts back to higher q_z in the supercritical regime, pointing towards desorption of CO₂. In Figure 1 (right) the corresponding electron density profiles are shown, with the covalently bonded OTS molecules on top of the silicon substrate. Next to the hydrocarbon chains of the OTS molecules, a CO₂ layer is adsorbed. Its density and thickness are increasing with increasing pressure and temperature in the subcritical regime. In the supercritical regime, no additional layer for CO₂ adsorption is needed any more but a significant increase in the electron density of the OTS layer is observed. In addition, the roughness of the layer increases significantly, which can be explained by a very thin, rough adsorption layer. Thus, it is assumed

that during the transition to the supercritical regime, a part of the CO₂ molecules penetrates into the OTS layer, while only a few molecules accumulate above the layer.

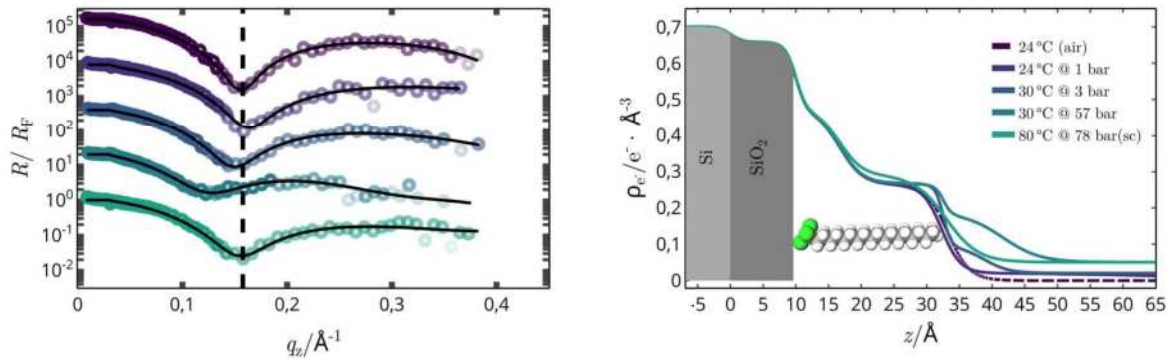


Figure 1: Left: Reflectivity curves for the pressure/temperature series with CO₂ (colors of the circles correspond to the legend on the right). The solid black lines represent the fits. The curves are shifted vertically for clarity. The dashed vertical line marks the first minimum of the ambient measurement and serves as guide to the eye. Right: Electron density profiles calculated from the reflectivity curves. The adsorbed CO₂ layer can be seen on top of the OTS molecules.

Acknowledgements: This work is supported by the Federal Ministry of Education and Research (BMBF project number: 05K19PEA). We also acknowledge the Delta machine group for providing synchrotron radiation and technical support.

References:

- 1 Mezger, M. et al. High-Resolution in Situ X-Ray Study of the Hydrophobic Gap at the Water: Octadecyl-Trichlorosilane Interface. Proc. Natl. Acad. Sci. U. S. A. 2006, 103 (49), 18401–18404.

A small- and wide-angle x-ray scattering study on morphology changes in a polyurethane shape memory polymer

Yucen Shen¹, Klaus Neuking¹, Gunther Eggeler¹, Michael Paulus², Christian Sternemann²

¹ Institut für Werkstoffe, Ruhr-Universität Bochum, 44801 Bochum, Germany

² Fakultät Physik/DELTA, Technische Universität Dortmund, 44221 Dortmund, Germany

Estane ETE 75DT3 (abbreviation: Estane), a type of polyether-based polyurethane, can be triggered to recover back by immersing in alcohols to an original or “memorized” shape after it was moderately deformed (programed). The exposure of Estane to ethanol changes the intermolecular hydrogen bond and acts as a plasticizer, resulting in the decrease of the recovery temperature below room temperature. At room temperature, the polymer chains therefore can relax and change back to their original, more randomly coiled state because of the driving entropic forces ^{1,2}.

As a type of polyurethane-copolymer, Estane consists of soft and hard segments, which are not compatible and have different glass transition temperatures. Due to the differences between the two segments, there are mainly two types of regions in Estane, a more amorphous region consisting of soft segments and a region consisting predominantly of dense hard segments ^{3,4}. During diffusion of the alcohol molecules in the polymer, the size of these two regions changes indicating the path of ethanol diffusion, which is closely related to the recovery mechanism. Small-angle X-ray scattering (SAXS) was used to investigate the field size changes. In the process of recovery, wide-angle X-ray scattering (WAXS) can display the chain relaxation.

SAXS and WAXS were performed at beamline BL2 (SAXS, photon energy: 12 keV) and at beamline BL9 (WAXS, photon energy: 27 keV). All the measurements were taken at room temperature. A MAR345 image plate detector was used for data collection at both beamlines. Fit 2D ⁵ was used for further data processing.

SAXS studies were carried to investigate the location of the ethanol in Estane. A series of SMPE samples with gradient ethanol concentrations were prepared. All the obtained 2D images are transferred into corresponding diffraction patterns. As it is shown in Figure 1, the decrease in the q value where the first scattering maximum is found indicates the increase in the size of the regions. With the increase of the ethanol concentration in Estane, the size of both the dense region and amorphous region is increasing. Ethanol diffuses easily into the loosely packed amorphous region, and with the hydrogen bond formation between hard segments and ethanol, it can also diffuse into the dense region and then realize the actuation.

The WAXS data were used to display the state of the chains throughout the whole shape memory cycle, in which the chains start from the randomly coiled state to oriented, and finally tend to relax back to the initial state. Initially, Estane shows an untextured structure factor because of the randomly coiled state, and a clear orientation dependent pattern after programming. After exposure to ethanol, the oriented chains tend to relax back to their original state, while still with residual orientation. The changes in the pattern exhibit the evolution of the polymer chains in the shape memory cycle and confirm the residual orientation leads to a partial recovery ratio.

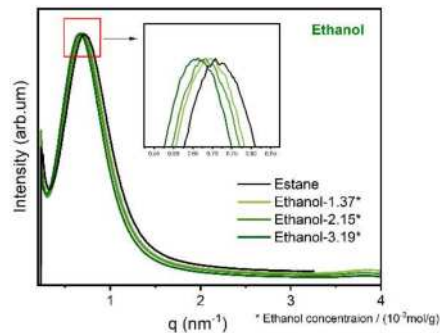


Figure 1 The 1D SAXS curves of Estane and Estane with different ethanol concentrations

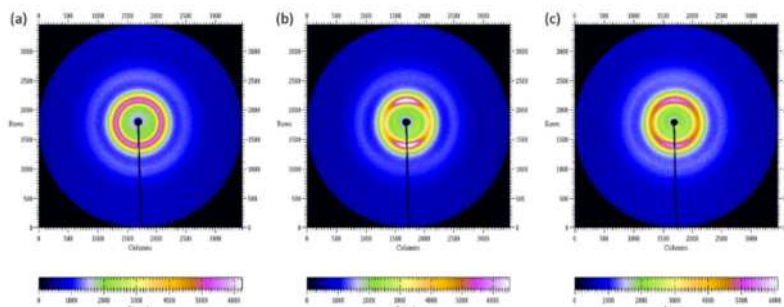


Figure 2 WAXS patterns of (a) initial Estane, (b) stretched Estane, and (c) Estane after recovery in Ethanol

References:

- (1) Dumlu, H.; Marquardt, A.; Zirdehi, E. M.; Varnik, F.; Shen, Y.; Neuking, K.; Eggeler, G. A mechanical analysis of chemically stimulated linear shape memory polymer actuation. *Materials* **2021**, *14* (3), 481.
- (2) Lu, H. B.; Huang, W. M.; Yao, Y. T. Review of chemo-responsive shape change/memory polymers. *Pigment & Resin Technology* **2013**, *42* (4), 237–246.
- (3) Seefried, C. G.; Koleske, J. V.; Critchfield, F. E. Thermoplastic urethane elastomers. I. Effects of soft-segment variations. *J. Appl. Polym. Sci.* **1975**, *19* (9), 2493–2502.
- (4) Seefried Jr, C. G.; Koleske, J. V.; Critchfield, F. E. Thermoplastic urethane elastomers. II. Effects of variations in hard-segment concentration. *Journal of Applied Polymer Science* **1975**, *19* (9), 2503–2513.
- (5) A. P. Hammersley, FIT2D: an introduction and overview. *European synchrotron radiation facility internal report ESRF97HA02T* **1997**, *68*, 58.

Acknowledgements:

We thank the DELTA team for the help during the synchrotron radiation measurements.

Investigation of temperature dependent aggregation dynamics of thermoresponsive polymers

Özgül Öztürk¹, Maximilian Meier², Karla Heckhäuser², Cleiton J.B. Kunzler², Ulrich Jonas², Christian Gutt¹

¹Department of Physics, University of Siegen, Walter-Flex-Str. 3, 57072 Siegen, Germany

²Department of Chemistry, University of Siegen, Adolf-Reichwein-Strasse 2 D-57076 Siegen, Germany

Copolymers are formed with the combination of multiple and chemically distinct monomers into a single chain. Block copolymers merge different types of covalently linked homoblocks, like hydrophilic and hydrophobic blocks, to produce complex ordered structures [1]. These block copolymers could have different phase transition temperatures owing to their chemical composition or assembled structure.

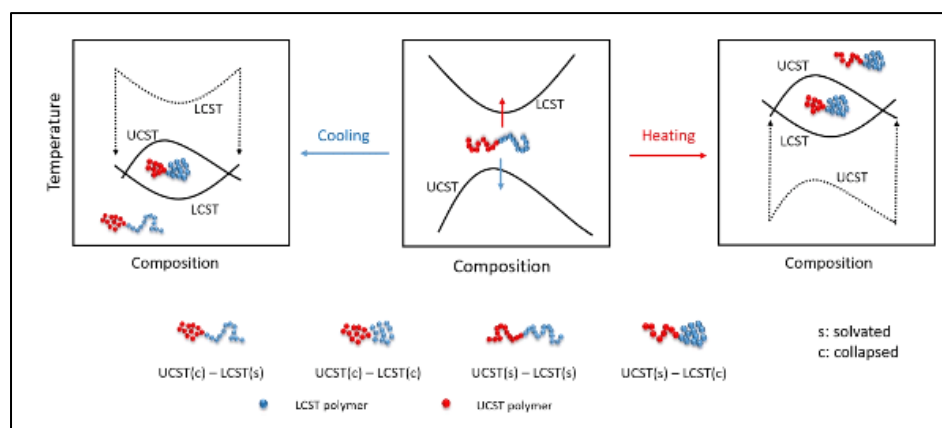


Figure 1 Schematic phase transition diagram caused by critical transition shifts triggered by the solvation of the neighbor block [2]

Because of their sizes, small angle X-ray scattering (SAXS) is ideal for characterizing their behavior with respect to temperature change.

The measurements of this study were done at BL2 in SAXS geometry with an energy of 12keV. Block LCST/UCST copolymers with different

critical solution temperatures (T_c), were inserted in glass capillaries and measured in 2°C steps. The temperature was increased by $0.29^\circ\text{C}/\text{min}$ and each step took 300s. Pure water sample using the same capillary was measured first to use for normalization.

By using the Kratky plot ($q^2I(q)$ vs q), deviations from the high q (scattering vector) behavior of the scattering intensity could be used to identify disordered states and distinguish them from the globular structures. In Figure 2, the Kratky plot for one of the LCST/UCST copolymer block is seen. At low q region a peak could be observed for the temperatures below and around LCST, 20°C . The amplitude of the peak decreases with increasing temperature and vanishes after 30°C . Beyond UCST, 40°C , the peak starts to reappear with a smaller amplitude, and it rises with increasing temperature. This peak indicates micelle like compact structures at large length scales. High q regime which presents negative deviations from a flat behavior demonstrates disordered chains. The decrease of intensity at low q intensity as a result of temperature increase marks that there is no temperature-induced clustering enhancement. The same measurements with the same copolymer block but with different weight percentages were performed and it is confirmed that the general behavior of the sample with respect to temperature change remains the same.

According to Porod, scattering measurements provide information on the mass fractal dimension by determining the exponent that describe the power law decay of the scattering intensity at values of q , that are larger than $1/R$, where R is the physical average radius, but sufficiently small that the particle surface is not being probed. This means the intensity decays as [3]

$$I(q) \propto \frac{c}{q^b}$$

where c is a constant and b is the mass fractal dimension. The value of b depends on whether the polymer is globule or swollen or has an ideal chain conformation [4].

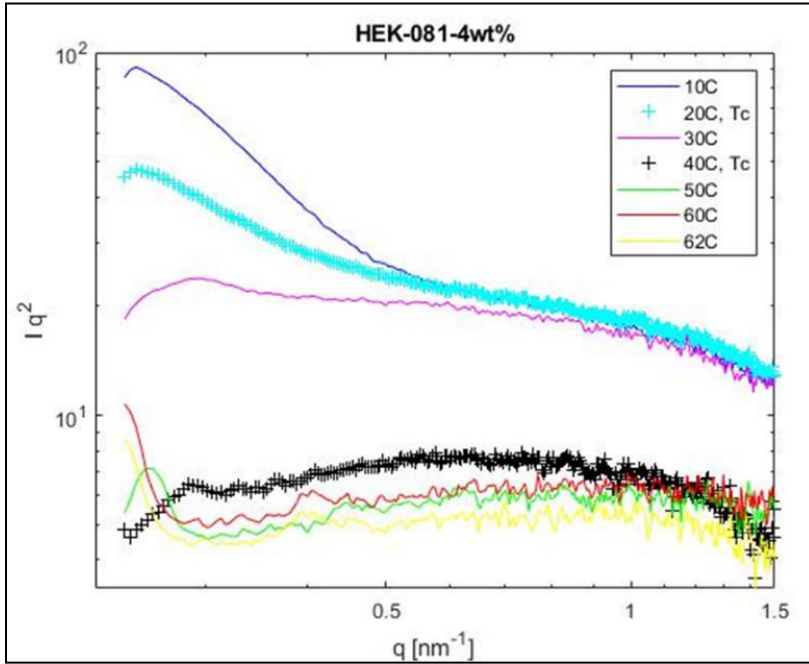
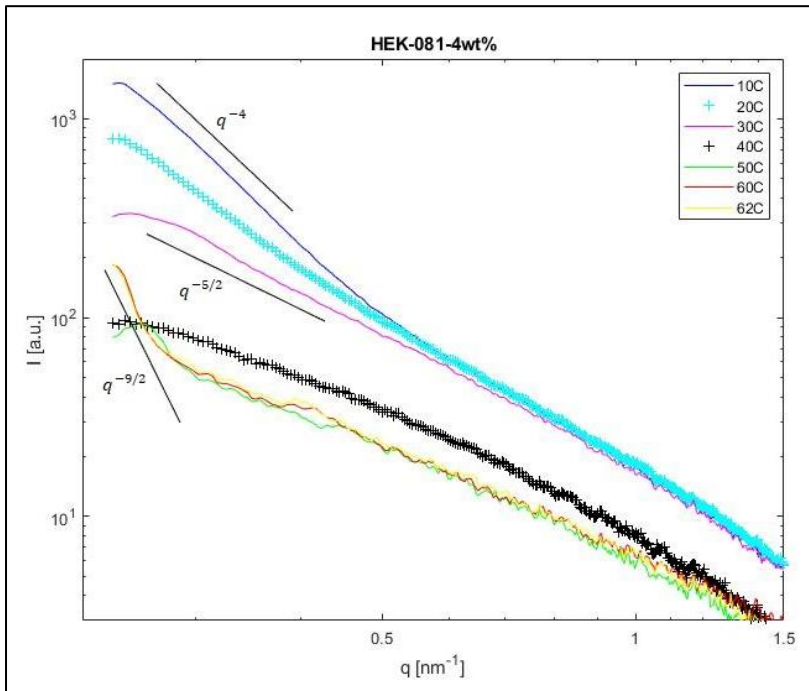


Figure 2 Kratky plot for a LCST/UCST copolymer block at different temperatures. For this sample LCST is 20°C and UCST is 40°C.



The Porod plots of the sample shown in Figure 3 has different b values in low q region as a function of temperature. For the temperatures below LCST, a power-law ($\sim q^{-4}$) dominates the scattering, which is a characteristic of collapsed structures with sharp interfaces. At 30°C b is found to be $-5/2$. At higher temperatures, another power law ($\sim q^{-2}$) is observed, which is attributed to an ideal chain conformation like partially folded proteins. After the UCST transition, b starts to increase again and reaches $-9/2$, indicating a more compact conformation. This behavior is in agreement with Figure 1 where the phase transition of such a coblock polymer is described.

This study provided a chance to further understand the thermoresponsive behavior of the phase transitions of LCST/UCST copolymer blocks.

Figure 3 Porod plot of the LCST/UCST copolymer block with the q dependence of the curves in the low q region.

References:

1. X. Zhou et.al, *J. Phys. Chem. B* 111, 5111–5115 (2007).
2. C. J. B. Kunzler, *PhD Thesis*, Universität Siegen, 2019.
3. G. Pizzorusso et.al., *Langmuir*, 28,3952-3961, 2012.
4. Y. Wie and M.J. A. Hore, *Journal of Appl. Phys.*, 129, 171101, 2021.

Probing chain alignment in polymer electrolytes upon ion transport in electric fields using *operando* 2D wide angle X-ray scattering

A. Kuhlmann¹, M. Huck¹, H.-G. Steinrück¹, C. Mönich², A. Hockmann², M. Schönhoff², C. Sternemann³

¹ Department Chemie, Universität Paderborn, 33098 Paderborn, Germany

² Institut für Physikalische Chemie, WWU Münster, 48149 Münster, Germany

³ Fakultät Physik/DELTA, Technische Universität Dortmund, 44227 Dortmund, Germany

Polymeric electrolytes for batteries are a safe alternative to commonly used flammable liquid organic electrolytes [1]. In order to develop well-performing electrolytes, it is crucial to understand the underlying ion and mass transport which is directly linked to the local structural properties of the electrolyte. Even though binary mixtures of poly(ethylene oxide) (PEO) and lithium bis(trifluoromethanesulfonyl) imide (LiTFSI) are well studied, there are disagreements of the exact transport parameters [2]. Drastic conductivity enhancements were found in mechanically stretched PEO-based electrolytes [3] and helical coordination arrangements of oligoether segments are considered relevant [4]. Furthermore, indications towards field-induced chain alignment have been found indirectly via electrophoretic NMR measurements [2].

The purpose of the performed experiments was to either support or debilitate the hypothesis that polymer chains orient in the electric field and/or align sterically-imposed under ion flux [5]. Here, electrolytes consisting of PEO with a molecular weight of 4000 g/mol (approx. 90 EO monomers), 600000 g/mol (approx. 13619 EO monomers) or 222 g/mol (approx. 4 EO monomers) and a lithium salt, being either LiTFSI (“large” anion) or LiClO₄ (“small” anion) with concentrations of $r = 0.1$ (Li⁺ to EO ratio) were prepared. The electrolyte with the smallest molecular weight serves as a negative control, since here no chain alignment is expected. We utilized *operando* 2D wide angle X-ray scattering (WAXS) at beamline BL9 of the DELTA synchrotron radiation source to test our hypothesis. A PEEK-based hermetically sealed Li|PEO|Li symmetric electrochemical cell was kept at 90 °C and a voltage of 0.25 or 0.5 V vs. Li/Li⁺ was applied. Diffraction data was collected by a MAR345 image plate detector with a beam energy of 27 keV.

The diffraction pattern of a sample with LiTFSI in 4000 g/mol PEO is shown in fig. 1. The peak in the region of 0.8-1.2 Å⁻¹ (peak 0) corresponds to interaction between neighboring TFSI⁻ anions while the peak between 1.2-1.7 Å⁻¹ (peak 1) (superposed by the three sharp peaks from the PEEK cell) corresponds to correlations between EO segments, and to short-range correlation between PEO and TFSI [6]. To investigate changes in the orientation of polymer chains, analysis of time-dependent changes during polarization is shown in fig. 2. A potential of 0.5 V was applied to the sample for 9 h and diffraction patterns were recorded every 5 min. A change of orientation is expected to be seen by evolution of two peaks separated by 180°

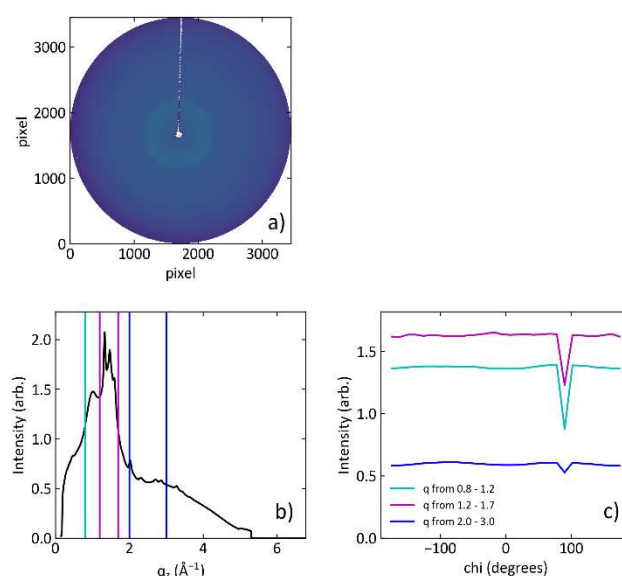


Fig. 1: Diffraction pattern of a sample consisting of LiTFSI in 4000 g/mol PEO. The beam energy was 27 keV. a) detector image; b) Intensity plot vs. q_z by integrating detector image from a); c) Signal intensity along the azimuthal angle for the q_z ranges marked in b). The mount of the beamstop causes the dip observed at 90°.

along the azimuthal angle in the regions of peak 0 and peak 1. Therefore, the change in intensity is plotted against the azimuthal angle for both peak regions. Around $\chi=0^\circ$, the results hint at the reduction of intensity for peak 0 and an increase in intensity for peak 1, but no clear evidence of an orientation of polymer chains could be observed.

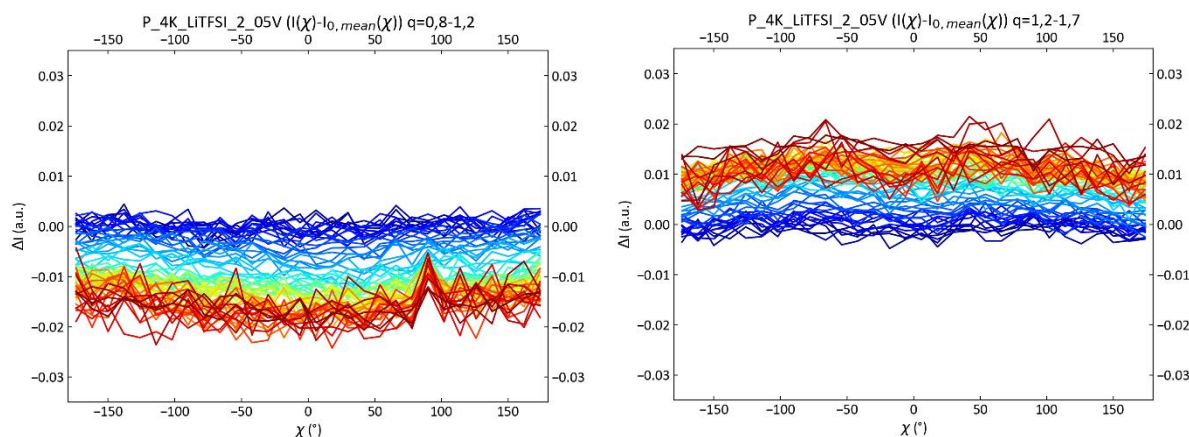


Fig. 2: Investigation of change in intensity along the azimuthal angle between $0.8\text{-}1.2 \text{ \AA}^{-1}$ (peak 0, left) and $1.2\text{-}1.7 \text{ \AA}^{-1}$ (peak 1, right). The first measurement is blue and the last one red. The interval for recording the patterns was 5 min.

If the beam is not in the center of the sample, a concentration gradient could be observed which shadows the investigation of orientation. This is tested by plotting the intensity versus q and subtract the intensity of the diffraction pattern before polarization. The result of two cells for selected times in the measurement during polarization and additional relaxation after polarization is shown in fig. 3. During polarization, an increase in intensity for peak 0 and a decrease in intensity of peak 1 are observed for cell 1 (LiTFSI in 4000 g/mol PEO). The opposite occurred for cell 2 with the same cell composition as cell 1. This means that the beam position with respect to the center of the cell is slightly shifted in different direction during measurement of both cells. After relaxation, this change was not reversed. Naturally, the relaxation takes a much longer time, but it is also possible that these changes are not based on concentration gradients and instead irreversible. More in-depth analysis towards testing our hypothesis is ongoing.

References

- [1] Hallinan *et al.*, MRS Bulletin **43**, 759 (2018).
- [2] Rosenwinkel, Schönhoff, JES **166**, A1977 (2019).
- [3] Golodnitsky *et al.*, Macromol. Symp. **203**, 27 (2003).
- [4] Golodnitsky *et al.*, JES **162**, A2551 (2015).
- [5] Wang, Lei, J. Polym. Sci. B **50**, 656 (2012).
- [6] Loo *et al.*, Macromolecules **54**, 6639 (2021).

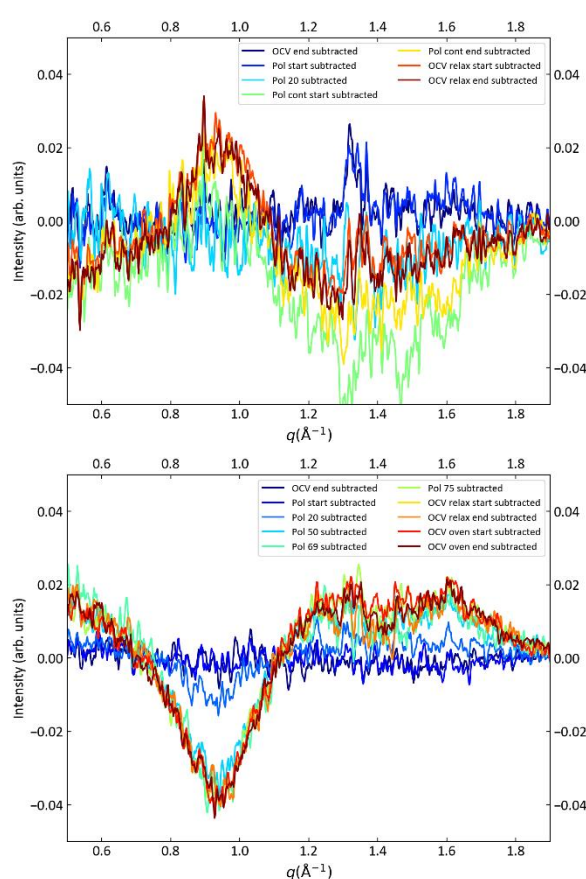


Fig. 3: Differential intensity of selected diffraction patterns during polarization with 0.5 V and relaxation of the cell 1 (top) and cell 2 (bottom). Subtraction is done with the initial state of the cell before polarization.

Effect of TEACl treatment on the surface structure of perovskite

Xin Zhang,^{#,§} Weiming Qiu,[#] and Christian Sternemann^{*}

[#]imec, Kapeldreef 75, 3001, Leuven, Belgium

^{*}Fakultät Physik/DELTA, TU Dortmund University, 44221 Dortmund, Germany

[§]Email: iamxinzhang@hotmail.com

The inverted p-i-n perovskite solar cells (PSCs) are promising candidates for upscaling towards commercialization. However, the interfaces between the perovskite and the charge transport layers contribute to major power conversion efficiency (PCE) loss and instability in these devices. For instance, the upper perovskite interface with the electron transport layer (ETL) has generally been neglected due to that the fullerene ETL is expected to passivate the perovskite surface defects.^{1,2} However, it has been revealed that only weak interactions are created between fullerene derivatives and perovskite.³ In addition, a flawed contact between the perovskite surface and C₆₀ molecules may induce deep-level defects, thus hindering the device performance.^{4,5} Therefore, modifying the perovskite upper interface is critically important. Recently it has been shown that by constructing heterojunctions or functionalizing the upper interface with organometallic compounds, both device efficiency and operational stability can be significantly improved.^{3,6,7}

In this study, we use 2-thiopheneethylammonium chloride (TEACl) to molecularly engineer the upper interface between perovskite and fullerene-C₆₀ electron transport layer (ETL), denoted as Upper in the following text. Based on the Upper condition, we also use TEACl to engineer the buried interface between perovskite and NiO_x based hole transport layer (HTL), denoted as Dual in the following text. From the scanning electron microscopy (SEM) as shown in **Figure 1a**, all the samples show a compact morphology with grain sizes ranging from hundreds of nanometers to a few microns. However, in the Upper and Dual samples, tiny flake-like structures appear on the perovskite grain surface. This is verified by AFM images as shown in **Figure 1b**, while from the AFM images acquired in tapping mode, it is evidenced that these structures spread over the entire surface of the film (**Figure 1c**). With the TEACl treatment, the root mean square (RMS) roughness (R_q) of the films is reduced by 2-3 nm.

In order to understand the impact of the TEACl surface treatment on the surface crystal structure of perovskite, we performed grazing incidence wide-angle X-ray scattering (GIWAXS) at beamline BL9 of the DELTA synchrotron radiation source.⁸ The incident energy was set to 15 keV and a beam size of $1.0 \times 0.05 \text{ mm}^2$ was used. The diffraction images were measured in grazing incidence geometry utilizing a MAR345 image plate detector. GIWAXS pattern of the samples were taken at two different angles of incidence, i.e., 1.0° and 0.15°. Before the measurement, the samples were stored under nitrogen flow in a desiccator. LaB₆ served as the calibration standard. The main results of the GIWAXS measurements are given in Figure 1. **Figure 2a** presents the 2D GIWAXS patterns of the corresponding films at 0.15°

angle of incidence, and the extracted out-of-plane diffraction profiles are given in **Figure 2b**. All the films exhibit the same diffraction ring positions at around 1 \AA^{-1} and 2 \AA^{-1} . However, when zoomed-in at around 0.9 \AA^{-1} , an additional peak located close to the perovskite main peak appears for the TEACl-treated films, which should be assigned to the tiny flake-like structures observed by SEM and AFM measurements (**Figure 1**). These structures are found to be ultrathin on the perovskite surface, as there is no difference between the spectra when the higher incident angle of 1.0° is used (**Figure 2c**). The analysis of these structures is still in progress.

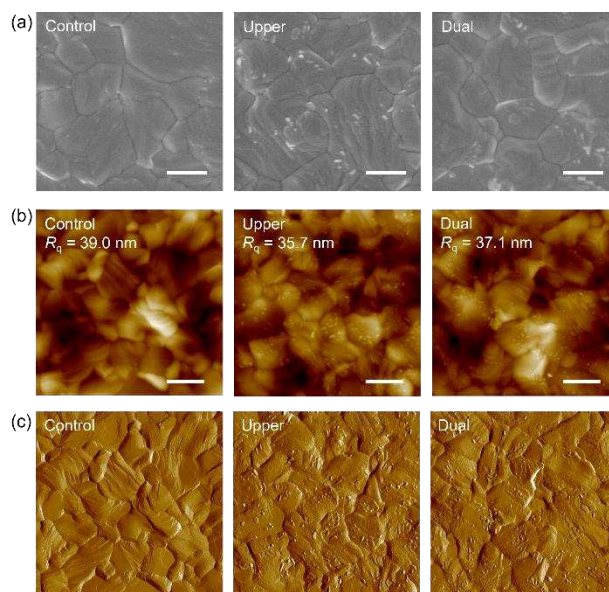


Figure 1. (a) Top-view SEM images with scale bars of 500 nm. (b) AFM topography images with scale bars of $1 \mu\text{m}$. (c) The AFM images acquired in tapping amplitude mode for the perovskite films based on different conditions. The imaged area is $5 \mu\text{m} \times 5 \mu\text{m}$ in all the three cases.

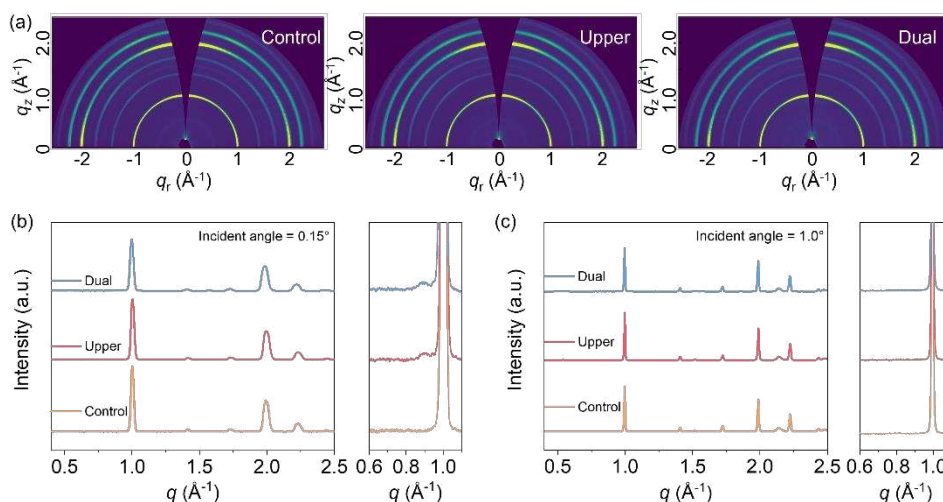


Figure 2. (a) 2D GIWAXS patterns of the perovskite films under different interface treatment conditions. The extracted out-of-plane profiles with an incident angle of (b) 0.15° , and (c) 1.0° . A zoomed-in view in the range of $0.6 \text{ \AA}^{-1} - 1.1 \text{ \AA}^{-1}$ is also shown on the right for each incident angle. The y-axis scale for the two zoomed-in graphs is the same.

Acknowledgements:

We acknowledge DELTA for providing synchrotron radiation at beamline BL9 and thank Hans-Georg Steinrück and Michael Paulus for fruitful discussions.

References:

1. Shao, Y., Xiao, Z., Bi, C., Yuan, Y. & Huang, J. Origin and elimination of photocurrent hysteresis by fullerene passivation in CH₃NH₃PbI₃ planar heterojunction solar cells. *Nat. Commun.* **5**, 5784 (2014).
2. Zhong, Y., Hufnagel, M., Thelakkat, M., Li, C. & Huettnner, S. Role of PCBM in the Suppression of Hysteresis in Perovskite Solar Cells. *Adv. Funct. Mater.* **30**, 1908920 (2020).
3. Azmi, R. *et al.* Damp heat-stable perovskite solar cells with tailored-dimensionality 2D/3D heterojunctions. *Science* **376**, 73–77 (2022).
4. Warby, J. *et al.* Understanding Performance Limiting Interfacial Recombination in pin Perovskite Solar Cells. *Adv. Energy Mater.* **12**, 2103567 (2022).
5. Chen, H. *et al.* Regulating surface potential maximizes voltage in all-perovskite tandems. *Nature* (2022) doi:10.1038/s41586-022-05541-z.
6. Li, X. *et al.* Constructing heterojunctions by surface sulfidation for efficient inverted perovskite solar cells. *Science* **375**, 434–437 (2022).
7. Li, Z. *et al.* Organometallic-functionalized interfaces for highly efficient inverted perovskite solar cells. *Science* **376**, 416–420 (2022).
8. Krywka, C. *et al.* The small-angle and wide-angle X-ray scattering set-up at beamline BL9 of DELTA. *J. Synchrotron Radiat.* **14**, 244–251 (2007).

Real-time investigation of phase transformations of MOF nanoparticles in responsive porous liquids

Athanasios Koutsianos, Sebastian Henke*

Anorganische Materialchemie – TU Dortmund, Otto-Hahn-Str. 6, 44227 Dortmund

Scientific Context

Porous liquids (PLs) have recently caught the attention of researchers owing to their unique combination of porosity and fluidity.¹ The incorporation of intrinsic porosity or cavities in a liquid can result in free-flowing materials that are capable of gas uptake that is significantly higher than the gas solubility of conventional (i.e. non-porous) liquids. Thus, PLs are extensively studied for their potential application in gas separations. Following this logic, we recently synthesised PLs based on responsive metal-organic frameworks (MOF) nanoparticles. The responsive MOFs display sigmoidal gas sorption isotherms triggered by discrete gas pressure-induced structural transformations (so called gate-opening) and hence feature higher working capacities in similar pressure swings. We envisaged that the incorporation of such kind of responsive MOF nanocrystals in a size excluded solvent could afford the formulation of responsive PLs exhibiting sigmoidal isotherms and hence unprecedented gas sorption properties.

A dispersion of nanocrystals of the canonical responsive ZIF-7 ($\text{Zn}(\text{bim})_2$; $\text{bim}^- = \text{benzimidazolates}$)² in a low vapour pressure silicone oil has indeed resulted in a liquid system featuring a sigmoidal shape isotherm during CO_2 sorption.³ ZIF-7 is known to transform from a narrow pore (*np*) phase to a large pore (*lp*) phase upon CO_2 sorption at ambient temperature, while N_2 is barely adsorbed and does not trigger the phase transformation.⁴ Collection of X-ray diffraction (XRD) data of the ZIF-7-included PLs *in situ* during gas uptake/release, previously allowed us to monitor structural changes of the MOF nanoparticles upon gas sorption in fluid suspension and experimentally prove that ZIF nanocrystals retain their flexible nature while being dispersed.³ With the aim to extract important information on the rate of the structural transformation of the MOF nanoparticles and how the rate depends on the flow rate of the gas, we performed a dedicated XRD experiment with the fast PILATUS 100k area detector allowing to collect XRD patterns every 5 seconds.

Experimental procedure

The ZIF-7 based PL was prepared by dispersing ZIF-7 nanoparticles (size about 100 nm) in silicone oil 704 to generate a nanoparticle suspension containing 10 wt% ZIF-7. An aliquot of the activated PL (ca. 1.5 mL) was loaded in a Schlenk finger tube (diameter approx. 1 cm). The sample was mounted in the centre of the goniometer of BL 9. The Schlenk tube was sealed with a septum and the tube's sidearm served as the gas outlet. The gas was bubbled through the PL via a needle pierced through the septum and connected to tubing. The tubing was connected to a three-way ball valve to switch between sorption gas (CO_2) and purge gas (N_2), while collecting diffraction patterns with a monochromatic X-ray beam ($\lambda = 0.459 \text{ \AA}$) using a PILATUS 100k detector. A gas flowmeter was connected before the Schlenk tube to regulate the flowrate (Figure 1). XRD patterns were

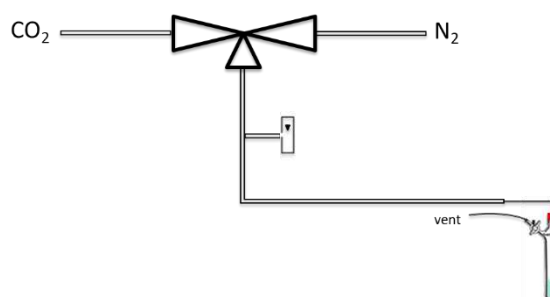


Figure 1. Schematic of the experimental setup used for the *in situ* XRD experiments during gas sorption by PLs containing ZIF-7 nanocrystals.

collected every 5 seconds. In order to increase the signal-to-noise ratio of the rather noisy diffraction patterns, six sequentially recorded patterns were merged, so that the final time resolution of the experiment was 30 seconds.

Results

At first, we collected a XRD pattern for the activated ZIF-7-based PL under ambient conditions. Despite the strong contributions of the solvent and the glass tube to the pattern, broad peaks assignable to the *np* phase of the ZIF nanoparticles are observable (Figure 2a, black line). Exposure of the PL to CO₂ followed by gas uptake, results in the structural transformation of the ZIF-7 nanoparticles from the *np* phase to the more crystalline *lp* phase, as manifested by the alterations in the obtained XRD pattern. Bubbling with N₂ causes CO₂ desorption and the consequent reversal to the *np* phase. Three different CO₂ and N₂ flowrates were tested, namely 0.5, 1.0 and 1.5 NL min⁻¹ (normal litre per minute, NLPM; 1 NLPM \approx 0.7773 mmol s⁻¹ for an ideal gas). It appears that the higher flowrate promotes a faster phase transition, with the time evolution of the pattern under 1.5 NL min⁻¹ (Figure 2e) being clearly faster than that of 0.5 NL min⁻¹ (Figure 2a), demonstrating quicker CO₂ sorption kinetics in the former. Interestingly, the effect of the N₂ gas flowrate on the kinetics of desorption of CO₂ from the PL appears to be much less pronounced.

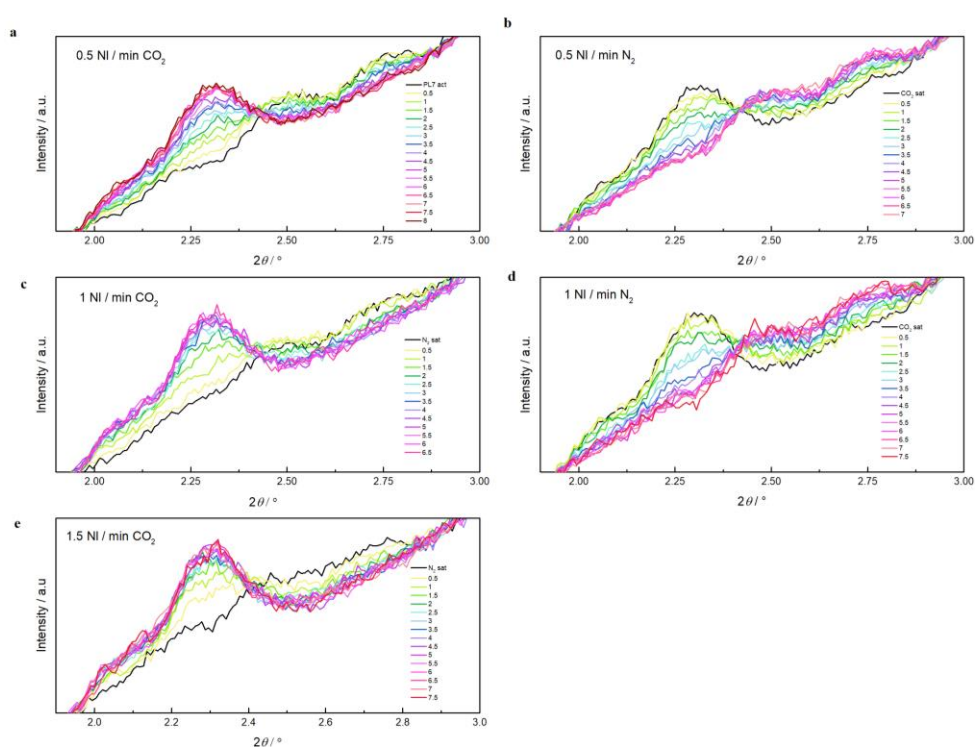


Figure 2. Time-resolved *in situ* XRD patterns during gas uptake by the ZIF-7-containing PL. Each pattern was obtained by merging six individual patterns, each collected with an exposure time of 5 seconds, giving a time resolution of 30 seconds.

The specific experiment conducted at BL9 allowed us to verify that the observed step in the gas sorption isotherm is driven by the structural transition of the porous ZIF constituent, as it was conceived during the conceptualization of the responsive PLs. Most importantly, we were able to obtain meaningful information on the rate of ZIF nanoparticles structural transformation

which are necessary for the use of PLs as breakthrough materials for actual high-throughput separation processes. We are currently working on a more detailed data analysis and hope that we can extract flowrate-dependent rate constants for the phase transformation of the ZIF-7 nanocrystals in the PL, by integration of the Bragg peaks and fitting the integrated intensities against a suitable rate law equation.

The authors gratefully thank the DELTA team and the beamline scientists of BL9, Dr. C. Sternemann and Dr. M. Paulus, for their outstanding support during the experiments.

References

1. Giri N, Del Pópolo MG, Melaugh G, Greenaway RL, Rätzke K, Koschine T, *et al.* Liquids with permanent porosity. *Nature* 2015, **527**(7577): 216-220.
2. Park KS, Ni Z, Côté AP, Choi JY, Huang R, Uribe-Romo FJ, *et al.* Exceptional chemical and thermal stability of zeolitic imidazolate frameworks. *Proceedings of the National Academy of Sciences* 2006, **103**(27): 10186-10191.
3. Koutsianos A, Pallach R, Frenzel-Beyme L, Das C, Paulus M, Sternemann C, Henke S. Breathing porous liquids based on responsive metal-organic framework particles. *ChemRxiv* 2022. This content is a preprint and has not been peer-reviewed
4. Du Y, Wooler B, Nines M, Kortunov P, Paur CS, Zengel J, *et al.* New High- and Low-Temperature Phase Changes of ZIF-7: Elucidation and Prediction of the Thermodynamics of Transitions. *Journal of the American Chemical Society* 2015, **137**(42): 13603-13611.

Photoswitching vesicles containing phospholipids and photo-sensitive azobenzene-glycolipids

Svenja Hövelmann^{1,2,3}, Rajendra Giri¹, Ella Dieball¹, Michael Paulus⁴, Bridget Murphy^{1,3}

¹Institute für experimentelle und angewandte Physik, Kiel University, Leibnizstr. 19, D-24118 Kiel, Germany,

²Deutsches Elektronen-Synchrotron DESY, Notkestraße 85, D-22607 Hamburg, Germany,

³Ruprecht Haensel Laboratory, Kiel University, D-24118 Kiel, Germany,

⁴Zentrum für Synchrotronstrahlung, Technische Universität Dortmund, Maria-Goeppert-Mayer-Str. 2, D-44227 Dortmund, Deutschland

Experimental Report

1) Actual experiment

The aim of this experiment was to investigate the effect of photoswitchable azobenzene glycoconjugates (AZ) on the structure of phospholipid vesicles composed of dipalmitoyl phosphatidylcholine (DPPC). The small angle x-ray scattering (SAXS) measurements were carried out at BL2 (DELTA) at a photon energy of 12 keV using a MAR345 detector in a q -range between 0.25 and 3.10 nm⁻¹ in the transmission geometry from glass capillary. The vesicles were prepared freshly before each measurement by adding a buffer solution (ph 7) to the dried films of the binary mixture of DPPC and AZ. The black curve in the Figure 1 represents the SAXS data from pristine DPPC vesicles which shows the first, second and third order diffraction peaks corresponding to the head-to-head distance or the membrane thickness of 6.32 nm which corroborates the reported values [1] for the well hydrated DPPC bilayer. An illumination device capable of providing visible ($\lambda = 455$ nm) and UV ($\lambda = 365$ nm) light was used to switch the azobenzene glycoconjugates between their *trans* and *cis* conformations *ex-situ*. For the *trans* conformation a lamellar structure with a membrane thickness of ~ 6.5 nm is found. Upon switching to the *cis* conformation, the lipid mesophase structure evolves to a more cubic-like phase. This is evident from the peak shift and additional peaks around the (100) reflection in the representative SAXS pattern (Figure 1) from 10% azobenzene-lipid (AZOL) containing DPPC vesicles. Though a significant reversible switching effect was noticeable at room temperature, it was not observed at any temperatures higher than 37°C. Repetitive and alternative UV and blue illuminations showed a reversible structural change in mixed vesicles of DPPC with 10% AZOL, 20% AZOL and 10% azobenzene molecule (AZ-67). Five different ratios of 10%, 20%, 50%, 70%, 100% were chosen for the mixture of DPPC and AZOL. Further nine different AZ molecules with alteration on the number of sugar groups (0, 1 and 2) in the head group, on the tail length (12 and 16 carbon atoms) and on the azobenzene-switch between the tail and head group were embedded into the DPPC vesicles at individual ratios.

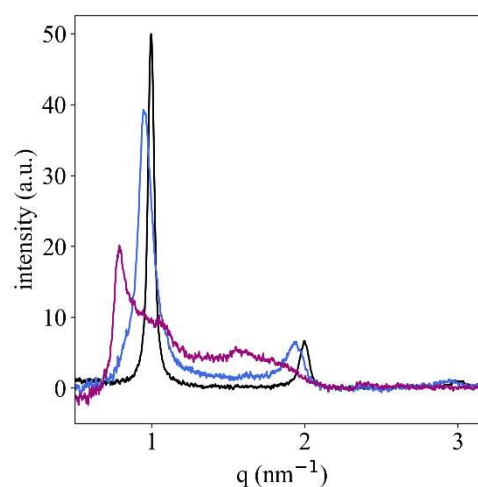


Figure 1 Data from the vesicles of pristine DPPC (black) and the binary mixture of DPPC and 10% AZOL in the *trans* state (blue) and *cis* state (purple) at room temperature.

2) Experimental equipment

During the beamtime two different sample setups were used.

The Lincolm stage was used as a sample holder for the temperature-controlled measurements in the range between 17 and 45°C.

For the measurements at room temperature, the Lincolm stage was replaced by a simpler sample holder to allow *in-situ* illumination followed by measurements. Our illumination device was mounted above the sample to allow direct illumination.

3) Achievement of aims

With SAXS, we successfully observed photoinduced reversible changes in the structure of binary mixed vesicles consisting of DPPC and photoswitchable glycoconjugates at different ratios. The reproducible structural changes were found for a ratio of 10% and 20% AZOL and 10% AZ-67. From mixtures with the same ratio of 10% but alteration on the number of sugar groups in the head group (1 and 2) we did not observe a photoinduced structural change. Also, with an increase of the ratio to 50% or 70% AZOL the switching effect was not visible. Although a detailed analysis is in progress, the initial stage of the analysis suggests for the 10% and 20% AZOL mixtures in the *trans* state a lamellar vesicle structure. This lamellar structure changes to a cubic-like ordering for the *cis* state upon UV irradiation. However, the exact structure of the vesicle containing *cis*-state AZs is yet to be understood and needs further analysis.

The analysis further suggests that at lower concentrations of AZs, the vesicle retains the typical lamellar structure of DPPC. Whereas at AZ concentrations higher than 50%, it shows a cubic structure similar to that observed in the *cis* state and does not show any switching effect. Further analysis is required to understand the switching behaviour at the molecular level.

[1] Kornmueller, K., Lehofer, B., Leitinger, G., Amenitsch, H., Prassl, R., (2018), Nano research **11**, 913-928. DOI: 10.1007/s12274-017-1702-4.

Insights into high-pressure and temperature induced phase transitions of fatty core packing in low-density lipoproteins

Susanne Dogan-Surmeier^{*a}, Michael Paulus^a, Nimmi Das A^{b,c,d}, and Christian Gutt^c

^aFakultät Physik/DELTA, Technische Universität Dortmund, Dortmund, Germany

^bDeutsches Elektronen-Synchrotron DESY, Notkestraße 85, Hamburg, 22607, Germany

^cDepartment Physik, University of Siegen, Siegen, 57072, Germany

^{*}corresponding author: susanne.dogan@tu-dortmund.de

Low-density lipoproteins (LDL) are the natural and major lipid transporters in the plasma that contribute to the progression of atherosclerosis and cardiovascular diseases, which are responsible for the vast majority of death in western civilizations¹. These lipoproteins are complex biological assemblies of lipids (free cholesterol (FC), cholesteryl esters (CE), triglycerides (TG) and phospholipids (PL)) and one copy of apolipoprotein B100 (>95 % of the protein proportion). The protein is attached through a disulfide bond and wraps around the LDL molecule. LDL has a core-shell structure with a particle diameter of around 18 - 25 nm^{2,3}. The hydrophobic core is basically buildup of TGs and CEs, whereas the shell essentially consists of an amphipathic lipid layer with PLs and free cholesterol molecules. A scheme of a LDL molecule and the effect of high hydrostatic pressure and temperature is shown in figure 1.

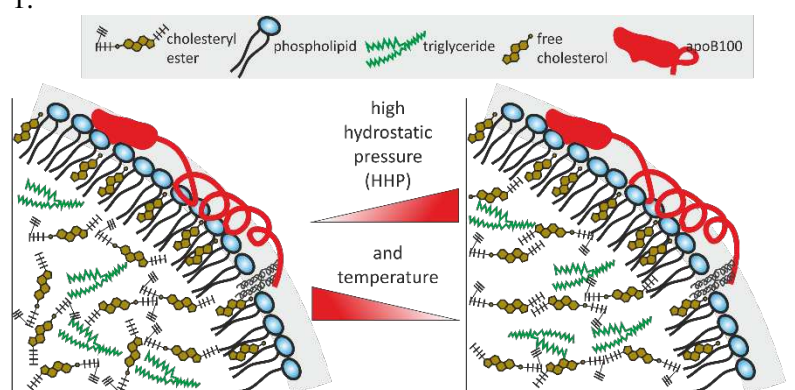


Figure 1: Cross-sectional scheme of LDLs phase transition (*left*: disordered fluid phase and *right*: smectic liquid crystalline state) induced via HHP and low temperatures.

Bad eating habits, overweight, smoking and less physical activities, but also hereditary diseases like familial hypercholesterolemia can lead to high LDL levels in blood. Beside

high plasma LDL levels, these particles are highly sensitive for chemical modulations which are an additional risk for the development of arteriosclerosis, for example the oxidized and small-dense LDL form^{4,5}.

Temperature and high hydrostatic pressure (HHP) can be described as independent thermodynamic parameters which can be applied to control and study the molecular core assembly in LDL particles. The melting of the core structure can be observed *in-situ*. Small-angle X-ray scattering (SAXS) in combination with HHP and temperature modulation can be thus used to investigate interaction processes and lipid arrangements of the lipid core in a non-destructive and non-invasive way.

In this study, we investigated the pressure-induced phase transitions as a function of temperature of human plasma LDL (hp-LDL) and purified and extracted human plasma LDL (ex-hp-LDL) using the SAXS setup at beamline 2 of DELTA⁶. The measurements were performed using the high hydrostatic pressure cell and suitable sample cells described in Krywka et al.⁷. The inner sample cell is equipped with polyimide windows to ensure X-ray penetration and hydrostatic pressure transfer. We used hp-LDL from Aviva systems biology (San Diego, CA, USA; $c = 52.04$ mg/ml) and exhp-LDL from Sigma Aldrich (Darmstadt, Germany; purity > 95% and $c = 200$ mg/ml). The samples were used as they were delivered. To study concentration-dependent effects, hp-LDL was dissolved in water (9:1) and measured at different temperatures under hydrostatic pressure increase. We used an incident energy of 12 keV with a beam size of 0.7×0.7 mm² and a MAR345 image plate detector to collect the diffraction data. The hydrostatic pressure was stepwise increased (0 - 4000 bar in 250 bar steps) and data were collected at constant temperatures (20 - 55°C) which was controlled via a chiller. The temperature series was measured with a Linkam stage and borosilicate capillaries and data were collected between 20 - 70°C.

Figure 2 shows SAXS intensity profiles with increasing temperature of exhp-LDL between 20 - 70°C. The most characteristic feature, a Bragg peak, at a scattering vector $q=1.7 \text{ nm}^{-1}$ is highlighted with a red arrow. This peak corresponds to the ordering of CE layers with a periodicity of about 3.7 nm (typical extension of a CE molecule). With the increase in temperature and crossing T_m ($> 30^\circ\text{C}$) the intensity of the Bragg peak decreased very clearly, indicating a melting of the lipid packing and transition into a more disordered phase. Thus, the core lipids show a thermal phase transition, which is also reported in

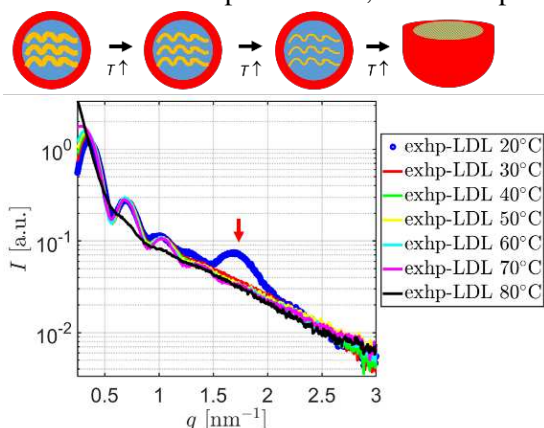


Figure 3: *Bottom*: SAXS data for LDL at different temperatures. The red arrow marks the development of a Bragg peak at $q=1.7 \text{ nm}^{-1}$. *Top*: Scheme of LDL particle structure in a cut-through showing the melting of the CE layers.

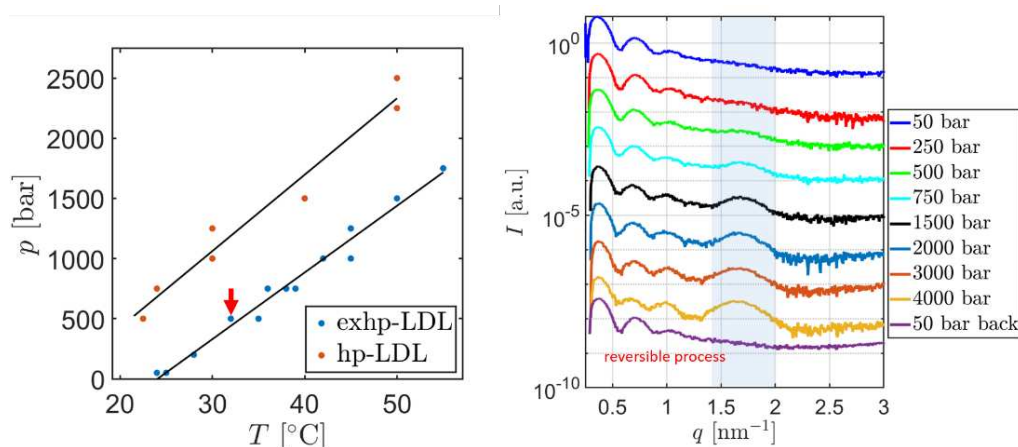


Figure 2: *Left*: Phase- $(T-p)$ -diagram of hp-LDL (red) and exhp-LDL (blue). *Right*: SAXS intensity data for exhp-LDL at 33°C .

residual molecules of human plasma, the exhp-LDL particles are in a pure buffer solution, which in general leads to a significant destabilization of the particles. We hypothesize that these residual molecules possibly enter the core through the osmotic pressure at the lipid membrane, preventing earlier crystallization of the cholesteryl esters, leading to a shift of the phase boundary to higher pressures. With this proposed mechanism, the LDL in natural environment would be protected from crystallization of the cholesterol core. Further analysis of the data is in progress.

References

1. Fra \acute{c} , W., Wojtasińska, A., Lisińska, W., Młynarska, E., Franczyk, B., and Rysz, J. (2022). Pathophysiology of Cardiovascular Diseases: New Insights into Molecular Mechanisms of Atherosclerosis, Arterial Hypertension, and Coronary Artery Disease. *Biomedicines* *10*, 1938. 10.3390/biomedicines10081938.
2. Kaitosaari, T., Rönnemaa, T., Viikari, J., Leino, A., Jokinen, E., and Simell, O. (2006). Low-density lipoprotein (LDL) particle size in healthy prepubertal children: the STRIP study. *Acta Paediatr* *95*, 1668–1673. 10.1080/08035250600746294.
3. Hevojoja, T., Pentikäinen, M.O., Hyvönen, M.T., Kovanen, P.T., and Ala-Korpela, M. (2000). Structure of low density lipoprotein (LDL) particles: Basis for understanding molecular changes in modified LDL. *Biochimica et Biophysica Acta (BBA) - Molecular and Cell Biology of Lipids* *1488*, 189–210. 10.1016/S1388-1981(00)00123-2.
4. Atherogenic Lipoprotein Particles in Atherosclerosis | Circulation <https://www.ahajournals.org/doi/full/10.1161/01.CIR.0000131511.50734.44>.
5. Nichols, M., Townsend, N., Scarborough, P., and Rayner, M. (2014). Cardiovascular disease in Europe 2014: epidemiological update. *European Heart Journal* *35*, 2950–2959. 10.1093/eurheartj/ehu299.
6. Tolan, M., Weis, T., Westphal, C., and Wille, K. (2003). DELTA: Synchrotron light in nordrhein-westfalen.
7. Krywka, C., Sternemann, C., Paulus, M., Tolan, M., Royer, C., and Winter, R. (2008). Effect of Osmolytes on Pressure-Induced Unfolding of Proteins: A High-Pressure SAXS Study. *ChemPhysChem* *9*, 2809–2815.
8. Liu, Y., Luo, D., and Atkinson, D. (2011). Human LDL core cholesterol ester packing: three-dimensional image reconstruction and SAXS simulation studies. *Journal of Lipid Research* *52*, 256–262. 10.1194/jlr.M011569.
9. Maric, S., Lind, T.K., Lyngsø, J., Cárdenas, M., and Pedersen, J.S. (2017). Modeling Small-Angle X-ray Scattering Data for Low-Density Lipoproteins: Insights into the Fatty Core Packing and Phase Transition. *ACS Nano* *11*, 1080–1090. 10.1021/acsnano.6b08089.

Acknowledgements

We thank the DELTA machine team for providing ⁸²Synchrotron radiation.

X-ray emission spectroscopy study of the spin transition upon CO₂ adsorption in an amine-functionalized porous coordination polymer

Víctor Rubio-Giménez,¹ Carlos Bartual-Murgui,¹ María Romero-Ángel,¹ Sergio Tatay,¹ Carlos Martí-Gastaldo,¹ Michael Paulus,² Christian Sternemann² and Jose A. Real¹

¹Instituto de Ciencia Molecular, Universitat de València, Catedrático José Beltrán 2, 46980 Paterna, Spain.

²Fakultät Physik / DELTA, Technische Universität Dortmund, Maria-Goeppert-Mayer-Str. 2, D-44227 Dortmund, Germany.

The introduction of amine functionalities in porous coordination polymers (PCPs) has been a successful strategy to promote the selective absorption of CO₂ gas for its capture, separation from gas mixtures or even sensing.^[1] Simultaneously, there is great interest in the spin crossover (SCO) phenomenon, a behaviour reported in first row d⁴-d⁷ transition metal complexes that involves the reversible conversion between two electronic states: low spin (LS) and high spin (HS).^[2] PCPs that present SCO have potential interest for memory and sensing applications as this spin switching effect can be induced from magnetic or electrical fields or from the presence of guest in the pores of the material.^[3,4]

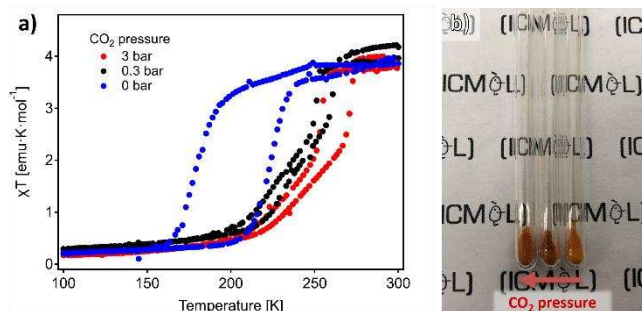


Figure 1. a) Variable temperature SQUID measurements of the ampoules in b) under three different CO₂ pressures. b) Picture of the powder samples of a 3D HCP in ampoules sealed under variable CO₂ pressure.

Hofmann-type coordination polymers (HCPs) are a class of metal-organic materials composed by layers of alternating octahedral Fe^{II} and square planar Pt^{II} centers connected via cyanide groups that generally display SCO behaviour.^[5,6] The Fe^{II} ions also are coordinated to two additional pillaring ligands, which stack the metal-cyanide sheets to form a 2D or 3D structure depending on their denticity. For the case of a 3D HCP, the layers are covalently bonded creating rectangular pore channels that run along the metal-cyanide sheets, making this kind of HCPs permanently porous. We prepared a mixed ligand 3D HCP with an amine functionalized axial ligand. Then, we investigated its SCO behaviour by using SQUID magnetometry (**Figure 1a**). This measurements show a very significant modification of the material's SCO behaviour by varying the relative CO₂ pressure. This observed modification of the SCO behaviour of a porous material in the presence of guest gas molecules, would be the most significant one reported so far, particularly with CO₂.^[7,8] However, our SQUID measurements could only be performed using sealed ampoules sealed under an fixed approximate CO₂ pressure (**Figure 1b**). Therefore, these did not allow to manipulate the sample temperature and CO₂ pressure at the same time and determine the spin state in an *in situ* manner.

We have performed a first test measurement of X-ray emission spectroscopy (XES) on powder samples under variable temperature, the sample atmosphere was varied between vacuum and CO₂ flow under ambient pressure. Preliminary XES Fe K $\beta_{1,3}$ fluorescence (7000-7100 eV) performed at

the BL2 beamline showed that 1) under vacuum there is a clear HS to LS transition. 2) A partial HS to LS transition was observed after flushing with CO₂ at -70°C. 3) The sample seems to go back to the HS state when heating back to room temperature under CO₂ flow. Nevertheless, there are several shortcomings with these measurements in the current set-up. First, the need to flush was caused by the pressure decrease due to CO₂ freezing when the sample chamber valve was closed, which should not have occurred at the measurement temperature. Moreover, radiation damage cannot be excluded. Thus, these measurements with CO₂ flushing require confirmation after implementing the necessary changes to the sample chamber and set-up. Furthermore, data quality can be significantly enhanced with better control of helium bag filling in combination with a larger amount of sample material.

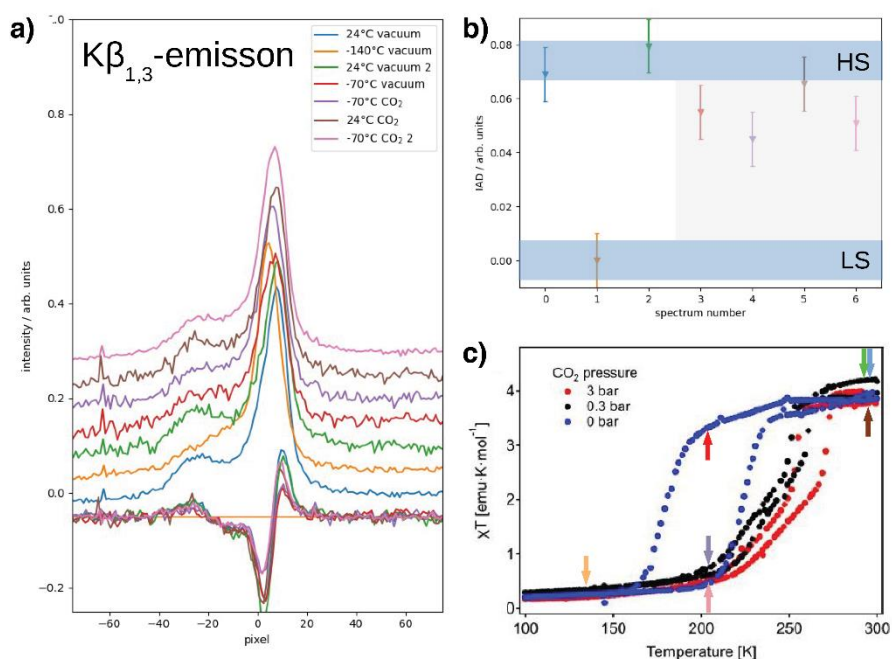


Figure 2. a) All XES Fe K $\beta_{1,3}$ fluorescence measurements performed at BL2 on a 3D HCP powder sample. b) Integrated Absolute Difference (IAD) calculated for the spectra shown in a). c) Temperature points measured with XES (a and b) overlaid on the previous variable temperature SQUID measurements.

- [1] A. J. Emerson, A. Chahine, S. R. Batten, D. R. Turner, *Coord. Chem. Rev.* **2018**, *365*, 1–22.
- [2] J. A. Real, A. B. Gaspar, V. Niel, M. C. Muñoz, *Coord. Chem. Rev.* **2003**, *236*, 121–141.
- [3] J. A. Real, A. B. Gaspar, M. C. Munoz, *Dalton Trans.* **2005**, *0*, 2062–2079.
- [4] E. Coronado, G. Minguez Espallargas, *Chem. Soc. Rev.* **2013**, *42*, 1525–1539.
- [5] M. C. Muñoz, J. A. Real, *Coord. Chem. Rev.* **2011**, *255*, 2068–2093.
- [6] K. Otsubo, T. Haraguchi, H. Kitagawa, *Coord. Chem. Rev.* **2017**, *346*, 123–138.
- [7] G. Mínguez Espallargas, E. Coronado, *Chem. Soc. Rev.* **2018**, *47*, 533–557.
- [8] M. Nakaya, R. Ohtani, S. Hayami, *Eur. J. Inorg. Chem.* **2020**, *2020*, 3709–3719.

Optimized Charge Transport in Molecular Semiconductors by Control of Fluid Dynamics and Crystallization Process

Okan Yildiz¹, Hanna Makowska², Shuanglong Wang¹, Zhitian Ling¹, Witold Waliszewski², Wojciech Pisula^{1,2}, and Tomasz Marszalek^{1,2*}

¹ Max Planck Institute for Polymer Research, Ackermannweg 10, 55128 Mainz, Germany

² Department of Molecular Physics, Faculty of Chemistry Lodz University of Technology, Zeromskiego 116, 90-924 Lodz (Poland)

* Email: marszalek@mpip-mainz.mpg.de

Semi-crystalline organic semiconductors (OSCs) have a proven potential as active layers in electronic thin film applications, such as transistors, sensors, integrated circuits, and displays. Over the past decades, the charge carrier mobility in organic field-effect transistors (OFETs) has improved by three to four orders of magnitude and is now higher than those of amorphous silicon devices. However, it remains challenging to fabricate large-area organic electronics, because defects in the crystalline morphology, such as deformation in the unit cell of the crystal structure, domain shape distortion, grain boundaries, and interruption of long-range in- and out-of-plane molecular order, which may occur at various length scales, critically affect the charge carrier transport, especially in field-effect transistors (FETs). To obtain defect-free thin-films requires a delicate control over the assembly of the OSC molecules during crystallization. Various solution-based methods have been introduced to control the deposition of the OSC films.

Firstly, meniscus-guided coating (MGC) techniques such as zone-casting, emerge as promising candidates, owing to their scalability and potential to optimally control the deposition and crystallization. The morphology of zone-cast thin films of the molecular semiconductor *C8-BTBT* can be categorized into three subregimes, featuring crystalline domains that are I) isotropic, II) unidirectional crystal stripes, and III) corrugated and dendritic. Whereas I) and II) are typically found in the evaporative coating regime, III) is primarily produced in the Landau-Levich regime. Increasing the solution concentration does not directly affect the morphology, but merely increases the critical casting speeds that mark the transitions between the morphology subregimes. Numerical simulation of the fluid dynamics in the coating bead and crystallization in the deposited film, explains the occurrence of morphology I by premature random nucleation resulting from a significantly elevated local solute concentration at low speed. The band-like structure, low roughness and, ***as shown by GIWAXS, significant molecular order obtained in subregime II, provides for optimal electrical performance in organic field-effect transistors.*** We expect the insight gained in this work, in particular the proposition of an optimal processing window, to be valuable for ensuring reproducible device manufacture by meniscus-guided coating techniques. [1]

Secondly, free-standing and flexible field-effect transistors based on TIPS-pentacene/polystyrene bilayers are obtained by well-controlled phase-separation of both components. The phase-separation is induced by solvent vapor annealing of initially amorphous blend films leading to crystallization of TIPS-pentacene as top layer. ***The crystallinity and blend morphology strongly depend on the molecular weight of polystyrene and under optimized conditions a distinct phase-separation with a well-defined and trap-free interface between both fractions is achieved.*** Due to the distinct bilayer morphology, the resulting flexible field-effect transistors reveal similar charge carrier mobilities as rigid devices and additionally pronounced environmental and bias stress stabilities. The performance of the flexible transistors remains stable up to a strain of 1.8%, while above

this deformation a close relation between current and strain is observed that is required for applications in strain sensors. [2]

Additionally, in the third project, the influence of end group substituents on surface morphology, microstructure and charge carrier transport in thin films of thiophene/phenylene based small-molecule semiconductors was investigated, in particular focusing on the model system PTPP. Three PTPP derivatives with varying degree of end group polarity have been analysed as potential active materials in organic field-effect transistors. More specifically, the end group polarity was altered by going from an alkyl derivative of PTPP (**1**) to an alkoxy derivative (**2**) with one oxygen atom in each end group to the glycol derivative (**3**) with two oxygen atoms in each end group while maintaining the overall length of the end groups constant across the three compounds. For all three derivatives, the effective charge carrier mobility increases with higher substrate temperature during sublimation that is related to growth of larger grains and higher film crystallinity. Furthermore, it is observed that the mobility decreases with higher polarity of the end groups, but at the same time the reliability of the devices significantly improves. These results provide fundamental understanding on the role of oxygen incorporation into semiconductor side chain/end group substituents as this approach has seen rapidly growing attention in recent years in the organic electronics community, not only for OFET and organic electrochemical transistor (OECT) applications, but also for organic thermoelectric and photovoltaic applications. [3]

Acknowledgement

This work was partially prepared as part of the „*Self-standing, flexible and solution processable organic field effect transistors for complementary inverter applications*” project that is carried out within the First Team programme of the Foundation for Polish Science co-financed by the European Union under the European Regional Development Fund (*First TEAM/2017-3/26*). W.P. acknowledge the National Science Centre, Poland, through the grant UMO-2015/18/E/ST3/00322. The researchers involved in this projects express their gratitude to Dr. Christian Sternemann and Dr. Michael Paulus for their help in the experiments.

References

1. Okan Yildiz, Zuyuan Wang, Michal Borkowski, Georg Fytas, Paul W. M. Blom, Jasper J. Michels, Wojciech Pisula, Tomasz Marszalek, „Optimized Charge Transport in Molecular Semiconductors by Control of Fluid Dynamics and Crystallization in Meniscus-Guided Coating”, *Adv. Funct. Mater.* **2022**, 32, 2107976;
2. Hanna Zajaczkowska, Lothar Veith, Witold Waliszewski, Malgorzata A. Bartkiewicz, Michal Borkowski, Piotr Sleczkowski, Jacek Ulanski, Bartlomiej Graczykowski, Paul W. M. Blom, Wojciech Pisula and Tomasz Marszalek, „Self-Aligned Bilayers for Flexible Free-Standing Organic Field-Effect Transistors”, *ACS Appl. Mater. Interfaces*, **2021**, 13, 59012;
3. W. Waliszewski, Z. S. Parr, A. Michalska, R. Halaksa H. Zajaczkowska, P. Sleczkowski, M. Neophytou, B. Luszczynska, P. W.M.Blom, C. B.Nielsen, T. Marszalek, W. Pisula, “*Role of oxygen within end group substituents on film morphology and charge carrier transport in thiophene/phenylene small-molecule semiconductors*”, *Organic Electronics*, **2022**, 109, 106608;

Apoferritin under high hydrostatic pressure

Gordon Scholz¹, Michael Paulus¹, Christian Gutt², Susanne Dogan¹

¹Fakultät Physik/DELTA, TU Dortmund, Dortmund, Germany

²Department Physik, Universität Siegen, Siegen, Germany

Ferritin is an iron storage and detoxification protein which can be found in plants, animals and bacteria. Typically, ferritin consists of 24 subunits, which are either identical or similar. It has a hollow spherical structure, which has an outer diameter of approximately 12 nm to 13 nm and an inner cavity diameter of about 7 nm to 8 nm. If there is no iron stored in the ferritin (in a form similar to ferrihydrite) and thus only the protein shell remains, the protein is called Apoferritin. The structure of Apoferritin is shown in figure 1. The individual subunits are composed of a bundle of four helices, which are arranged in two antiparallel pairs of helices, and a fifth shorter helix. Under neutral conditions, the inner surface of ferritin has a negative charge density and the net charge on the outer surface is close to zero or slightly positive. The cavity is connected to the surface via eight triaxial channels and six quadriaxial channels to the external environment. The pore size is between 3 and 5Å.

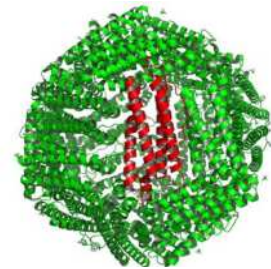


Figure 1: Structure of Apoferritin, one subunit is shown in red [1]

While the behaviour of apoferritin under variation of temperature and pH has already been studied [2,3], there are no studies on apoferritin under high hydrostatic pressures. Thus, in this study we investigated the structural stability of apoferritin under high hydrostatic pressure. The focus was on the pressure-induced change of the protein structure as well as the protein-protein interaction in concentrated solutions. Measurements were performed with apoferritin (Merck GmbH; product number: A3641) in a 0.135M NaCl saline solution, with a concentration of 35mg/ml. To determine the form factor, the solution was measured pressure-dependently as supplied. To investigate the protein-protein interaction, the solution was centrifuged in a filter tube (Amicon, Merk, 10,000 MWCO) at 10000 g for 30 minutes yielding a concentration of 30 wt%. The 30 wt% solution and a 15 wt% mixture with buffer were measured. To determine the scattering background, buffer solution was also measured as a function of pressure between 50 bar and 4 kbar. The measurements were performed at beamline BL2 using the high-

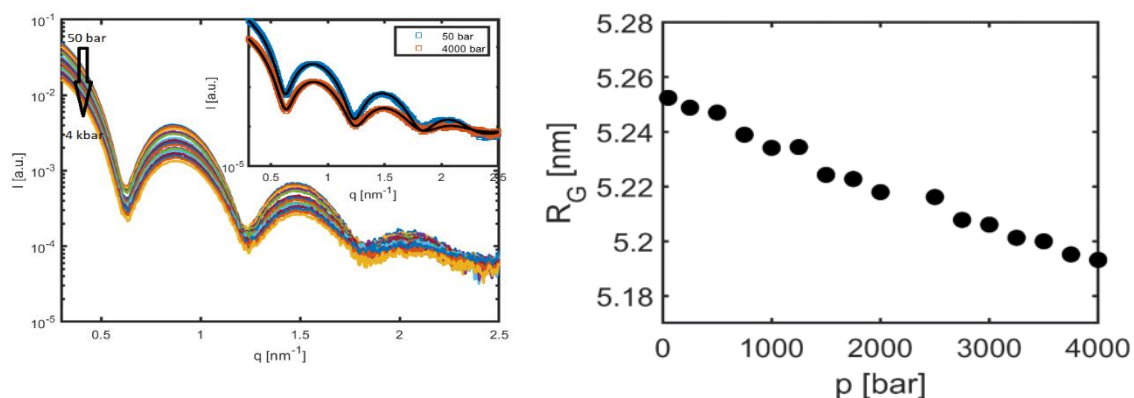


Figure 2: Left: Pressure dependent SAXS measurements of apoferritin at low concentration. The inset shows two curves taken at 50 bar and 4 kbar respectively. The black lines are fits to the data using a hollow sphere model. Right: Radius of gyration obtained from the fits.

pressure setup.

Figure 2 depicts the pressure-dependent measurements used to determine the form factor. A decrease in intensity with increasing pressure can be seen, resulting from a reduction of the scattering contrast between protein and water with increasing compression of the water. However, a very slight shift of

the oscillation extrema to larger q is also observed, which indicates a compression of the protein. The scattering data were fitted with a spherical shell model. The outer and inner radius of the sphere were chosen as variation parameters. The form factor $P(q)$ of a spherical shell can be described by $P(q)=(1/V)^2[V_1\cdot\varphi(q\cdot R_1)-V_2\cdot\varphi(q\cdot R_2)]^2$ with $V_i=(4/3)\pi R_i^3$ and $\varphi(x)=3(\sin(x)-x\cos(x))/x^3$ and $V=V_1-V_2$. [4] Exemplary fits are shown in the inset of figure 2 as black lines. Subsequently, the gyration radius was calculated by $R_g=(3/5\cdot(R_1^5-R_2^5)/(R_1^3-R_2^3))^{1/2}$ [4]. The gyration radii are shown in figure 2 on the right. The radii decrease linearly with increasing pressure. However, the decrease ($R_{4000\text{bar}}/R_{50\text{bar}}=0.9886/4000$ bar) is less than one would expect from a compression scaling with the water phase ($\sim 0.947/4000$ bar). We assume that during compression the water can penetrate the hollow sphere and thus there is no pressure gradient between the protein interior and the outer water phase. A final measurement at 50 bar showed that the compression is reversible (data are not shown).

The pressure-dependent SAXS data of the highly concentrated solution are shown in figure 3 (left, solid lines). Compared to the form factor measurements (dashed lines), the data show significant changes due to protein-protein interactions. To extract the structure factor, the data were divided by the respective form factors. Figure 3, right shows the structure factors for the 30 wt% (red) and the 15 wt% protein solutions at 50 bar. It becomes clear that there is a repulsive interaction between the proteins, which increases with increasing concentration. The effect of the change in concentration (lower protein-protein distance and increased order at high concentration) can be clearly seen in an increased oscillating structure factor. The pressure dependence of $S(q)$ is shown in figure 4. It is noticeable that

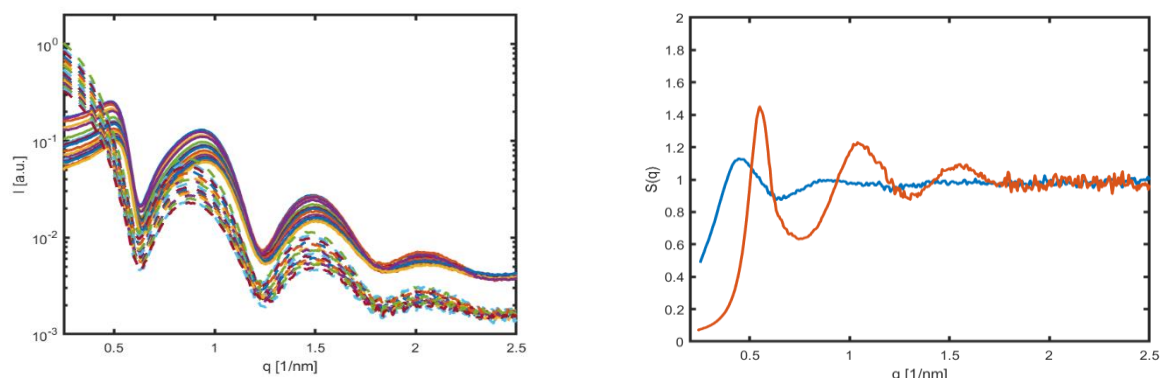


Figure 2: Left: Pressure-dependent measurements of the 30 wt% solution together with the form factor measurements (dashed lines). Right: Structure factors of 30 wt% (red) and 15 wt% (blue) solutions.

the first maximum is clearly sharper with increasing pressure, i.e. the amplitude increases while the half-width decreases. Furthermore, it shifts slightly to larger q values with increasing pressure, which can be explained by the compression of the liquid. Overall, the effects indicate a compression and an increase of the internal order in the system. However, the evaluation of the data is still in progress.

Acknowledgment

We kindly acknowledge the support of the DELTA machine group and the provided synchrotron radiation.

References

- [1] L. Sangeetha Vedula et al., Journal of Biological Chemistry 284, 24176–24184 (2009). [2] Simonetta Stefanini et al., Archives of Biochemistry and Biophysics 325, 58–64 (1996). [3] Mihee Kim et al. Biomacromolecules 12, 1629–1640 (2011). [4] L. Melníková et al., Colloids and Surfaces B: Biointerfaces 123, 82–88 (2014).

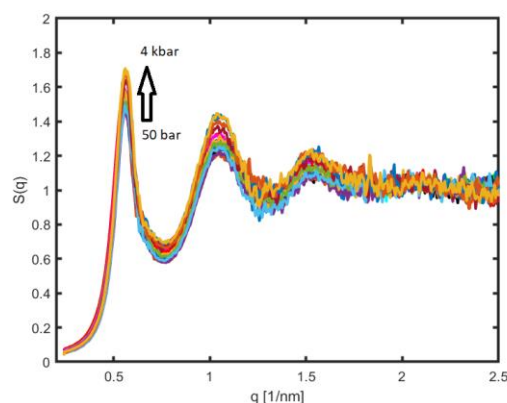


Figure 4: Pressure-dependent structure factors of the 30 wt% solution.

Oxidation Resistance of PECVD Ti-Si-C-N Nanocomposite Coatings

Thewes, A.¹; Kipp, C.¹; Reinders, P.M.^{1,2}; Brückner, T.²; Sternemann, C.³; Paulus, M.³

IOT TU Braunschweig, 44145 Dortmund, Germany

Fraunhofer Institute for Surface Engineering and Thin Films IST, Dortmund 44145, Germany

Fakultät Physik/DELTA, Technische Universität Dortmund, 44221 Dortmund, Germany

Introduction

Nanocomposite coatings received increasing attention in recent years due to outstanding mechanical and thermal properties primarily provided by their nanostructure [MOR20], [PIL08], [THA13]. The nanocomposite structure, consisting of an amorphous (a-) matrix enveloping nanocrystalline (nc-) grains, offers advanced mechanical properties, e.g. high hardness. The oxidation resistance of Ti-Si-C-N coatings is investigated in this study. Tribological tests by Ma et al. [MA07] showed lower coefficients of friction for Ti-Si-C-N compared to Ti-Si-N at room temperature as well as at 550 °C.

Method

Ti-Si-C-N coatings were deposited on mirror finished (polished) DIN 1.2343 hot working steel and single-crystalline Si-wafers via Plasma Enhanced Chemical Vapor Deposition (PECVD). TiCl_4 , $\text{Si}(\text{CH}_3)_4$, CH_4 , and N_2 were used as precursor gases with addition of H_2 for reduction of TiCl_4 and Ar to support the glow discharge during coating deposition. The chemical composition was determined via Electron Probe Microanalysis (EPMA). X-ray diffraction (XRD) measurements were performed at Beamline BL9 [KRY06] of the synchrotron light source DELTA (TU Dortmund, Dortmund, Germany). In order to determine the lattice orientation with respect to the samples surface, a MAR345 image plate detector was used. The energy of the incident photon beam was $E_0 = 27 \text{ keV}$ and the beam size was set to $1.0 \times 0.7 \text{ mm}^2$ ($h \times v$). The angle of incidence was 1° . These experiments were carried out at room temperature and elevated temperatures of 750 °C, 775 °C, and 800 °C. Raman spectroscopy was performed on samples tempered in air for 30 min at 850 °C to identify amorphous phases in the nanocomposite, because XRD won't yield this information.

Results and discussion

EPMA measurements revealed a chemical composition of 30.9 at.-% Ti, 10.5 at.-% Si, 41.0 at.-% C, and 14.8 at.-% N with additional 1.3 at.-% O and 1.6 at.-% Cl as residual elements from the deposition process. The XRD experiments yield information on lattice structure and phase configuration. Figure 1 shows the two-dimensional diffraction images of a Ti-Si-C-N layer in the as-deposited state. A distinct texture in the scattering intensity of the layer indicating an orientation of the (00l) planes of the cubic layer structure parallel to the substrate surface is observed.

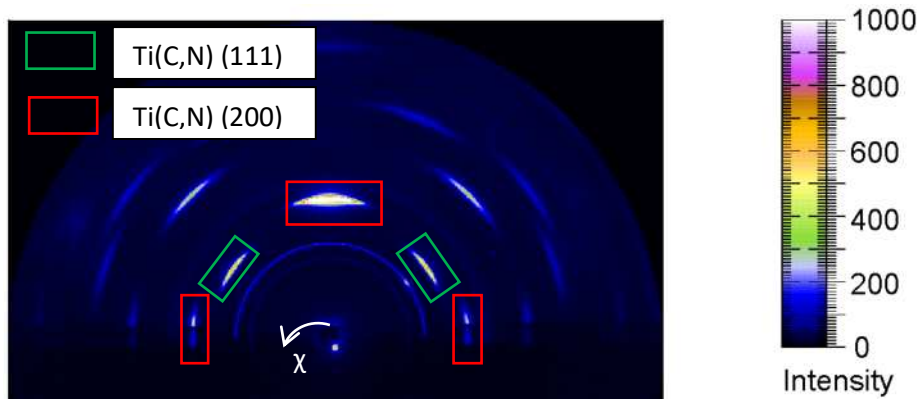


Figure 1: 2D X-ray diffraction image of the Ti-Si-C-N coating measured with a MAR345 image plate detector at room temperature.

Further experiments at elevated temperatures were carried out. The MAR345 image was azimuthally integrated in χ -angles of $-10^\circ < \chi < 10^\circ$ (see fig. 1). This way, the (200) Ti(C,N) reflex was under closer investigation. The diffraction patterns are shown in fig. 2. The Bragg reflection observed at 8.5° stems from the graphite dome that is part of the heating cell. At room temperature, a strong (200) Ti(C,N) reflex was found. With an increase in temperature, the intensity of the Ti(C,N) reflex decreases the more the samples are heated. This is probably due to oxidation processes in the surface-near zone that lead to a depletion of Ti(C,N) grains close to the surface. In addition, the Ti(C,N) reflex shifts slightly towards higher 2θ angles with increasing temperature, as indicated by the chain lines in fig. 2, right hand side. The Ti-Si-C-N coating is oxidation resistant up to 800°C , as there is no TiO_2 detected in the diffraction patterns. The formation of TiO_2 has been observed in comparable coatings (Ti-Si-B-C-N) when oxidized and was reported by the authors in the DELTA User Reports of 2019, 2020, and in [THE22].

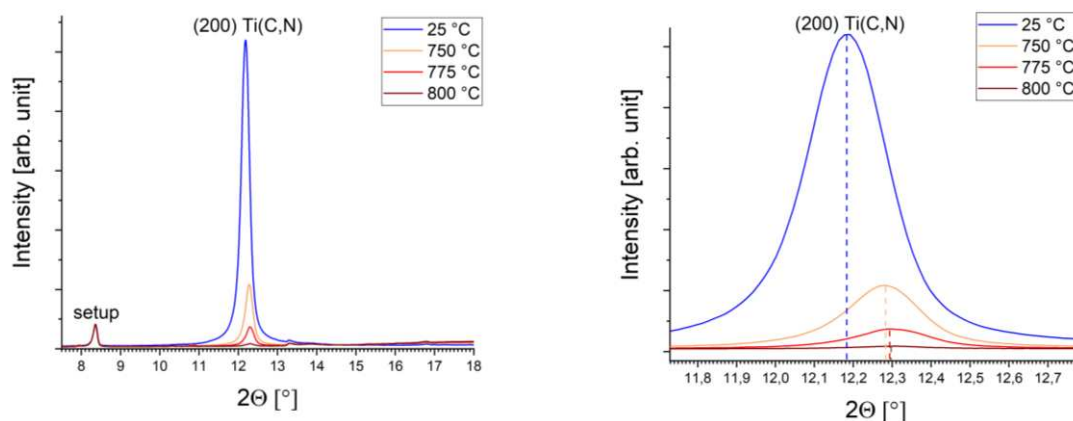


Figure 2: Diffraction patterns of Ti-Si-C-N at different temperature levels as an overview (left hand side) and the Ti(C,N) reflexes in detail (right hand side)

Raman spectroscopy showed a strong response at 1300 cm^{-1} and 1600 cm^{-1} correspond to D-band and G-band, respectively. These are characteristic for amorphous carbon, which is part of the amorphous matrix of the nanocomposite coating. As these measurements were carried out on samples after they were oxidized in an oven in air for 30 min, this shows that part of the as-deposited structure must be intact, as amorphous carbon would burn at 850°C in contact with air. This indicates, that there is a thin oxidation resistant layer on top of the coating that hinders diffusion of oxygen towards the Ti(C,N) grains or amorphous carbon matrix.

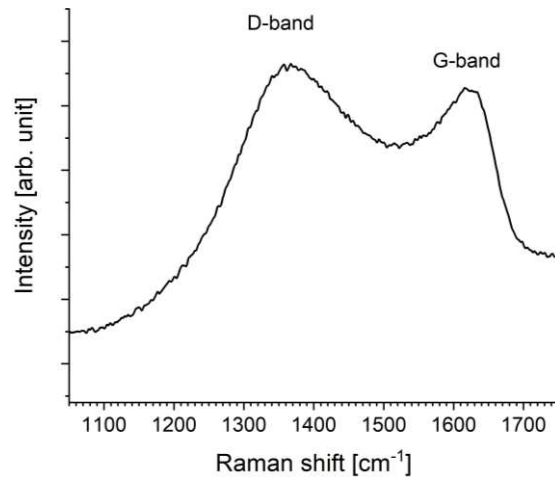


Figure 2: Raman scattering pattern of the Ti-Si-C-N sample

Conclusion

X-ray investigation of Ti-Si-C-N nanocomposite coatings at elevated temperatures showed no sign of oxidation in form of rutile or anatase. Raman spectroscopy verified occurrence of amorphous carbon after oxidation in air at 850 °C for 30 min. The Ti(C,N) grains identified by XRD and the amorphous carbon identified by Raman spectroscopy would oxidized at 550 °C and 400 °C, respectively. Thus, formation of a thin passivation layer with diffusion barrier properties (concerning oxygen) must have formed on the surface. Candidates are amorphous phases of Si₃N₄, SiO₂, or a combination of both. Further investigations will be carried out to increase the understanding of the mechanisms of oxidation in Ti-Si-C-N nanocomposite coatings.

In summary, the Ti-Si-C-N coatings offer high oxidation resistance of at least 850 °C, while the carbon content is relatively high with 41 at.-%. These coatings are a possible candidate for tribological applications at high temperature, where carbon can decrease the coefficient of friction (as shown by Ma et al. [MA07]).

Acknowledgment

We kindly acknowledge the support of the DELTA machine group and provision of synchrotron radiation beamtime.

Literature

- [KRY06] Krywka, C. et al.: The new diffractometer for surface X-ray diffraction at beamline BL9 of DELTA. *Journal of synchrotron radiation* Pt 1/13, S. 8–13, 2006.
- [MA07] Ma, S. L. et al.: Synthesis and characterization of super hard, self-lubricating Ti–Si–C–N nanocomposite coatings. *Acta Materialia* 18/55, S. 6350–6355, 2007.
- [MOR20] Moritz, Y. et al.: Oxidation behavior of arc evaporated TiSiN coatings investigated by in-situ synchrotron X-ray diffraction and HR-STEM. *Surface and Coatings Technology* 404, S. 126632, 2020.
- [PIL08] Pilloud, D. et al.: Study of the structural changes induced by air oxidation in Ti–Si–N hard coatings. *Surface and Coatings Technology* 11/202, S. 2413–2417, 2008.
- [THA13] Thangavel, E. et al.: Synthesis and characterization of Ti–Si–C–N nanocomposite coatings prepared by a filtered vacuum arc method. *Applied Surface Science* 265, S. 60–65, 2013.
- [THE22] Thewes, A. et al.: Ti-Si-B-C-N plasma enhanced chemical vapor deposition nanocomposite coatings for high temperature applications. *Thin Solid Films* 760, S. 139507, 2022.

Surface passivation of perovskite nanocrystals

Bapi Pradhan^{1,§}, and Christian Sternemann²

¹Department of Chemistry, KU Leuven, Celestijnenlaan 200F, 3001 Heverlee, Belgium

²Fakultät Physik/DELTA, TU Dortmund University, 44221 Dortmund, Germany

[§]Email: bapi.pradhan@kuleuven.be

Inorganic perovskites nanocrystals (PNCs) with narrow emission line width are outstanding candidates for the next-generation color-saturated optoelectronic devices. They have emerged as promising photoactive materials due to their tunable emission wavelength, narrow photoluminescence (PL) bandwidth, low-cost processing, high color purity, PL quantum yield (PLQY) up to 100% and a versatile surface chemistry. These fascinating features have facilitated the fabrication of efficient light-emitting diodes (LEDs) with external quantum efficiencies (EQEs) > 20%. Noticeable is the improvements in performance of CsPbI₃-based LEDs, with an outstanding EQE ~ 23%. However, it is well known that this perovskite is prone to deterioration of its PL properties and stability as consequence of the fast α -to- δ phase transformation, limiting its use in long-term applications. Their electroluminescence performance and stability are limited by structural sensitivity and inferior carrier transport. These limitations are closely related to the surface defects-mediated nonradiative losses on the NCs. Diverse strategies have been studied to improve the stability and the optical performance of red-emitting PNCs such as ligand surface passivation with capping ligands with better binding energy than traditional oleic acid/oleylamine, modified synthetic routes for nanocrystals growth and purification, and composition engineering.

Herein, we present the demonstration of a facile surface passivation strategy for CsPbI₃ PNCs by using guanidinium iodide (GuI) for the fabrication of stable red perovskite LEDs. The obtained GuI-passivated PNCs exhibited high brightness, high dispersibility, and good stability for months under ambient conditions. Bright-red LEDs fabricated using those NCs displayed impressive device figures of an EQE of 12.35% for electroluminescence at 685 nm, a lower turn-on voltage close to 2.4V, and maximum luminance of 4624 cd/m². The operational half-life time T_{50} of the GuI-treated device was 50 mins at the current density of 20 mA/cm², which is superior to the untreated device under the same condition. PLQY is well improved for a single GuI passivated PNC, indicating that passivation reduces random switching between different intensity states leading to enhanced performance and stability of the LED. The above strategies demonstrate the initial promise of GuI passivated perovskite PNCs for stable red LED application.

To confirm the Gu incorporation and further understand the GuI binding motifs on the CsPbI₃ PNCs surface, FTIR spectroscopy was performed to investigate the surface chemistry of the NCs. As shown in **Figure 1**, the same vibration bands, including COO⁻ stretching and C=C-H stretching (1546 cm⁻¹), appear in all three samples, indicating that the ligand OAm was still adsorbed on the NCs surface. GuI binding is evident based on the emergence of FTIR peaks at wavenumbers 3340 and 1662 cm⁻¹ that are present in the spectra for Gu⁺ and NCs stabilized with GuI, which can be assigned to the -NH₂ symmetric and -C=N stretching vibrations, respectively. Meanwhile, the peak intensity increases with more Gu incorporation. The peaks at 2850-2950 cm⁻¹ correspond to functional groups in the C-H stretching mode of the ligand. Due to the low concentration of GuI in the precursor, only slight enhanced peaks representing GuI can be

seen. Above all observation suggests that Gu is present in CsPbI_3 PNCs and interacts with PNCs in some way.

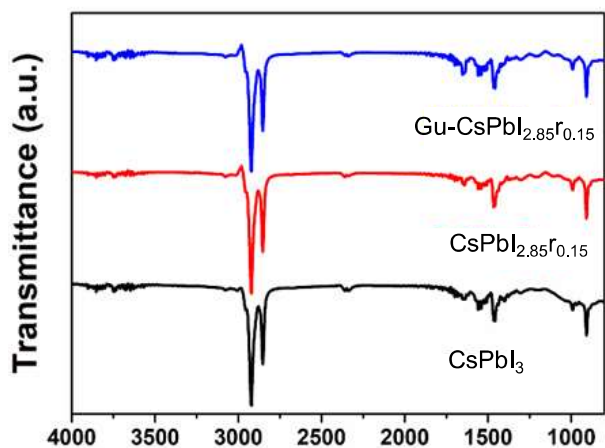


Figure 1. FTIR spectra of pristine and Gu- CsPbI_3 PNCs.

Grazing incident wide angle x-ray scattering (GIWAXS) was used to resolve the structural state of CsPbI_3 PNCs samples in absence and presence of Gu. **Figure 2a** shows 2D GIWAXS patterns of CsPbI_3 and $\text{Cs}_{1-x}\text{Gu}_x\text{PbI}_3$ PNCs films. **Figure 2b** shows the 1D line cuts extracted from out-of-plane directions, 2D GIWAXS patterns show a clear scattering feature visible at 10.3 nm^{-1} , corresponding to perovskite diffraction (100). All the diffraction peaks of (100), (110), (111), (200), (210), and (211) indicate the presence of α -cubic phase with high crystallinity, and a preferable orientation relative to the substrate. As the Gu content increases, a slight shifting of the diffraction peaks to lower q is detected, indicating lattice expansion, presumably by the incorporation of Gu into the structure.

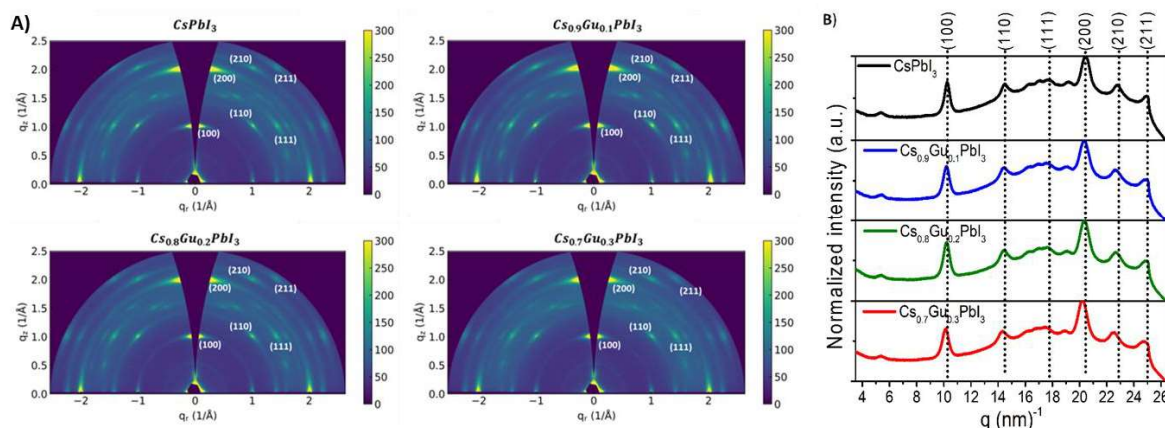


Figure 2. A) 2D GIWAXS rings of 1 layer of reference and different proportion of Gu incorporated perovskite NCs film. B) Out-of-plane line-cuts from 2D GIWAXS patterns of CsPbI_3 and $\text{Cs}_{1-x}\text{Gu}_x\text{PbI}_3$ PNCs thin films.

Influence of bias voltage on the structural properties of TiAlN coatings deposited by hybrid DC/HiPIMS technology

Dominic Stangier^{1*}, Nelson Filipe Lopes Dias¹, Christian Sternemann²,
Michael Paulus², Wolfgang Tillmann¹

¹Institute of Materials Engineering, TU Dortmund University, Germany
44227 Dortmund, Leonhard-Euler-Straße 2

²Fakultät Physik / DELTA, TU Dortmund University, Germany
44227 Dortmund, Maria-Goeppert-Mayer-Straße 2

*corresponding author: dominic.stangier@tu-dortmund.de

In addition to the challenges of economical production, modern manufacturing technology is simultaneously confronted with the continuing trend towards miniaturization and more complex shaped products [FLE07, MER12]. In this context, machining processes and, in particular, micromachining of high-speed tool steels have proven to be a promising approach for future applications [KRE18a]. Compared to thermally based removal principal such as laser ablation or electronic discharge machining (EDM) [HÄF13, RAJ16, IOR02], milling processes offer the advantage of realizing damage-free, high quality surface finishing without the need for additional post-treatments. The positive influence on the subsurface region in terms of surface quality and the residual stresses can be attributed to the mechanical principle of action [TIL22, MEI22]. In order to realize the machining process while ensuring high process reliability and an excellent service life of the tools, high requirements are made for the properties of the PVD thin films protecting the micro-tools. A promising approach is the deposition of wear-resistant TiAlN PVD coatings using hybrid high-energy sputtering (HiPIMS) technology, which enables the near-net shaped coating of milling tools with a diameter of $D < 1$ mm [KRE18b]. Compared to conventional DC sputtering, HiPIMS technology offers a multiple increase in power density due to the pulsed discharge of cathodes as well as an associated increase in ionization of the sputtered species [GRE19]. This leads to a dense thin film growth with improved mechanical properties [TIL19]. So far, existing investigations focus predominantly on the variation of the pulse patterns of the cathodes in terms of changing the frequency or pulse duration for a targeted control of the voltage and current characteristics of the cathodes [BOB16, CHA14, HSI13, SEV17]. In this context, the influence of the applied bias voltage at the handling system for the synthesis of hybrid DC/HiPIMS thin films was not addressed with respect to the crystalline growth of the TiAlN systems so far.

As substrate fine grained cemented carbide material with 9 wt. % Co with a hardness of 1600 HV was used and coated in two-fold rotation. Before the deposition process, the substrates were exposed to a sequence of heating and etching processes to clean the surfaces from oxides and to remove the Co matrix for a better adhesion of the coating system. Additionally, a thin

metallic Ti interlayer was applied and subsequently the TiAlN coating was deposited using a hybrid DC/HiPIMS configuration of the cathodes. The variation of the bias voltage was conducted for $U_B = -60$ V, $U_B = -100$ V, $U_B = -140$ V and $U_B = -180$ V to influence the kinetic energy and the crystalline growth during the deposition process. The investigation at BL9 of DELTA were carried out at a photon energy of $E = 20$ keV ($\lambda = 0.6199$ Å) with an image plate detector MAR345 for the analysis of the texturing of the coatings. To ensure a surface sensitive measurement, a low angle of incidence ($\omega = 0.5^\circ$) with an exposure time of $t = 300$ s was chosen. For the calibration of the detector and the distance of the measurements, LaB₆ was used.

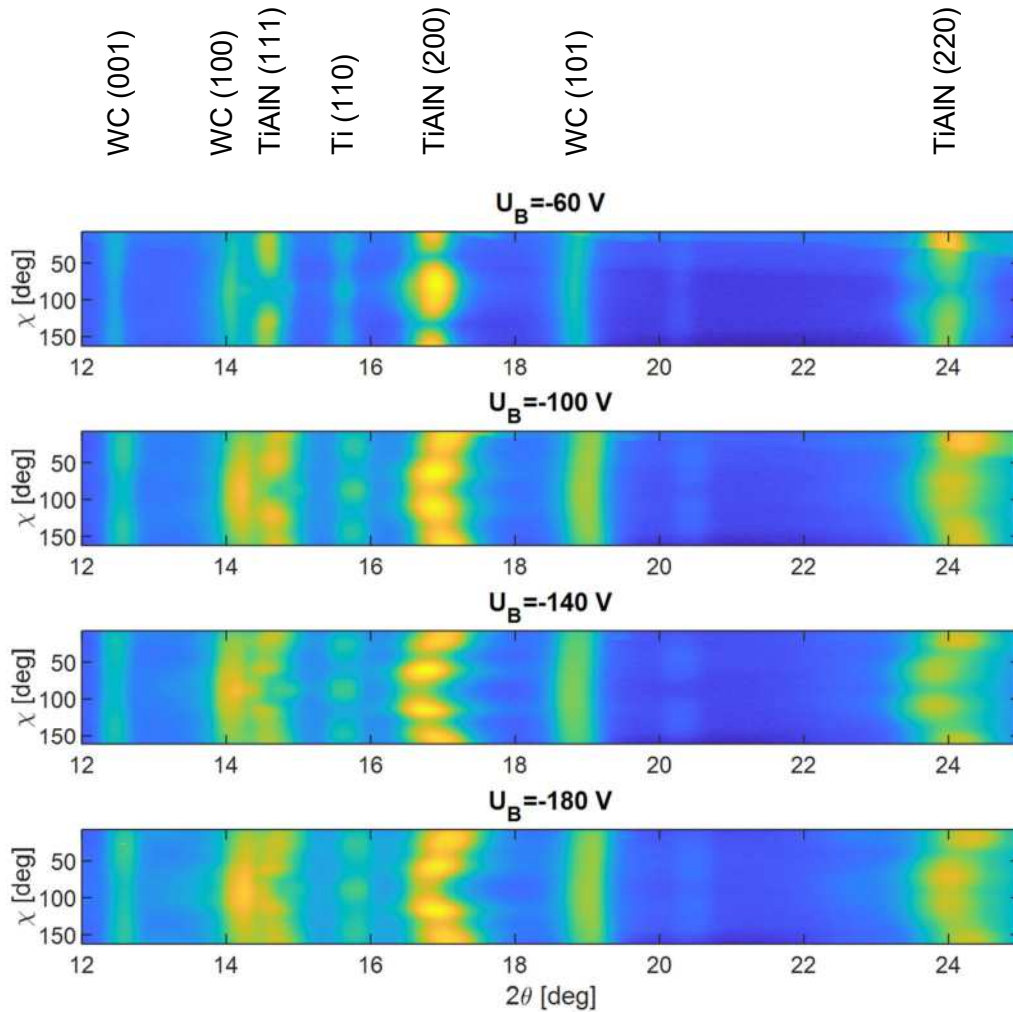


Figure 1: 2D-GIXRD logarithmic diffraction patterns of the deposited DC/HiPIMS TiAlN coatings ($\lambda = 0.6199$ Å; $E = 20$ keV) measured with an angle of incidence of $\omega = 0.5^\circ$ plotted as a function of the azimuth angle in dependency of the scattering angle 2Θ for the different level of bias voltage

As illustrated in Figure 1, the 2D diffraction patterns of the coating systems deposited by different bias voltages prove the before mentioned architecture. The presence of the hexagonal WC phase, which originates from the cemented carbide substrate material and the missing of crystalline Co Bragg-reflection is a clear indicator for the surface sensitivity of the setup. With an increasing bias voltage, a higher intensity of the substrate Bragg reflections can be noticed,

which can be correlated with the decreasing coating thickness due to densification and resputtering effects of deposited thin film material [BOB18]. Furthermore, no changes of the intensity for the azimuth angle of the substrate material can be recognized, which can be directly linked to the manufacturing process in terms of sintering of the cemented carbide material. In contrast to these findings, a strong texturing can be observed for the crystalline phases of the PVD coating. The hexagonal phase of the Ti reflection in (110)-orientation close to $2\Theta = 16^\circ$ shows a weak shift in the intensity for the azimuth angle. This effect can be explained by the used DC sputter mode of the power supply for interlayer leading to a low ionization and low kinetic energy, which is directly linked to the applied bias voltage and therefore leading to similar results. However, the TiAlN coating shows a strong texturing effect for the (111)-, (200)- and (220)-growth direction, which is even increasing for higher bias voltages. For the lowest value of $U_B = 60$ V, the dominant intensity shifts from the in-plane orientation for an azimuth of $\chi = 90^\circ$ to higher and lower values. This effects can be explained by the high kinetic energy of the ions in the deposition process which leads to a defect-induced disturbance of the crystalline growth inhibiting the surface diffusion trying to minimize the surface energy [ABA08].

As presented, the crystalline growth of TiAlN coatings can be controlled by the applied bias voltage in DC/HiPIMS process. For this reason, one may propose, that the resulting mechanical and tribological properties are directly influenced by this process parameter. Nevertheless, the performance of the developed coating systems has to be evaluated in real milling processes to determine the performance of the coatings.

Acknowledgements

The authors gratefully acknowledge the DELTA machine group for providing synchrotron radiation at BL9 and the German Research Foundation for the financial support of the project (TI 343/187-1; project number 445127534) “Effects and interactions for interface and cutting-edge conditioning in hard machining”.

References

- [ABA08] Abadias, G.: *Stress and preferred orientation in nitride-based PVD coatings*, Surface & Coatings Technology, 202 (2008), S. 2223–2235.
- [BOB16] Bobzin, K.; Brögelmann, T.; Brugnara, R. H.; Kruppe, N. C.; Chromy, S.: *Influence of HPPMS pulse parameters on the reactive gas N_2 and on the properties of (Cr, Al)N coatings*, Surface & Coatings Technology, 293 (2016), S. 28–34.
- [BOB18] Bobzin, K.; Brögelmann, T.; Kruppe, N. C.; Engels, M.: *Investigations on the substrate bias influence on reactive HPPMS plasmas*, Thin Solid Films, 663 (2018), S. 62–72.
- [CHA14] Chang, C.-L.; Shih, S.-G.; Chen, P.-H.; Chen, W.-C.; Ho, C.-T.; Wu, W.-Y.: *Effect of duty cycles on the deposition and characteristics of high power impulse magnetron sputtering deposited TiN thin films*, Surface and Coatings Technology, 259 (2014), S. 232–237.

- [FLE07] Fleischer, J.; Kotschenreuther, J.: *The manufacturing of micro molds by conventional and energy-assisted processes*, The International Journal of Advanced Manufacturing Technology, 33 (2007), S. 75–85.
- [GRE19] Greczynski, G.; Petrov, I.; Greene, J. E.; Hultman, L.: *Paradigm shift in thin-film growth by magnetron sputtering: From gas-ion to metal-ion irradiation of the growing film*, Journal of Vacuum Science & Technology A, 37 (2019), 60801.
- [HÄF13] Häfner, T.; Reg, Y.; Hetzner, H.; Schmidt, M.: *Microstructuring Tools for Sheet Bulk Metal Forming - A Designated Application for Picosecond Laser*, Journal of Laser Micro/Nanoengineering, 8 (2013), S. 39–44.
- [HSI13] Hsiao, Y.-C.; Lee, J.-W.; Yang, Y.-C.; Lou, B.-S.: *Effects of duty cycle and pulse frequency on the fabrication of AlCrN thin films deposited by high power impulse magnetron sputtering*, Thin Solid Films, 549 (2013), S. 281–291.
- [IOR02] Iordanova, I.; Antonov, V.; Gurkovsky, S.: *Changes of microstructure and mechanical properties of cold-rolled low carbon steel due to its surface treatment by Nd:glass pulsed laser*, Surface and Coatings Technology, 153 (2002), S. 267–275.
- [KRE18a] Krebs, E.: *Simulationsgestützte Mikrofräsbearbeitung gehärteter Werkzeugstähle zur Herstellung filigraner Formelemente und funktionaler Oberflächenstrukturen*. Schriftenreihe des ISF, 92, Vulkan-Verlag GmbH, Essen, Dissertation, 2018.
- [KRE18b] Krebs, E.; Wolf, M.; Biermann, D.; Tillmann, W.; Stangier, D.: *High-quality cutting edge preparation of micromilling tools using wet abrasive jet machining process*, Production Engineering, 12 (2018), S. 45–51.
- [MEI22] Meijer, A.; Stangier, D.; Tillmann, W.; Biermann, D.: *Induction of residual compressive stresses in the sub-surface by the adjustment of the micromilling process and the tool's cutting edge*, CIRP Annals, 71 (2022), S. 97–100.
- [MER12] Merklein, M.; Allwood, J. M.; Behrens, B.-A.; Brosius, A.; Hagenah, H.; Kuzman, K.; Mori, K.; Tekkaya, A. E.; Weckenmann, A.: *Bulk forming of sheet metal*, CIRP Annals - Manufacturing Technology, 61 (2012), S. 725–745.
- [RAJ16] Raju, L.; Hiremath, S. S.: *A State-of-the-art Review on Micro Electro-Discharge Machining*, Procedia Technology, 25 (2016), S. 1281–1288.
- [SEV17] Severin, S.; Naveed, M.; Weiß, S.: *Effect of HPPMS Pulse-Frequency on Plasma Discharge and Deposited AlTiN Coating Properties*, Advances in Materials Science and Engineering, 2017 (2017), 4850908.
- [TIL19] Tillmann, W.; Grisales, D.; Stangier, D.; Ben Jebara, I.; Kang, H.: *Influence of the etching processes on the adhesion of TiAlN coatings deposited by DCMS, HiPIMS and hybrid techniques on heat treated AISI H11*, Surface & Coatings Technology, 378 (2019), 125075.
- [TIL22] Tillmann, W.; Stangier, D.; Meijer, A.; Krebs, E.; Ott, A.; Platt, T.; Lopes Dias, N. F.; Hagen, L.; Biermann, D.: *Adapting the Surface Integrity of High-Speed Steel Tools for Sheet-Bulk Metal Forming*, Journal of Manufacturing and Materials Processing, 6 (2022), 37.

Influence of increased temperature on the compound layer of nitrided steels

Kipp, C. ¹; Reinders, P. ¹; Brückner, T. ²; Paschke, H. ²; Thewes, A. ³; Sternemann, C. ⁴; Paulus, M. ⁴

¹ Institute for Surface Technology IOT TU Braunschweig, 38108 Braunschweig, Germany

² Fraunhofer Institute for Surface Engineering and Thin Films IST, 44145 Dortmund, Germany

³ Institute for Surface Technology IOT TU Braunschweig, 44145 Dortmund, Germany

⁴ Fakultät Physik/DELTA, Technische Universität Dortmund, 44221 Dortmund, Germany

Introduction

Nitriding is a well-established thermochemical process for surface modification of metallic materials (e.g. steel, aluminum, titanium) to harden the surface layer and reduce corrosion and wear on the surface [Hof97]. Complex component geometries as well as internal contours can be treated without special requirements. A distinction is made between salt bath nitriding, gas nitriding and plasma nitriding [Lie14].

Plasma nitriding offers the advantage that the formation of the nitriding zone can be specifically adjusted within wide ranges [Lie14]. By using a plasma, atomic nitrogen is generated from a nitrogen-hydrogen atmosphere, which can diffuse temperature-controlled into the material [Bla10]. In the workpiece, the nitrogen causes a transformation of the original surface by forming a nitrided zone. This can consist of a compound layer (CL) on the surface and a subsequent diffusion zone (DZ) beneath it, also called a precipitation zone. The formation of a CL can be avoided by the selection of appropriate process parameters [Pas12].

In steels, a complete transformation of the original material surface takes place in the CL with the formation of iron nitrides. γ' - and ϵ -nitrides have been detected so far [Hof96], [Kar92]. They are of ceramic nature with increased hardness and brittleness, although there are differences between the nitrides [Spi86].

In contrast to the CL, no complete transformation of the material takes place in the DZ. Here, nitride precipitates are formed, depending on the alloy content and composition of the steel. In the case of low-alloy steels, precipitates of γ' -nitride form predominantly in the DZ. In high-alloy steels which contain special nitride formers such as Cr, Al, Mo, W, V or Si, small, finely distributed, hard and very temperature-resistant nitride precipitates of these elements are formed. These provide precipitation hardening and thus an increase in hardness and strength. [Lie14]

Further effects of the special nitrides are partly massive volume changes, which lead to large lattice deformations and residual compressive stresses [Oet91]. These lead to an increase in fatigue strength [Den02], [Mac82].

The typical plasma treatment process is as follows: A vacuum is created in the vessel chamber and the components are heated to the requested temperature using an external heater. Now the nitrogen-hydrogen atmosphere is let in and the plasma is ignited to start the nitriding process. During the nitriding process itself, the formation of the nitrided zone can be influenced by varying the temperature, time, pressure, pulse voltage, pulse duration, pulse pause and by the ratio of nitrogen to hydrogen. After completion of the actual nitriding process, the samples are cooled down in vacuum.

In plasma nitriding, attention is usually only paid to the treatment step and how it influences the nitriding result. It is mainly not discussed in which way other process steps influence the nitriding result. However, individual publications show the influence of the cooling step in gas nitriding [Bur92], [Jac95]. Burger was able to show that the composition of the compound layer varies depending on whether gas nitriding is cooled with ammonia or without ammonia. Own investigations were carried out to investigate whether cooling also has an influence in plasma nitriding. It was found that cooling mainly influences the thickness and the composition of the compound layer. The following figure

(**Fehler! Verweisquelle konnte nicht gefunden werden.**) shows the composition of a sample without and with annealing treatment. This annealing treatment was carried out directly after the nitriding treatment. There for, the temperature of 520°C was kept in vacuum for 4h.

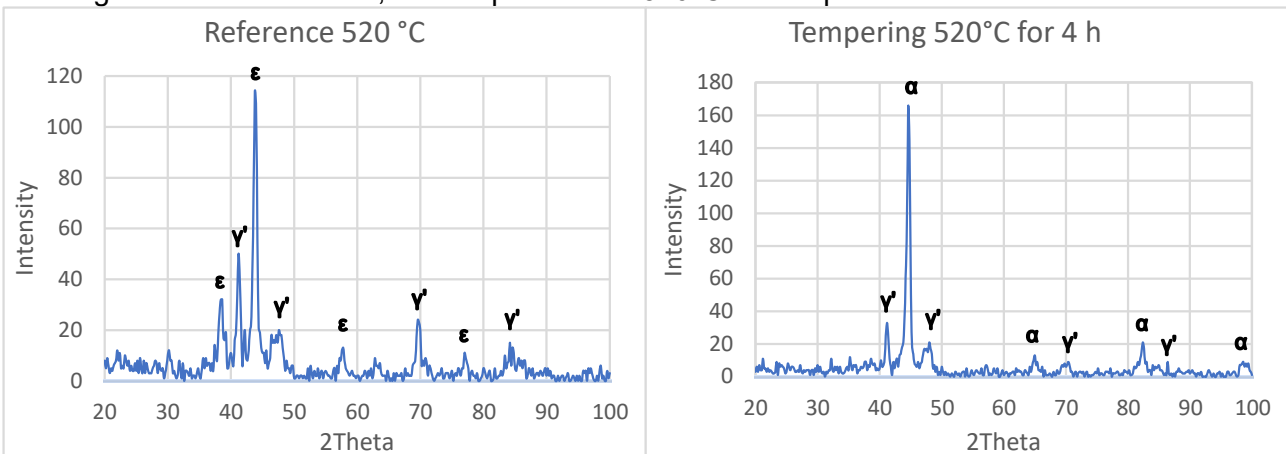


Figure 1: XRD measurements without tempering (left) and with tempering (right) of the 1.2343 sample

It could be seen that a degradation of the compound layer occurs and that this phenomenon plays a role in plasma nitriding processes. In the reference, there is a strong ϵ containing compound layer and after annealing it consists almost of alpha iron (α) and a small amount of γ' -nitride. This degradation of the compound layer should be reproduced in detail and therefore a series of XRD measurements was carried out at DELTA.

Experimental

For this series of tests, the same steel (DIN 1.2343, X37CrMoV5-1) was used as in the preliminary tests.

Table 1: composition of the ferritic martensitic steel 1.2343 [Weg19]

Elements	C	Si	Mn	Cr	Mo	V	Fe
Content in m. %	0,36 - 0,42	0,90 - 1,20	0,30 - 0,50	4,80 - 5,50	1,10 - 1,40	0,25 - 0,50	Bal.

These samples were nitrided in a warm-wall plasma nitriding system. The parameters were as follows:

Table 2: parameters for plasma nitriding

Temperature	480 °C
Time	12 h
Pressure	300 Pa
Voltage	500 V
Gas atmosphere	80% N ₂ , 20% H ₂
Pulse pause ratio	100 μ s to 300 μ s

This resulted in an almost pure ϵ -nitride compound layer on the surface. In the next step this sample was heated to 500°C in a vacuum and were analyzed every 15 min. over 3 h. Afterwards, the sample was heated up to 600°C and were tempered for 1 h. In this way, the degradation of the ϵ -nitride into α - iron should be tracked.

Results and Discussion

First, the tests at 500°C are presented, followed by a discussion of the results of the experiments at 600°C.

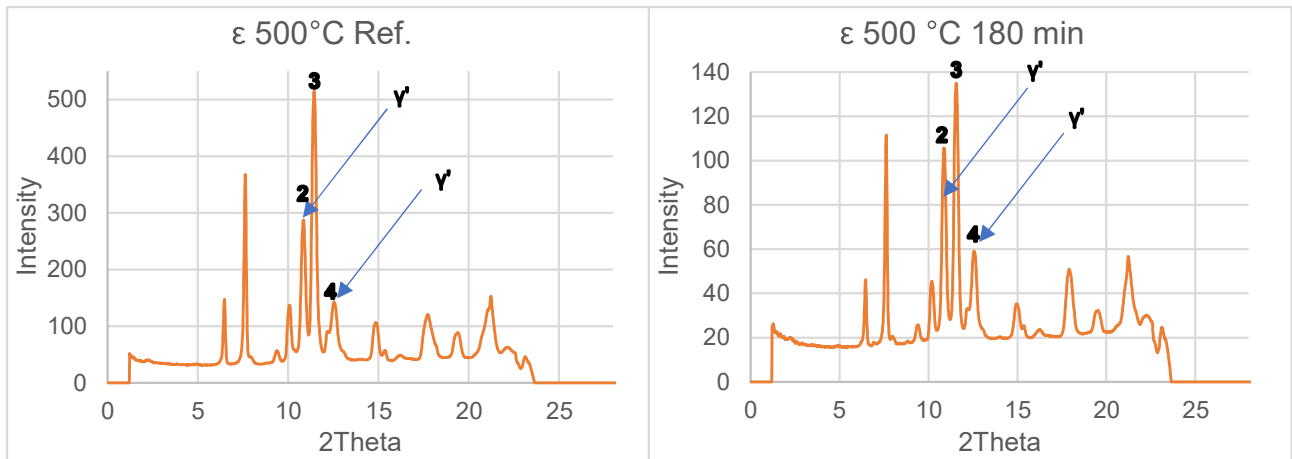


Figure 2: XRD measurements (DELTA), reference (left), after 180 min with 500°C (right)

Relatively small changes occurred in the head treatments at 500 °C. Nevertheless, a change in the peaks is visible. The peaks for ε-nitride decrease slightly and the peaks for γ'-nitride increase (see Figure 2).

A closer look at the peak ratios between ε- and γ'-peaks reveals that there are changes towards a higher fraction of γ'. This is shown in the following table:

Table 3: Peak intensity of the sample after specific tempering time and their ratios to each other

Tempering Time [min.]	Peak 2 (γ)	Peak 3 (ε)	Peak 4 (γ)	3 to 2 ratio	3 to 4 ratio
0	287	514	142	1,8	3,6
60	229	385	115	1,7	3,3
120	154	240	82	1,6	2,9
150	124	178	67	1,4	2,7
180	104	135	58	1,3	2,3

The changes that occurred during this period are significantly less than had been expected with regard to the preliminary tests, where a nearly complete decomposition of the compound layer occurred after 4 h with 520°C.

After increasing the temperature to 600°C, a clear change in composition was noticeable.

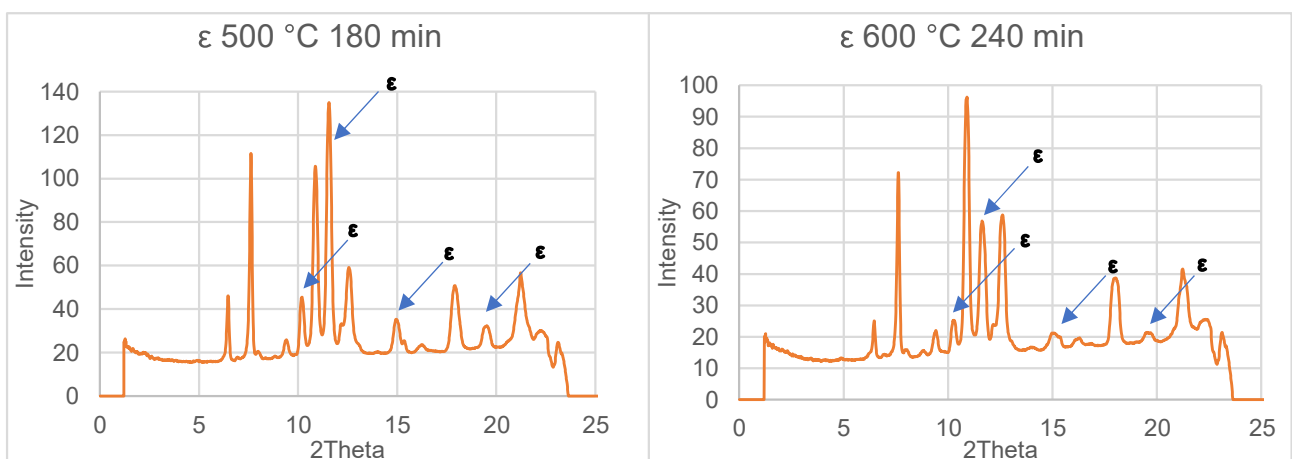


Figure 3 XRD measurements (DELTA), after 180 min with 500°C (left), after 1 h with 600°C (240 min total time) (right)

All peaks associated with ε-nitride have decreased significantly and, in some cases, have almost completely disappeared (see Figure 3). This shows a major shift of phase composition in the compound layer from ε to γ'. A degradation of the compound layer towards α-iron is not visible.

Even though a degradation of the ε-nitride compound layer could be clearly demonstrated, a big difference was found in the results of the own preliminary tests and the investigations at DELTA. In contrast to the own preliminary tests, the transformations occurred much slower. After 3 h at 500°C,

there was only a slight transformation in the direction of γ' -nitride, whereas in our own preliminary tests at 520°C and 4 h (see *Figure 1*), an almost complete decomposition of the compound layer was observed. The reasons for these differences still need to be discussed.

Conclusions

Due to the differences in the results between the preliminary tests and the tests carried out, it is difficult to make a conclusive statement on the results.

Nevertheless, it could be shown that a degradation of the ϵ -nitride compound layer occurs and that it transforms into a γ' -nitride compound layer. Accordingly, the degradation of the compound layer can be confirmed in principle and thus the cooling conditions should also be considered for the nitriding result in plasma nitriding processes, as they can influence the composition of the compound layer in plasma nitriding processes.

Acknowledgment

We kindly acknowledge the support of the DELTA machine group and the provided synchrotron radiation.

Literature

- [Bla10] Blasek, G.; Bräuer, G.: Vakuuum - Plasma - Technologien. Beschichtung und Modifizierung von Oberflächen. Leuze, Bad Saulgau, 2010.
- [Bur92] Burger, W.; Reichert, P.; Ziese, J.: Einfluß verschiedener Abkühlatmosphären beim Gas nitrocarbieren auf den Verbindungsschichtaufbau. HTM 6/47, S. 331–336, 1992.
- [Den02] Dengel, D.: Zur Dauerfestigkeit nitrierter Stähle. HTM Z. Werkst. Wärmebeh. Fertigung 57 5, S. 316–326, 2002.
- [Hof96] Hoffmann, R.; Mittemeijer, E.; Somers, M. A. J.: Verbindungsschichtbildung beim Nitrieren und Nitrocarbieren. HTM Härtereitechnische Mitteilungen 51 Nr. 3, S. 162–165, 1996.
- [Hof97] Hoffmann, F. et al.: Verschleißwiderstand nitrierter und nitrocarbierter Stähle. HTM Härtereitechnische Mitteilungen 52, S. 376–386, 1997.
- [Jac95] Jacobs, H.; Rechenbach, D.; Zachwieja, U.: Untersuchungen zur Struktur und zum Zerfall von Eisennitriden: γ' -Fe₄N und ϵ -FeN. HTM 4/50, S. 205–213, 1995.
- [Kar92] Karamiş, M. B.: Some effects of the plasma nitriding process on layer properties. Thin Solid Films 217, S. 38–47, 1992.
- [Lie14] Liedtke, D.: Wärmebehandlung von Eisenwerkstoffen. expert-Verl, Renningen, 2014.
- [Mac82] Macherauch, E.; Kloos, K. H.: Bewertung von Eigenspannungen: Eigenspannungen und Lastspannungen, S. 175–194, 1982.
- [Oet91] Oettel, H.; Schreiber, G.: Eigenspannungsbildung in der Diffusionszone: Nitrieren und Nitrocarbieren, S. 139–151, 1991.
- [Pas12] Paschke, H. et al.: Optimized plasma nitriding processes for efficient wear reduction of forging dies. Archives of civil and mechanical engineering 4/12, S. 407–412, 2012.
- [Spi86] Spies, H.-J.: Einfluss des Gasnitrierens auf die Eigenschaften der Randschicht von Eisenwerkstoffen. Freiburger Forschungshefte 249/B, S. 8–21, 1986.
- [Weg19] Wegst, C.; Wegst, M.: Stahlschlüssel. Verlag Stahlschlüssel Wegst GmbH, Marbach, 2019.

Synthesis of sulfur-containing nanoparticles based on Cu and Mo

Wolfgang Tillmann¹, David Kokalj^{1*}, Finn Ontrup¹, Julia Urbanczyk¹
Christian Sternemann², Michael Paulus²

¹Institute of Materials Engineering, TU Dortmund University, Germany
44227 Dortmund, Leonhard-Euler-Straße 2

²Fakultät Physik / DELTA, TU Dortmund University, Germany
44227 Dortmund, Maria-Goeppert-Mayer-Straße 2

* corresponding author: david.kokalj@tu-dortmund.de

For highly stressed surfaces, especially for forming or cutting tools enhanced service times and lower frictional forces are required, which can be met by means of thin-film technology. In this respect, doping of transition metal nitride thin films with Cu [1] and MoS₂ [2] represents an established concept for friction reduction. However, when sputtering MoS₂ in nitrogen-containing environments, nitrogen is incorporated in the MoS₂ crystal by substituting sulfur, so that the S/Mo ratio is changed [3]. As a consequence, increased friction coefficients are reported [4].

In a previous study [5] it was shown that a hybrid approach consisting of the injection of nanoparticles into sputtered thin films can be used to generate multiphase nanocomposite films without the chemistry of the respective phase components being affected by the other components. Therefore, the first step of this study is to determine whether nanoparticles of the friction-reducing materials Cu and MoS₂ can be produced by means of arc synthesis in order to embed them in wear-resistant nitride thin films in the next step.

The nanoparticles based on Cu and Mo were synthesized using an atmospheric arc discharge reactor. In general, the reactor system consists of the chamber, a power source, a gas supply, and a horizontally arranged tungsten cathode. The anode is oriented perpendicular to the cathode. The anode comprises the material, which is vaporized during nanoparticle synthesis and can be vertically positioned, relative to the cathode by means of a micrometer drive. A plasma cutter (S-Plasma 85CNC, Stamos Welding Group, Germany) acts as the power source for the cathode and anode. The detailed setup of the reactor and a description of the process are explained in more detail in [6]. The Cu and Mo nanoparticles were synthesized using pure Cu and Mo rods. Since only electrically conductive materials can be processed by means of DC arc synthesis, the synthesis of MoS₂ nanoparticles represents a challenge. Hence, the sulfur-containing nanoparticles were prepared using two-phase Cu-MoS₂ and Mo-MoS₂ composite rods, in which the Cu and Mo components ensure the electrical conductivity. All nanoparticles were produced in an atmosphere containing Ar and N₂. The exact production parameters of the nanoparticles and the explanation of the production of the composite rods can be taken from [7] and [8].

The phase analysis of the nanoparticles was performed at the beamline BL9 using a photon energy of 27 keV ($\lambda = 45.9$ pm). In order to be able to study the structure of the nanoparticles in transmission, they were injected into XRD capillaries (Hilgenberg GmbH, Germany) with an outer diameter of 1.0 mm and a wall thickness of 0.01 mm. For photon detection an image plate detector MAR345 (marXperts GmbH, Germany) was used. The plotted diffraction patterns were converted to a wavelength of $\lambda = 154.1$ pm (Cu-K α_1).

The results of the diffraction experiments are presented in Fig. 1. The diffractogram of the Cu nanoparticles exhibits three reflections in the investigated range at $2\theta \sim 43.3^\circ$, 50.4° , and 74.1° , that can be assigned to the cubic Cu phase of the space group (225). Based on the diffractogram of the Mo nanoparticles, a single-phase structure of the cubic Mo phase (space group (229)) can be assigned to them. Although a gas mixture of argon and nitrogen gas was used for the synthesis of the Mo nanoparticles, no molybdenum nitrides formed as intended. Based on the Richardson

equation, a current of $I = 15$ A results in a cathode temperature of ~ 2600 °C, which corresponds to the melting point of molybdenum. The γ - Mo_2N phase reveals a lower melting temperature of ~ 2000 °C [9], so that a reduction of the γ - Mo_2N phase to Mo is possible at the calculated cathode temperature, which explains the absence of a molybdenum nitride phase.

In contrast to the Cu and Mo nanoparticles, the sulfur-containing nanoparticles reveal a multiphase structure. The Cu-MoS₂ nanoparticles do not show the phases present in the rods, so that a reaction between Cu and MoS₂ has taken place during nanoparticle synthesis. The Bragg reflections can be assigned to the hexagonal CuS phase of the space group (194). Other reflections correspond to the cubic Cu_{7.2}S₄ phase of the space group (225). Based on the present phase composition, the MoS₂ phase is expected to decay during the synthesis of the nanoparticles due to the different vapor pressures of Mo and S. Since Cu shows a lower vaporization temperature than Mo at atmospheric pressure, more Cu than Mo is vaporized. Therefore, the resulting metal vapor of Cu and S enables the formation of the intermetallic CuS and Cu_{7.2}S₄ phases.

The diffractogram of Mo-MoS₂ nanoparticles also shows numerous reflections. These reflections represent the rhombohedral MoS₂ and Mo₃S₄ phases of the space group (160), which resemble the hexagonal crystal system. In addition, small amounts of metallic molybdenum can be detected. Therefore, the ratio of Mo to MoS₂ in the rod must be set precisely so that the desired MoS_x phase is formed depending on the different evaporation properties of Mo and S after the decomposition of the MoS₂ phase. The reflections of the MoS_x phases are superimposed by the molybdenum oxides Mo₄O₁₁ and Mo₉O₂₅, which are so-called Magnéli phases.

In summary, single-phase Cu and Mo nanoparticles, which can be used for friction reduction, can be prepared by arc synthesis. In contrast, nanoparticles based on Cu-MoS₂ and Mo-MoS₂ do not reveal a single-phase crystal structure, which furthermore differs from the physical structure of the used rods. However, the Cu-MoS₂ and Mo-MoS₂ nanoparticles reveal phase components that also exhibit friction-reducing properties.

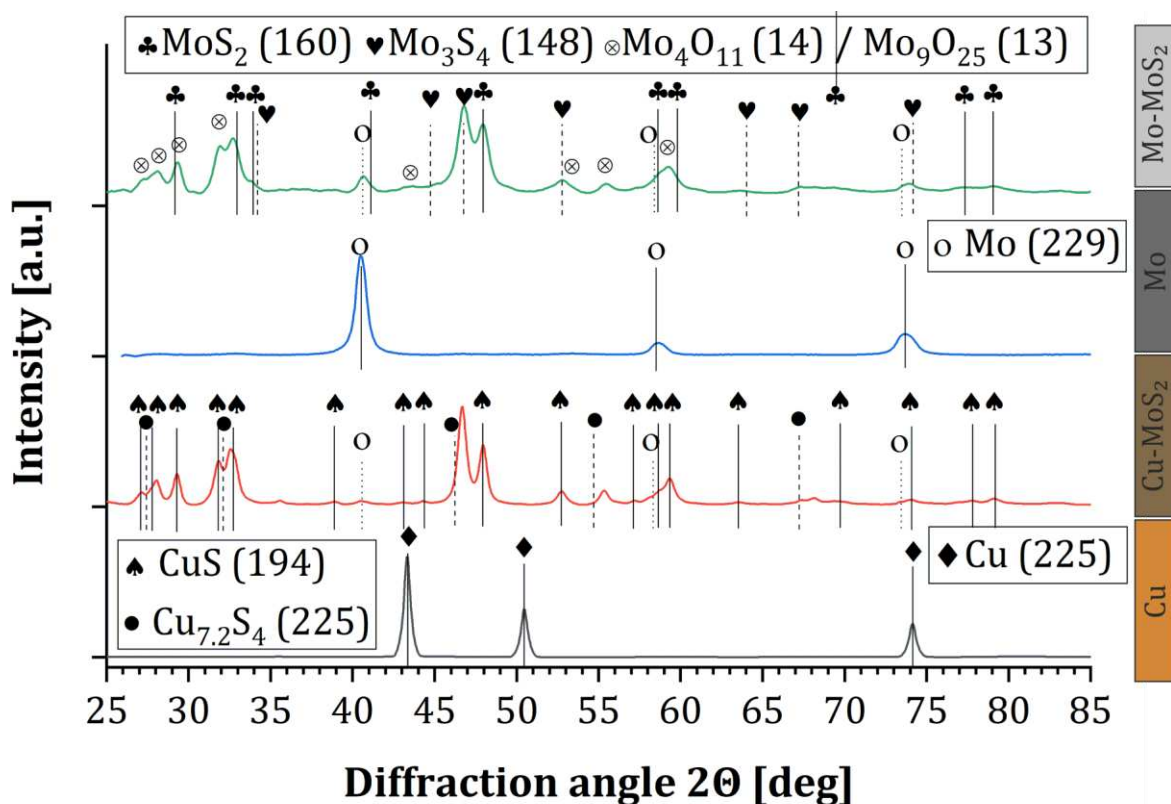


Fig. 1: XRD pattern of the synthesized Cu, Cu-MoS₂, Mo und Mo-MoS₂ nanoparticles (from bottom to top).

Acknowledgements

The authors gratefully acknowledge the DELTA machine group for providing synchrotron radiation and their support at Beamline BL9.

References

- [1] X. Xu, F. Su, Z. Li, Microstructure and tribological behaviors of MoN-Cu nanocomposite coatings sliding against Si₃N₄ ball under dry and oil-lubricated conditions, *Wear* 434-435 (2019) 202994. <https://doi.org/10.1016/j.wear.2019.202994>.
- [2] D. Kokalj, J. Debus, D. Stangier, H. Moldenhauer, A. Nikolov, A. Wittig, A. Brümmer, W. Tillmann, Controlling the Structural, Mechanical and Frictional Properties of MoS_x Coatings by High-Power Impulse Magnetron Sputtering, *Coatings* 10 (2020) 755. <https://doi.org/10.3390/coatings10080755>.
- [3] X. Zhang, L. Qiao, L. Chai, J. Xu, L. Shi, P. Wang, Structural, mechanical and tribological properties of Mo-S-N solid lubricant films, *Surface and Coatings Technology* 296 (2016) 185–191. <https://doi.org/10.1016/j.surfcoat.2016.04.040>.
- [4] W. Tillmann, A. Wittig, H. Moldenhauer, C.-A. Thomann, J. Debus, D. Aurich, A. Bruemmer, Nitrogen doping of MoS_x thin films sputtered by reactive High Power Impulse Magnetron Sputtering, *Thin Solid Films* 713 (2020) 138267. <https://doi.org/10.1016/j.tsf.2020.138267>.
- [5] W. Tillmann, D. Kokalj, D. Stangier, Q. Fu, F.E. Kruis, L. Kesper, U. Berges, C. Westphal, On the synthesis and structural evolution of artificial CrN/TiN nanocomposites, *Applied Surface Science* 535 (2021) 147736. <https://doi.org/10.1016/j.apsusc.2020.147736>.
- [6] M. Stein, F.E. Kruis, Optimization of a transferred arc reactor for metal nanoparticle synthesis, *J Nanopart Res* 18 (2016) 258. <https://doi.org/10.1007/s11051-016-3559-y>.
- [7] J. Urbanczyk, Synthese und Analyse von MoN-basierenden Kompositschichten mittels Injektion von Nanopartikeln auf Basis von Übergangsmetallnitriden. Masterarbeit, Dortmund, 2022.
- [8] F. Ontrup, Synthese und Analyse von MoN-basierenden Kompositschichten mittels Injektion von Cu-MoS₂ Nanopartikeln. Masterarbeit, Dortmund, 2022.
- [9] H. Jehn, P. Ettmayer, The molybdenum-nitrogen phase diagram, *Journal of the Less Common Metals* 58 (1978) 85–98. [https://doi.org/10.1016/0022-5088\(78\)90073-5](https://doi.org/10.1016/0022-5088(78)90073-5).

Advanced Arc-Enhanced Glow Discharge Etching High-Speed Tool Steel Substrates for PVD Deposition of TiAlN

Dominic Stangier^{1*}, Nelson Filipe Lopes Dias¹, Christian Sternemann²,
Michael Paulus², Wolfgang Tillmann¹

¹Institute of Materials Engineering, TU Dortmund University, Germany
44227 Dortmund, Leonhard-Euler-Straße 2

²Fakultät Physik / DELTA, TU Dortmund University, Germany
44227 Dortmund, Maria-Goeppert-Mayer-Straße 2

*corresponding author: dominic.stangier@tu-dortmund.de

In thin film technology, especially physical vapor deposition (PVD), the process parameters as well as the resulting coating properties have been subject of many research activities [BOB17]. However, limited attention is paid to the plasma based pre-treatment of the substrate material by ions prior to the deposition process, which plays a crucial role for the adhesion of the coating system and therefore for the overall performance of the substrate coating compound [TIL19b]. In order to ensure a high adhesion, the natural oxide layers as well as residuals or other surface contaminations need to be removed. For this reason, the performed etching process needs to be specifically adapted for the substrate material and the subsequently applied coating systems. For cemented carbide tools, Breidentein et al. showed the significance of residual stress along the process chain and their influence on the coating adhesion for different pre-treatments [BRE13]. The same correlations were observed by Tillmann et al. who had a closer look at noble gas etching and metal ion etching of nano-grained WC-Co showing an improved adhesion for CrAlN coatings [TIL19a]. The differences in the topography are in direct correlation to the observations by Bouzakis et al. and Alves et al. who reported about the removal of the Co matrix material [BOU10, ALV17]. Similar findings for the ion etching process are reported by Gassner et al., who additionally found an influence of the applied bias voltage on the shape of the WC grains [GAS17]. Nevertheless, only limited information can be found about the plasma based etching process for high-speed tool steels. For this reason, the influence of different bias voltage levels for a highly efficient etching process is presented and evaluated in terms of the interactions of the subsequent deposition of a TiAlN coating.

The investigations were carried out in an industrial coating device METAPLAS.DOMINO kila flex (Oerlikon Balzers, Liechtenstein) which is equipped with an arc-enhanced glow discharge (AEGD) etching module as electron source. For the advanced etching options, the evaporators are switched to anodes during the etching process. The surface treatment is conducted for one hour using the different bias levels of $U_B = -100$ V, $U_B = -200$ V, $U_B = -300$ V, $U_B = -400$ V and $U_B = -500$ V. Each substrate condition was realized for the etched surface as well as for

the subsequent deposition of the TiAlN coating by arc evaporation using APA evaporators with electromagnetic coil systems. Coin shaped samples made out of AISI M2 with a diameter of $D = 30$ mm were used as substrate material. The XRD measurements at DELTA are performed at beamline BL9 using a photon energy of $E = 20$ keV ($\lambda = 0.6199$ Å) and the 2D image plate detector MAR345. The angle of incidence was set to $\omega = 0.5^\circ$ with an exposure time of $t = 300$ s.

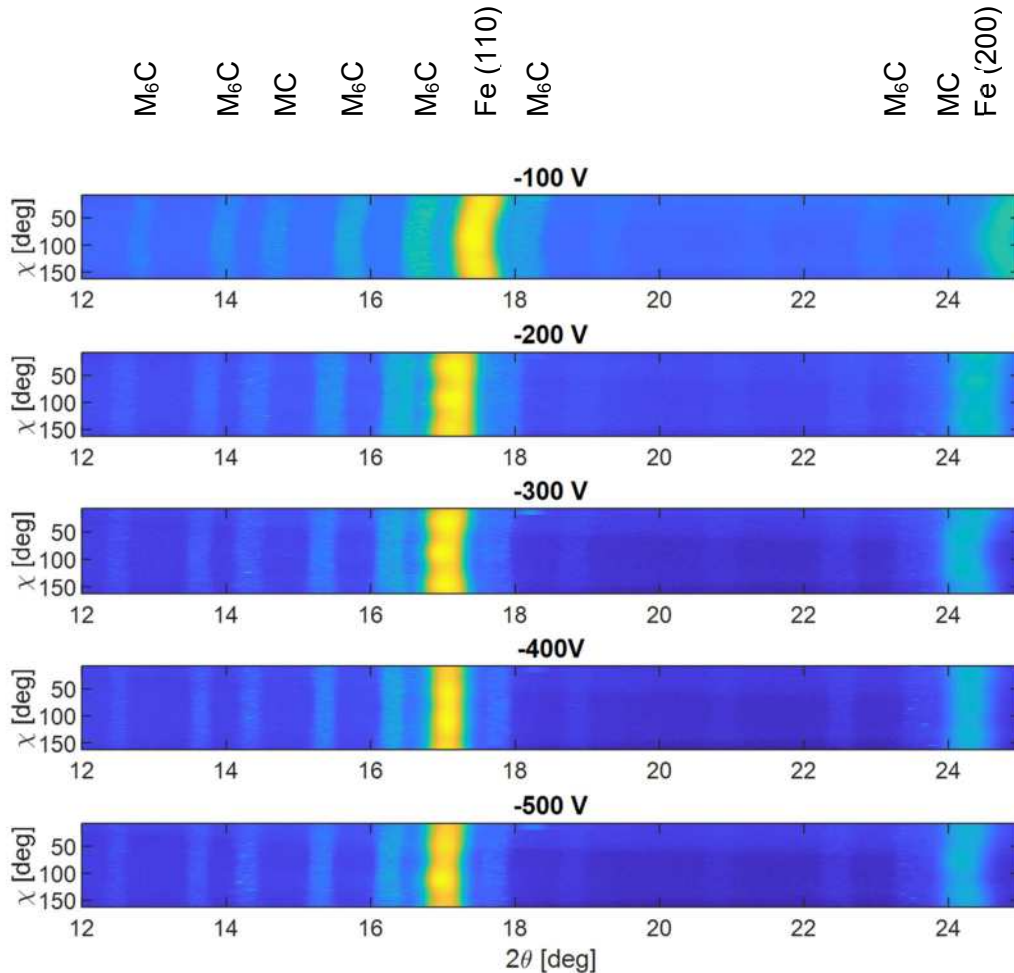


Figure 1: 2D-GIXRD logarithmic scaled diffraction patterns ($\lambda = 0.6199$ Å; $E = 20$ keV) of the AISI M2 substrates after the advanced AEGD etching process

The diffraction patterns, as presented in Figure 1, show the influence of the bias voltage on the crystalline structure of the surface region in dependency of the applied bias voltage during the etching process. As expected the cubic phase with a dominant (111)-orientation for the Fe Bragg reflection is noticed as well as small intensities of different carbides. Furthermore, the results can be separated in two groups with a threshold of $U_B = -200$ V. On the one side, the patterns show a similar behavior for higher bias voltages and, on the other side, a shift to higher 2Θ values is observed for the lowest bias potential. This behavior can be explained by the lower kinetic energy, which does not lead to a material removal on the surface of the substrate material. The densification in combination with the induced defects lead to the observed shift of the pattern. These findings are in direct correlation to the model introduced by Anders, which shows a transition from coating to etching in dependency of the kinetic energy [AND10]. In this regard, higher bias voltages lead to the desired etching process and

removal of the substrate material. This can be underlined by the narrowing of the Bragg-reflection of the Fe (111)-orientation with increasing bias voltages, which leads to healing effects caused by the additional heat input.

In addition to the investigation of the substrate material, the subsequently applied TiAlN coatings was also investigated. The results are illustrated in Figure 2 proving the findings of the etching process. Although the substrate material was differently treated, the PVD coatings show a similar crystalline structure. All coatings consist of fcc-TiAlN phase with a dominant (200)-orientation, which is characteristic for ternary nitrides. Therefore, one may conclude, that the growth as well as the properties of the PVD coating are not affected by the plasma based pre-treatment. Additionally, the previously induced stresses by the lower bias voltage are still present in the substrate after the deposition of the coating.

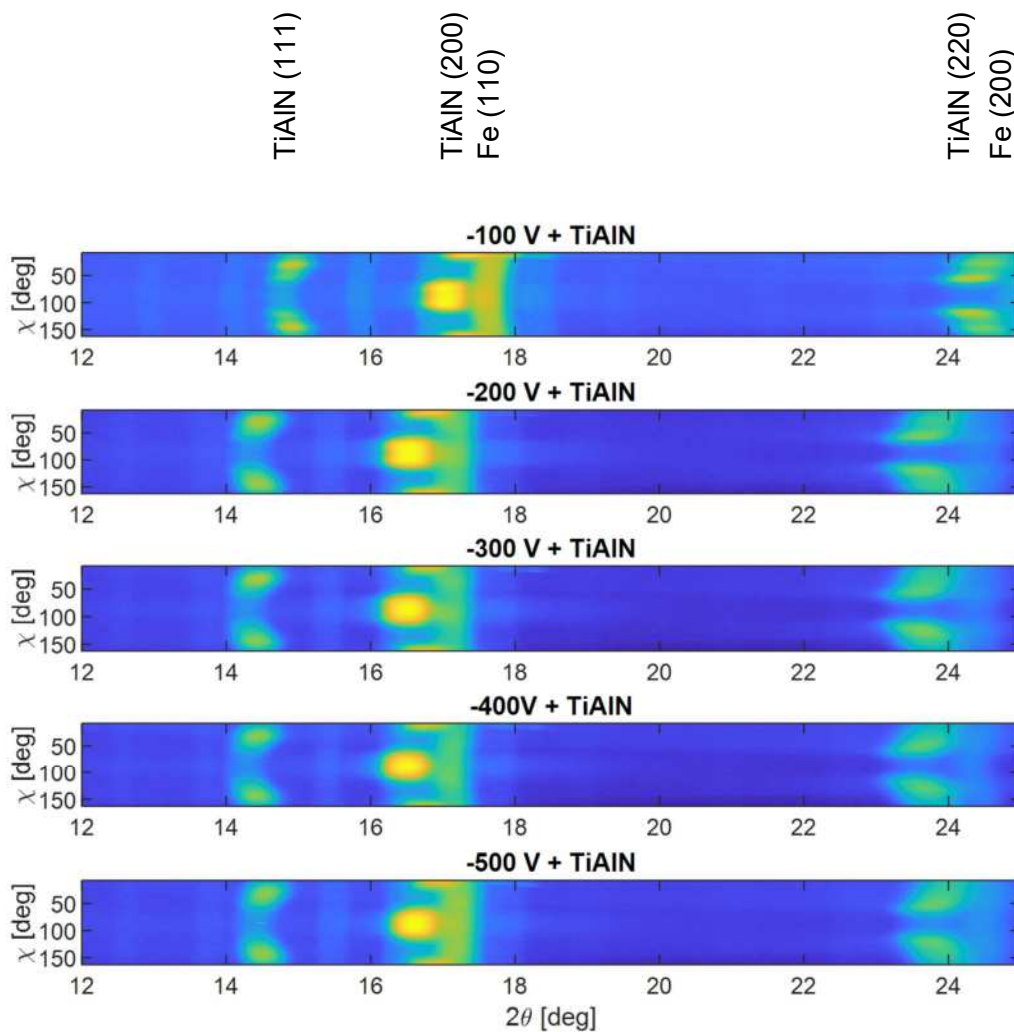


Figure 2: 2D-GIXRD diffraction patterns of the etched and TiAlN coated substrate material ($\lambda = 0.6199 \text{ \AA}$; $E = 20 \text{ keV}$) measured with an angle of incidence of $\omega = 0.5^\circ$ plotted as a function of the azimuth angle in dependency of the scattering angle 2Θ

Summarizing the findings of the study, advanced AEGD etching is a highly promising technology for the pre-treatment of substrate materials, especially high-speed steels. The kinetic

energy level can be adjusted by changing the bias voltage, which results in a good etching of the surface. Further investigations in terms of coating adhesion and depth resolved residuals stresses should be performed.

Acknowledgements

The authors gratefully acknowledge the DELTA machine group for providing synchrotron radiation at BL9 and the German Research Foundation for the financial support of the project (TI 343/187-1; project number 445127534) “Effects and interactions for interface and cutting-edge conditioning in hard machining”.

References

- [ALV17] Alves, S. M.; Albano, W.; Oliveira, A. J. de: *Improvement of coating adhesion on cemented carbide tools by plasma etching*, Journal of the Brazilian Society of Mechanical Sciences and Engineering, 39 (2017), S. 845–856.
- [AND10] Anders, A.: *A structure zone diagram including plasma-based deposition and ion etching*, Thin Solid Films, 518 (2010), S. 4087–4090.
- [BOB17] Bobzin, K.: *High-performance coatings for cutting tools*, CIRP Journal of Manufacturing Science and Technology, 18 (2017), S. 1–9.
- [BOU10] Bouzakis, K.-D.; Makrimalakis, S.; Katirtzoglou, G.; Skordaris, G.; Gerardis, S.; Bouzakis, E.; Leyendecker, T.; Bolz, S.; Koelker, W.: *Adaption of graded Cr/CrN-interlayer thickness to cemented carbide substrates' roughness for improving the adhesion of HPPMS PVD films and the cutting performance*, Surface and Coatings Technology, 205 (2010), S. 1564–1570.
- [BRE13] Breidenstein, B.; Denkena, B.: *Significance of residual stress in PVD-coated carbide cutting tools*, CIRP Annals - Manufacturing Technology, 62 (2013), S. 67–70.
- [GAS17] Gassner, M.; Schalk, N.; Sartory, B.; Pohler, M.; Czettel, C.; Mitterer, C.: *Influence of Ar ion etching on the surface topography of cemented carbide cutting inserts*, International Journal of Refractory Metals and Hard Materials, 69 (2017), S. 234–239.
- [TIL19a] Tillmann, W.; Hagen, L.; Stangier, D.; Krabiell, M.; Schröder, P.; Tiller, J.; Krumm, C.; Sternemann, C.; Paulus, M.; Elbers, M.: *Influence of etching-pretreatment on nano-grained WC-Co surfaces and properties of PVD/HVOF duplex coatings*, Surface & Coatings Technology, 374 (2019), S. 32–43.
- [TIL19b] Tillmann, W.; Grisales, D.; Stangier, D.; Ben Jebara, I.; Kang, H.: *Influence of the etching processes on the adhesion of TiAlN coatings deposited by DCMS, HiPIMS and hybrid techniques on heat treated AISI H11*, Surface & Coatings Technology, 378 (2019), 125075.

An X-ray diffraction study on AlCrVYN thin films

Eric Schneider¹, Finn Ontrup², Nicola Thiering¹, Susanne Dogan¹, Jaqueline Savelkouls¹
Kevin Lehninger¹, Christian Sternemann¹, Michael Paulus¹, Nelson Filipe Lopes Dias²
Wolfgang Tillmann², Metin Tolan¹

¹Fakultät Physik/DELTA, TU Dortmund University, 44221 Dortmund, Germany

²Fakultät Maschinenbau, Institute of Materials Engineering, TU Dortmund University, 44221 Dortmund, Germany

In production engineering, major efforts are made to optimize tool coatings for applications exposed to elevated process temperatures. A specific focus lies especially on dry machining or machining with minimum quantity lubrication. Thus, depending on the material and tool design such as the shape of the cutting edge, temperatures between 300°C and 1000°C can occur during turning operations [1]. In order to enable machining of high-strength materials, the high-temperature properties of the tool coatings need to be tailored according to the application. The addition of vanadium to AlCrN favours the formation of so-called Magneli phases to reduce the friction at high temperatures [2], whereas small amounts of yttrium improves the oxidation resistance [3]. The aim of this project is to obtain a fundamental understanding of the dependence between deposition parameters, coating structure, and oxidation behavior.

For the X-ray diffraction (XRD) studies, AlCrVYN thin films were deposited on WC-Co substrates by high power impulse magnetron sputtering (HiPIMS) with varying pulse length t (40 and 80 μ s) and pulse frequency f (500, 1000, and 2000 Hz). Both parameters control the duty cycle (on-time) of the magnetron cathode. During the XRD measurements, the coated WC-Co substrates were stepwise heated, between 25°C and 1000°C, in an Anton Paar heating cell. Furthermore, selected samples were annealed *ex situ*. Figure 1 shows the setup used at beamline BL9 at DELTA. We used a photon energy of 27 keV and a beam size of 1.5 x 0.1 mm² (h x v). The scattered intensity was detected by a MAR345 image plate detector.

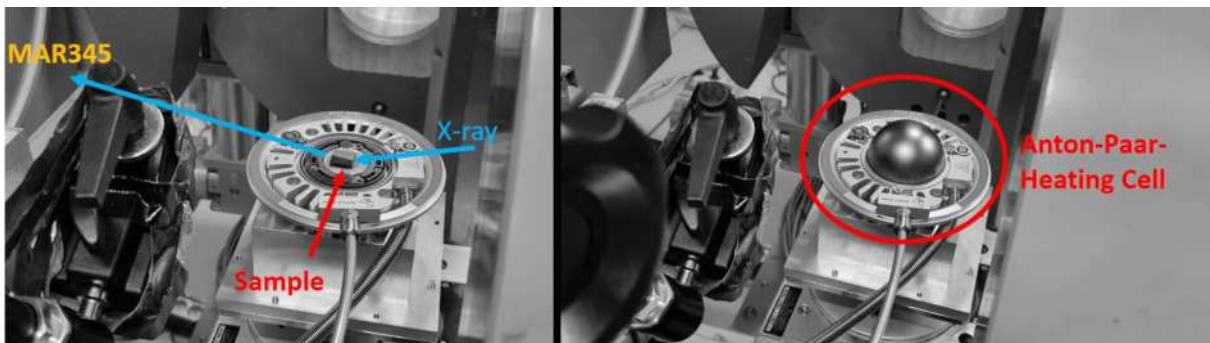


Figure 1: Heating-setup at beamline BL9. Left: Installed sample without graphite dome. Right: After installation of the graphite dome for heating above 200°C.

An evaluation of the data shows clear dependency on the manufacturing parameters of both the thermal stability of the samples and the occurrence of residual stresses in the layer. Figure 2 compares the diffraction patterns of the samples prepared with different deposition parameters. We observe textured Bragg reflections of the layer. The relatively weak and azimuthally inhomogeneous signal of the Co matrix in which the WC is embedded can be seen. In figure 2, the 2D diffraction images were integrated either in the horizontal or in the vertical scattering plane to plot the intensity of all samples as a function of 2θ . It turns out, that the CrN (222) reflection is shifted between the horizontal and the vertical scattering plane. That clearly shows the presence of residual stress within the layer.

Besides the influence of the deposition parameters on the structure of the thin films, their oxidation behavior was also investigated. Between 800°C and 850°C, the oxidation of the thin films sets in for all

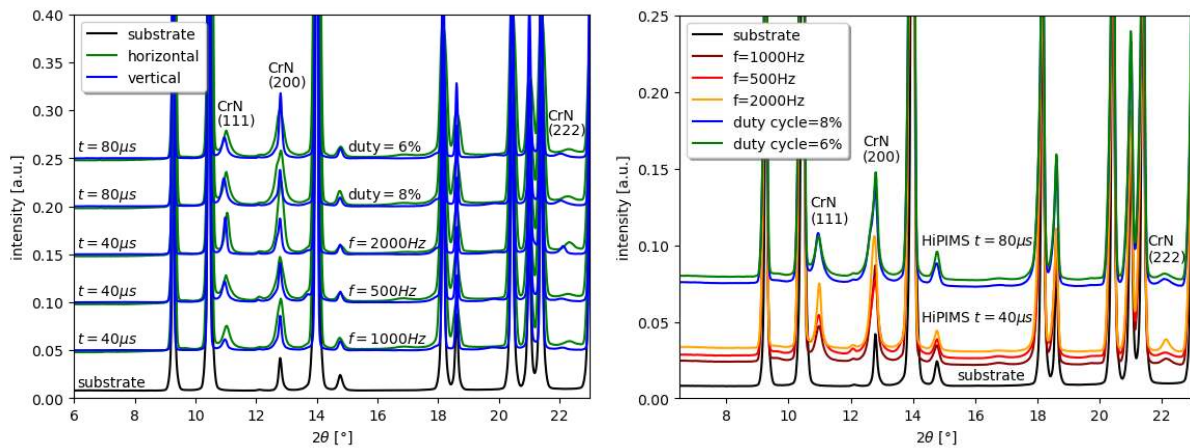


Figure 2: Left: Comparison between diffraction patterns obtained by integration of the 2D diffraction images in the horizontal and vertical scattering plane for different production parameters. Right: Comparison of the total diffractograms of the different samples. The labelling of the data shows the different deposition parameters.

samples. For a detailed study of the oxidation process, the samples were compared after *ex situ* heating to 850°C (see figure 3). In contrast to the results presented in figure 2 at room temperature, the heated samples show significantly more reflections, which can be attributed to the oxidation process. It is noticeable here that the sample produced with the highest (lowest) HiPIMS frequency has the lowest (highest) number of additional reflections indicating different state of oxidation. The large number of oxide phases potentially being present in the layer complicates a phase analysis of the

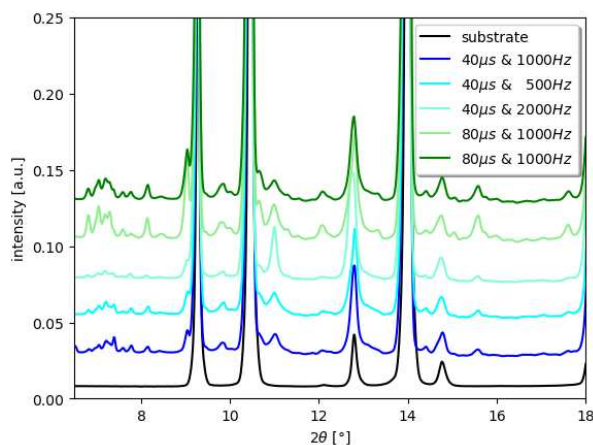


Figure 3: Comparison of the oxidation process of the samples after ex-situ heating to 850°C.

XRD measurements. For this reason, further measurements with XANES (X-ray absorption near-edge structure spectroscopy) were carried out at BL10 of DELTA to better constrain the appearance of oxides in the samples.

References

- [1] K.-M. Li, S.Y. Liang, Modeling of Cutting Temperature in Near Dry Machining, *J. Manuf. Sci. Eng.* 128 (2006) 416–424.
- [2] W. Tillmann, D. Kokalj, D. Stangier, M. Paulus, C. Sternemann, M. Tolan, Investigation on the oxidation behavior of AlCrVxN thin films by means of synchrotron radiation and influence on the high temperature friction, *Applied Surface Science*, Volume 427, Part B, 2018, Pages 511-521.
- [3] F. Rovere, P.H. Mayrhofer, A. Reinholdt, J. Mayer, J.M. Schneider, (2008): The effect of yttrium incorporation on the oxidation resistance of Cr–Al–N coatings. In: *Surface and Coatings Technology* 202, Issue 24, S. 5870-5875,

Acknowledgments

We thank the DELTA team for providing synchrotron radiation. This work was supported by the DFG via TO 169/21-1 and TI 343/190-1.

A study on the phase evolution in ID-HVOF sprayed coatings using WC-CoCr feedstocks with different WC particle sizes

Leif Hagen¹, Mark Dennis Kensy¹, Michael Paulus², Wolfgang Tillmann¹

¹Institute of Materials Engineering, TU Dortmund University, Germany
44227 Dortmund, Leonhard-Euler-Straße 2

²Fakultät Physik / DELTA, TU Dortmund University, Germany
44221 Dortmund

*corresponding author: leif.hagen@tu-dortmund.de

High velocity oxy-fuel (HVOF) spraying meets new challenges when it comes to the coating of inner surfaces of cylindrical parts such as landing gear components or extruder barrels. Technological challenges are largely related to the assembly space for depositing the coating as well as the associated stand-off distances required to ensure a sufficient heat and momentum transfer of spray particles. Enabling the coating of internal diameter (ID), the HVOF spray torch has to be smaller compared to conventional ones, while at the same time the component to be coated entails short spray distances. The compact design implies a lower torch power, resulting in reduced heat input into the spray particles at short stand-off distances. WC-CoCr coatings deposited by HVOF already become a promising candidate to protect tribologically stressed inner surfaces against wear. For ID HVOF spraying with limited assembly space, the use of fine-structured agglomerated and sintered WC-CoCr feedstocks, i.e. smaller WC-CoCr agglomerate sizes than those in the range of $-45 +15\mu\text{m}$, enables a sufficient heat and momentum transfer of spray particles even at short stand-off distances. Small WC-CoCr agglomerates, including submicron-sized WC particles, are prone to overheat during spraying, which in turn favours undesirable phase transformation processes, such as oxidation and decarburization. In particular, WC decomposition phenomena and the formation of W_2C and eta carbides (i.e. M_6C , M_{12}C phases, M = metal) impair the mechanical properties, and can thus be detrimental to the wear resistance of the tribologically stressed surfaces.

In order to examine the effect of the WC particle size on the phase evolution in ID HVOF sprayed WC-CoCr coatings, various agglomerated sintered WC-CoCr 86 10 4 feedstocks which are composed of different WC particle sizes, ranging from coarse sized (Fisher sub-sieve size (FSSS) = $2.5\ \mu\text{m}$, referred to as CS), medium sized (FSSS = $0.8\ \mu\text{m}$, referred to as MS) to fine sized (FSSS = $0.4\ \mu\text{m}$, referred to as FS), were utilized for the spraying experiments. In addition, an agglomerated sintered and plasma-spheroidized WC-CoCr 86 10 4 feedstock was used, providing a different particle morphology with fine-sized WC particles according to the manufacturer's specifications (FSSS = $1.5\ \mu\text{m}$, referred to as FS-P). The WC-CoCr agglomerates predominantly exhibit a spherical shape, but slightly differ in their microporosity. As verified by a Hall flowmeter, FS and MS exhibit an apparent density of $4.54\ \text{g}/\text{cm}^3$ and $4.67\ \text{g}/\text{cm}^3$, whereas CS and FS-P demonstrate an apparent density of $5.75\ \text{g}/\text{cm}^3$ and $5.99\ \text{g}/\text{cm}^3$, respectively. In preparation for the ID HVOF spraying experiments, round ($50\ \text{mm} \times 70\ \text{mm} \times 10\ \text{mm}$) 1.3343 high speed steel specimens were employed as substrates. Prior to

the coating deposition, the substrate surfaces were grit-blasted with corundum and cleaned in an ultrasonic ethanol bath. The ID-HVOF spraying system ID RED with the CPF2-Twin powder feeder system (Thermico, Germany), mounted on an industrial robot (type IRB4600/60, ABB, Switzerland), was utilized to conduct the spraying experiments. The spray parameter settings derived from preliminary tests. Here, the kerosene, oxygen, and hydrogen flow were set to 4.03 SLPH, 190 SLPM, and 130 SLPM, respectively. A powder feed rate of 20 g/min was used within the experiments, whereas the powder carrier gas flow was 8.0 SLPM, using nitrogen. Regarding the handling parameters of the spray torch, a spray distance of 65.17 mm and a gun velocity of 500 mm/s with a track pitch of 2 mm for the meander-shaped spray path were utilized to deposit the coatings. 20 passes were executed in order to generate an adequate coating thickness for FS, MS, CS and FS-P of approximately $194.0 \pm 3.8 \mu\text{m}$, $159.1 \pm 1.9 \mu\text{m}$, $86.1 \mu\text{m} \pm 2.0 \mu\text{m}$, and $184.0 \pm 1.8 \mu\text{m}$. To minimize the heat input into the substrate during spraying, a backside cooling was applied. The phase composition of both the WC-CoCr feedstocks and the ID HVOF sprayed WC-CoCr coatings was determined by means of X-ray diffraction (XRD) at the beamline BL9 of DELTA. The photon energy was set to 15 keV. The measurements were performed at an angle of incidence of 5° , whilst the beam-size was $0.2 \times 1.0 \text{ mm}^2$ (v x h). The samples were investigated using a PILATUS 100 k detector system (DECTRIS, Switzerland). To calibrate the setup, a LaB_6 reference was measured. The phase analysis was conducted with the program package Match! (CRYSTAL IMPACT, Germany) using the crystallographic open database [1]. To determine the crystallite size and residual microstresses (type II residual stresses), the program package MAUD [2] was used. The residual stress σ was finally determined by $\sigma = Y\varepsilon$ with the Young's modulus Y of the investigated material (703.2 GPa for WC [3]).

With regard to the diffractograms of the WC-CoCr feedstocks, clear Bragg reflections of hexagonal WC, cubic $\text{Co}_3\text{W}_3\text{C}$ are visible (see Figure 1). The presence of $\text{Co}_3\text{W}_3\text{C}$ in the

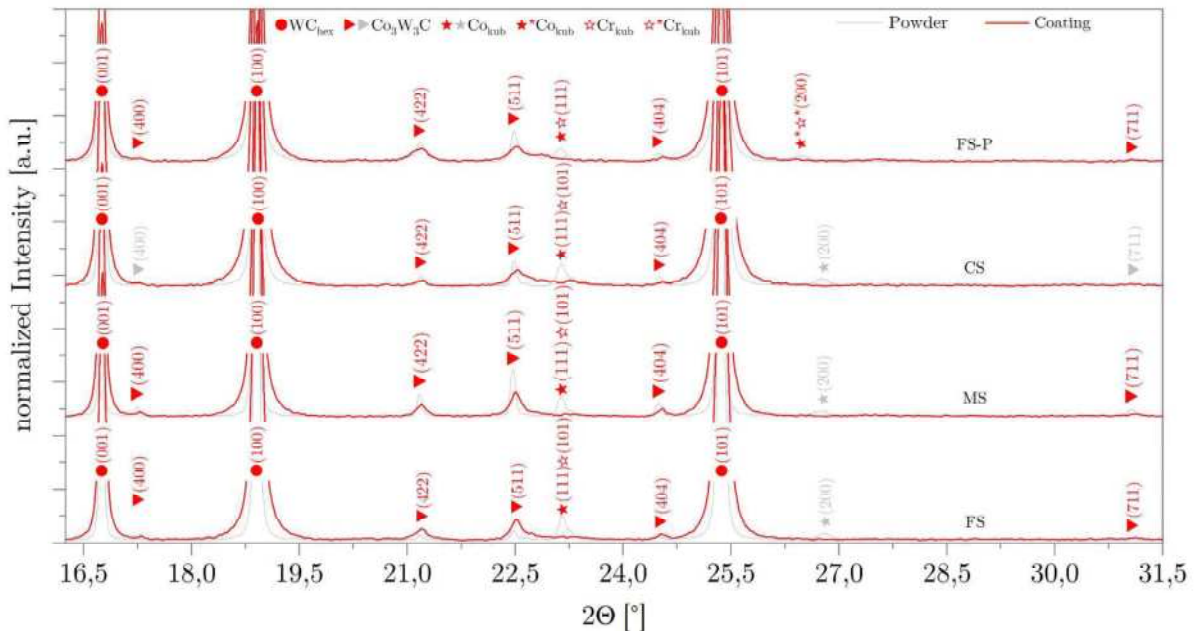


Figure 1: XRD patterns obtained from the WC-CoCr feedstocks as well as the produced WC-CoCr coatings.

starting powder is attributed to the manufacturing process. Furthermore, the spectra show reflections of cubic Co or Cr, which cannot be separated from each other due to their similar

lattice parameters. The sample FS-P shows a slight splitting of the Co/Cr reflections which can be explained by the presence of two different cubic phases with slightly varying lattice parameters (0.3588 nm; 0.36023 nm). The XRD patterns obtained from the different WC-CoCr coatings indicate the absence of further Bragg reflections. However, all WC-CoCr coatings show a clear decrease in the Co/Cr signal. Phase transformation processes caused by the coating process are therefore not recognizable. Nevertheless, it is noticeable that W_2C as well as Co_6W_6C cannot be found within the experimental resolution. It is known that Co_3W_3C and Co_6W_6C are thermodynamically stable, while Co_6W_6C is the most thermodynamically stable form. Moreover, MC-type carbides form preferably in reactions with W_2C rather than hexagonal WC. It is therefore assumed that the absence of W_2C and Co_6W_6C is due to the reduced heat input into the spray particles, which implies a short dwell time and low torch power.

Compared to the WC-CoCr feedstocks, a broadening of the Bragg reflections can be observed, which on the one hand indicates the occurrence of microstresses, and on the other hand a reduction in crystallite size. Analysing the widths of the WC reflections with the program package MAUD, information about the crystallite sizes and strain in the feedstock and the coating can be obtained (Table 1). It becomes clear that the coating process causes a

Table 1: WC crystallite size and residual stress in the WC phase of the samples examined.

sample type	crystallite size [nm]		residual stress [GPa]	
	powder	layer	powder	layer
FS	86.3	46.6	0.91	1.22
MS	95.7	46.7	0.85	1.17
CS	71.1	42.1	1.05	1.34
FS-P	62.0	44.4	0.96	1.23

reduction in crystallite size and an increase in microstresses. While the WC-CoCr starting powders have WC crystallite sizes between 62 nm and 96 nm, those of the WC-CoCr coatings lie in a relatively narrow range between 42 nm and 47 nm. Furthermore, it is found that the powder samples CS and FS-P exhibit smaller WC crystallite sizes compared to FS and MS. This trend remains even after coating deposition. When considering the residual stresses, it becomes clear that the coating process results in a significant increase in residual stresses.

Acknowledgements: The authors gratefully acknowledge the DELTA machine group for providing synchrotron radiation and their support at BL9.

References

- [1] A. Vaitkus, A. Merkys, S. Gražulis, Validation of the Crystallography Open Database using the Crystallographic Information Framework, *J. Appl. Crystallogr.* 54(2), 2021, 661–672.
- [2] L. Lutterotti, Total pattern fitting for the combined size-strain-stress-texture determination in thin film diffraction, *Nucl. Instrum. Methods. Phys. Res. B* 268, 2010, 334–340.
- [3] D. V. Suetin, I. R. Shein, A. L. Ivanovskii, Elastic and electronic properties of hexagonal and cubic polymorphs of tungsten monocarbide WC and mononitride WN from first-principles calculations, *Phys. stat. sol. (b)* 245, 2008, 1590–1597.

Oberflächenanalyse von lichtbogengespritzten amorphen und In-Situ-legierten Schichten.

Kimberly Porscha, Hagen Steinhoff, Mohamed Abdulgader*

Lehrstuhl für Werkstofftechnologie, TU Dortmund University, 44221 Dortmund, Germany

**mohamed.abdulgader@tu-dortmund.de*

Das Lichtbogendrahtspritzen (LDS) ist ein sehr wirtschaftliches Verfahren, bei welchem Draht als Spritzzusatzwerkstoff genutzt wird. Besonders durch die Verwendung preisgünstiger Rohmaterialien kann es als eine Alternative zu den bekannten Herstellungsverfahren für amorphe Schichten (mittels pulverbasierten Spritzverfahren) und Formgedächtnislegierungen (FGL) (mittels pulvermetallurgischen Verfahren) angesehen werden [KOG22, ING22]. In einem am Lehrstuhl für Werkstofftechnologie (LWT) der TU Dortmund neuartigen Versuchsaufbau wurden mittels zwei synchron genutzten Spritzbrennern Aluminium (Al), Titan (Ti), Nickel (Ni) und Kupfer (Cu) für die Anwendung amorpher Schichten sowie geeignete NiTi-Kombinationen für FGL-Applikationen spritztechnisch hergestellt. Amorphe Metalle sowie NiTi-FGL bieten eine hohe Härte und eignen sich damit maßgebend für Verschleiß- und Korrosionsschutzbeschichtungen [HEG17].

Aus den aufgeführten Gründen sollen daher bekannte Werkstoffkombinationen für amorphe Schichten und FGL mittels Lichtbogendrahtspritzen erzeugt werden. Ziel ist es, Informationen über den Anteil der erforderlichen Phasen und ihrer Legierungsbildung miteinander zu erhalten, um optimale glas- und formgedächtnisbildende Eigenschaften der Materialzusammensetzung und der Spritzparameter bestimmen zu können.

Die Phasenanalyse der erzeugten Schichten wurde mit folgenden Parametern an der Beamline BL9 des DELTA an der Technischen Universität Dortmund durchgeführt:

- Messaufsatz: MAR345
- Wellenlänge: 0,4591 Å
- Theta: 3 °
- Messzeit: 120 Sekunden

Mithilfe der Analysesoftware „Match!“ konnten die im weiteren Verlauf aufgeführten Phasen ermittelt werden. Um eine Vergleichbarkeit zwischen den im Folgenden dargestellten Phasen zu ermöglichen, wurden ausgewählte 2D-Diffraktogramme übereinander angeordnet und ihre jeweiligen Intensitäten normiert.

Ergebnisse amorphe Schichten

Das 2D-Diffraktogramm in Abbildung 1 zeigt, dass keine größeren amorphen Phasen in der AlTiNiCu-Schicht gebildet werden konnten. Die Form der spitzen Peaks weisen auf verschiedene kristalline Strukturen hin. Bei der Probe wurde mit Primärgasdrücken

von 8 Bar und einem Sekundärgasdruck von 2 Bar gespritzt. In der Schicht liegt Ti, Al, Ni und Cu in ungebundener Form vor. Zusätzlich sind intermetallische Verbindungen zwischen NiTi, CuNi, AlTi gebildet worden. Viele dieser Verbindungen liegen an ähnlichen zwei Theta-Winkeln wie bei den einzelnen reinen Elementen. Zusätzlich gehen Ti und Cu in der Form von TiO und Cu₂O Verbindungen mit Sauerstoff ein. Diese entsprechen separaten Peaks, können aber auch überlagernd an anderen Peaks entdeckt werden. Generell können viele der Peaks in den höheren zwei Theta-Winkelbereichen entweder Ti und Al oder Ni und Cu und deren Verbindungen zugeordnet werden. Demgegenüber können die Peaks mit den höchsten Intensitäten im Bereich um 13 ° mehreren Elementen zugeordnet werden. Die Elemente gehen nur teilweise eine Verbindung untereinander ein, daher bildet sich keine homogene Schicht aus.

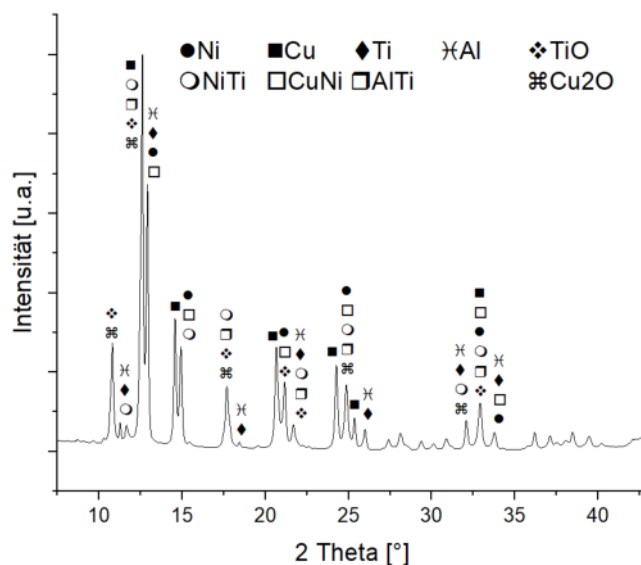


Abbildung 1: Schicht erzeugt durch Lichtbogenspritzen mit vier verschiedenen Spritzzusatzwerkstoffen (Ti, Al, Ni und Cu) und unter Verwendung von Sekundärgas

Ergebnisse zum In-Situ-Legieren beim LDS (NiTi-FGL)

Eine Charakteristik des Lichtbogendrahtspritzprozesses ist das nicht-achsensymmetrische Aufschmelzen der Elektrodenspitzen, das für die Partikelerzeugung verantwortlich ist [HUS07]. Vor allem bei zwei unterschiedlichen Drahtwerkstoffen wird daher empfohlen, dass das Material mit einem höheren Schmelzpunkt als Anode und demnach das Material mit einem niedrigeren Schmelzpunkt als Kathode verwendet werden sollte [WAT02]. Außerdem zeigen Untersuchungen, dass insbesondere Ti bei höheren Temperaturen zu einer erhöhten Affinität zu Sauerstoff und Stickstoff neigt [CHE22].

Daher wurden für die folgenden 2D-Diffraktogramme Titan als Anode (Schmelzpunkt 1668 °C) [CHE22] und Nickel (Schmelzpunkt 1455 °C) [HOL95] ausgewählt. Aufgrund des hohen Reaktionsvermögens von Ti wurden die dargestellten Spritzversuche unter Argonatmosphäreals Inertgas durchgeführt. Um den Einfluss der

Verfahrensgeschwindigkeit der Spritzpistole auf die Schicht zu untersuchen, wurde diese variiert. Wie in Abbildung 2 entnommen werden kann, hat eine unterschiedliche Verfahrensgeschwindigkeit von 18.000 mm/s, 36.000 mm/s und 72.000 mm/s keinen wesentlichen Einfluss auf die Phasenbildung in der NiTi-Beschichtung, weshalb die Zuordnung der jeweiligen Phasen lediglich im oberen Diffraktogramm erfolgt. Neben den signifikanten Peaks von reinem Ni und reinem Ti können übergreifende NiTi-Phasen festgestellt werden. Die Ursache der erhöhten Intensität bei ungefähr 22 ° bei der Probe V26.1 ist bislang ungeklärt und bedarf weiteren Untersuchungen. Trotz einer Argonatmosphäre konnten geringe Anteile von Titanoxiden in der Beschichtung festgestellt werden.

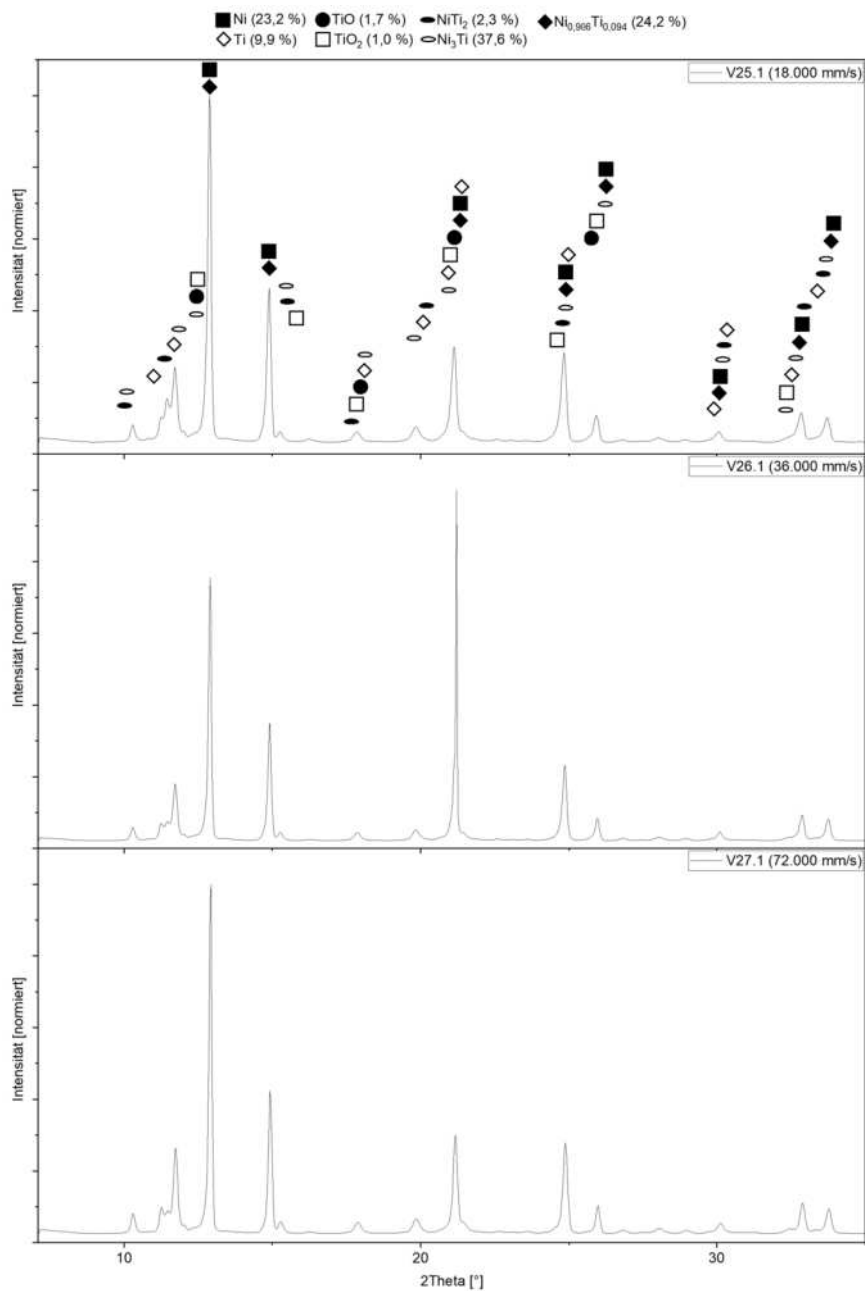


Abbildung 2: Einfluss der Variation der Verfahrensgeschwindigkeit der Spritzpistole auf die Bildung von NiTi-Phasen beim Lichtbogendrahtspritzen.

Formgedächtnislegierungen liegen nur in bestimmten Legierungszusammensetzungen vor. Bei einer NiTi-FGL liegt dabei der Atomprozentsatz von Ti bei annähernd 50 % [KUM22]. Dieses Verhältnis konnte bislang nicht in den untersuchten Beschichtungen festgestellt werden. Nachgelagerte REM-Untersuchungen zeigen jedoch einen übergreifenden Anteil an Ti von 48 Gew.-% (dunkle Lamellen) und 52 Gew.-% an Ni (helle Lamellen) im Beschichtungssystem, die durch geeignete Nachbehandlung in Näherung zu einer Ni_{0,507}Ti_{0,493}-FGL führen könnte (siehe Abbildung 3) [HOR91].

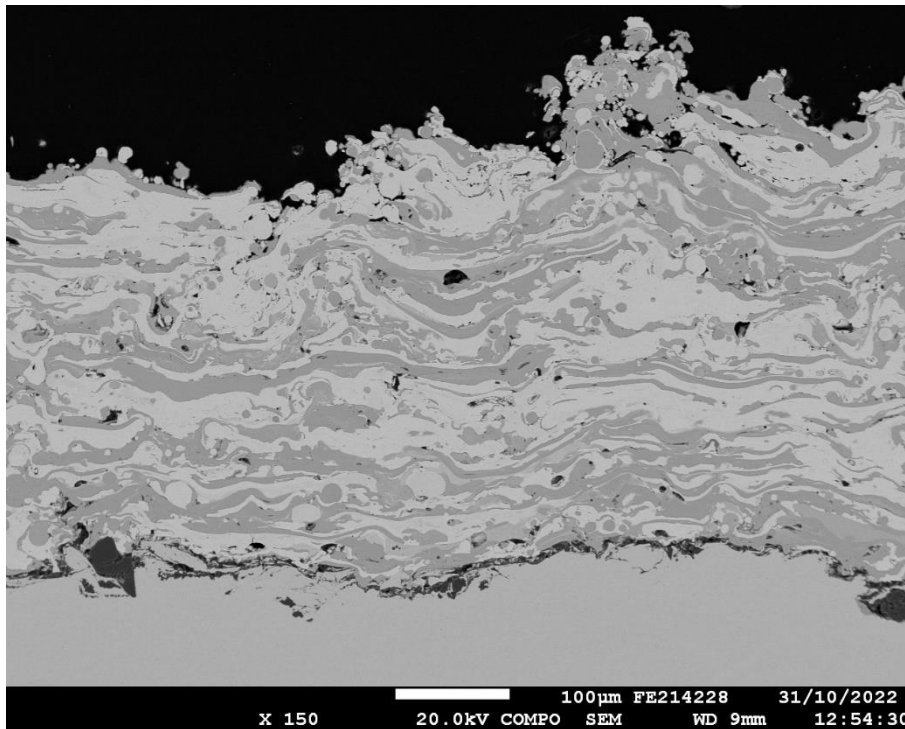


Abbildung 3: REM-Aufnahme einer NiTi-Schicht im Compo Modus

The authors gratefully acknowledge the DELTA machine group for providing synchrotron radiation and their support at Beamline BL9.

Literaturverzeichnis

- [CHE22] Chemie.de: Titan (Element), in: Chemie.de, https://www.chemie.de/lexikon/Titan_%28Element%29.html (2022).
- [HEG17] Hegels, D.: Optimierung thermischer Verhältnisse bei der Bahnplanung für das thermische Spritzen mit Industrierobotern, Dissertation, Dortmund, 2017.
- [HOL95] Holleman-Wiberg: *Lehrbuch der Anorganischen Chemie*, Verlag de Gruyter, Berlin, 101. Auflage, (1995), ISBN 3-11-012641-9.
- [HOR91] Hornbogen, E.: *Legierungen mit Formgedächtnis*, Westdeutscher Verlag. N388, (1991), ISBN 3-531-08388-0
- [HUS07] Hussary, N. A.; Heberlein, J.: *Effect of System Parameters on Metal Breakup and*

Particle Formation in the Wire Arc Spray Process, Journal of Thermal Spray Technology. 16 (2007), S. 140–152.

- [ING22] Maaß, B., Kortmann, A., Großmann, C.: *Formgedächtnis-Technik*, in: Anwenderkurs der Firma Ingpuls GmbH (2022).
- [KOG22] Koga, G. Y.; Bolfarini, C.; Kiminami, C. S. et al.: *An Overview of Thermally Sprayed Fe-Cr-Nb-B Metallic Glass Coatings: From the Alloy Development to the Coating's Performance Against Corrosion and Wear*, Journal of Thermal Spray Technology, 4 (2022), S. 923–955.
- [KUM22] Kumar Patel, S., Roshan, R.: *NiTi superalloys*, in: Nickel-Titanium Smart Hybrid Materials, Elsevier Inc., (2022), S. 105-121.
- [WAT02] Watanabe, T.; Sato, T.; Nezu, A.: *Electrode phenomena investigation of wire arc spraying for preparation of Ti-Al intermetallic compounds*, Thin Solid Films. 407 (2002), S. 98–103.

In situ XRD investigation of crystallization in FeCoSiB metallic glass

N. Hayen¹, B. M. Murphy^{1,3}, P. Jordt¹, L. Petersdorf¹, M. Paulus², C. Sternemann²

¹Institut für Experimentelle und Angewandte Physik, Christian-Albrechts-Universität zu Kiel, Leibnizstraße 19, 24118 Kiel, Germany

²Fakultät Physik/DELTA, Technische Universität Dortmund, Maria-Goeppert-Mayer-Str. 2, 44227 Dortmund, Germany

³Ruprecht Haensel Laboratory, Christian-Albrechts-Universität zu Kiel, 24118 Kiel, Germany

Our investigations focus on the metallic glass $(\text{Fe}_{0.9}\text{Co}_{0.1})_{78}\text{Si}_{12}\text{B}_{10}$ (FeCoSiB) as a promising material for the fabrication of highly sensitive magnetic field sensors within the SFB 1261 project. The main advantages of this material include high magnetostriction and favourable soft magnetic behaviour [1]. A thermal annealing procedure is a necessary step in the preparation of sensor prototypes, during which the magnetic properties of FeCoSiB have been observed to degrade depending on annealing temperature [2].

Our experiment therefore aimed to investigate the structural changes in the metallic glass *in situ* with time-resolved X-Ray Diffraction (XRD) during the annealing process. It was performed at beamline BL9 of the DELTA synchrotron radiation source utilizing the *in situ* heating setup with an Anton-Paar cell. To maximize the coverage in reciprocal space, an energy of 25 keV with a beam size of 1mm x 0.1mm (h x v) was chosen alongside the MAR3450 2D detector with minimal distance (335 mm) between sample and detector. The samples were 1 μm thick films of FeCoSiB deposited on 10mm x 10mm x 1mm Fused Silica wafer substrates, which were aligned in reflection geometry and heated at a constant rate of 3°C/min from room temperature to a maximum of 850°C. A diffraction image was recorded every 200 seconds including readout time, leading to a final temperature resolution of 10°C per image.

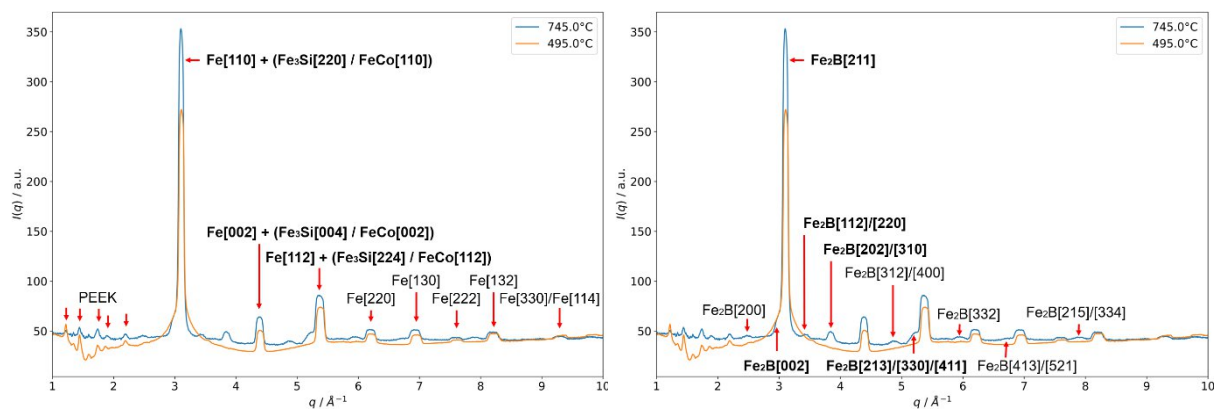


Figure 1: Diffraction patterns of the two distinct crystalline phases that were found at high temperatures. On the left, the Bragg reflections in the orange curve at 495°C are marked; they are associated with α -Fe, α -(Fe, Si) and α -(Fe, Co) structures. On the right, the additional reflections observed at 745°C are labelled; they can collectively be assigned to the compound Fe_2B .

These *in situ* measurements yielded new information about the crystallization behaviour of FeCoSiB. During heating two separate phase transitions were observed, figure 1 shows two exemplary diffraction patterns that clearly show the formation of additional Bragg reflections at high temperatures. Figure 2 includes the whole temperature series from room temperature to 850°C and shows the evolution of the diffraction pattern over time. The two crystallization

transitions were found to occur at 440°C and 560°C respectively, where the first, previously reported transition leads to the formation of α -Fe and Fe-Si and Fe-Co alloys with the same structure. The second transition predicted at 560°C [3] is associated with the formation of Fe₂B and has been observed *in situ* for the first time with this specific material composition.

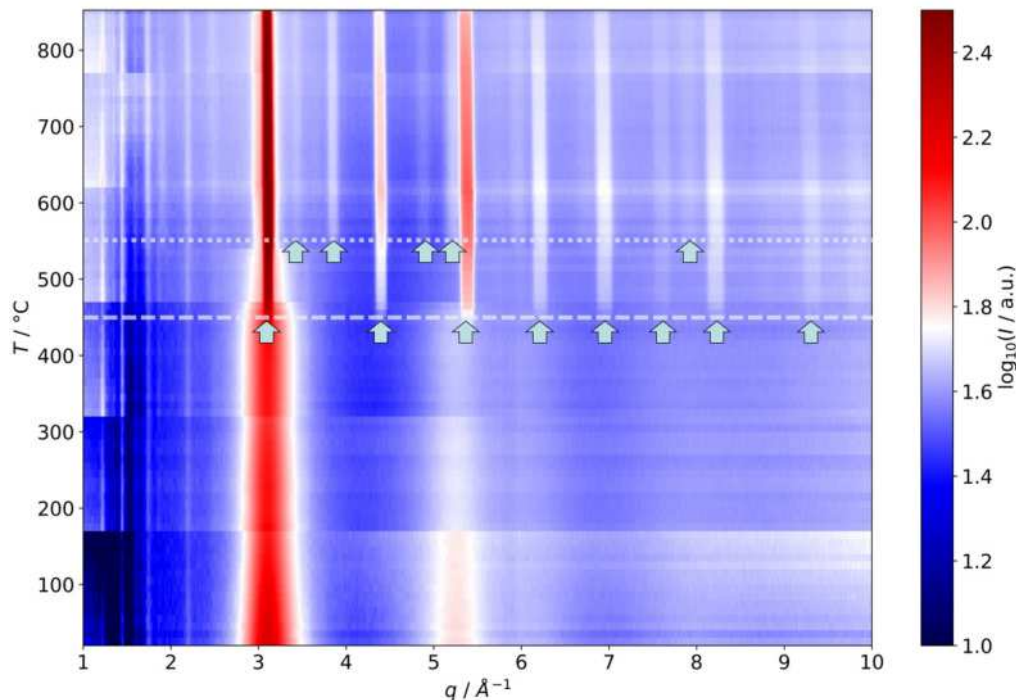


Figure 2: Full *in situ* temperature series for one of the FeCoSiB samples; the obvious discontinuities every 150°C stem from realignments of the sample as the temperature was increased. The data shows two separate crystallization phase transitions occurring at 440°C (dashed line) and 560°C (dotted line) respectively.

This experiment has returned valuable information on the two crystallization phases and has allowed the observation of the second transition *in situ*, for a first time. These results have since been critical in informing further investigations into this material and will further be useful when attempting to identify the structural changes FeCoSiB undergoes during annealing before the crystallization point.

References

- [1] V. Hrkac, E. Lage, G. Köppel, J. Strobel, J. McCord, E. Quandt, D. Meyners, and L. Kienle, Amorphous FeCoSiB for exchange bias coupled and decoupled magnetoelectric multilayer systems: Real-structure and magnetic properties, *J. Appl. Phys.* 116, 134302 (2014). (<https://doi.org/10.1063/1.4896662>)
- [2] C. T. Koops, S. B. Hrkac, M. Abes, P. Jordt, J. Stettner, A. Petraru, H. Kohlstedt, V. Hrkac, N. Wolff, L. Kienle, O. H. Seeck, G. Nisbet, O. M. Magnussen, and B. M. Murphy, Elastic Coupling at Epitaxial Multiferroic Interfaces: *in situ* X-ray Studies of Electric Field Induced Strain, *IFMBE*, volume 77 (2019). (https://doi.org/10.1007/978-3-030-31866-6_38)
- [3] A. J. Kailath, A. Kumar, and A. Mitra, Effect of metalloids on crystallization and magnetic behaviour of FeCoSiB based metallic glass, *Bull. Mater. Sci.*, volume 29, nr. 2 (2006).

Acknowledgements

We would like to thank the DELTA team for both their support and for providing us access to synchrotron radiation. We acknowledge funding of this project by the DFG via project A6 in SFB 1261 „Biomagnetic Sensing“.

Characterization of ZTO/Ag/ITO thin films using X-ray reflectivity

Steffen Bieder¹, Patrick Schlenz², Susanne Dogan-Surmeier¹, Christian Albers¹, Michael Paulus¹, Eric Schneider¹, Nicola Thiering¹, Christian Sternemann¹, and Steffen Cornelius²

¹Fakultät Physik/DELTA, Technische Universität Dortmund, D-44221 Dortmund, Germany

²Fraunhofer-Institut für Organische Elektronik, Elektronenstrahl- und Plasmatechnik FEP, Winterbergstrasse 28, D-01277 Dresden, Germany

Within the EU research program NanoQI, Hyper Spectral Imaging (HSI) will be implemented for in-line quality control of roll-to-roll produced coatings, analyzing thickness variations of coatings during the production process via spatial detection of reflected light in the UV/VIS/NIR optical range. As part of this program, differently composed thin film layers were examined by X-ray reflectivity (XRR) measurements at beamline BL9. The layer thicknesses obtained by the analysis of the X-ray reflectivities will be subsequently used as ground truth data for the training of an evaluation algorithm of HSI data measured for the same layer systems.

The thin-film multilayers were produced at Fraunhofer FEP using a vacuum web coater and consisted of zinc tin oxide (ZTO), silver (Ag), and indium tin oxide (ITO), deposited on flexible polyethylene (PET) foils (see sketch in figure 1, left). The individual layers are applied to the PET film by roll-to-roll coating via magnetron sputtering and were produced over a width of 220 mm perpendicular to the transport direction. Such multilayers can be applied e.g. as transparent electrodes and gas diffusion barriers. After HSI measurement of the coated foils, three samples were cut out from the center and from the edges of the foil and then laminated onto a glass substrate. These samples were then studied using XRR in order to analyze the film thickness, density and roughness of the individual layers. Measurements were taken on each sample at five different positions as shown in figure 1. The X-ray beam had an energy of 8.048 keV and a size of 1.0 x 0.1 mm² (h x v). The angle of incidence was scanned between 0.2° - 4° corresponding to momentum transfers q_z perpendicular to the surface between 0.014 – 0.28 1/Å, respectively.

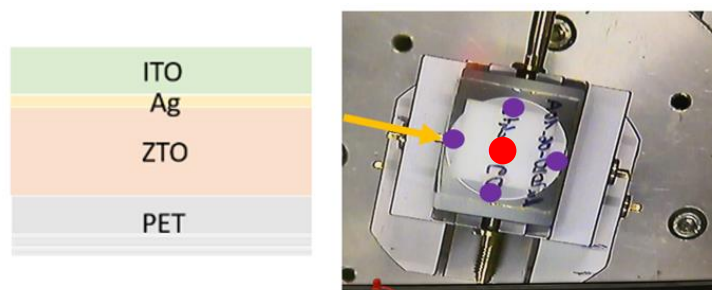


Figure 1: Schematic of the layer system (left). Sample mounted at the experiment (right). The arrow indicates the direction of the incident X-rays and the points (purple and red) mark the measurement positions.

Figure 2 (left) shows exemplary XRR measurements of three samples extracted from the center and both edges (denoted left and right), each measured in the central part (position indicated by the red dot in Fig. 1 right) of the sample. The data were evaluated and the corresponding density profiles are presented in figure 2 (right). The results reveal that the thickness of all three sub-layers decreases towards the edge of the PET film perpendicular to its transport direction. All data obtained for the layer thickness determined for positions perpendicular to the transport direction are compiled in figure 3 indicating a clear thickness gradient for all single layers due to the production process.

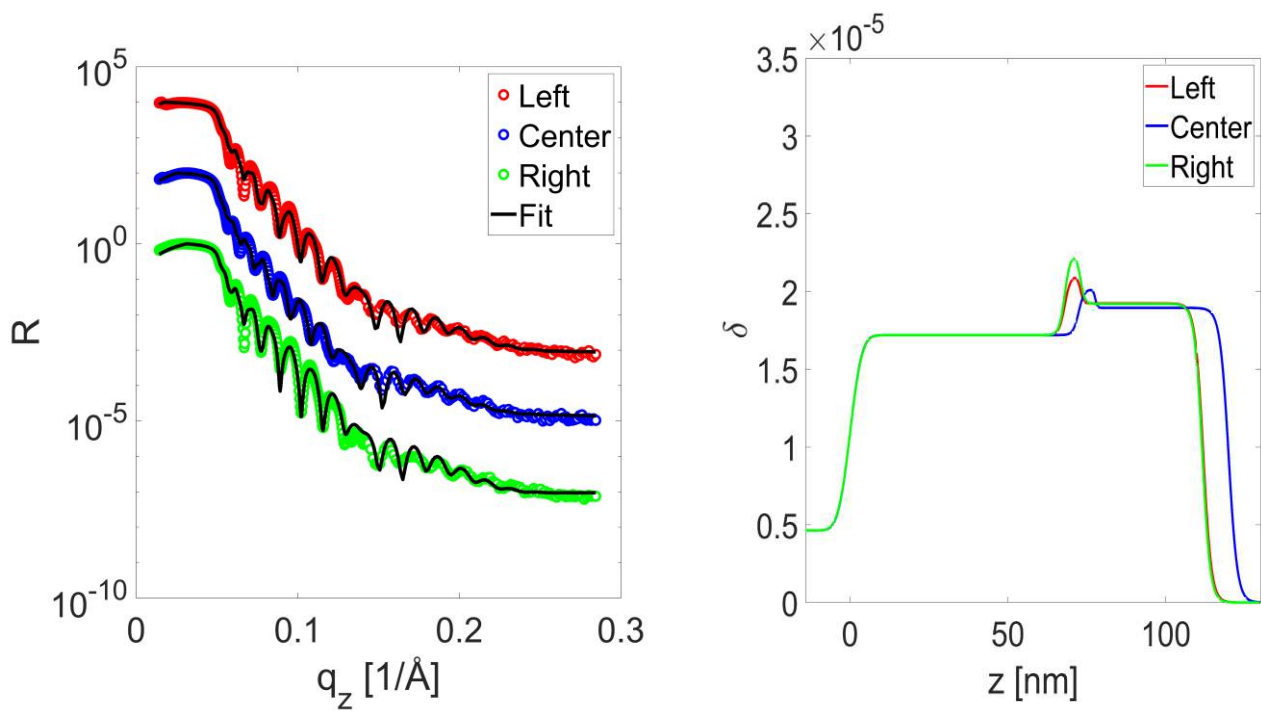


Figure 2: X-ray reflectivities ($R(q_z)$) taken from the central position of the three samples (left). The curves have been shifted vertically for clarity. The fits of the data using the effective density model are shown as black lines. The corresponding dispersion (δ) profiles perpendicular to the sample height (z) are compared and show reduced layer thicknesses for samples extracted from the foil's edges (right).

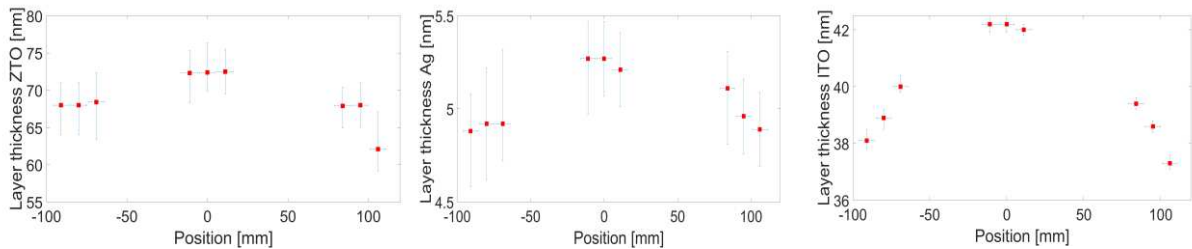


Figure 3: The layer thickness of the three layers (ZTO – left, Ag – center and ITO – right) estimated for the direction perpendicular to the roll's transport direction. The errors are estimated via variation of refinement parameters.

These results obtained in this study will be subsequently used as training data for the HSI data evaluation with the aim to create layer thickness libraries.

Acknowledgments

We acknowledge funding from the European Union's Horizon 2020 research and innovation program under grant agreement No. 862055. We thank DELTA for providing synchrotron radiation.



Low-temperature plasma nitriding to enhance tribocorrosive resistance of corrosion-resistant steel

Brückner, T.¹; Paschke, H.¹; Thewes, A.²; Reinders, P.³; Kipp, C.⁴; Sternemann, C.⁵; Paulus, M.⁵

¹ Fraunhofer Institute for Surface Engineering and Thin Films IST, 44145 Dortmund, Germany

² IOT TU Braunschweig, 44145 Dortmund, Germany

³ Fraunhofer Institute for Surface Engineering and Thin Films IST, 38108 Braunschweig, Germany

⁴ IOT TU Braunschweig, 38108 Braunschweig, Germany

⁵ Fakultät Physik/DELTA, Technische Universität Dortmund, 44221 Dortmund, Germany

Introduction

Tribocorrosion occurs under both mechanical and chemical loads and often results in an increased wear volume than it is the case for the sum of only wear and only corrosion [Wats95]. Therefore, materials which provide a good corrosion resistance as well as wear resistance are needed. One way to achieve this aim is the treatment of corrosion resistant steels by Low-Temperature Plasma Nitriding (LT-PN). This process creates a nitrogen-rich surface with different designation, depending on the lattice structure of the base material. The so-called expanded austenite (γ -phase – FCC) or expanded martensite (α -phase – BCC). This treatment finally leads to higher tribocorrosion resistance [Hahn22].

One of the key parameters in diffusion treatment is the temperature. Usually plasmanitriding processes are carried out at temperatures of about 530°C. In case of corrosion-resistant steel this would lead to a higher hardness, but also would decrease the corrosion resistance due to the formation of CrN. In LT-PN the lower treatment temperature of less than 450°C is known to circumvent that [Borg05]. Due to the large influence of the temperature on the formation of phases or precipitations, knowledge about the stability or decomposition of the expanded austenite/martensite is of interest.

Experimental

LT-PN was carried out on martensitic (M340) and austenitic (CN0.85) steel. The chemical composition is shown in table 1.

Table 1: Chemical composition in wt-%

	C	Cr	Mn	Mo	Ni	V	Si	N	Fe
M340	0.54	16.88	0.40	1.0	-	0.11	0.45	0.23	balance
CN0.85	0.26	18.25	17.85	0.05	0.15	0.08	0.25	0.59	balance

The treatment route for CN0.85 started with a preheating step. When the temperature reached 200°C, a plasma fine cleaning step was carried out for 2 h to remove the native chromium oxide passivation layer. During this time the batch was heated up to 380°C. The nitriding step was conducted for 16 h at 380°C with a H₂:N₂-ratio of 80:20. For the M340 the chamber was heated up to 360°C. After that a plasma fine cleaning step was conducted for 0.5 h followed by the nitriding step (8h, 360°C, H₂:N₂-ratio: 20:80). The presence of a nitrogen-rich layer was verified by layer measurements on cross sections using V2A etchant.

XRD measurements were performed at beamline BL9 of the synchrotron light source DELTA (TU Dortmund, Dortmund, Germany) [Kryw06]. A MAR345-detector was used and the energy of the incident photon beam was 25 keV with a beamsize of 1.0 x 0.2 mm² (h x v). XRD-measurements at room temperature for the untreated and LT-PN-state were carried out before heating the samples up as reference for later evaluation. Measurements to analyse the temperature effect were carried out at 420°C for both CN0.85 and M340 and at 550°C for M340. Therefore, the samples were heated up to the desired temperature, which took about five minutes. After the temperature was reached, every five minutes an XRD-measurement was executed to visualise changes in the pattern conditioned by the holding time. The holding time for the CN0.85 was 75 minutes, for M340 (420°C) 90 minutes and M340 (550°C) 115 minutes.

Results and Discussion

The observed thickness of the nitrogen-rich layer was about 6-7 μm for the M340 and about 3.0-3.5 μm for the CN0.85. The lower diffusion depth for the CN0.85 (despite higher nitriding time) can be explained by the different crystal structure of M340 and CN0.85, because diffusion is faster in BCC lattice structure than in FCC lattice structure [Pine13] [Bern08].

XRD-results before and after treatment as base for further investigations at elevated temperatures are shown in figure 1. In the untreated state for CN0.85 there are comparatively sharp peaks visible. Compared to XRD-measurements with nearly the same composition they assigned to the γ -phase [Gavr06]. The treated sample shows new reflexes shifted towards lower diffraction angles. The shift is a sign for the formation of expanded austenite (γ_N) which has already been observed elsewhere [Foss06]. For the M340 the α -phase dominates and a peak shifting could be observed as well, but it was not as pronounced as in the CN0.85 sample.

In both cases a broadening of the peaks could be observed. A possible explanation for that could be the overlay of different peaks, as peaks of possible nitrides are located close to the peak positions of the γ/γ_N -phase or α -phase respectively. Further it can be assumed that there is a gradient of nitrogen concentration between surface and substrate along the diffusion layer, influencing the pattern as well. Another reason could be the lattice expansion or induction of lattice defects due to the interstitially solved nitrogen atoms. This is mentioned as a possible reason for peak broadening elsewhere [Unga04].

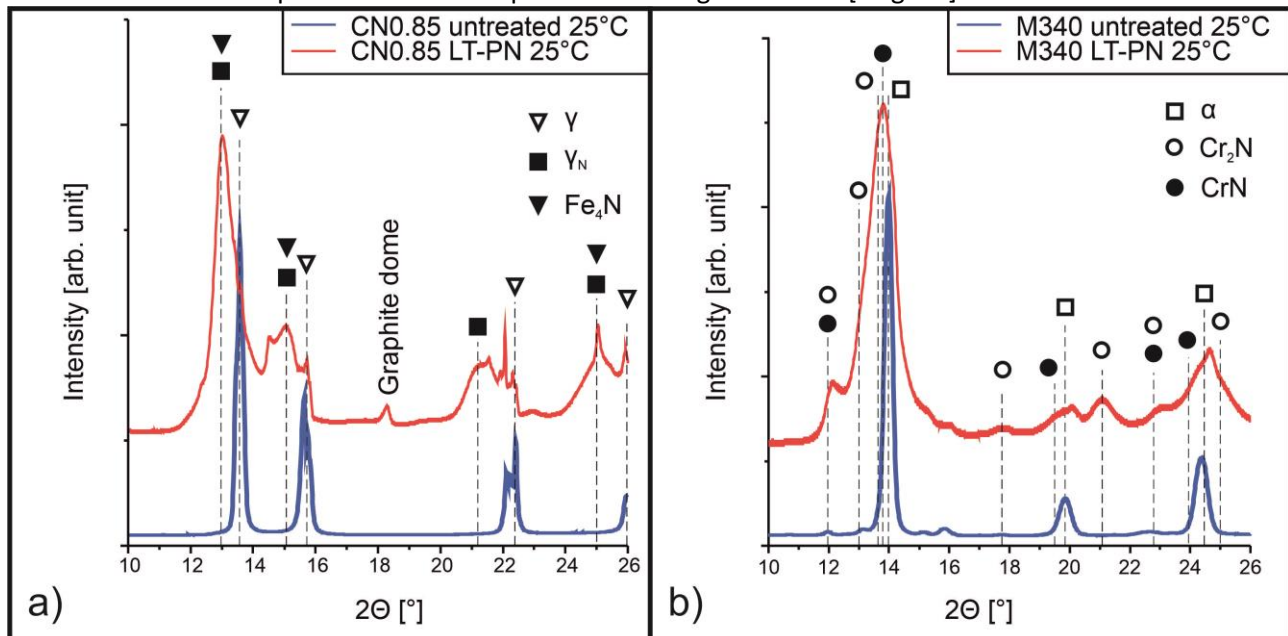


Figure 1: XRD-results of untreated and LT-PN samples: a) CN0.85 b) M340. Data for peak positions were derived from [Gavr06], [Ming06] and [Brue10]

As it can be seen in figure 2, for the sample of CN0.85 the annealing temperature of 420°C shows a slight change in intensity around 13.6°. As it matches with the position of the γ -phase seen in the untreated case, it is possible, that decomposition of the expanded austenite took place and nanocrystalline γ -Fe forms. The formation of a significant sharp peak at 13.8° is visible as well, directly after the sample was heated up. This peak is also visible in measurements after a longer holding time. On the one hand the shape suggests the presence of a large crystal and could have its origin in a large crystallite in the substrate hit by chance. On the other hand this peak coincides with the position for CrN, which supports the assumption that γ_N decomposes, at least partially. Furthermore the peak at 13° does not change significantly, indicating there still has to be an amount of expanded phase which remains stable. For the M340 some changes were detected which occur even more visible in the sample annealed at 550°C and are discussed in the following. According to the data measured for M340 annealed at 550°C (fig. 3), one could expect the formation of CrN due to the significantly higher temperature than during plasma treatment. But for the peak at about 12°, which suggests the existence of CrN, it can be seen that this peak flattens with time. This could be seen as a sign of lower CrN-content. Likewise, conclusions can be drawn from the development of the peak at 13.6°.

It can be noticed that only the left part of the peak is shifting, which suggests there are at least two phases pictured in this peak. The left and decreasing part could belong to CrN again and supports the previously described theory of CrN-reduction. On the other hand it can be noticed that the strong peak at ca. 13.6° is shifting only slowly towards a larger angle and not reaching the state of the original, untreated material. This could indicate, that parts of the expanded martensite are still stable. But due to the fact, that the expanded phase and CrN as well as Cr₂N show peaks at almost the same position, it is also possible that nitrides of chromium are formed even though the phases are indistinguishable in the diffraction pattern.

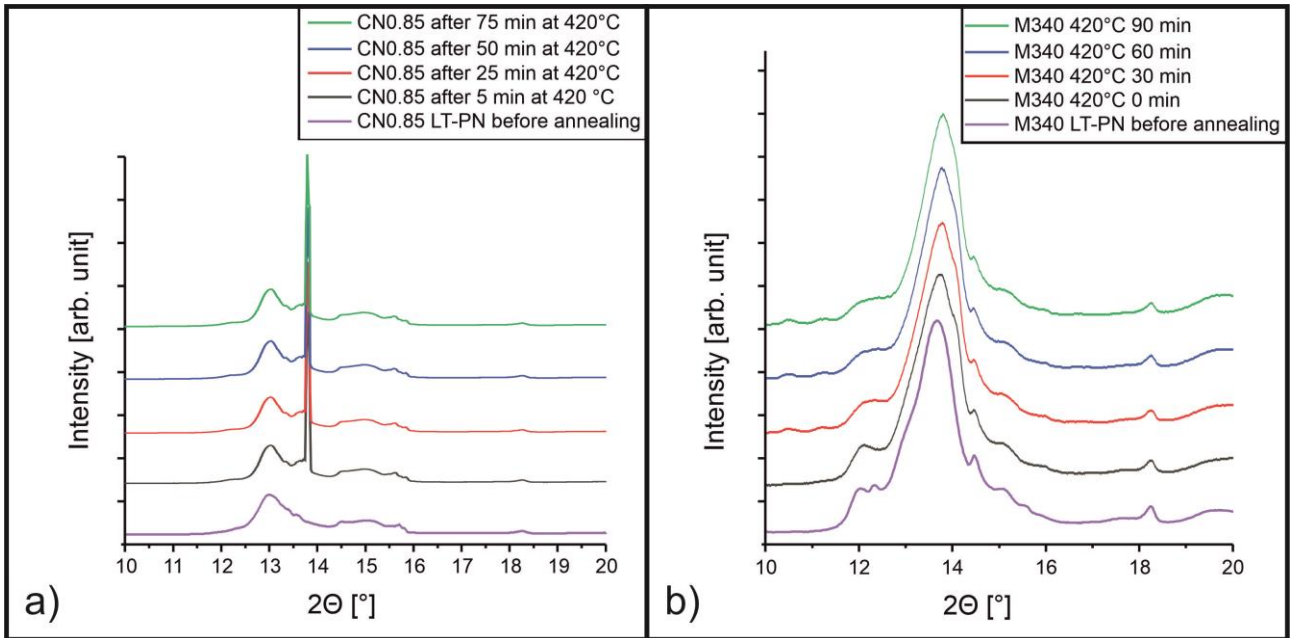


Figure 2: XRD-results of LT-PN before annealing and after annealing at 420°C at several time spots: a) CN0.85 b) M340

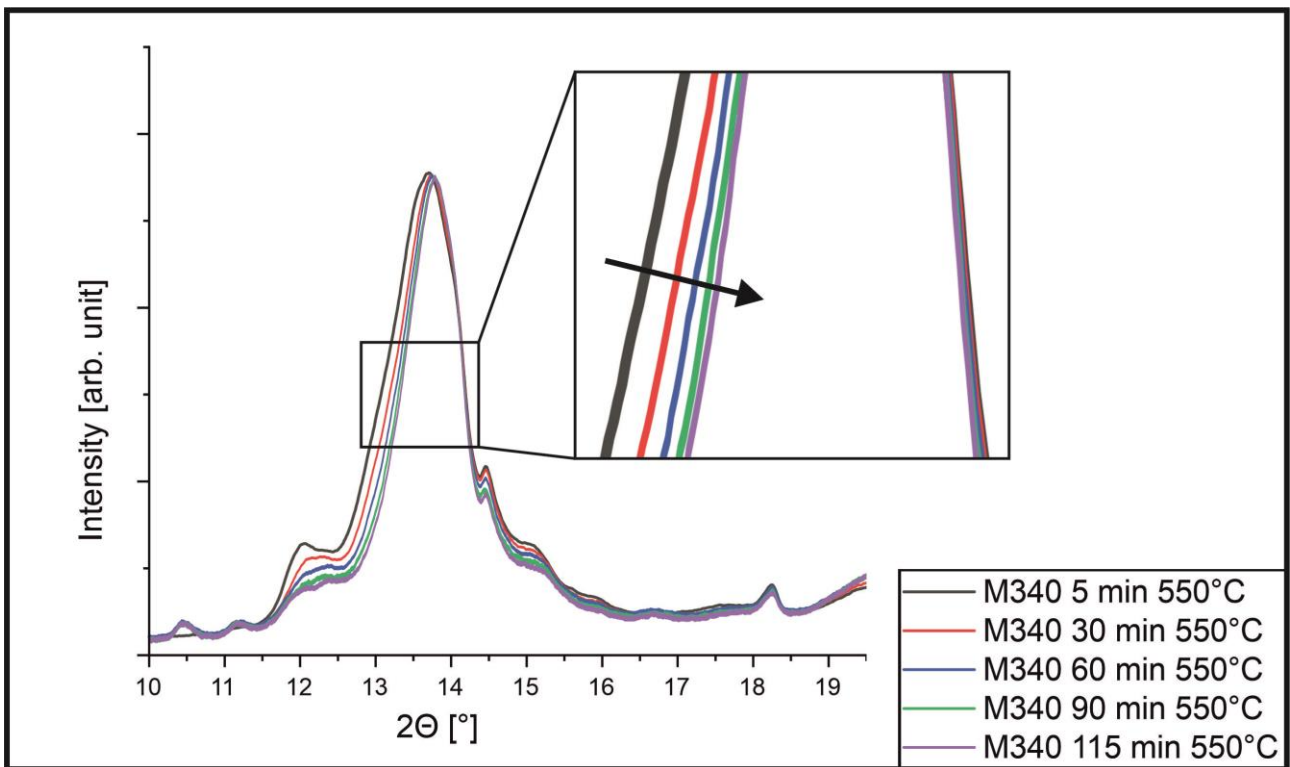


Figure 3: Shifting of XRD-peak while annealing (M340, 550°C)

Conclusions

Even though interpretation of the data is challenging, several useful hints were obtained, which provide approaches for further investigations.

A significant change in XRD-pattern between untreated and treated samples could be observed. This change indicates the existence of an expanded phase.

XRD measurements at elevated temperatures allow to indicate small changes in the peaks shape and position. It follows, that temperature has an influence even at quite moderate temperature and short amount of time. But all in all, the initial state of the untreated samples was not reached during the tested period. In conclusion, even long exposition to elevated temperatures does not reverse the effects of nitriding, adding a moderate thermal stability to the hard and corrosion resistant surfaces. Further experiments on corrosion resistance could give additional information about corrosion properties after annealing.

Acknowledgment

We kindly acknowledge the support of the DELTA machine group and the provided synchrotron radiation. The performed measurements do also contribute helpful insights to the project „Energieeffizienz durch Standzeiterhöhung von Lagern unter tribokorrosiven Betriebsbedingungen – BMWK POSEIDON II“ within the subproject of the Fraunhofer IST (FKZ 03ET1477D) „Randschichtmodifikation des Grundmaterials, Duplexbehandlungen“. We are thankful to the BMWK for the given financial support.

Literature

- [Wats95] Watson, S.W.; Friedersdorf, F.J.; Madsen, B.W.; Cramer, S.D.: Methods of measuring wear-corrosion synergism. *Wear* 181-183 p. 476-484 (1995)
- [Hahn22] Hahn, I.; Siebert, S.; Theisen, W.; Weber, S.; Fluch, R.; Paschke, H.; Brückner, T.: Erhöhte Tribokorrosionsbeständigkeit von mechanisch und chemisch beanspruchten Oberflächen. Conference proceedings, 63. Tribologie-Fachtagung Göttingen (2022)
- [Borg05] Borgioli, F.; Fossati, A.; Galvanetto, E.; Bacci, T.: Glow-discharge nitriding of AISI 316L austenitic stainless steel: influence of treatment temperature. *Surface & Coatings Technology* 200 p. 2474– 2480 (2005)
- [Kryw06] Krywka, C.; Paulus, M.; Sternemann, C.; Volmer, M.; Remhof, A.; Nowak, G.; Nefedov, A.; Pöter, B.; Spiegel, M.; Tolan, M.: The new diffractometer for surface X ray diffraction at beamline BL9 of DELTA, *Journal of Synchrotron Radiation* 13 p. 8-13 (2006)
- [Pine13] Pinedo, C.E.; Varela, L.B.; Tschiptschin, A.P.: Low-temperature plasma nitriding of AISI F51 duplex stainless steel. *Surface & Coatings Technology* 232 p. 839–843 (2013)
- [Bern08] Berns, H.; Theisen, W.: *Eisenwerkstoffe – Stahl und Gusseisen*. 4.Auflage Springer-Verlag Berlin Heidelberg (2008)
- [Gavr06] Gavriljuk, V.G.; Tyshchenko, A.I.; Razumov, O.N.; Petrov, Y.N.; Shanina, B.D.; Berns, H.: Corrosion-resistant analogue of Hadfield steel. *Materials Science and Engineering A* 420 p. 47–54 (2006)
- [Foss06] Fossati, A.; Borgioli, F.; Galvanetto, E.; Bacci, T.: Glow-discharge nitriding of AISI 316L austenitic stainless steel: influence of treatment time. *Surface & Coatings Technology* 200 p. 3511 – 3517 (2006)
- [Unga04] Ungar, T.: Microstructural parameters from X-ray diffraction peak broadening. *Scripta Materialia* 51 p. 777–781 (2004)
- [Ming06] Mingolo, N.; Tschiptschin, A.P.; Pinedo, C.E.: On the formation of expanded austenite during plasma nitriding of an AISI 316L austenitic stainless steel. *Surface & Coatings Technology* 201 p. 4215 – 4218 (2006)
- [Brue10] Brühl, S.P.; Charadia, R.; Simison, S.; Lamas, D.G.; Cabo, A.: Corrosion behavior of martensitic and precipitation hardening stainless steels treated by plasma nitriding. *Surface & Coatings Technology* 204 p. 3280–3286 (2010)

Solid solutions $\text{Ln}_x\text{U}_{1-x}\text{C}_2$ with $\text{Ln} = \text{Sm}, \text{Er}$

C. Tobeck and U. Ruschewitz*

Department für Chemie, Universität zu Köln, 50939 Köln, Germany

*email: uwe.ruschewitz@uni-koeln.de

Almost 10 years ago we found that within the solid solution $\text{Yb}_x\text{Ca}_{1-x}\text{C}_2$ intriguing valence changes of Yb occur leading to a drastic decrease of the unit cell volume with increasing x , i.e. increasing Yb contents.^[1] XANES investigations revealed that with low Yb contents the CaC_2 host lattice forces Yb into the divalent Yb^{2+} state, whereas at higher Yb contents an $\text{Yb}^{+2.7}$ intermediate state is reached close to the +2.81 state observed in pure YbC_2 .^[2] In this context we are searching for other solid solutions, in which a host lattice forces the embedded cations to undergo interesting valence changes. UC_2 seems to be an interesting candidate, which is known to contain U^{4+} in the pristine material,^[3] however in solid solutions with LnC_2 carbides also the U^{3+} state seems to be achievable. Recently, we found that UC_2 can be synthesized in phase-pure and highly crystalline form in an arc-melting furnace. Similarly, we attempted to react different lanthanides with UO_2 and purified graphite in an arc-melting furnace. The X-ray powder diffraction data confirm the successful synthesis of the respective solid solutions. In Figure 1 our results obtained for the solid solutions $\text{Ln}_x\text{U}_{1-x}\text{C}_2$ with $\text{Ln} = \text{Sm}$ (left), Er (right) are shown. The respective lattice parameters were obtained by *LeBail* fits of high-resolution synchrotron powder diffraction data recorded at BL9 of the DELTA synchrotron facility.

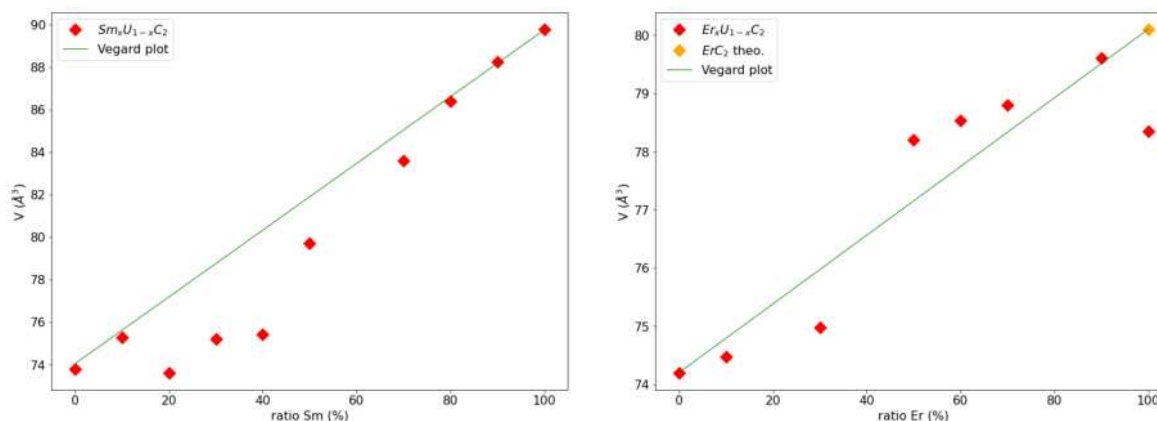


Figure 1. Unit cell volumes of solid solutions $\text{Ln}_x\text{U}_{1-x}\text{C}_2$ with $\text{Ln} = \text{Sm}$ (left) and Er (right) as obtained from *LeBail* fits of BL9 data.

The results in Figure 1 show surprising and somewhat confusing results. However, a more detailed analysis using EDX showed that the real Sm contents of the solid solution $\text{Sm}_x\text{U}_{1-x}\text{C}_2$ is much lower than the Sm ratio in the starting mixture, which is given on the x axis. We assume that Sm evaporates in the arc-melting furnace. Therefore, the reaction conditions for the synthesis of this solid solution have to be improved. On the other hand, EDX of the solid solution $\text{Er}_x\text{U}_{1-x}\text{C}_2$ shows a very good agreement between the analysed and initial Er ratio so

that the deviations from Vegard behaviour in Figure 1 (right) seem to be realistic. The refined lattice parameters of our synthesized ErC₂ sample deviate very much from the literature data given as ErC₂ theo. in Figure 1 (right), which was used for the calculation of the Vegard plot. The reasons for this deviation are unknown at the moment. A detailed analysis of the U valence states in these materials is underway. However, first results of XPS investigations are not very promising, as charging effects hamper a reliable determination of valence states. Therefore, we have also started to synthesize solid solutions Ln_xU_{1-x}C₂ with other lanthanides (Ln = Pr, Nd, Tb, Dy, Ho, Tm, Yb, Lu).

- [1] P. Link, P. Glatzel, K. Kvashnina, D. M. Trots, R. I. Smith, U. Ruschewitz, *Inorg. Chem.* **2013**, *52*, 7020-7030.
- [2] P. Link, P. Glatzel, K. Kvashnina, R. I. Smith, U. Ruschewitz, *Inorg. Chem.* **2011**, *50*, 5587-5595.
- [3] R. E. Jilek, E. Bauer, A. K. Burrell, T. M. McCleskey, Q. Jia, B. L. Scott, M. F. Beaux, T. Durakiewicz, J. J. Joyce, K. D. Rector, J. Xiong, K. Gofryk, F. Ronning, R. L. Martin, *Chem. Mater.* **2013**, *25*, 4373-4377.

Uncovering the thermal behaviour of pristine and linker-exchanged ZIF-8 with variable temperature X-ray powder diffraction

Wenlong Xue, Chinmoy Das, Roman Pallach, Sebastian Henke*

Anorganische Materialchemie – TU Dortmund, Otto-Hahn-Str. 6, 44227 Dortmund

Scientific context

Some metal-organic frameworks (MOFs)^[1], networks composed of organic ligands and metal nodes, can be transformed into glasses via the traditional melt-quenching method. The MOF glasses are deemed to overcome the lack in processability (i.e. moldability, shapeability) of crystalline MOFs, thus setting the stage for facilitated applications of these materials in technological processes. Hitherto, glass formation by melt-quenching has only been achieved by a handful of porous 3D zeolitic imidazolate frameworks (ZIFs), in parallel with a few non-porous 1D and 2D metal-phosphates and metal-triazolates. The melting is enabled by dynamic dissociation/association of metal-linker bonds, reminiscent of the scenarios in structurally similar silicates and zeolites. The fact that only a very small number of ZIFs (e.g. ZIF-4 [Zn(im)₂, im⁻ = imidazolate], ZIF-zni [Zn(im)₂], and ZIF-62 [Zn(im)_{2-x}(bim)_x with 0 < x < 0.35, bim⁻ = benzimidazolate]) form melt-quenched glasses is reasoned in too low thermal stability of the other ZIFs, so that they decompose before they can melt at elevated temperature^[2]. Thus, chemical procedures for a systematic melting point lowering of ZIFs need to be developed in order to (i) expand the structural and compositional space of ZIF glasses and (ii) to allow for a lower temperature processing of the glasses making them applicable for a wider range of applications.

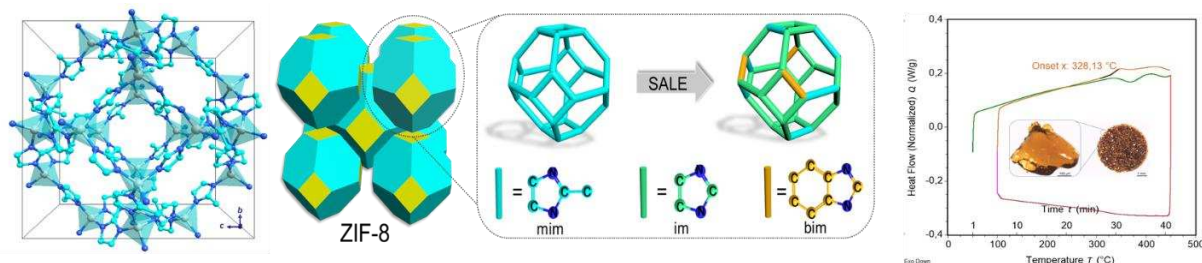


Fig. 1 Structure of the ZIF-8 framework viewed along the crystallographic a axis (left). Zn, C and N atoms are shown in grey, cyan and blue, respectively. Coordination polyhedra around the Zn^{2+} atoms are shown in teal. H atoms are omitted for clarity. Scheme of the SALE of $\text{ZIF-8-mim}_x\text{im}_y\text{bim}_z$ where mim^- linkers are post-synthetically exchanged against im^- and bim^- linkers (middle). DSC data of a representative $\text{ZIF-8-mim}_x\text{im}_y\text{bim}_z$ of the nominal composition $\text{ZIF-8-mim}_{0.14}\text{im}_{0.78}\text{bim}_{0.08}$. Heating and cooling rates are $\pm 10 \text{ }^\circ\text{C min}^{-1}$. 2nd upscan: The composite glass features a T_g of 328 °C. The inset shows a micrograph of a shard of the composite glass (right).

$\text{ZIF-8}^{[3]}$, also known as MAF-4 (MAF = metal azolate framework), is a ZIF possessing large spherical cavities with a diameter of about 1 nm but small apertures (ca. 3.4 Å diameter, if expansion via linker torsional motion is ignored). This iconic material features the sodalite (**sod**) topology, consists of Zn^{2+} and 2-methylimidazolate (mim^-) in 1:2 stoichiometry ($\text{Zn}(\text{mim})_2$, Fig. 1 left) and possesses a remarkably high thermal and chemical stability (ZIF-8 is stable in 8 mol/L aqueous NaOH solution at 100 °C!)^[3a]. Remarkably easy to assemble in particulate, nanoparticulate, thin-film, 2D opal, and even membrane form, ZIF-8 is the single most extensively studied ZIF material, both from a fundamental and from an applied/application perspective. Unfortunately, this important material cannot be transformed into a glass for use in a wider range of applications. To address this challenge, we exchanged a large fraction of

the mim^- linkers of ZIF-8 to im^- and bim^- by post-synthetic solvent-assisted linker exchange (SALE)^[4] under complete retention of the high porosity structure with **sod** topology (Fig. 1 middle).

In November 2021, we started to investigate the structural response of conventional crystalline ZIF-8 (i.e. $\text{Zn}(\text{mim})_2$), and one of the ZIF-8 derivatives derived via SALE (i.e. $\text{ZIF-8-mim}_{0.14}\text{im}_{0.78}\text{bim}_{0.08}$) using temperature-dependent X-ray powder diffraction (XRPD) with the Anton Parr heating stage available at BL9 of DELTA. For conventional ZIF-8, the XRPD pattern remains similar upon heating from 30 °C to about 470 °C. No melting of ZIF-8 is observed in that temperature range and the framework structure remains intact. After partial linker exchange, the XRPD data of the linker-exchanged derivative $\text{ZIF-8-mim}_{0.14}\text{im}_{0.78}\text{bim}_{0.08}$ behaves very differently and displays a non-crystalline state after reaching temperatures of approx. 300 °C. Combined with the DSC data, we can infer that $\text{ZIF-8-mim}_{0.14}\text{im}_{0.78}\text{bim}_{0.08}$ melts at about 300 °C (Fig. 1 right). These data demonstrate that partial linker exchange in ZIF-8 leads to a significantly reduced melting temperature (i.e. lowering of the melting point below the decomposition temperature) finally enabling the formation of a ZIF-8 glass upon cooling. This also proves that not only the much denser ZIFs with **cag** topology (i.e. ZIF-4, ZIF-62) can melt and form glasses, but also ZIFs with the highly porous **sod** topology, as long as the linker chemistry supports this. The obtained results are crucial for the future development of the topical and dynamic field of ZIF glasses as they set the stage for further derivatization, diversification, and composite formation of ZIF glasses, to generate new glassy materials beyond the state of the art.

Experimental setup and aims

In order to complete and extend our study, we collected variable temperature X-ray powder diffraction (VT-XRPD) data for eight more $\text{ZIF-8-mim}_x\text{im}_y\text{bim}_z$ derivatives as well as four other related MOF materials. All samples were sealed in quartz capillaries and investigated in the temperature range from ambient temperature up to about 420 °C (heating stage temperature, not sample temperature) in steps of 25 to 50 °C (as appropriate) using the Anton Parr heating stage with a graphite dome. The sample temperature was determined by a temperature calibration of the setup using temperature dependent XRPD measurements of Silicon. After reaching about 420 °C, the samples were returned to ambient temperature for another data collection to check whether the samples had maintained the non-crystalline state or if the sample shows any kind of structural flexibility. The DSC data for each sample were subsequently correlated with the obtained VT-XRPD data to obtain the most accurate phase transition information. This allowed us to evaluate the impact of increased linker exchanges on the thermal behaviour of a compound family of the same structure type (i.e. ZIF-8 type with **sod** topology) with different chemical compositions setting the stage for the formulation of important structure-composition-property relationships in glass forming MOFs.

Results

All new investigated linker-exchanged ZIF-8 samples showed a loss of Bragg scattering and the emergence of diffuse scattering characteristic for ZIF liquid formation upon heating. Three of the most representative ones are selected here for report presentation and comparison with the pristine ZIF-8 (Fig. 2). For the original ZIF-8, the *in situ* VT-XRPD maintained almost the same diffraction peak at high temperatures (Fig. 2a). This is due to the strong coordination bond

formed between mim^- and Zn^{2+} ion, which makes ZIF-8 highly temperature stable (decomposition temperature is 541 °C). As we expected, with the addition of appropriate amounts of imidazole and benzimidazole during SALE, a series of glass formers were obtained. ZIF-8- $\text{mim}_{0.15}\text{im}_{0.74}\text{bim}_{0.11}$ vanishes all Bragg diffraction after 307 °C, showing diffuse scattering with characteristics for a liquid/glass (Fig. 2b). Likewise, *in situ* VT-XRPD was performed on other similar glass formers ZIF-8- $\text{mim}_{0.17}\text{im}_{0.75}\text{bim}_{0.08}$ and ZIF-8- $\text{mim}_{0.16}\text{im}_{0.72}\text{bim}_{0.12}$. They demonstrated the almost identical results as ZIF-8- $\text{mim}_{0.15}\text{im}_{0.74}\text{bim}_{0.11}$, with complete the loss of Bragg diffraction and long-range ordering above 307 °C (Fig. 2c-d). Importantly, when cooling the liquid ZIFs back to room temperature, a recrystallisation of the crystalline framework is not observed, visualised by the persistence of diffuse scattering.

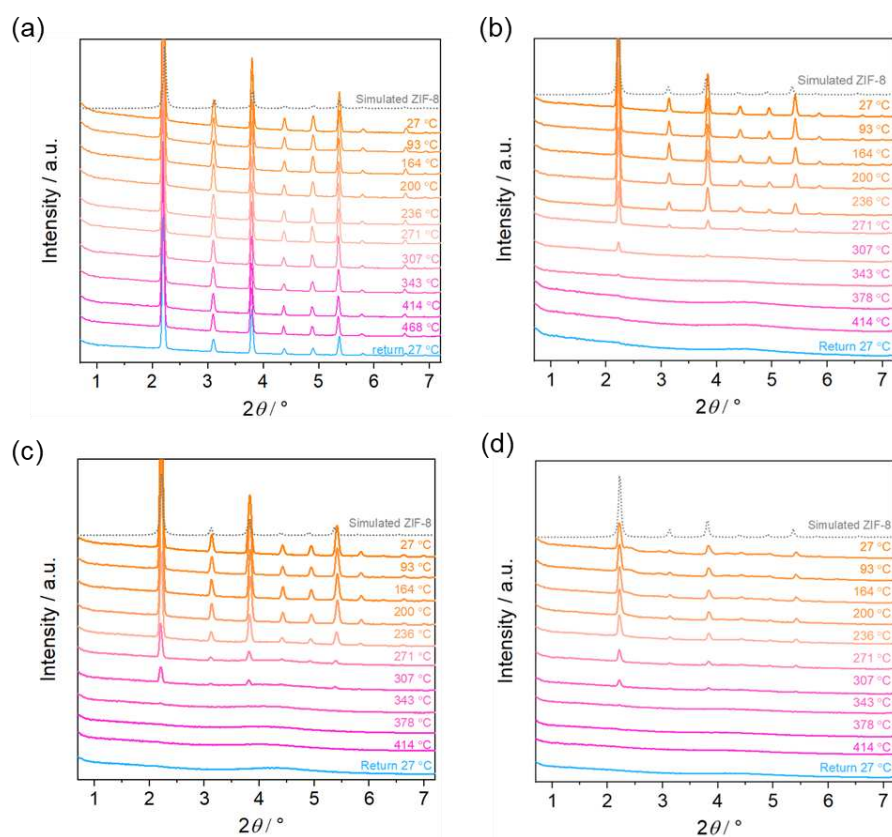


Fig. 2 Compilation of VT-XRPD patterns of ZIF-8 and three ZIF-8- $\text{mim}_x\text{im}_y\text{bim}_z$ materials. The patterns are not normalised but vertically offset for clarity. (a) ZIF-8, (b) ZIF-8- $\text{mim}_{0.15}\text{im}_{0.74}\text{bim}_{0.11}$, (c) ZIF-8- $\text{mim}_{0.17}\text{im}_{0.75}\text{bim}_{0.08}$ and (d) ZIF-8- $\text{mim}_{0.16}\text{im}_{0.72}\text{bim}_{0.12}$.

In summary, BL9 enabled us to monitor the phase transformation of ZIF-8- $\text{mim}_x\text{im}_y\text{bim}_z$ materials. The results clearly demonstrate the melting/glass formation process of ZIF-8 derivatives. Importantly, ZIF-8 glasses break the ‘spell’ that ZIF glasses are usually formed only by **cag** and **zni** topologies. This provides a new perspective on the increased structural complexity of the linker exchange processes of highly porous crystalline ZIFs that form the ZIF liquids and glasses.

The VT-XRPD data acquired during this beamtime are part of a manuscript which will be submitted for publication soon. The authors thank the DELTA group for the granted beamtime and the beamline scientists of BL9, C. Sternemann and M. Paulus, for their invaluable support during the experiments.

References

- [1] a) *Chem. Soc. Rev.* 2009, 38, 1213-1477; b) *Chem. Soc. Rev.* 2011, 40, 453-1152; c) *Chem. Rev.* 2012, 112, 673-1268.
- [2] a) T. D. Bennett, et al., *J. Am. Chem. Soc.* 2016, 138, 3484; b) S. Horike, et al. *Angew. Chem. Int. Ed.* 2020, 59, 2. c) L. Frenzel-Beyme, et al., *J. Mater. Chem. A*, 2019,7, 985-990. d) L. Frenzel-Beyme, et al., *J. Am. Chem. Soc.* 2019, 141, 31, 12362–12371.
- [3] a) K. S. Park, et al., *Proc. Natl. Acad. Sci. U.S.A*, 2006, 103, 10186-10191. b) X.-C. Huang, et al., *Angew. Chem. Int. Ed.* 2006, 45, 1557 –155.
- [4] O. Karagiari, et al., *J. Am. Chem. Soc.* 2012, 134, 18790 –18796.

Hard X-ray spectroscopy

X-ray absorption studies of the EBDC fungicide Maneb in solid state

L. Kubens^{a,b}, J. Bornhorst^a, F. Mohr^b, D. Lützenkirchen-Hecht^c

a) Lebensmittelchemie, Fakultät für Mathematik und Naturwissenschaften, Bergische Universität Wuppertal, Gaußstraße 20, 42119 Wuppertal

b) Anorganische Chemie, Fakultät für Mathematik und Naturwissenschaften, Bergische Universität Wuppertal, Gaußstraße 20, 42119 Wuppertal

c) Physik, Fakultät für Mathematik und Naturwissenschaften, Bergische Universität Wuppertal, Gaußstraße 20, 42119 Wuppertal

The manganese containing Maneb is a member of the ethylenebis(dithiocarbamate) (EBDC) group of fungicides and was patented in the 1940s.^[1] Despite Maneb is in use in large quantities for over 70 years, the chemical structure is still unknown. Single crystals from DMF or DMSO solution were obtained by slow evaporation. X-ray diffraction data shows the coordination polymer of Maneb with DMF or DMSO molecules in *cis*-configuration, however, the solid-state structure of Maneb still remains unknown. Based on the molecular formula, it is assumed that Mn is surrounded by only four sulfur atoms. However, Mn(II) prefers an octahedral coordination structure with six coordination atoms. *Ciampolini et. al* have shown in 1975 that Mn in bis(diethyldithiocarbamate)-manganese (II) is coordinated by four sulfur atoms of the chelate rings and two sulfur atoms from neighboring molecules.^[2] The intramolecular sulfur bridges would therefore be a possible molecular structure for Maneb. In order to learn more about Maneb, we synthesized Maneb by reacting the diammonium ethylene bis(dithiocarbamate) with an equimolar amount of Mn(II)chloride in water.

In the present contribution, we have performed X-ray absorption fine structure measurements at the Mn K-edge to elucidate the short range order structure around the X-ray absorbing Mn-atoms. The experiments have been performed using the Si(111) channel-cut monochromator at beamline 10, and N₂-filled ionization chambers as detectors for the incident and transmitted intensities. The sample consist on finely dispersed Maneb powders on adhesive tape, and several tapes were stacked to obtain a sufficient absorption signal. High-quality EXAFS data were recorded at room temperature as well as in a liquid nitrogen bath cryostat at 77 K. In Fig. 1(a), the X-ray absorption near edge structure of Maneb is compared to several Mn reference compounds such as Mn-metal, different oxides of different chemical valence (MnO (Mn²⁺), Mn₂O₃ (Mn³⁺), Mn₃O₄ (Mn²⁺/Mn³⁺), MnO₂ (Mn⁴⁺)) and manganese sulfide (MnS, Mn²⁺). As can be seen, in particular the XANES spectra of MnS and Maneb appear similar in the edge region from about 6535 eV to ca. 6570 eV, however, the absorption fine structure obeys different minima and maxima for larger photon energies. The edge position determined from the different samples is displayed in the inset of Fig. 1(a) – as can be seen, a linear correlation between the edge position and the chemical valence exists, with a slope of 3.08 eV per valence. According to the edge position measured for the Maneb samples of 6544.36 eV ± 0.15 eV, a manganese 2+ species is very likely for Maneb.

The magnitude of the Fourier-transform of the k³-weighted EXAFS fine structure |FT (χ(k)*k³)| is shown in Fig. 1(b). An intense nearest neighbor peak is detected at about 2.2 Å radial distance. A simple first shell fit assuming only one Mn-S bond does not lead to an acceptable quality of the fit. We thus have

refined our fit model assuming two different coordination spheres, with a shorter and a longer Mn-S bond, respectively. Fit parameters are the amplitude reduction factors for both shells (S_{01}^2 , S_{02}^2), the two coordination distances (R_1 , R_2), the mean square disorder which was assumed to be identical in both shells ($\sigma_1^2 = \sigma_2^2$), and a possible correction of the edge position (inner potential shift, ΔE_0 , identical for both shells). In sum 6 fit parameters were thus used. Quantitative results gave $S_{01}^2 = 0.69 \pm 0.16$; $S_{02}^2 = 0.68 \pm 0.12$, $R_1 = 2.59 \text{ \AA} \pm 0.01 \text{ \AA}$, $R_2 = 2.74 \text{ \AA} \pm 0.03 \text{ \AA}$, $\sigma_1^2 = \sigma_2^2 = 3.22 \times 10^{-3} \pm 1.91 \times 10^{-3} \text{ \AA}^2$ and $\Delta E_0 = 3.96 \pm 1.22 \text{ eV}$. The fit gave a quality of $\chi = 1.51 \%$, which appears reasonable for the investigated ranges in k - and R -space. Both, the fits for 77 K and for room temperature, the optimized values for S_{01}^2 and S_{02}^2 gave identical values within the error of the experiments, i.e. the data supports the presence of two different Mn-S shells with four shorter and two longer Mn-S bonds with about 0.15 Å difference in bond length. The values obtained for $\sigma_1^2 = \sigma_2^2 = 3.22 \times 10^{-3} \text{ \AA}^2$ are meaningful as well, compared e.g. to ZnO at 77 K, with values of $\approx 4 \times 10^{-3} \text{ \AA}^2$, and only half of the value found for room temperature measurements. Compared to ZnO, the slightly larger bond length together with smaller values of σ^2 suggest the presence of a strong Mn-S bond in the case of Maneb. Further details are given in [3] and will be presented in an upcoming publication.

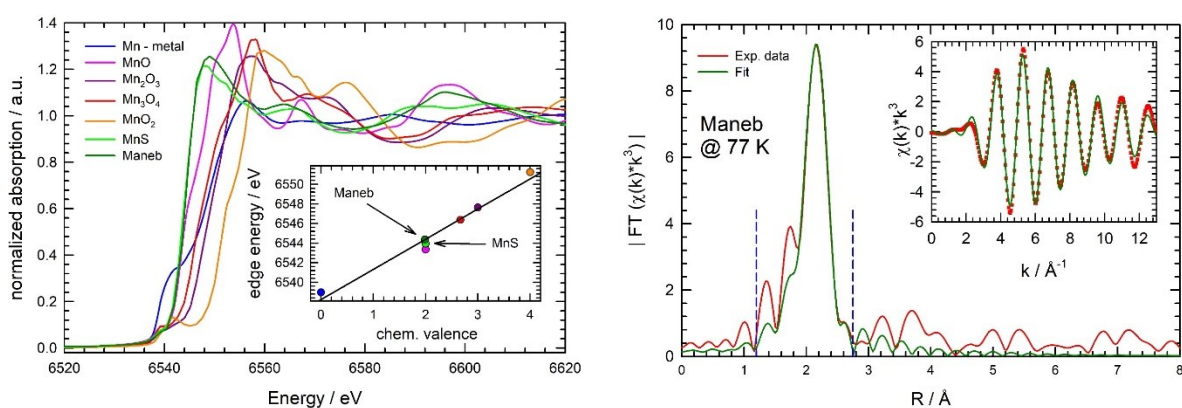


Figure 1: X-ray absorption near-edge (XANES) of different Mn reference materials (left) and the magnitude of the Fourier transformation of the k^3 -weighted EXAFS fine structure $|\text{FT}(\chi(k) \cdot k^3)|$ for Maneb at the Mn K-edge. (k -range for the FT: $1.98 \text{ \AA}^{-1} \leq k \leq 12.94 \text{ \AA}^{-1}$). A fit of the experimental data to a model consisting of 4 Mn-S bonds with a shorter bond length of 2.59 Å and two Mn-S coordinations with 2.74 Å is provided. See text for more details.

Acknowledgement

We gratefully acknowledge the DELTA machine group for providing synchrotron radiation reliably.

References:

- [1] United States Patent Office Number: US2504404A - Manganous ethylene bis-dithiocarbamate and fungicidal compositions containing same, Apr. 18, 1950
- [2] M. Ciampolini *et. al.*, *J. Chem. Soc., Dalton Trans.* **1975**, 2051
- [3] L. Kubens *et. al.*, *50. Deutscher Lebensmittelchemikertag, Hamburg, 19.-21.9.2022.*

Time-resolved, quick X-ray absorption spectroscopy at DELTA beamline 10

D. Lützenkirchen-Hecht, F. Eckelt, S. Paripisa, L. Voss, F. Braun, P. Rothweiler, R. Wagner

Bergische Universität Wuppertal – Fakultät für Mathematik und Naturwissenschaften, Gauß-Str. 20, 42097 Wuppertal, Germany.

The extended X-ray absorption fine structure (EXAFS) contains element-specific information about the local geometric structure of solids and liquids, i.e. bond distances, coordination numbers and the local disorder around an X-ray absorbing element can be determined (see, e.g. [1, 2]). In an EXAFS experiment, the absorption coefficient is measured within the vicinity of an absorption edge of a selected element with high accuracy [1]. Covering a photon energy range of about 1 keV or more, a typical measurement employing an integration time of several seconds for each data point in the spectrum on a step-by-step basis typically takes 10-30 minutes depending e.g. on the concentration of the absorber atom and the sample environment. Due to the advances of synchrotron light sources in the past years, e.g. by using insertion devices, the photon flux provided allows a substantial reduction of the integration time, and measurements may be performed “on-the-fly” within a couple of seconds for individual spectra nowadays (Quick-EXAFS, see ref. [3-6]). These capabilities are very interesting for time-resolved studies of chemical reactions [7], phase transformations [8], corrosion processes [9] and thin film growth phenomena [10], to mention just a few. Continuing activities that began after the installation of the new wiggler at beamline 8, 9 and 10 [11], we further investigated the opportunities for time-resolved EXAFS experiments at beamline 10 here. Beamline 10 appears to be well-suited for quick-EXAFS measurements due to the use of a compact, mechanically stable channel-cut monochromator, and a short distance to the wiggler device [12].

The experiments presented here make use of N₂- and Ar-filled ionization chambers for the measurements of the incident and transmitted X-ray intensities of a Cu metal reference foil cooled to liquid nitrogen temperature in a bath cryostat. The measurements were performed at the Cu K-edge (8980 eV), with a scan range covering the spectral range from 8800 eV to 10000 eV, i.e. 1200 eV with 1400 data points in total. The acquisition time per data point was systematically varied, and in Fig. 1, scans performed with acquisition times down to 10 ms per point are compared. Both the normalized absorption data as well as the extracted, k³-weighted EXAFS fine structure oscillations k³·χ(k) are shown there.

As can be seen, almost noise-free absorption data can be collected up to ca. 9600 eV, i.e. about 600 eV above the Cu K-edge for all the spectra, corresponding to a photoelectron wave number of more than 12.6 Å⁻¹. As can be seen in the insert of Fig. 1, well reproducible fine structure oscillations are detectable up to even 16 Å⁻¹. This implies that the evaluation of EXAFS data k³·χ(k) from such a large range in k-space would allow to extract meaningful structural information from the data accordingly [13]. We have thus performed a quantitative fitting of the EXAFS data to compare the results obtained. The results gave identical results for the first shell parameters, i.e. a bond length of R₁ = 2.540 ± 0.002 Å, a mean square displacement σ₁² = 4.075 × 10⁻³ Å² ± 1.5279 × 10⁻⁴ Å², and an amplitude reduction factor of S₀² = 0.843 ± 0.025, without any systematic dependence on the scan speed or the integration time for each data point as one may expect. It is thus planned to perform a more detailed EXAFS analysis beyond the first shell, including a careful assessment of the errors. Furthermore it is planned to make use of these capabilities for time-resolved EXAFS experiments in the near future.

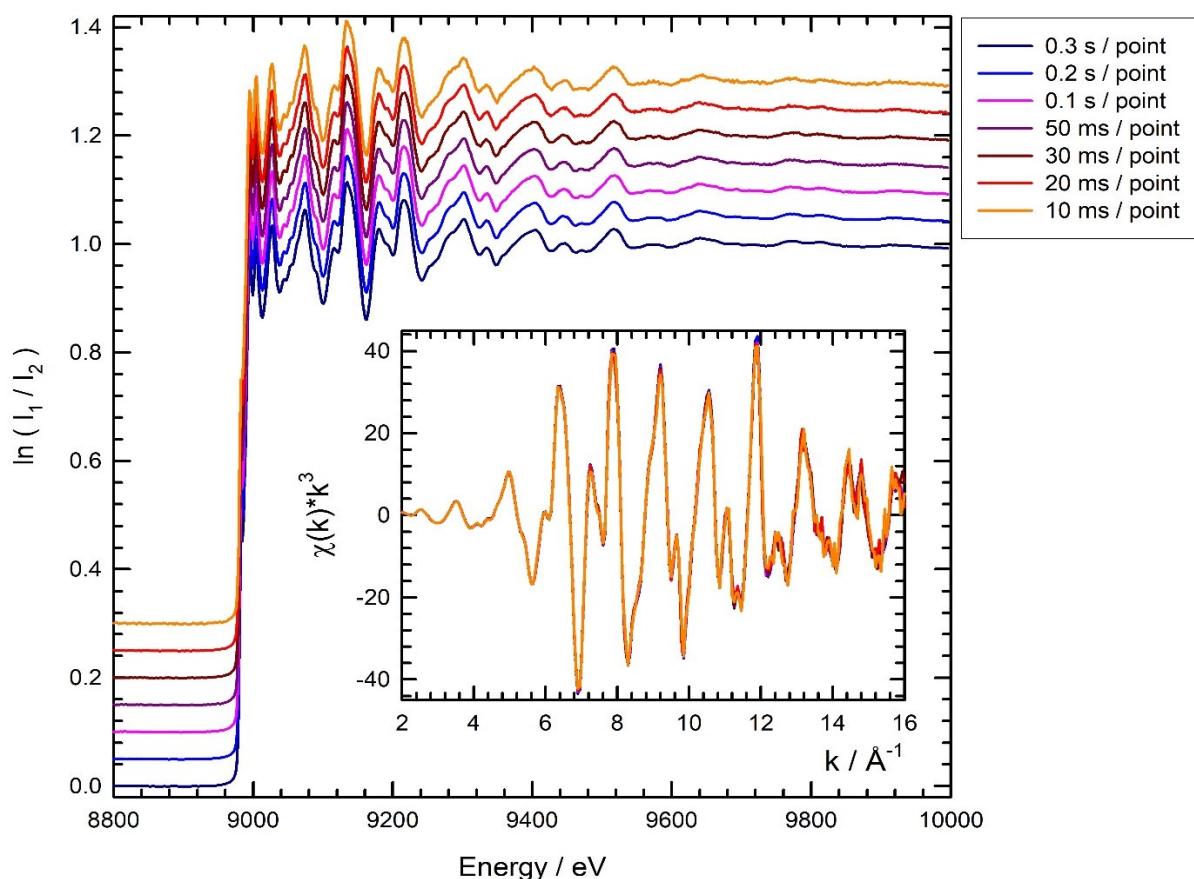


Fig. 1: Comparison of Cu K-edge X-ray absorption data of a Cu metal foil measured at 77 K employing different scan speeds and integration times per data point as indicated. In the insert, the k^3 -weighted EXAFS fine structures $\chi(k) \cdot k^3$ are shown.

Acknowledgements:

The authors like to thank the DELTA machine group for the delivery of a high-quality beam.

References:

- [1] D.C. Koningsberger, R. Prins (Eds.): X-Ray Absorption, Principles, Applications, Techniques of EXAFS, SEXAFS and XANES, John Wiley & Sons, New York (1988).
- [2] J.J. Rehr, R. C. Albers, Rev. Mod. Phys. 72 (2000) 621.
- [3] R. Frahm, R. Frahm, Nucl. Instrum. Methods Phys. Res. A 270 (1988) 578.
- [4] J. Stötzel, D. Lützenkirchen-Hecht and R. Frahm, Rev. Sci. Instrum. 81 (2010) 073109.
- [5] O. Müller, D. Lützenkirchen-Hecht and R. Frahm, Rev. Sci. Instrum. 86 (2015) 035105.
- [6] B. Bornmann, J. Kläs, O. Müller, et al., AIP Conf. Proc. 2054 (2019) 040008.
- [7] F. Eckelt, F. Eckelt, P. Rothweiler, L. Voss, F. Braun, A. Saric, M. Vrankic, D. Lützenkirchen-Hecht, Materials 15 (2022) 8186.
- [8] A. Ribeiro Passos, C. La Fontaine, S.H. Pulcinelli, C.V. Santilli, V. Briois, Phys. Chem. Chem. Phys. 22 (2020) 18835.
- [9] D. Lützenkirchen-Hecht, R. Frahm, J. Phys. Chem. B 105 (2001) 9988.
- [10] D. Lützenkirchen-Hecht, J. Stötzel, J. Just, O. Müller, B. Bornmann, R. Frahm, Phys. Stat. Sol. a 219 (2022) 2100514.
- [11] D. Lützenkirchen-Hecht, A. Šarić, F. Eckelt, M. Vrankić, S. Paripsa, R. Wagner, DELTA annual report (2021), p. 25.
- [12] D. Lützenkirchen-Hecht, R. Wagner, S. Szillat, et al., J. Synchrotron Rad. 21 (2014) 819.
- [13] E. Stern, Phys. Rev. B 48 (1993) 9825.

EXAFS investigations of Nb interlayer on Nb₃Sn coatings on Cu

F. Braun^a, L. Voss^a, N. Schäfer^b, M. Major^b,
L. Alff^b, D. Lützenkirchen-Hecht^a

^a Faculty of Mathematics and Natural Sciences-Physics Department, Bergische Universität Wuppertal, Gauss-Str. 20, D-42119 Wuppertal, Germany

^b Institute of Materials Science, FB11, Technical University of Darmstadt, Alarich-Weiss-Str. 2, D-64287 Darmstadt, Germany

Most modern particle accelerators rely on superconducting radio frequency (SRF) cavities. These are typically manufactured using deep drawn niobium sheets of high purity which are then welded to form cavities. Conventional approaches to prepare an accelerator cavity involve a large number of process steps, e. g. mechanical grinding and polishing, buffered chemical polishing, electro polishing, etc. [1]. Due to the fact that superconducting RF currents are only present in the near surface region of the cavities, an alternative procedure uses pure copper as a base for the cavities, and only a thin, μm -thick layer of Nb₃Sn is coated on the precisely formed Cu-substrates. This strategy reduces the amount of the rare Nb material involved, as well as it facilitates the molding of the cavity form. Furthermore, in case of a quench, metallic copper has a substantially larger electrical conductivity in its normal-conducting state.

For the present investigation, we therefore investigated thin Nb₃Sn films on Cu substrates. The films were prepared by co-sputtering of metallic Nb and Sn on copper substrate heated to 520 °C. Heat was introduced by a projection lamp from the backside while the temperature was measured directly in the surface of the substrate. The stoichiometry was controlled by the sputtering power of each sputtering gun independently. The power ratio was found to result in the proper stoichiometry for 30 W Sn and 158 W Nb. The coating process took 90 minutes in total and resulted in about 1 μm layer thickness. The process was conducted in a vacuum chamber filled with 10^{-2} mbar argon as the sputtering gas.

The co-sputtering process allows an unprecedented low synthesis temperature [2]. For this reason, it is possible for the first time to coat copper with Nb₃Sn. Before this work, thermal approaches needed about 930 °C in order to obtain a phase pure synthesis [3], that can however not be used for deposition on Cu substrates due to the copper melting point being around 1080 °C. Furthermore it is expected that copper inter-diffusion starts at about 50 % of the melting point, i.e., for temperatures above 400 °C. Nb₃Sn thin films grown at around 500 °C have shown excellent performance, although a weak copper signal could be observed by X-ray photoelectron spectroscopy (XPS). It is to be clarified, if the copper signal comes from diffusion of copper into the Nb₃Sn film or whether it originates from the substrate due to cracks in the layers. The following experiments should thus provide information about the neighboring atoms to solve the unexpected occurrence of copper in the film at these rather low temperatures. Additionally, it is important to quantify the ability of a niobium interlayer (low self-diffusion coefficient) to inhibit the copper diffusion into the superconducting film. Therefore one Nb₃Sn film was directly coated on the mechanically polished and cleaned copper substrate (sample S1), while for sample S2, a niobium interlayer was used.

Here we have used X-ray absorption spectroscopy (XAS) experiments at the Cu K-edge (8980 eV) to investigate a possible intermixing of Cu and Nb/Sn and the inner film-substrate interface. In case of an intermixing, the substantially different backscattering amplitudes and phases of Nb should substantially modify the EXAFS of metallic Cu. By a variation of the incidence angle Θ , the information depth can be adjusted so that a major portion of the detected fluorescence EXAFS signal at the Cu K-edge originates from the interface region, and not from the bulk of the Cu substrate. The experiments were carried out at the wiggler beamline BL10 at the DELTA storage ring (Dortmund, Germany) operating with 80-130 mA of 1.5 GeV electrons [4]. Cu K-edge spectra were collected using a Si(111)-channel cut monochromator and a N₂-gas-filled ionization chamber for the incident beam, while a large area passivated implanted planar silicon (PIPS) detector was used to collect the excited Cu fluorescence from the Nb₃Sn-coated Cu specimen. In Fig. 1, the normalized fluorescence-mode X-ray absorption fine structure is depicted for both samples, and the extracted, k^2 -weighted EXAFS fine structures $\chi(k) \cdot k^2$ are compared in the insert. As can be seen, the amplitude for the EXAFS is larger for sample S2 in comparison to S1, suggesting a more developed structure in sample S2.

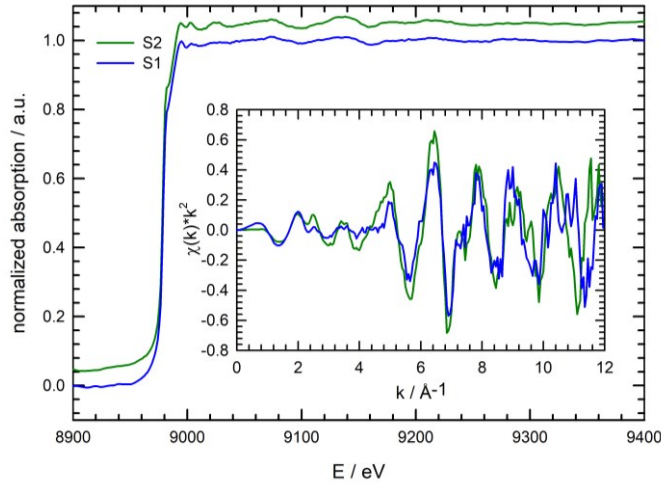


Fig. 1: Normalized fluorescence mode EXAFS data at the Cu K-edge for Nb₃Sn-thin films on a copper substrate for an incidence angle of $\Theta = 3.6^\circ$. Sample S1 corresponds to a layer of Nb₃Sn on top of the Cu substrate, while S2 refers to a sample with an additional Nb interlayer (see text for more details). In the insert, the k^2 -weighted EXAFS fine structure oscillations $\chi(k)*k^2$ are presented for both samples.

The magnitude of the Fourier-transform of the k^2 -weighted EXAFS fine structure oscillations measured above the Cu K-edge $|FT(\chi(k)*k^2)|$ for samples S1 and S2 is presented in Fig. 2, together with data of a Cu metal reference foil. Well in agreement with the larger amplitudes of the extracted EXAFS fine structures $\chi(k)*k^2$ for sample S2, the FT of the latter spectrum shows a substantially larger amplitude for the Cu-Cu shell of the Cu substrate for a radial distance of $R \approx 2.3 \text{ \AA}$. In addition, a shift of the first shell peak to larger distances is observed for S1, as can be seen in particular in comparison to the Cu reference material, which is absent for sample S2. This shift observed for S1 suggest that larger atoms, most likely Sn, have diffused into the Cu substrate during the coating process for this sample. Obviously, the identical first shell positions for sample S2 and the Cu reference indicate the absence of intermixing processes here, implying that the Nb interlayer may suppress related diffusion processes effectively. Additional measurements including a systematic variation of the incidence angles to provide more information on the interdiffusion processes as well as a more detailed data analysis are planned for the future.

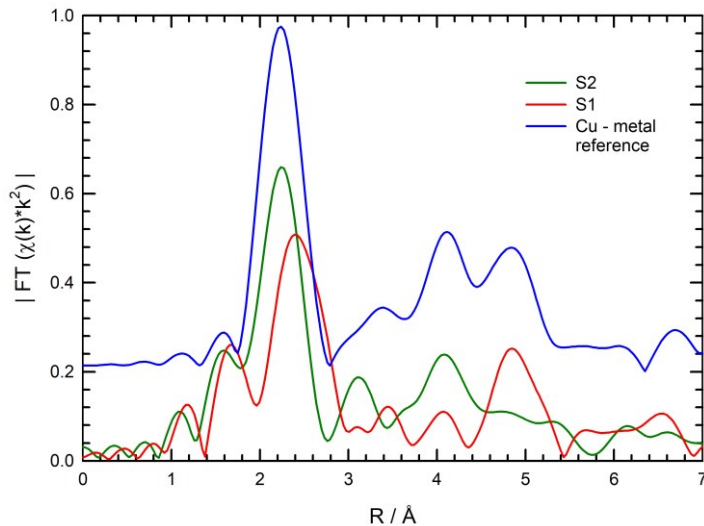


Fig. 2: Magnitude of the Fourier transforms of the k^2 -weighted EXAFS fine structure oscillations $|FT(\chi(k)*k^2)|$ measured above the Cu K-edge of samples S1 and S2 for an incidence angle of $\Theta = 3.6^\circ$. For comparison the FT of a Cu metal reference foil is also provided (k -range for the FT $1.7 \text{ \AA}^{-1} < k < 10.9 \text{ \AA}^{-1}$, data are not corrected for phase shifts).

Acknowledgements

We gratefully acknowledge the DELTA machine group for providing synchrotron radiation reliably. The experiments were financially support by the German Federal Ministry of Education and Research (BMBF) under project no. 05K22PXB.

References

- [1] W. Singer, X. Singer, A. Brinkmann, et al., Supercond. Sci. Technol. 28 (2015) 085014(12).
- [2] N. Schäfer, N. Karabas, J. P. Palakkal, S. Petzold, M. Major, N. Pietralla, L. Alff, J. Appl. Phys. 128 (2020) 133902.
- [3] E. Barzi, M. Bestetti, F. Reginato, D. Turrioni, S. Franz, Supercond. Sci. Technol. 29 (2015) 015009.
- [4] D. Lützenkirchen-Hecht, R. Wagner, S. Szillat, et al., J. Synchrotron Rad. 21 (2014) 819.

XANES Investigation of the Solid solution $\text{Er}_x\text{U}_{1-x}\text{C}_2$

C. Tobeck, S. Kirchhoff, D. Lützenkirchen-Hecht and U. Ruschewitz*

Department für Chemie, Universität zu Köln, 50939 Köln, Germany

*email: uwe.ruschewitz@uni-koeln.de

In 2013, we demonstrated that a valence change of ytterbium occurred in the solid solution $\text{Yb}_x\text{Ca}_{1-x}\text{C}_2$ in dependence of x .^[1] Using XANES spectroscopy we showed that at low Yb contents the CaC_2 host lattice forces Yb into the divalent +2 state, whereas at higher Yb contents an intermediate state of +2.7 is observed, which is close to pure YbC_2 with +2.81.^[2]

Since there is a large number of different oxidation states of uranium in its compounds, UC_2 seems to be a good candidate for similar valence changes in its solid solutions with e.g. LnC_2 (Ln: La-Lu). By arc melting of UO_2 with purified graphite and the respective lanthanide, we synthesized crystalline and phase-pure solid solutions of type $\text{Ln}_x\text{U}_{1-x}\text{C}_2$. Due to the different electronic structures of its end members $\text{U}^{\text{IV}}(\text{C}_2)$ and $\text{Ln}^{\text{III}}(\text{C}_2)$ crystallizing in the same structure type ($I4/mmm$, $Z = 2$), these solid solutions are interesting systems to be studied.

Here we present XANES- L_{III} edge spectroscopic studies of uranium and erbium in the solid solution $\text{Er}_x\text{U}_{1-x}\text{C}_2$ measured at BL8 and BL10 of the DELTA synchrotron facility. Figure 1 shows

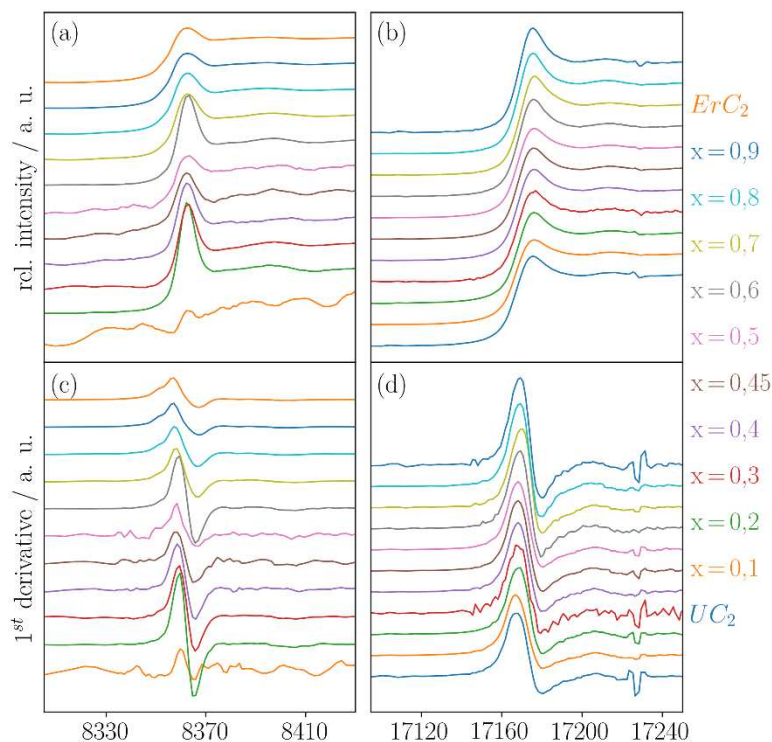


Figure 1: XANES L_{III} edge spectra of erbium (a) and uranium (b) in the solid solution $\text{Er}_x\text{U}_{1-x}\text{C}_2$ with their first derivatives (c and d).

the XANES- L_{III} edge spectra of erbium (a) and uranium (b) with their first derivatives (c and d). In the spectra of erbium, there is a decrease in the area of the white line (a) and a slight shift in the edge position (c) with a discontinuity between $x = 0.5$ and 0.6 . The changes in the L_{III} spectra of uranium (b) and its first derivative are not as strong, but a shift is also clearly visible. This becomes more obvious, when the parameters extracted from the XANES spectra are plotted against the amount of erbium (Figure 2: Er L_{III} spectra; Figure 3: U L_{III} spectra).

It can be seen that with increasing erbium content, there is a transfer of electron density from the uranium to the erbium atom. However, the discontinuities of the white line areas and the positions of the edge energies are not yet understood.

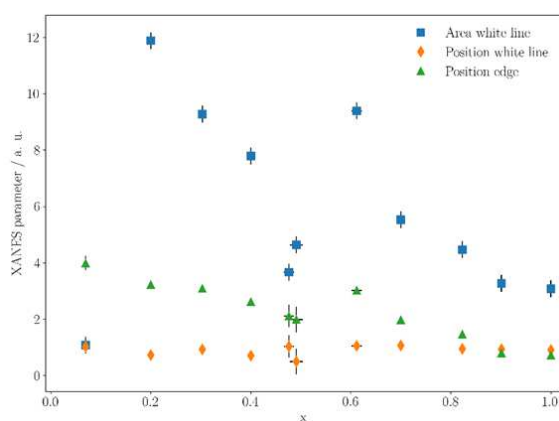


Figure 2: Extracted parameters from the Er L_{III} XANES spectra of $Er_xU_{1-x}C_2$.

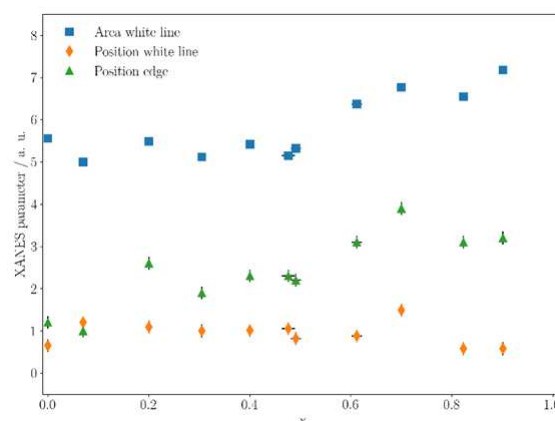


Figure 3: Extracted parameters from the U L_{III} XANES spectra of $Er_xU_{1-x}C_2$.

For a deeper understanding, further investigations like XANES measurements at the $M_{4,5}$ edge and theoretical methods like multiplet calculations need to be performed.

- [1] P. Link, P. Glatzel, K. Kvashnina, D. M. Trots, R. I. Smith, U. Ruschewitz, *Inorg. Chem.* **2013**, *52*, 7020-7030.
- [2] P. Link, P. Glatzel, K. Kvashnina, R. I. Smith, U. Ruschewitz, *Inorg. Chem.* **2011**, *50*, 5587-5595.

An X-ray absorption near-edge structure study on AlCrVYN thin films

Eric Schneider¹, Finn Ontrup², Nicola Thiering¹, Susanne Dogan¹, Steffen Bieder¹, Christian Sternemann¹, Michael Paulus¹, David Kokalj², Dominic Stangier², Nelson Filipe Lopes Dias², Ralph Wagner³, Dirk Lützenkirchen-Hecht³, Wolfgang Tillmann², Metin Tolan¹

¹Fakultät Physik/DELTA, TU Dortmund University, 44221 Dortmund, Germany

²Fakultät Maschinenbau, Institute of Materials Engineering, TU Dortmund University, 44221 Dortmund, Germany

³Fakultät für Mathematik und Naturwissenschaften, Fachgruppe Physik, University of Wuppertal, 42119 Wuppertal, Germany

In production engineering, major efforts are made to optimize tool coatings for applications exposed to elevated process temperatures. A specific focus lies especially on dry machining or machining with minimum quantity lubrication. Thus, depending on the material and tool designs, temperatures between 300°C and 1000°C can occur during operations [1]. In order to enable machining of high-strength materials, the high-temperature properties of the tool coatings need to be tailored according to the application. The addition of vanadium to AlCrN favours the formation of so-called Magneli phases to reduce the friction at high temperatures [2], whereas small amounts of yttrium improves the oxidation resistance [3]. The aim of this X-ray absorption study is to obtain a fundamental understanding of the oxidation behavior of these coatings during temperature treatment of thin films produced with varying deposition parameters.

For the X-ray absorption near-edge structure (XANES) studies, AlCrVYN thin films were grown by direct current magnetron sputtering (dcMS) with varying bias voltage, substrate temperature and coating design and high power impulse magnetron sputtering (HiPIMS) with varying pulse length t (40 and 80 μ s) and pulse frequency f (500, 1000, and 2000 Hz). Both parameters control the duty cycle (on-time) of the magnetron. We studied coated WC-Co substrates that were stepwise heated *ex situ*, between 25°C and 1000°C. Figure 1 shows the setup used at beamline BL10 at DELTA. The XANES measurements

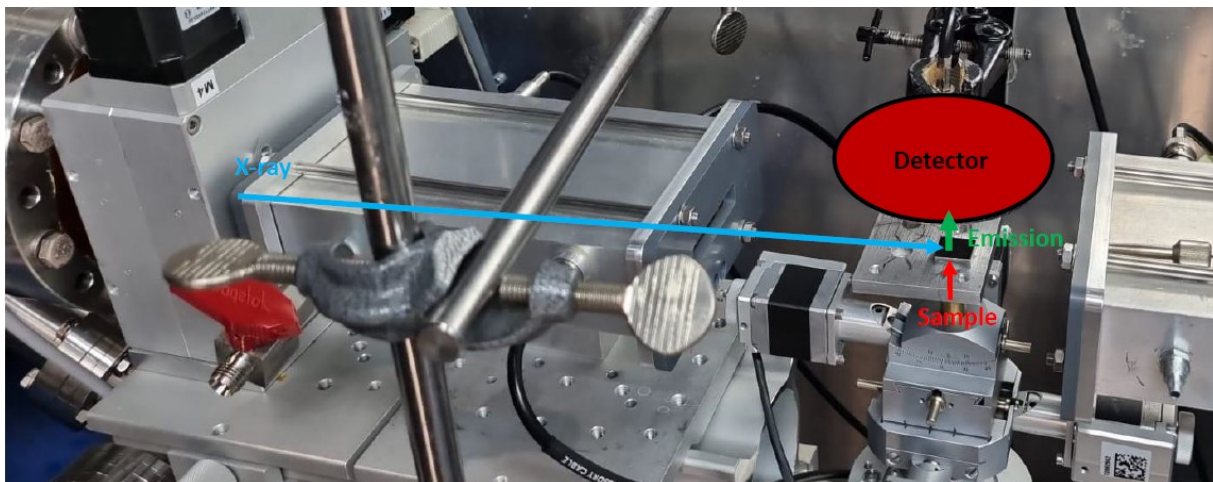


Figure 1: XANES fluorescence detection setup at beamline BL10. During the measurements, the sample is aligned to an grazing angle of 4°. Measurements were taken in a range from 5404 eV to 5585 eV to detect the vanadium K-edge.

were performed in fluorescence detection mode at the vanadium K-edge (5465 eV) using a grazing angle of 4°, to identify vanadium to be present in different oxidation states. In this setup we used a beam size of 0.2 x 8.0 mm² ($v \times h$).

At high temperatures, the samples exhibit a variety of oxide phases, which are difficult to analyse with XRD only. Therefore, the oxide formation of the thin films is investigated using XANES as an alternative method for the determination of vanadium oxides via the analysis of the pre-edge peaks of the XANES spectra. Similar to iron oxides, the pre-edge area and main-edge position provide information about

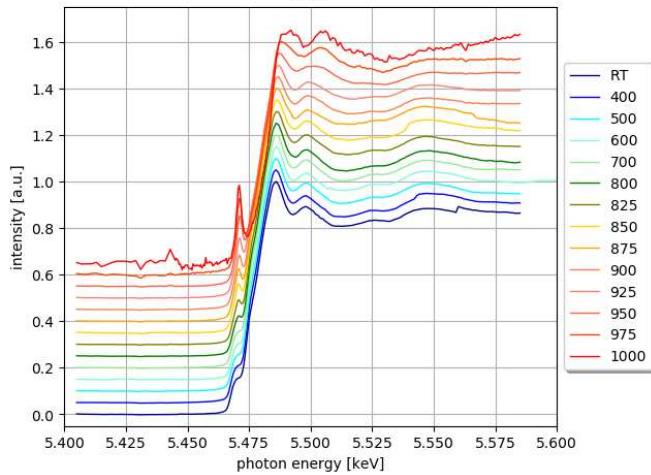


Figure 2: Oxidation behavior of a -150V bias voltage sample. Heating was carried out step by step *ex situ* up to 1000°C.

the oxidation state of vanadium [4, 5]. Figure 2 shows the oxidation behavior of a sample produced with an increased bias voltage of 150 V. By comparing the pre-edge of the samples with the pre-edges of the references, i.e. vanadium oxides of different oxidation state ranging from 0 to 5, the average oxidation state of the film can be assigned. It can be noticed that the use of high bias voltages and low heating powers (dcMS) favor presence of higher oxidation states of vanadium. Furthermore, we find evidence that HiPIMS samples produced with higher pulse durations and frequencies exhibit a higher degree of oxidation, as shown in figure 3.

Finally, it should be mentioned that the resulting oxides have not yet reached the desired degree of oxidation. Therefore, the investigations will be continued with the variation of additional deposition parameters. Work will also be continued on the reference samples for further minimization of possible error sources.

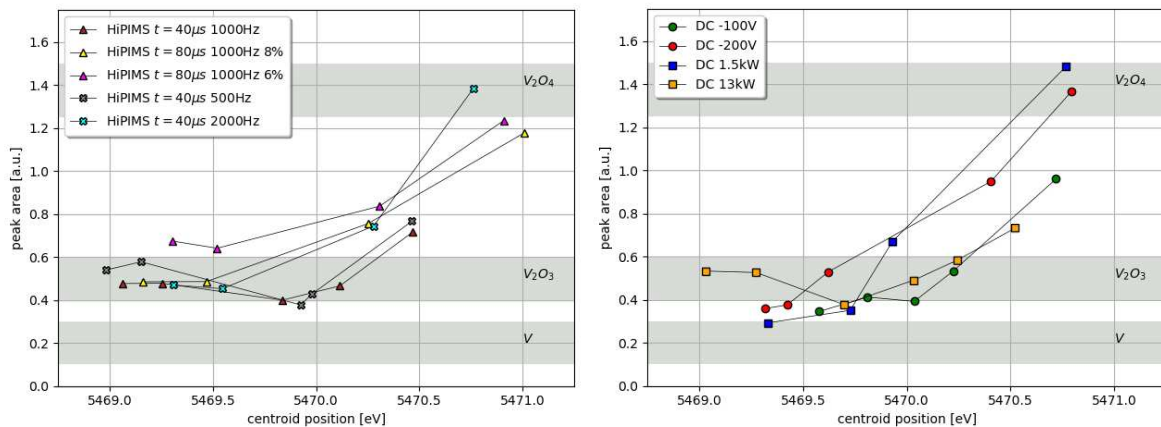


Figure 3: Comparison of the oxidation behavior of all samples based on the position and area of the pre-edge. The grey areas indicate the pre-edge behavior of reference samples.

References

- [1] K.-M. Li, S.Y. Liang, Modeling of Cutting Temperature in Near Dry Machining, *J. Manuf. Sci. Eng.* 128 (2006) 416–424.
- [2] W. Tillmann, D. Kokalj, D. Stangier, M. Paulus, C. Sternemann, M. Tolan, Investigation on the oxidation behavior of AlCrVxN thin films by means of synchrotron radiation and influence on the high temperature friction, *Applied Surface Science*, Volume 427, Part B, 2018, Pages 511-521.
- [3] F. Rovere, P.H. Mayrhofer, A. Reinholdt, J. Mayer, J.M. Schneider, (2008): The effect of yttrium incorporation on the oxidation resistance of Cr–Al–N coatings. In: *Surface and Coatings Technology 202*, Issue 24, S. 5870-5875,
- [4] M. Wilke, G. M. Partzsch, R. Bernhardt, D. Lattard, Determination of the iron oxidation state in basaltic glasses using XANES at the K-edge, *Chemical Geology*, Volume 213, Issues 1–3, 2004, Pages 71-87
- [5] W. Tillmann, L. Hagen, D. Kokalj, M. Paulus, M. Tolan, Temperature-induced formation of lubricous oxides in vanadium containing iron-based arc sprayed coatings, 2018

Acknowledgments

We thank the DELTA team for providing synchrotron radiation. This work was supported by the DFG via TO 169/21-1 and TI 343/190-1.

EXAFS investigations of PtCu Nanoalloys on Nitrogen-Doped Carbon for Applications in Fuel Cells

B. Wu,^{[a],[b]} J. Xiao,^[c] L. Li,^[a] Y. Wu,^[a] X. Tang,^[a] T. Hu,^[b] M. Qiu,^[c] F. Braun,^[d] F. Eckelt,^[d]
L. Voss,^[d] D. Lützenkirchen-Hecht,^[d] K. Yuan,^[a] Y. Chen^{[a], [e]}

[a] College of Chemistry and Chemical Engineering/Institute of Polymers and Energy Chemistry (IPEC), Nanchang University, Nanchang, 330031, China

[b] School of Physics and Materials, Nanchang University, Nanchang, 330031, China

[c] Central China Normal University, Wuhan, 430079, China

[d] Faculty of Mathematics and Natural Sciences-Physics Department, Bergische Universität Wuppertal Gauss-Str. 20, D-42119 Wuppertal, Germany

[e] National Engineering Research Center for Carbohydrate Synthesis/Key Lab of Fluorine and Silicon for Energy Materials and Chemistry of Ministry of Education, Jiangxi Normal University, Nanchang, 330022, China

Due to their zero carbon emissions, high reliability, and high efficiency, proton exchange membrane fuel cells (PEMFCs) have attracted high scientific interest [1, 2]. Traditional electrocatalysts, however, show several constraints in terms of stability and slow reaction kinetics of the cathodic oxygen reduction reaction (ORR), so that currently platinum-based catalysts are the most promising materials in PEMFCs, in particular due to their superior electrocatalytic properties towards the ORR. To substantially reduce the deployment of Pt while maintaining a high activity, recent activities try to develop single atom Pt catalysts. For example, catalysts with a small Pt content have been realized by nanostructuring and size-controlling of Pt and Pt-alloy nanoparticles [3-5]. Downsizing of the Pt-containing particles however will result in excessive OH⁻ adsorption on the Pt surfaces [6, 7], and smaller particles may easily agglomerate to form larger assemblies which further reduces ORR activity [8]. Similar degradation processes also occur under the working conditions in a PEMFC. Thus, new strategies are required to overcome these existing limitations, one of which is the coating of the nanoparticles with graphitic carbon layers, which improves durability but however reduces activity of the catalysts [9].

Another approach is to dope Pt and other heteroatoms such as Fe or Co into a carbon matrix, which has proven to stabilize the catalysts on one hand, and furthermore the stress/strain and ligand effect of the heteroatoms lead to an optimization of the electronic structure and improves the adsorption strength of oxygenated intermediates simultaneously [10, 11]. A disadvantage of the doping is a possible loss of the introduced heteroatoms during potential cycling, which reduces the possible lifetime of a fuel cell device.

We thus have replaced Fe or Co doping by employing copper instead: Cu has a substantially more anodic dissolution potential of $E(\text{Cu}^{2+}/\text{Cu}) = +0.3$ V against standard hydrogen electrode (SHE) compared to iron with $E(\text{Fe}^{2+}/\text{Fe}) = -0.5$ V SHE, cobalt with $E(\text{Co}^{2+}/\text{Co}) = -0.2$ V SHE and even nickel with $E(\text{Ni}^{2+}/\text{Ni}) = +0.1$ V SHE. From an electrochemical perspective, thus, the use of Cu-heteroatoms appears attractive as a co-dopant for Pt-Cu alloys in a carbon matrix, i.e., potentially stable Cu species in PtCu nanoalloys play a vital role in sustaining ligand and strain effects, which are both beneficial for improving activity and durability of a PEMFC [12]. Here, we will report on the synthesis and the structure of PtCu nanoalloys rooted on nitrogen-doped carbon nanosheets (PtCuNC-700) as robust and efficient ORR catalysts by a straightforward molten salt synthesis approach.

In a first step, Cu was immobilized on carbon nanosheets (NCs) by a molten salt assisted pyrolysis as detailed in ref. [13]. Together with $\text{Pt}(\text{acac})_2$, this Cu/NC-precursor was dispersed in oleylamine and brought to reaction at 190 °C. The obtained product was subsequently annealed at 700 °C, followed by acid washing to produce PtCuNC-700. For comparison, a nitrogen-free sample (PtCuC-700) as well as a copper-free sample (PtNC-700) were fabricated by a similar approach. The samples were then investigated by transmission mode X-ray absorption spectroscopy at DELTA beamline 10, both at the Cu K-edge (8980 eV) as well as at the Pt L₃-edge (11564 eV) making use of the radiation from the recently installed wiggler in conjunction with a Si(111) channel cut monochromator and ionization chambers as detectors for incident and transmitted beams. The powder samples were homogeneously distributed on self-adhesive tape, and several tapes were stacked to obtain an absorption suited for X-ray absorption experiments without any additional treatment.

In Fig. 1(a), the Pt L₃-edge XANES of PtCuNC-700, PtCuC-700 and a Pt foil are compared. As can be seen, the white line intensities of PtCuNC-700 and PtCuC-700 are substantially reduced compared to that of a Pt metal foil. This observation suggests an increased occupation of 5d-electron levels, and a charge transfer from Cu to Pt in the PtCu nanoalloys. Furthermore, as depicted in the insert of Fig. 1(a), the edge positions of the L₃-edge

of PtCuNC-700 and PtCuC-700 are slightly shifted towards higher binding energies, suggesting a slight oxidation of the two nanoalloy materials. However, the edge position of PtCuNC-700 is closer to that of the Pt reference foil, indicating a more metallic behavior of the latter sample.

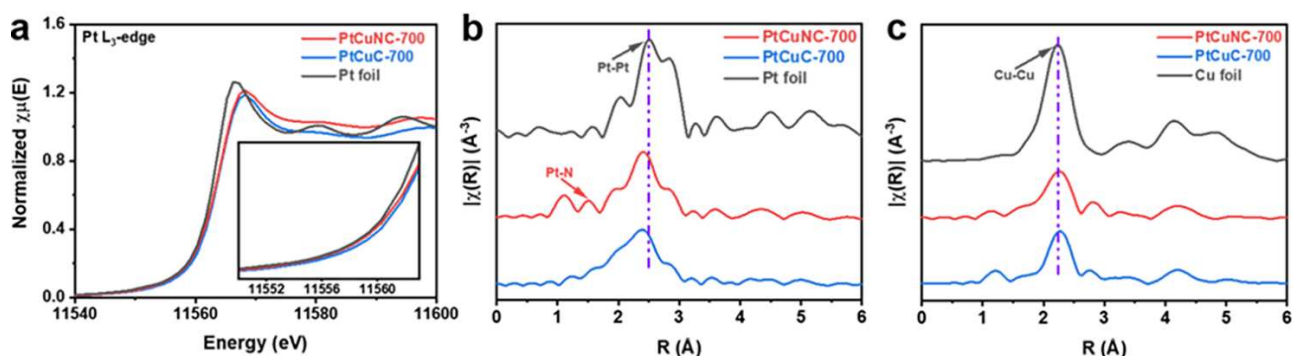


Fig. 1: (a) Comparison of Pt L₃-edge XANES spectra of PtCuNC-700, PtCuC-700 and Pt-metal foil. (b) Magnitude of the Fourier-transform of the k^3 -weighted EXAFS fine structure oscillations $\chi(k)*k^2$ of PtCuNC-700, PtCuC-700 and Pt foil at the Pt L₃-edge. (c) Magnitude of the Fourier-transform of the k^2 -weighted EXAFS fine structure oscillations $\chi(k)*k^3$ of PtCuNC-700, PtCuC-700 and a Cu-metal foil at the Cu K-edge.

The magnitude of the Fourier-transforms of the k^2 -weighted EXAFS fine structure spectrum at the Pt L₃-edge for PtCuNC-700 exhibits a dominant peak located at 2.4 Å in R space as can be seen in Fig. 1(b), which is related to Pt-Pt and Pt-Cu contributions. Compared to the Pt reference metal, the Pt-Pt peak is shifted to smaller radial distances and exhibits a smaller magnitude as well. Both features are indicative for the incorporation of Cu atoms in the first coordination sphere around Pt, and the formation of Pt-Cu bonds. Noticeable is a small peak in the Fourier-transform of PtCuNC-700 at 1.6 Å, which is absent for PtCuC-700 and the Pt foil. This feature can be assigned to Pt-N bonds, and confirm the close interaction of PtCu nanoalloys with the N-atoms of the carbon nanosheets.

The analysis of the Cu K-edge EXAFS is presented in Fig. 1(c). Compared to a Cu metal foil, the amplitude of the first nearest neighbor peak is substantially reduced in PtCuNC-700 and PtCuC-700. In addition, the peak position is slightly shifted to larger bond distances, in agreement with the Pt L₃-edge data, i.e., incorporation of larger Pt atoms in the first coordination sphere of Cu slightly increases the average bond length. In conclusion, the present experiments show the successful preparation of PtCu nanoalloys on N-doped carbon materials. The electrochemical properties of these materials and their application in proton exchange membrane fuel cells will be subject of a forthcoming publication [15].

Acknowledgement

We gratefully acknowledge the DELTA machine group for providing synchrotron radiation reliably.

References

- [1] K. Jiao, J. Xuan, Q. Du, et al., *Nature* **2021**, 595, 361.
- [2] J. Fan, M. Chen, Z. Zhao, et al., *Nat. Energy* **2021**, 6, 475.
- [3] L. Huang, S. Zaman, X. Tian, Z. Wang, et al., *Acc. Chem. Res.* **2021**, 54, 311.
- [4] S. L. A. Bueno, H. M. Ashberry, I. Shafei, S. E. Skrabalak, *Acc. Chem. Res.* **2021**, 54, 1662.
- [5] X. Duan, F. Cao, R. Ding, et al., *Adv. Energy Mater.* **2022**, 12, 2103144.
- [6] K. J. J. Mayrhofer, B. B. Blizanac, M. Arenz, et al., *J. Phys. Chem. B* **2005**, 109, 14433.
- [7] M. Shao, A. Peles, K. Shoemaker, *Nano Lett.* **2011**, 11, 3714.
- [8] J. M. Yoo, H. Shin, D. Y. Chung, Y. Sung, *Acc. Chem. Res.* **2022**, 55, 1278.
- [9] Z. Li, J. Zou, X. Xi, et al., *Adv. Mater.* **2022**, 34, 2202743.
- [10] K. Jiang, D. Zhao, S. Guo, et al., *Sci. Adv.* **2017**, 3, 1601705
- [11] C. Yang, L. Wang, P. Yin, et al., *Science* **2021**, 374, 459.
- [12] J. Zhang, Y. Yuan, L. Gao, G. Zeng, M. Li, H. Huang, *Adv. Mater.* **2021**, 33, 2006494.
- [13] H. Chen, D. Wang, Y. Yu, et al., *J. Am. Chem. Soc.* **2012**, 134, 18453
- [14] D. Lützenkirchen-Hecht, R. Wagner, S. Szillat, et al., *J. Synchrotron Rad.* **2014**, 21, 819.
- [15] B. Wu, J. Xiao, L. Li, et al., *CCS Chem.* **2022**, submitted.

Notes

Notes